Investigation of New Target Materials for Direct Dark Matter Detectors

DISSERTATION

der Mathematisch-Naturwissenschaftlichen Fakultät

der Eberhard Karls Universität Tübingen

zur Erlangung des Grades eines

Doktors der Naturwissenschaften

(Dr. rer. nat.)

vorgelegt von

Christof Sailer

aus Sulz a. N.

Tübingen

2014

Contents

CONTENTS

List of Figures

List of Tables

Abstract

Nowadays there is strong evidence that a large fraction of the matter in the universe is of a yet unknown type, which is usually called dark matter (DM). It is not composed of quarks and also not interacting electromagnetically. The CRESST dark matter search is looking for signatures of these DM particles by calorimetrically measuring the recoil energies of particles hitting an array of well shielded $CaWO_4$ crystals with $\sim 10\,kg$ combined mass at operating temperatures of a few mK. Electromagnetically interacting particles are discriminated by simultaneously measuring the produced scintillation light for each recoil. As the current upper limits for the DM-to-normal matter interaction cross section are on the level of $8 \cdot 10^{-46}\,cm^2$, large target masses are needed to achieve sufficient sensitivities to detect the DM recoils.

Therefore, in order to increase the capacity for testing, characterizing and further improving CRESST-type detectors, a new shallow underground laboratory was set up during this thesis. The setup was commissioned and tested by operating a standard low temperature detector with a Sapphire absorber. Stable operating conditions and a good detector resolution could be achieved.

One of the crucial components of a CRESST detector is the superconducting phase transition thermometer that allows to measure temperature changes of the absorber crystal on the order of µKs. In order to measure the superconducting transition curve of such thermometers, the necessary equipment was set up and tested. Several measurements with already characterized and not yet investigated transition edge sensors (TES) were performed yielding well resolved R(T) curves with good reproducibility.

One of the major advantages of the CRESST-type detectors is the flexibility in choice of the target material, as there is a large number of scintillating crystals available. This is of importance, as the DM cross section is expected to scale with mass number A^2. Therefore, this thesis investigated the possible use of Sodium Iodide (NaI) and Lithium Fluoride (LiF) as absorber crystals. NaI is interesting, as there is a claim of a DM-induced modulation signal in NaI(Tl) scintillation counters by the DAMA collaboration, attributed to Earth's motion relative to a DM halo. This thesis discusses if a NaI crystal can be used in a CRESST-type DM detector and under which conditions the DAMA signal could be probed with such a device. It is shown that only a small target mass of $\sim 1\,kg$ is enough to test this claim. As NaI is highly hygroscopic, it has never been used in low temperature detectors. In this work a handling procedure was developed and tested that allows to operate such crystals in a dilution refrigerator. It has been shown that the cooling and the gluing of the thermometer can be achieved without damaging the material. The operation of a prototype could though not yet be demonstrated due to contacting issues, which can however be overcome.

As a part of the investigation, the light yield (LY) of pure NaI and NaI(Tl) under α irradiation was measured as a function of the temperature, to check if there is sufficient light at low temperatures to allow for efficient discrimination of electromagnetically interacting particles. For pure NaI a LY of 1.2 times that of $CaWO_4$ was measured at $6\,K$, which is also found for NaI(Tl). Comparing to available data at $78\,K$, it seems that even a factor of up to 2.15 is possible. The LY data of pure NaI above $4\,K$ confirmed the findings of the only available study on this subject and was extended below $4\,K$ for the first time. For NaI(Tl) an increase in the LY below $60\,K$ was discovered. Decay time studies of the pure and the doped sample were performed and gave strong indications that the LY behavior of NaI(Tl) at low temperatures is dominated by the "pure" lattice properties and thus no longer associated to the Tl^+ centers, but due to self-trapped exciton emission.

LiF was studied as a possible option to monitor the neutron flux inside the CRESST setup, as neutrons can mimic DM signals. Additionally, the LY of LiF was measured to check if the crystal could also be used for DM detection. At $1.6\,K$ a value of $450 \pm 50\,(ph/MeV)$ was found for a synthetically grown crystal and $420 \pm 50\,(ph/MeV)$ for a natural crystal of similar size at $1.8\,K$. The values agree well with the only other available publication on this subject. No difference between the natural and the synthetic sample could be found. A slightly better neutron detection performance was calculated for LiF, compared to $CaWO_4$, yet due to the low light output the material can not be used for DM detection.

Investigating the decay time behavior of LiF below $60\,K$, a fast decay time constant with $\tau = 5 \pm 0.8\,ns$ was discovered that has not been reported in literature yet.

Zusammenfassung

Es gibt heutzutage starke Hinweise darauf, dass ein großer Teil der Materie im Universum aus unbekannten Teilchen, gewöhnlich Dunkle Materie (DM) genannt, besteht. Diese sind nicht aus Quarks aufgebaut und wechselwirken nicht elektromagnetisch. Das CRESST Experiment zur Suche nach DM hält nach Spuren dieser Teilchen Ausschau, indem die Rückstoßenergien von Teilchen in gut abgeschirmten $CaWO_4$ Kristallen mit ca. 10 kg Gesamtgewicht, die bei Temperaturen von einigen mK betrieben werden, kalorimetrisch gemessen werden. Elektromagnetisch wechselwirkende Teilchen können durch die gleichzeitige Messung des pro Rückstoß produzierten Szintillationslichts diskriminiert werden. Da die derzeitige Obergrenze für den Wechselwirkungsquerschnitt von Dunkler Materie im Bereich von $8 \cdot 10^{-46} \, cm^2$ liegt, sind große Detektormassen notwendig, um genügend Sensitivität zu erreichen, damit DM-Rückstöße nachgewiesen werden können. Deshalb wurde im Rahmen dieser Arbeit ein neues Untergrundlabor eingerichtet, um Detektoren vom CRESST-Typ zu testen, zu charakterisieren und weiterzuentwickeln. Zur Inbetriebnahme und zur Überprüfung des Aufbaus wurde ein Standard-Tieftemperaturdetektor mit Saphirabsorber betrieben. Dabei wurden stabile Betriebsbedingungen und eine gute Detekorauflösung erreicht.

Eine der wichtigsten Komponenten eines CRESST-Detektors ist das supraleitende Phasenübergangsthermometer (SPT), welches die Messung von Temperaturänderungen des Absorberkristalls im Bereich von µK ermöglicht. Um die supraleitenden Übergangskurven dieser Thermometer zu messen, wurde die notwendige Messausrüstung aufgebaut und getestet. Mehrere Messungen mit bereits vermessenen und noch unvermessenen SPTs wurden durchgeführt. Die Messungen lieferten gut aufgelöste und reproduzierbare R(T) Kurven.

Einer der größten Vorteile der CRESST-Detektoren ist die Flexibilität in der Wahl des Absorbermaterials, da es eine große Anzahl an szintillierenden Kristallen gibt. Dies ist wichtig, da man erwartet, dass der DM-Wirkungsquerschnitt mit der Massenzahl A^2 skaliert. Darum wurde in dieser Arbeit der mögliche Einsatz von Natriumiodid (NaI) und Lithiumfluorid (LiF) als Absorberkristall untersucht. NaI ist deshalb interessant, weil die DAMA Kollaboration behauptet, ein von DM erzeugtes, modulierendes Signal in ihren NaI(Tl) Szintillationszählern zu beobachten, das der Bewegung der Erde relativ zu einem DM-Halo zugeschrieben wird. Diese Arbeit diskutiert, ob NaI-Kristalle in DM-Detektoren vom CRESST-Typ eingesetzt werden können und unter welchen Bedingungen solch ein Instrument das DAMA-Signal untersuchen könnte. Es wird gezeigt, dass eine kleine Detektormasse von ~ 1 kg ausreicht, um die Behauptung zu überprüfen. Da NaI stark hygroskopisch ist, wurde das Material bisher noch nicht in Tieftemperaturdetektoren eingesetzt. In dieser Arbeit wurde eine Prozedur zur Handhabung entwickelt und getestet, die es ermöglicht, die Kristalle in einem Mischkryostaten zu betreiben. Es wurde gezeigt, dass das Abkühlen und das Kleben des Thermometers durchgeführt werden können, ohne das Material zu beschädigen. Der Betrieb eines Prototyps konnte jedoch aufgrund von Kontaktierungsschwierigkeiten noch nicht demonstriert werden. Letztere sind jedoch lösbar.

Im Zuge dieser Untersuchung wurde die Temperaturabhängigkeit der Lichtausbeute (LA) von reinem NaI und NaI(Tl) bei α-Anregung gemessen, um zu überprüfen, ob bei tiefen Temperaturen genügend Licht vorhanden ist, um elektromagnetisch wechselwirkende Teilchen effizient zu diskriminieren. Für reinen NaI wurde bei 6 K eine 1,2-fache LA im Vergleich zu $CaWO_4$ gemessen, ebenso für NaI(Tl). Vergleiche mit vorhandenen Daten bei 78 K legen nahe, dass sogar ein Faktor von bis zu 2,15 möglich ist. Die gemessene LA von reinem NaI oberhalb von 4 K bestätigen die Ergebnisse der bislang einzigen verfügbaren Studie zu diesem Thema und wurde in dieser Arbeit erstmals unter 4 K gemessen. Für NaI(Tl) wurde unterhalb von 60 K ein erneuter Anstieg der LA entdeckt. Untersuchungen der Abklingzeiten der reinen und der dotierten Probe wurden durchgeführt und ergaben starke Hinweise darauf, dass das Verhalten der LA von NaI(Tl) bei tiefen Temperaturen von den "reinen" Gittereigenschaften dominiert ist und deshalb nicht länger mit den Tl^+ Zentren assoziiert, sondern durch "self-trapped" Exziton-Emission verursacht ist.

LiF wurde als mögliche Option den Neutronenfluss im CRESST-Aufbau zu überwachen, untersucht, da Neutronensignale ununterscheidbar von DM Signalen sind. Zusätzlich wurde die LA von LiF gemessen, um zu überprüfen, ob sich der Kristall auch zur DM-Detektion eignet. Bei 1,6 K wurde für einen synthetisch hergestellten Kristall ein Wert von $450 \pm 50 \, (ph/MeV)$ und $420 \pm 50 \, (ph/MeV)$ für einen natürlich gewachsenen Kristall gleicher Größe bei 1,8 K gemessen. Diese Werte stimmen sehr gut mit der einzig anderen

verfügbaren Studie zu diesem Thema überein. Zwischen der natürlichen und der synthetischen Probe konnte kein Unterschied festgestellt werden. Eine leicht höhere Neutronennachweiswahrscheinlichkeit, verglichen mit $CaWO_4$, konnte für LiF berechnet werden. Jedoch kann das Material aufgrund der geringen Lichtausbeute nicht zur DM-Detektion eingesetzt werden.

Bei Untersuchungen der Abklingzeiten von LiF unter $60\,K$ wurde eine schnelle Abklingzeit mit $\tau = 5 \pm 0.8\,ns$ entdeckt, die bisher noch nicht in der Literatur zu finden ist.

List of Abbreviations

APF	additional positive feedback
CDM	cold dark matter
CMB	Cosmic Microwave Background
cMSSM	constrained Minimal Supersymmetric Model
CND	CRESST-like NaI detector
COBE	Cosmic Background Explorer
CRESST	Cryogenic Rare Event Search with Superconducting Thermometers
DAMA	Dark Matter Experiment, Italy
DAQ	data acquisition
DM	dark matter
DMS	dark matter search
DSNB	diffuse supernova background
ESD	electrostatic discharge
EURECA	European Underground Rare Event Calorimeter Array
FADC	Flash Analog to Digital Converter
fcc	face-centered cubic
FiFo	Fan In - Fan Out
FLL	flux-locked loop
FLRW	Friedmann-Lemaître-Robertson-Walker
GF	gravitational focusing
GPIB	General Purpose Interface Bus
iDM	inelastic dark matter
INFN	Istituto Nazionale di Fisica Nucleare
LD	light detector
LHC	Large Hadron Collider
LNGS	Laboratori Nazionali del Gran Sasso
LTD	low temperature detector
LVD	Large Volume Detector
LY	light yield
MAX	Measurement and Automation Explorer
MCA	Multi Channel Analyzer
MoND	Modified Newtonian Dynamics
NIM	Nuclear Instrumentation Module
NTD	neutron transmutation doped
OFHC	oxygen-free high conductivity
p.e.	photo electron(s)
PD	phonon detector
PID	proportional, integral, differential
PMT	photomultiplier tube
PSA	pulse-shape analysis
PTB	Physikalisch-Technische Bundesanstalt
PXI	PCI eXtensions for Instrumentation
q.e.	quantum efficiency
QCD	quantum chromodynamics
RMS	root mean square
ROI	region of interest
SD	spin-dependent
SDSS	Sloan Digital Sky Survey
SI	spin-independent
SQUID	Superconducting Quantum Interference Device
STE	self-trapped exciton

SUSY .... supersymmetry
SX .... self-trapped exciton emission
TDC .... Time to Digital Converter
TDE .... thermodynamical equilibrium
TES .... transition edge sensor
TF .... timing filter
UHV .... ultra-high vacuum
UV .... ultraviolet
VI .... Virtual Instrument
WIMP .... weakly interacting massive particle
WMAP .... Wilkinson Microwave Anisotropy Probe

1

Introduction

Starting in the early years of the 20th century, many discoveries in astronomy helped us to refine our view on the evolution of the Universe, formation and composition of matter and the general energy content of the Universe. In particular it was suggested, that most of the matter in the Universe is of a yet unknown kind, called *dark matter* (DM). Nowadays, nearly 80 years after the term was first coined, the nature of this matter still remains unclear. In the search for DM the fields of particle physics and astrophysics have converged and a lot of effort is currently made, to pin down this "missing mass" in the Universe. This chapter will first introduce the missing mass problem (sec. 1.1) and the pieces of evidence that suggest the presence of a dark matter component in the Universe. In sec. 1.2 the direct dark matter search experiment CRESST II will be presented, as this thesis was carried out within this collaboration. Besides setting up a new test facility, which will be described in chapter 2, new target materials for the CRESST experiment were investigated. In sec. 1.3 a long standing claim of the detection of a dark matter signal by the DAMA collaboration will be discussed, followed by an overview on the current experimental status of direct dark matter detection (sec. 1.4) and a short discussion on the controversial claims. The last section 1.5 will then introduce a concept investigated during this thesis that might help to clarify the situation.

1.1 Dark matter and cosmology

1.1.1 The missing mass problem

In 1933 the Swiss physicist Fritz Zwicky noticed a peculiar behavior in the velocity distribution of galaxies in the Coma Cluster: Calculating the mean velocity of the galaxies in the cluster by measuring the cluster's mass using the Mass-luminosity relation and comparing it to the velocity distribution obtained by his measurements, he realized that the cluster's total mass would have to be much higher. He thus concluded that [...]*if this should be confirmed, it would lead to the astonishing result that dark matter is present at a much higher density than luminous matter*[1] [1]. Although he overestimated the mass discrepancy as he used Hubble's inaccurate value for the Hubble constant [2], modern values for the Coma Cluster's velocity dispersion agree well with Zwicky's results [2, 3]. He thus started the discussion about the *missing mass problem* in the Universe and was the first one to realize that *dark matter* could be present in galaxy clusters. However, his use of the phrase *dark matter* was different to the current understanding of the term, as it simply indicated that this matter was *non-luminous*. Yet, also already in 1937, he expressed his belief that deriving the masses of clusters and nebulae from luminosities and the inner rotation might be unreliable [4], which can be seen as a first hint on a supposed dark halo around those objects. In the same publication he also suggested to use gravitational lensing as a tool to further examine the problem. In 1979 the first gravitationally lensed object was found by Walsh, Carswell and Weymann. They observed a double radio signal from the quasar Q0957+561 and identified it as a gravitationally lensed signal of one single object, due to the similarity in the respective spectra [5]. The lensing object was later found to be Q0957+561 G1, which is a giant elliptical galaxy [6]. Many other discoveries of gravitational lenses followed and finally confirmed Zwicky's prediction and his findings of missing mass in clusters.

---

[1] His paper was published in German. The quote was translated by the author.

As reported in Ashman's review on the early history of dark matter [7], Zwicky's findings were mostly ignored or forgotten well up into the 1970s, although meanwhile multiple discoveries of missing mass systems had emerged. Already in 1939 Babcock reported [...] *unexpectedly large circular velocities of* [...] *the outer parts of the spiral* [8] galaxy M31, better known as the Andromeda Nebula. Similar results accumulated, showing that the circular velocities of galaxies diverged from the theoretical expectation with increasing distance from their luminous centers, which led Ostriker, Peebles and Yahil to note in 1974, that the [...] *masses of ordinary spiral galaxies may make a cosmologically interesting contribution* [9]. It became clear that most rotation curves of spiral galaxies did not show a Keplerian drop-off in velocity once the tracing objects were located outside the luminous center. Thus the idea of a dark halo surrounding the galaxy and extending well beyond the visible cores became more popular.

A particularly interesting example for such a rotation curve can be found in fig. 1.1, which was obtained by Carignan and Purton [10] for the galaxy DDO 154. The curve could be measured out up to six times the optical radius R_{H0}. Measuring the H I flux[2], the mass of the hydrogen gas could be derived and the contributions of the star and gas component to the rotational velocity at a distance R is given in fig. 1.1 as the lower dashed and the dash-dotted lines. Obviously they cannot account for the high velocities measured. Assuming a dark halo (long dashed line), the curve can be fitted well. At large distance the velocity drops again. The upper dashed line shows the Keplerian drop-off $\sim \sqrt{MG/r}$ for a galaxy of $3.0 \times 10^9 \, M_\odot$ mass, indicating that the edge of the dark halo has been probed by the tracing objects, limiting the total size of the galaxy to $\leq 8 \, \mathrm{kpc}$. The derived values imply that about 90 % of the total mass of DDO 154 is dark.
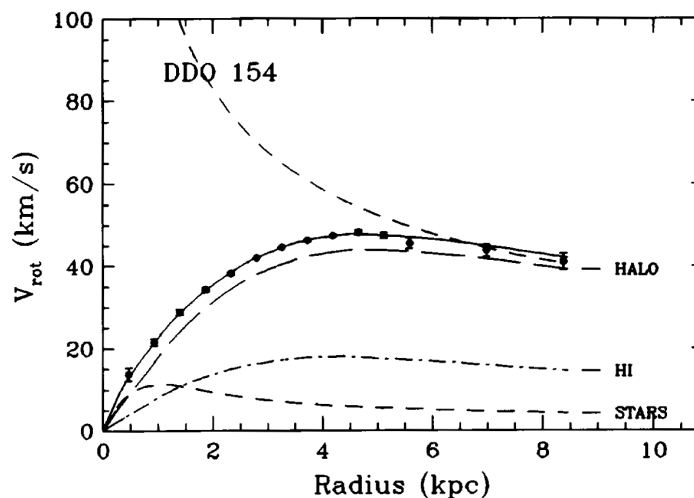
Figure 1.1: Rotation curve of DDO 154. Values for H I mass and the mass of luminous matter have been measured, indicating that about 90 % of the galaxy consists of dark matter. The decreasing velocities at high radii suggest that the edge of the dark halo is reached. The upper dashed line shows the expected Keplerian drop-off for a disk mass of $3.0 \times 10^9 \, M_\odot$. Figure as in [10].

The peculiar behavior of rotational curves has also spurred discussion on the validity of Newton's law in the limit of small accelerations. In 1983 Milgrom proposed that this law could break down at accelerations that are small, compared to a certain scale parameter a_0, thus replacing $\mathbf{F} = m \cdot \mathbf{a}$ by

$$\mathbf{F} = m\mu(a/a_0)\mathbf{a} \tag{1.1}$$

where the function $\mu(x \gg 1) \approx 1$, preserving the well known Newtonian behavior, and $\mu(x \ll 1) \approx x$, leading to a different force for small accelerations as encountered e. g. in galaxies [11]. Milgrom showed that

---

[2]Neutral hydrogen produces a characteristic signal in the radio band due to it's hyperfine transition. The corresponding wavelength is 21 cm.

rotational curves could thus be explained without the assumption of a dark matter halo. Yet there are other indications for dark matter that can not easily be explained by the Modified Newtonian Dynamics (MoND) hypothesis, such as the matter density distribution in galaxy mergers. This will be discussed in the following.

In 2006 Clowe et al. published a report on combined observations of the merging cluster 1E 0657-558, also called the Bullet Cluster[3]. This cluster consists of two separated mass concentrations, one smaller, western subcluster and the main eastern cluster [12]. They are separated by 0.72 Mpc on the sky and have hot x-ray emitting plasma concentrations that trail behind the stellar components, leaning toward the center of the total system. Examinations in x-ray by the Chandra Satellite indicate that the smaller subcluster penetrated the main cluster some 100 Myr ago [12], leading to a mixing of the electromagnetically interacting plasma clouds that slowed them down with respect to the stellar components, since the latter behave like a collisionless medium. As the main mass of a cluster, under the assumption of a no-dark matter system, should be in the plasma[4], lensing data was obtained using the Hubble Space Telescope to examine the gravitational profile. The combined results can be found in fig. 1.2. The color image (left) and x-ray image (right) are supplemented with green contours in both panels, indicating the gravitational contours obtained by weak lensing[5]. The white contours show the errors on the positions of the obtained matter centers, corresponding to 68.3 %, 95.5 %, and 99.7 % confidence levels. The blue plus signs denote the centers of the hot plasma clouds. The white horizontal bar is indicating 200 kpc to set the scale.
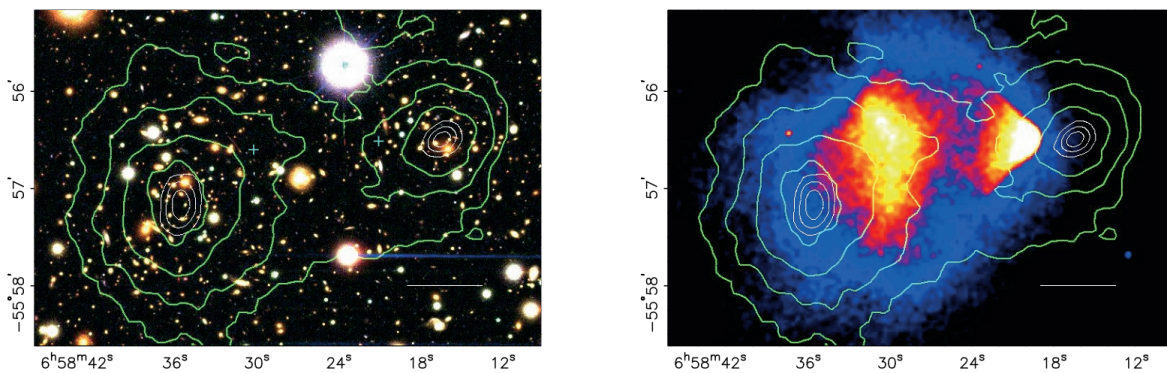
Figure 1.2: The merging cluster 1E 0657-558 color image (left) and x-ray image (right). The green contours in both panels are derived by weak lensing. The white contours show the errors on the positions of the obtained matter centers, corresponding to 68.3 %, 95.5 %, and 99.7 % confidence levels. The blue plus signs denote the centers of the hot plasma clouds. The white horizontal bar is indicating 200 kpc. Figures as in [12].

The mass centers are clearly found to coincide with the stellar components, not with the plasma. Thus there has to be another matter component, by far exceeding the stellar mass and also behaving collisionless - like the stars. This strongly supports the assumption that large amounts of the mass of galaxies and clusters are made up by dark matter, interacting only gravitationally and maybe on the weak scale or even lower. Thus the dark matter components would also pass each other without interacting, staying ahead of the slowed plasma [12].

A similar situation has been found in the collision cluster MACS J0025.4-1222, reported in 2008 by Bradač et al. in [13]. Fig. 1.3 shows the combined results[6]. The optical image (color image) and near infrared (yellow)

---

[3]Strictly speaking this name applies only to the smaller "projectile" cluster that has penetrated the bigger cluster.

[4]Clowe cites $1-2\,\%$ of the total mass in the stellar component as opposed to $2-15\,\%$ in the plasma. The rest being "missing mass", e. g. dark matter or the effect of a different Newtonian behavior.

[5]As opposed to strong gravitational lensing, this method does not search for multiple images of a singular object, but uses a statistical approach to look for characteristic distortions of multiple background galaxies.

[6]The image has been taken from the Hubble release. For the detailed contours of x-ray and lensing data check the cited publication [13].

where obtained by Hubble, the x-ray data (violet, middle) by Chandra and lensing data by Hubble is given in blue. As in the Bullet Cluster case, the mass centers are not found in the hot gas, but alongside the stellar components. Again, this strongly supports the dark matter interpretation.

Figure 1.3: Collision cluster MACS J0025.4-1222. Optical image and near infrared (yellow) by Hubble, x-ray (violet, middle) by Chandra and lensing data (blue). As in the Bullet Cluster case, the mass centers are not found in the hot gas, but alongside the stellar components. Image credit: NASA, ESA, CXC, M. Bradac (University of California, Santa Barbara), and S. Allen (Stanford University).

Some efforts have been made by the MoND community in order to show that these cases can also be understood in the MoND framework. Yet the bottom line seems to be that also an additional "dark" mass component is needed [14, 15].

1.1.2 The Cosmic Microwave Background and Baryonic Acoustic Oscillation

One of the great successes of the Big Bang theory was the prediction of the Cosmic Microwave Background (CMB), originating from the epoch of Recombination, where the early, hot Universe had cooled enough to allow the formation of neutral atoms. Thus the photons and matter could decouple, releasing the CMB photons approximately 378,000 years after the Big Bang[7] with a black-body energy spectrum, today peaking at $2.72548 \pm 0.00057 \, \text{K}$ [16]. Fluctuations around the mean temperature of the order 10^{-5} in the CMB have been discovered by the Cosmic Background Explorer (COBE) satellite [17, 18] and since then measurements have been refined by the Wilkinson Microwave Anisotropy Probe (WMAP) [19] and the Planck satellite [20].

The current sky map by Planck can be found in fig. 1.4. The warmer (red) anisotropies represent overdense regions in the primordial plasma, the cooler spots (blue) regions with lower density. Those fluctuations are considered to be the seeds for structure formation in the following evolution of the Universe. As the Universe at the time of Recombination was still hot, the processes back then can be described by plasma and standard particle physics. In order to evaluate the anisotropy data, the map in fig. 1.4 is presented as a temperature angular power (TT) spectrum. The corresponding plot can be found in fig. 1.5. The spectrum shows the acoustic oscillations in the photon-baryon plasma, where the photons exercise a radiative pressure that hinders baryons from clustering, while the gravitational interaction will favor forming overdense regions. The

---

[7]Estimating the time requires a cosmological model. The number stated is derived using the ΛCDM model, which is considered the standard model of cosmology.
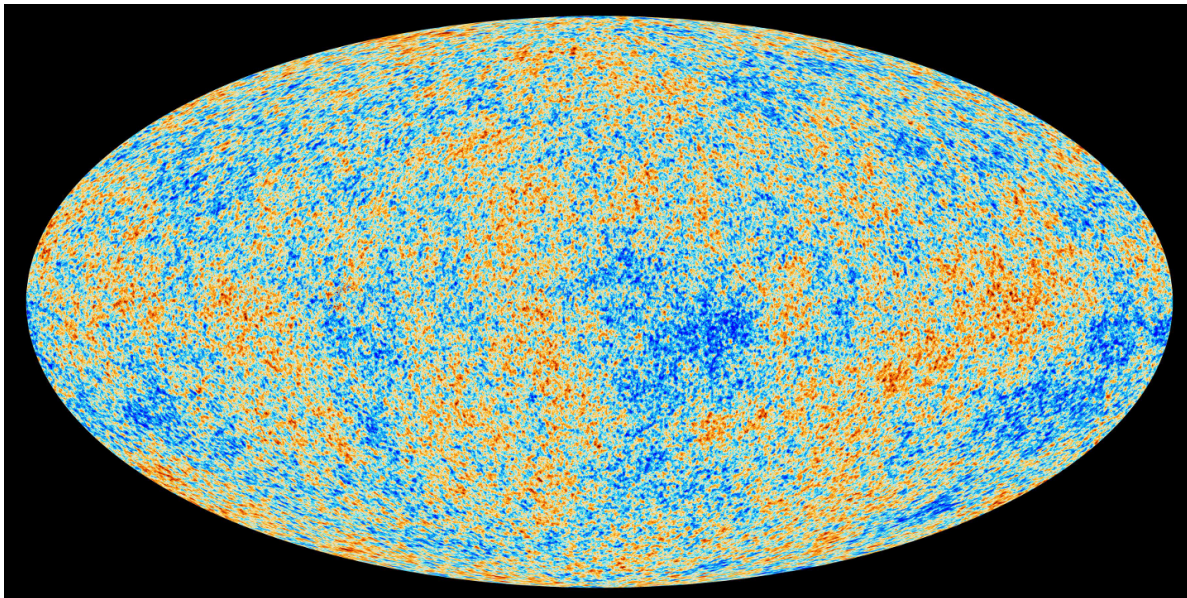
Figure 1.4: The Planck CMB sky map of 2013. Temperature fluctuations relative to the mean $2.725\,\mathrm{K}$ are given in red (hotter) and blue (cooler). The temperature range is $\pm\,200\,\mu\mathrm{K}$. Foreground e. g. due to movement dipole and the galactic plane, is subtracted. This image is an imprint of the matter density distribution at the time of recombination in the early Universe, around $378\,000\,\mathrm{yr}$ after the Big Bang. Image credit: ESA and the Planck Collaboration

overall spectrum, the peak-heights, positions, the damping, and the odd-to-even peak ratio allows to measure the baryon density, curvature of the Universe, dark matter density, reionization redshift and other important parameters. The red line in fig. 1.5 shows the best fit of the ΛCDM model[8], which is also called the standard model of Big Bang cosmology and uses the Friedmann-Lemaître-Robertson-Walker (FLRW) metric. Using this simple model, described by only six parameters, the CMB data can be fitted quite well. Yet there are deviations at low multipoles that are currently discussed, e. g. there might be hints for inflation in the data [21].

The latest cosmological parameters derived from such a TT power spectrum give the following composition for the energy content of the Universe: $68.3\,\%$ are in dark energy, $26.8\,\%$ in dark matter and $4.9\,\%$ in baryonic matter [20]. Alternative fits assuming a non-dark matter model can not reproduce the spectrum that well. Thus the CMB provides another hint for the existence of dark matter.

If the pre-CMB Universe can really be described as a baryon-photon plasma, one would expect another distinct feature from the decoupling epoch: As already discussed, the counterplay between gravitation and photon pressure will lead to acoustic oscillations in the plasma. Considering an overdense fluctuation before decoupling, baryons and photons move outward the region together, according to the respective plasma frequency. After decoupling, the photons escape and since the radiation pressure is now gone, gravitation will form baryon clusters at the sound horizon. This should lead to a preferred distance of galaxies, that can be extracted by statistically comparing the distances of one galaxy to all other galaxies.

This feature has indeed been measured in the Sloan Digital Sky Survey (SDSS) data. The project was started to build a map of large parts of the Universe by mapping the positions of luminous objects to reveal the large scale structure of matter. The map obtained by SDSS can be found in fig. 1.6. Analyzing the correlation function of comoving galaxy separation distance, the collaboration could confirm that there is a distinct, preferred spacing of galaxies. In fig. 1.7 this shows up as a peak at $\sim 100\,\mathrm{h}^{-1}\,\mathrm{Mpc}$, where h is the

---

[8]Λ stands for a cosmological constant term to explain the accelerated expansion of the Universe, CDM for *cold dark matter*.
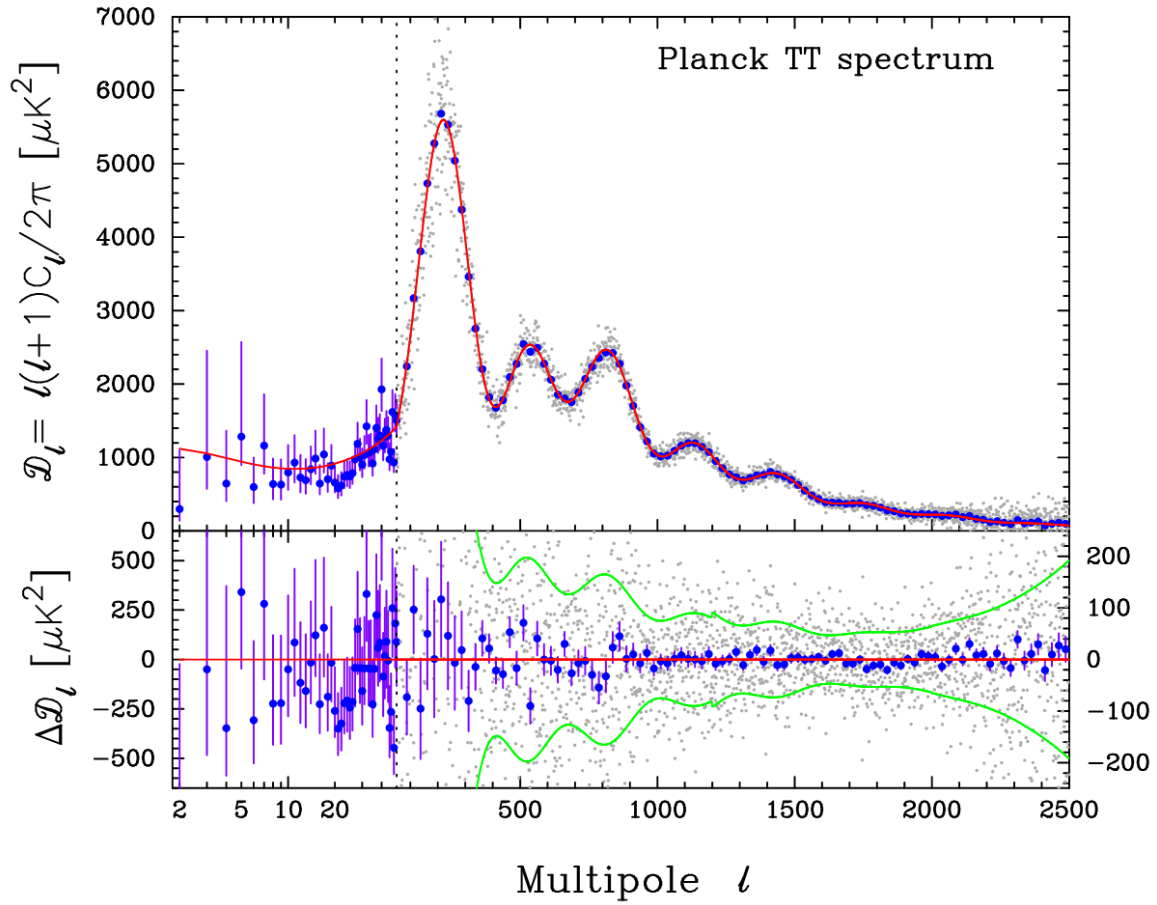
Figure 1.5: The foreground-subtracted Planck CMB temperature angular power (TT) spectrum. The gray points represent the counts for the respective multipoles, blue represents the binned data ($\Delta l \approx 31$) with related errors. The lowest order multipoles $l = 2$-50 are represented with a different scale. The red line shows the best fit for the minimal ΛCDM model. The lower part gives the resulting residuals. The green lines show the 1σ errors on the individual power spectrum estimates at high multipoles. [20]
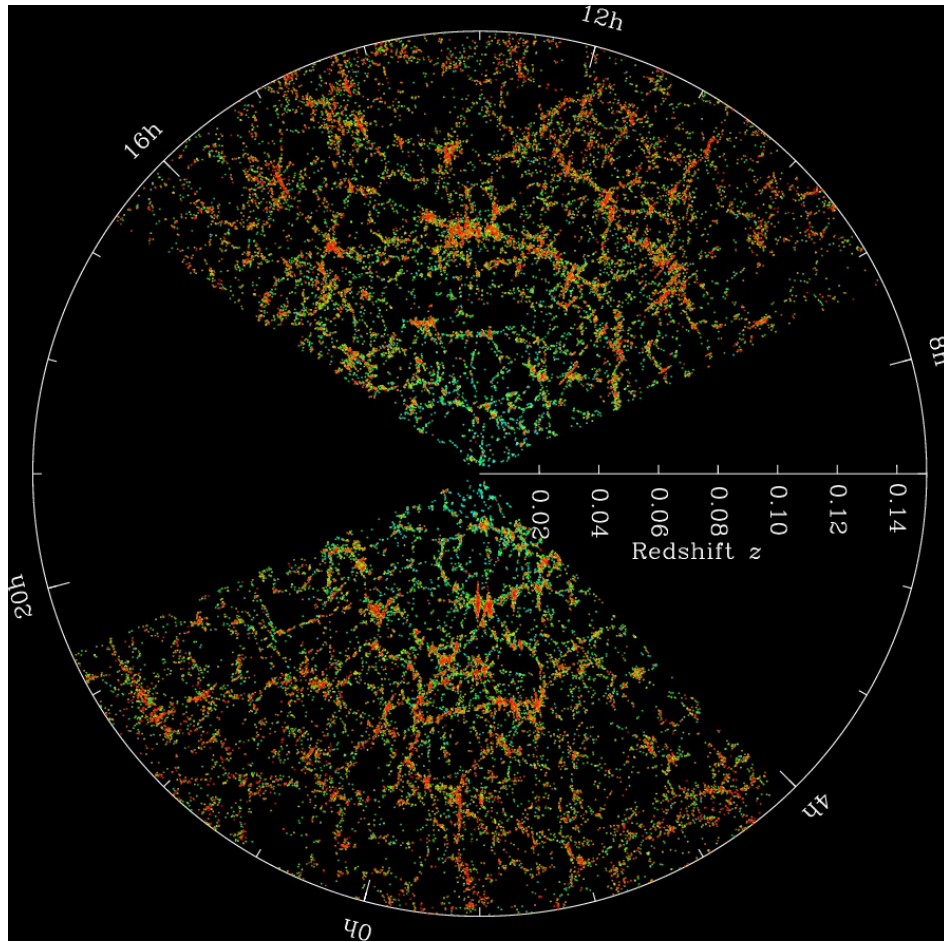
Figure 1.6: The SDSS map of the Universe. The outer galaxies are at a distance of roughly 630 Mpc or 2 Gly. Credit: M. Blanton and the Sloan Digital Sky Survey.

dimensionless Hubble constant, defined as $H_0 = 100\,h\,km\,s^{-1}\,Mpc^{-1}$. The solid lines represent different fits for CDM models, where the total matter density $\Omega_m h^2$ is varied. The inset shows an expanded view with linear vertical axis, while the main plot uses a mixed linear/logarithmic scaling [22].
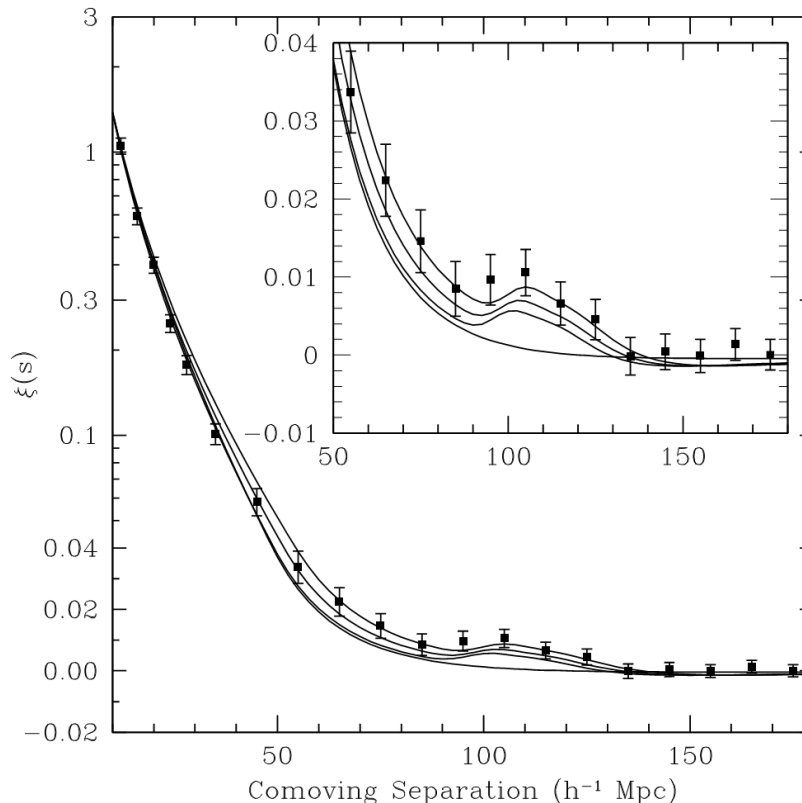
Figure 1.7: The SDSS acoustic peak at $\sim 100\,h^{-1}\,Mpc$. The sound horizon at the decoupling can be seen as a peak in the mean distance between galaxies in large structure survey data. The function ξ is the correlation function of comoving galaxy separation distance and thus a measure to find a galaxy in the vicinity at a given distance s of another one. The solid lines represent different fits for CDM models, where the total matter density $\Omega_m h^2$ is varied. The inset shows an expanded view with linear vertical axis, while the main plot uses a mixed linear/logarithmic scaling. [22]

Eisenstein et al. conclude that *the small amplitude of the features requires that there exist matter at $z \sim 1000$ that does not interact with the photon-baryon fluid, i. e., dark matter.* Detailed studies of the BAO feature have followed since then and confirmed these findings. Some of the more recent results can be found in [23] and [24].

The next section will summarize and supplement the discussed missing mass systems.

1.1.3 Missing mass on different scales

In conclusion one can say that nowadays there is evidence for missing mass in a lot of systems on different size scales (e. g. likewise mass scales) obtained with different experimental methods. Tab. 1.1 gives a non-exhaustive overview, ordered by increasing system size, to demonstrate that systematics of the observational method and the scale of the systems are unlikely to be the cause of the apparent mass deficit. Only in systems of stellar or smaller dimensions no missing mass has been found yet. The lack of evidence for such systems is no surprise, as the coupling constant for gravitational interaction is $\sim 10^{-45}$, resulting in very small effects

on the particle level.

System	observational method(s)	system size	e.g. reported in
dwarf irregular galaxies	H1 line rotational curves	$\sim 1\text{-}10\,\mathrm{kpc}$	[25], [10]
spiral galaxies e.g. Milky Way	mostly rotational curves satellite dynamics, radial velocities	$\sim 3\text{-}40\,\mathrm{kpc}$ $\sim 31\text{-}37\,\mathrm{kpc}$	[7] [26]
elliptical galaxies	line profiles, strong gravitational lensing, X-ray temperatures and velocity dispersion	$\leq 100\,\mathrm{kpc}$	[27–29]
massive elliptical galaxies	e.g. clustering of submillimeter galaxies	$\leq 1.8\,\mathrm{Mpc}$	[30]
galaxy clusters	e.g. week lensing	$\sim 2\text{-}10\,\mathrm{Mpc}$	[31]
Baryonic Acoustic Oscillations	statistical analysis of large structure data	$\sim 1.66\,\mathrm{Gpc}^{\dagger}$	[22–24, 32]
CMB	anisotropy power spectrum	$\sim 14\,\mathrm{Gpc}$	[19], [20]

Table 1.1: Observational evidence for missing mass (when considering only baryonic, radiative matter) ordered by increasing system size e.g. likewise rising mass. Note that both, the list of systems and the list of citations are not exhaustive. Systematic effects of a certain method of observation can most likely not be an explanation for the apparent missing mass, as the evidence is based on multiple, different experimental techniques.
† approximated as spherical diameter of the SDSS survey volume.

After having discussed the evidence for the presence of a dark matter component in the Universe, the next section will focus on the properties of dark matter and shortly discuss the basic concepts for dark matter detection.

1.1.4 Dark matter properties

The basic properties of dark matter can be derived from the observations presented in the last section. As the effects of dark matter are clearly visible in gravitational systems, the new particles should have non-zero mass. In addition, dark matter should not interact electromagnetically, as it does not interact with the primordial photon-baryon plasma, which means it can neither absorb nor emit photons. Due to constraints from the CMB and collider-experiment results, strong interaction is also ruled out. One is thus left with a massive particle, possibly interacting on the weak scale or lower - if there should be a fifth force, or in the worst case scenario for experimental detection, only gravitationally. Particle interactions on the weak scale are nowadays accessible for particle detectors, despite rather low ($\leq \mathrm{pb}$) cross sections.

Depending on the nature of these particles, furthermore denoted as χ, two main concepts of detection are available:

If dark matter can decay into standard model matter (SM), either by annihilation $\chi + \chi \to \mathrm{SM}$ or directly as $\chi \to \mathrm{SM}$, one might be able to detect the signal from these processes e.g. as an excess of photons or cosmic rays. This is the so-called *indirect dark matter search* (indirect DMS). The cross section for the decay/annihilation of these particles has to be small, otherwise dark matter produced in the Big Bang would have already decayed in large quantities and the abundance of dark matter today could not be matched.

The other concept assumes that dark matter is stable and DM particles could interact with normal matter via elastic scattering as $\chi + \mathrm{SM} \to \chi + \mathrm{SM}$. These experiments are classified as *direct dark matter searches*

(direct DMS). As the nature of DM is yet unknown, experiments of both search concepts are needed. This thesis will focus on the direct dark matter detection. For an overview on the status and concepts of indirect searches the reader is referred to e. g. [33, 34].

The DM overdensity on Earth can be derived by observing the kinematics of a large number of stars at a few kpc distance from the Galactic mid plane. Multiple surveys have been performed and state $\rho = 0.3 \pm 0.1 \, \mathrm{GeV}$ cm^{-3}, see e. g. [35]. To compare this number: The overall DM density in the Universe is derived from the CMB data as explained in sec. 1.1.2 and currently given as $\rho \simeq 1.27 \times 10^{-6} \, \mathrm{GeV \, cm}^{-3} \simeq 1.27 \, \mathrm{keV \, cm}^{-3}$ when using the 2013 Planck value [20]. Due to this overdensity it might be possible to directly detect DM particles on Earth, if the DM-to-standard matter cross section is not too low.

The interaction cross section σ_{int} depends on the mechanism through which the particle couples to standard matter. Fig. 1.8 shows some dark matter candidates and their corresponding mass regions and interaction cross sections σ_{int}. Standard neutrinos are nowadays ruled out as primary DM component: Comparing the matter density $\rho_m = 0.3175 \, \rho_c = 1.51 \, (\mathrm{keV/c}^2) \, \mathrm{cm}^{-3}$ with the number density of neutrinos in the Universe, which is fixed by the ν-electron decoupling in the early Universe to $\sim 112 \, \mathrm{cm}^{-3}$ per flavor, the sum of all three neutrino masses would have to be $\simeq 13 \, \mathrm{eV/c}^2$ to make up for the total DM in the Universe. Yet, due to their low mass, the velocities of these particles would provide a "radiative" pressure, hindering structure formation. As the large scale structure of the Universe has been mapped by the SDSS (see sec. 1.1.2) and 2dF sky surveys, the matter distribution can be used as input for simulations of structure formation under the assumption of a certain value for $\Sigma m_{\nu_{e,\mu,\tau}}$. Values obtained are much lower than $13 \, \mathrm{eV/c}^2$. The current limit for $\Sigma m_{\nu_{e,\mu,\tau}}$ is $0.23 \, \mathrm{eV/c}^2$ according to [20]. Thus neutrinos can not make up a major fraction of DM.
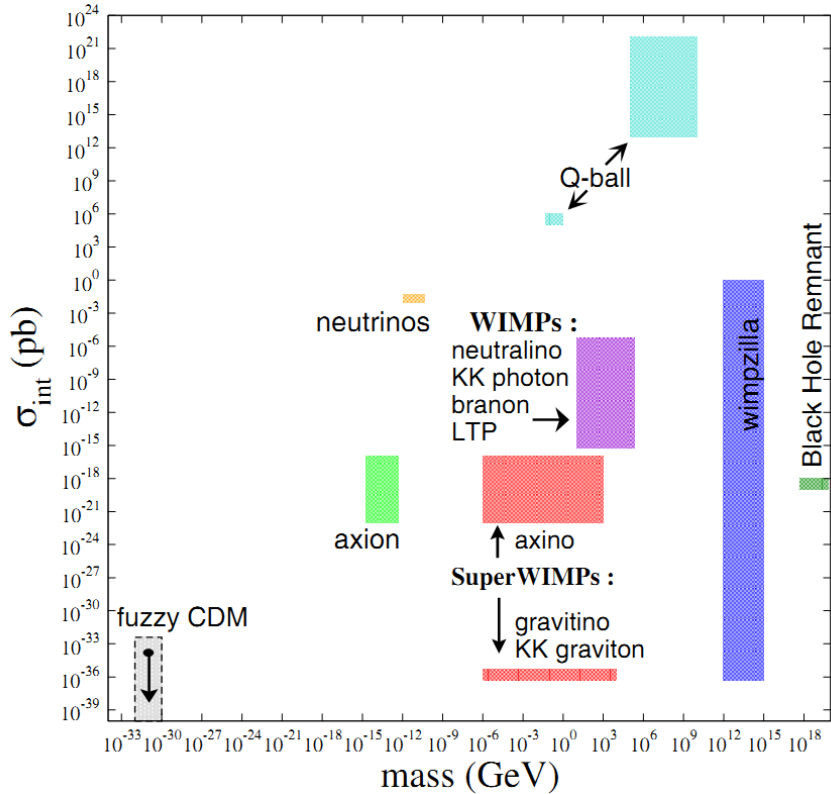

Figure 1.8: Some dark matter candidates, corresponding mass regions and interaction cross sections σ_{int}. This work will focus on WIMPs. [36]

Axions, as introduced by Peccei and Quinn [37] to solve the strong CP-violation problem in quantum chromodynamics (QCD), might provide a suitable DM candidate, if they exist. Q-balls are stable non-topological solitons, which appear in supersymmetric extensions of the standard model and carry both, Baryon and Lepton numbers [38]. There are searches for signatures of such particles e. g. in the Large Hadron Collider (LHC) data at CERN. Axino and Gravitino particles are also candidates that require Supersymmetry (SUSY) to be realized in nature. Weakly Interacting Massive Particles (WIMPs) also occur in SUSY-models, though not exclusively. Even if SUSY does not exist, WIMP particles might still be found in nature. Yet, the currently most favored WIMP candidate, the neutralino, is the lightest, stable particle in different SUSY models. It is a superposition of the supersymmetric partners of the photon, Z^0 and the Higgs-bosons [39]. The composition depends on the specific model, e. g. it can be more Higgsino- or Photino-like. Fuzzy CDM postulates ultra-light scalar particles with m $\sim 10^{-22}$ eV that initially are in a Bose-Einstein condensate phase, stabilizing gravitational collapses due to their wave properties [40]. Like the Graviton, the suspected force carrier of gravitation, which is also a possible DM candidate, fuzzy CDM is currently not accessible by any direct detection approach. For the even more exotic candidates like Black Hole remnants and Wimpzillas see [41] and [42]. At present, axions and WIMPs are the most favored candidates for direct detection experiments. This work will focus on the weakly interacting massive particles.

1.1.5 Direct dark matter detection

WIMPs might be detected by elastic scattering on standard matter targets. If an incident DM particle with energy E_χ and mass m_χ scatters elastically and coherently on a target nucleus of mass m_T, it will deposit the recoil energy E_R as

$$E_R = E_\chi \frac{2\mu^2}{m_\chi m_T}(1 - cos\theta) \qquad (1.2)$$

where μ is the reduced mass $m_\chi m_T/(m_\chi + m_T)$ and θ the scattering angle of the DM particle. The incident energy E_χ is defined by the WIMP mass and the velocity distribution in Earth's rest frame. Studying the spherically averaged equilibrium cold dark matter halo profiles in N-body simulations, circular velocity distributions can be calculated, see e. g. [43]. These profiles usually are approximated by a Maxwell-Boltzmann velocity distribution, assuming that the halos are non-rotating and were thermalized by fluctuations in the gravitational potential during the initial collapse, which is a process called "violent relaxation" [44]. Thus the WIMP velocity distribution can be written as

$$f(\mathbf{v}, \mathbf{v}_\oplus) = e^{(\mathbf{v}+\mathbf{v}_\oplus)^2/v_0^2} \qquad (1.3)$$

where $\mathbf{v}$ is the velocity onto the target and $\mathbf{v}_\oplus$ Earth's velocity. Following [45] the differential particle density can be written as

$$dn = \frac{n_0}{k}f(\mathbf{v}, \mathbf{v}_\oplus)d^3v \qquad (1.4)$$

with the normalization constant k ensuring that

$$\int_0^{v_{esc}} dn \equiv n_0 = \frac{\rho_\chi}{m_\chi} \qquad (1.5)$$

The maximum allowed velocity is of course the galactic escape velocity $v_{esc} \simeq 600$ km/s. For practical purposes $v_{esc} \to \infty$ is a good approximation [45]. Therefore

$$k = (\pi v_0^2)^{3/2} \qquad (1.6)$$

Considering a target nucleus with mass A and denoting the WIMP interaction cross section as σ, the event rate per unit mass is

$$dR = \frac{N_A}{A}\sigma v dn \qquad (1.7)$$

with $N_A = 6.022 \cdot 10^{26}$ kg^{-1}. In the limit of zero momentum transfer, where $\sigma = \sigma_0$, the total rate will then be obtained by integrating eq. 1.7 as

$$R = \frac{N_A}{A}\sigma_0 \int v dn \equiv \frac{N_A}{A}\sigma_0 n_0 \langle v \rangle \qquad (1.8)$$

using eqs. 1.4 and 1.6. As for a Maxwell-Boltzmann distribution $\langle v \rangle = \frac{2}{\sqrt{\pi}} v_0$ holds, one can write the rate R_0 in these limits as

$$R_0 = \frac{2}{\sqrt{\pi}} \frac{N_A}{A} \sigma_0 v_0 \frac{\rho_\chi}{m_\chi} \tag{1.9}$$

In order to estimate event rates, eq. 1.9 can be rewritten using $\rho_\chi = 0.4 \, \text{GeV} \, \text{c}^{-2} \, \text{cm}^{-3}$ and $v_0 = 230 \, \text{km} \, \text{s}^{-1}$ to

$$R_0 = 0.054 \left(\frac{100}{A} \right) \left(\frac{100 \, \text{GeV}/c^2}{m_\chi} \right) \left(\frac{\sigma_0}{1 \, \text{pb}} \right) \left(\frac{\rho_\chi}{0.4 \, \text{GeV}/(c^2 \text{cm}^3)} \right) \left(\frac{v_0}{230 \, \text{km/s}} \right) \text{kg}^{-1}\text{d}^{-1} \tag{1.10}$$

So for weakly interacting particles very low count rates are expected.
Defining r to be

$$r = \frac{4\mu^2}{m_\chi m_T} \tag{1.11}$$

eq. 1.2 can be expressed as

$$E_R = \frac{1}{2} E_\chi r (1 - cos(\theta)) \tag{1.12}$$

and the recoil energy range is thus given as $0 \leq E_R \leq E_\chi \cdot r$. Assuming isotropic scattering in this energy range, the differential rate is given by

$$\frac{dR}{dE_R} = \int_{E_{min}}^{E_{max}} \frac{1}{Er} dR(E) = \frac{1}{E_0 r} \int_{v_{min}}^{v_{max}} \frac{v_0^2}{v^2} dR(v) \tag{1.13}$$

with the energy $E_0 = \frac{1}{2} m_\chi v_0^2 = (\frac{v_0^2}{v^2})E$ and $E_{min} = \frac{E_R}{r}$ as the smallest incident energy that can produce a recoil of E_R. The minimal velocity is associated to E_{min} as

$$v_{min} = \sqrt{2E_{min}/m_\chi} = \sqrt{\frac{E_r}{E_0 r}} v_0 \tag{1.14}$$

Again, taking the limiting case $v_{min} = 0$ and $v_{max} = \infty$ eq. 1.13 yields

$$\frac{dR(0, \infty)}{dE_R} = \frac{R_0}{E_0 r} \frac{k_0}{k} \frac{1}{2\pi v_0^2} \int_{v_{min}}^{v_{max}} \frac{1}{v} f(\mathbf{v}, \mathbf{v}_\oplus) d^3 v \tag{1.15}$$

which leads to

$$\frac{dR(0, \infty)}{dE_R} = \frac{R_0}{E_0 r} e^{-E_R/E_0 r} \tag{1.16}$$

for $\mathbf{v}_\oplus = 0$. For practical cases these results have to be corrected for non-zero $\mathbf{v}_\oplus$ and finite escape velocity v_{esc}. Also for large momentum transfers $q = \sqrt{2m_T E_R}$ the wavelength h/q is getting comparable to the nuclear radius, resulting in a loss of coherence, as the substructure of the nucleus starts to be resolved. Usually this effect is accounted for by introducing a form factor. Details on the different proposed form factor corrections can be found in [45]. As one wants to compare results by different direct detection experiments, the Helm form factor is usually used, see [46]. In addition to the spin-independent (SI) case discussed above, there might also be the case of spin-dependent (SD) WIMP-nucleon interaction, which is covered in detail in [39]. Here only the result for the SD cross section will be given:

Following [39, 45, 47] the general form is given as

$$\sigma_T = 4G_F^2 \mu_T C_T \tag{1.17}$$

where G_F is the Fermi coupling constant, μ_T the reduced mass of the WIMP-target nucleus system and C_T a material dependent spin-dependent enhancement factor given as

$$C_T = (8/\pi)(a_p \langle S_p \rangle + a_n \langle S_n \rangle)^2 (J+1) J \tag{1.18}$$

with the effective neutron and proton coupling strengths a_n, a_p and the total nuclear spin J.

This work will mainly focus on the SI case. The spin-independent recoil spectrum for a $100\,\text{GeV/c}^2$ WIMP with $\sigma = 10^{-8}$ pb and an exposure of $100\,\text{kg}\,\text{d}$ for Tungsten, Calcium and Oxygen is given in fig. 1.9. The dip in the Tungsten spectrum is due to the form factor correction. All three target nuclei are used simultaneously in the CRESST II experiment, which will be presented in the next section.
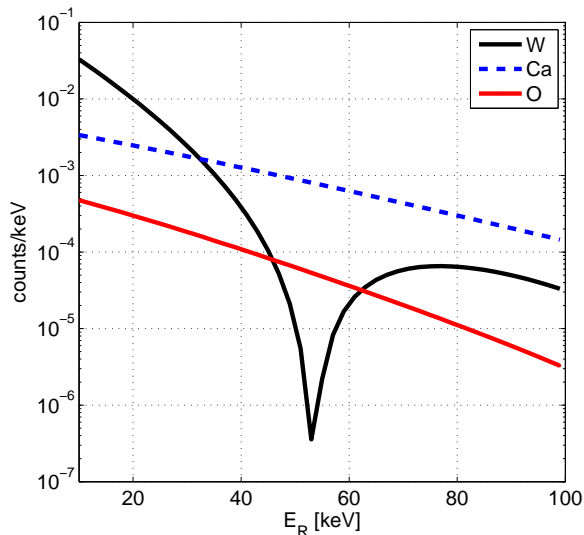
Figure 1.9: Recoil spectra of a $100\,\text{GeV/c}^2$ WIMP on Tungsten (black solid), Calcium (blue dashed) and Oxygen (red solid) with $\sigma = 10^{-8}$ pb and $100\,\text{kg}\,\text{d}$ exposure. The dip in the Tungsten spectrum is due to the form factor correction.

1.2 CRESST II

In the following, the direct dark matter search experiment CRESST II (Cryogenic Rare Event Search with Superconducting Thermometers) will be introduced, as the work presented in this thesis was carried out in the context of this collaboration. The goal was to set up an additional test facility for the experiment and to investigate alternative target crystals.

The CRESST II experiment is a direct DMS experiment looking for recoils of DM particles in low temperature calorimeters. It is situated in hall A of the Gran Sasso National Laboratory (LNGS[9]) in Italy which is run by the INFN[10]. The underground laboratory is covered by approximately 1,400 m of rock which corresponds to 3,500 m water equivalent (m.w.e). The cosmic muon flux is thus reduced to about $1\,\text{count}/(\text{m}^2\,\text{h})$ [48]. An overview of the setup can be found in fig. 1.10. The actual detector modules are placed in the carousel (CA) which is cooled to mK temperature using the dilution refrigerator (DR). To shield the experiment from potential radioactivity related to the dilution refrigerator material, a cold finger (CF) separates both components. Radioactivity of the surrounding is shielded, or moderated in case of neutrons, using polyethylene (PE) as a neutron shield, low background Lead (PB), high purity Copper (CU) against γ-background and the Nitrogen-purged Radon box (RB) against Radon-related background. The plastic scintillator muon veto (MV) is used to tag the remaining μ-induced events in the underground laboratory. In 2013 and additional inner PE shield was installed in the cold box around the carousel, which is not visible in the sketch.

---

[9]Laboratori Nazionali del Gran Sasso - Gran Sasso National Laboratory.
[10]Istituto Nazionale di Fisica Nucleare - National Institute for Nuclear Physics, Italy.
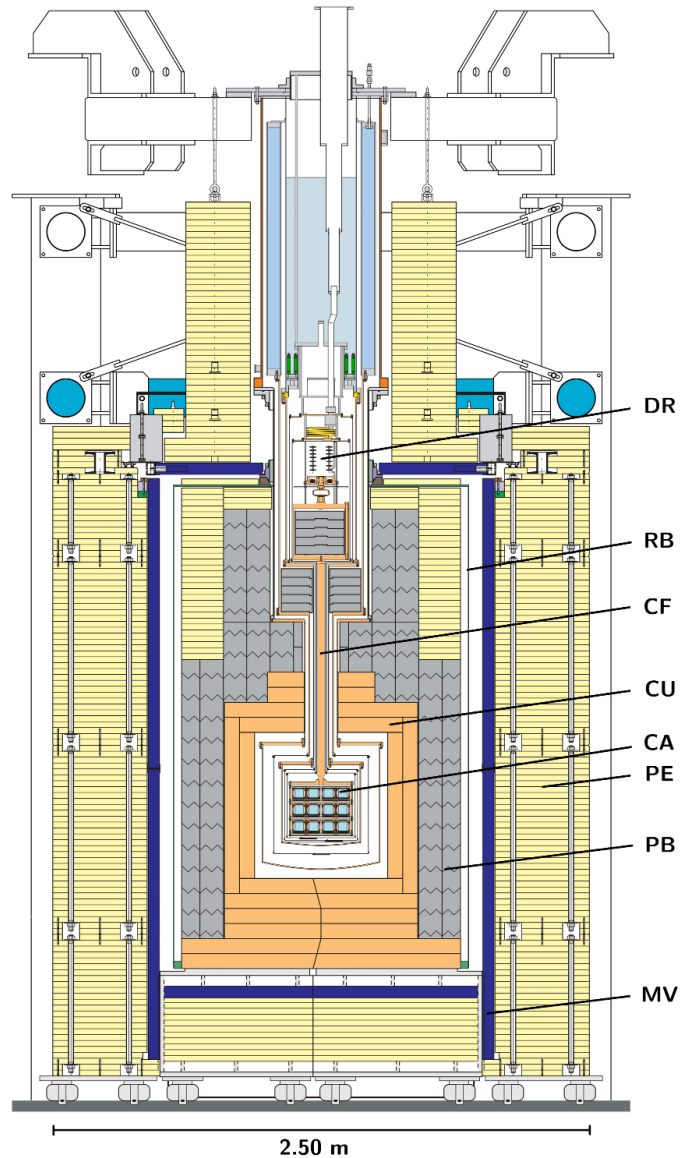
Figure 1.10: Sketch of the CRESST II setup at LNGS. The detector modules are placed in the carousel (CA) which is cooled to mK temperature using the dilution refrigerator (DR). To shield the experiment from potential radioactivity related to the DR, a cold finger (CF) separates both components. Radioactivity of the surrounding is shielded or moderated using polyethylene (PE), low background Lead (PB), high purity Copper (CU) and the Nitrogen-purged Radon box (RB). The plastic scintillator muon veto (MV) is used to tag the remaining μ-related events in the underground laboratory. In 2013 and additional inner PE shield was installed in the cold box round the carousel, which is not visible in the sketch.

The material used for the calorimeters is $CaWO_4$ in cylindrical crystals of $\sim 300\,g$ each, which is scintillating upon particle excitation. A fraction of 1–2 % of the deposited energy is converted to light, the rest is detected as recoil energy in the calorimeter [48]. The light is also measured calorimetrically, using a Silicon or a Silicon on Sapphire (SOS) absorber. Both, the $CaWO_4$ calorimeter, also called phonon detector (PD), and the light detector (LD) are enclosed in a highly reflective scintillating housing, in order to enhance the light collection efficiency and to veto surface events, mainly due to α background. A sketch of such a detector module can be found in fig. 1.11. Light and phonon detector are equipped with Tungsten Transition Edge Sensors (TES). These are superconducting metal films, operated in the transition range, which will be discussed in detail in sec. 2.3. The typical critical temperature T_c of those sensors is $\sim 15\,mK$. The dilution refrigerator necessary to provide such temperatures, the need for such low temperatures in general and details on the signal formation will also be discussed in chapter 2.
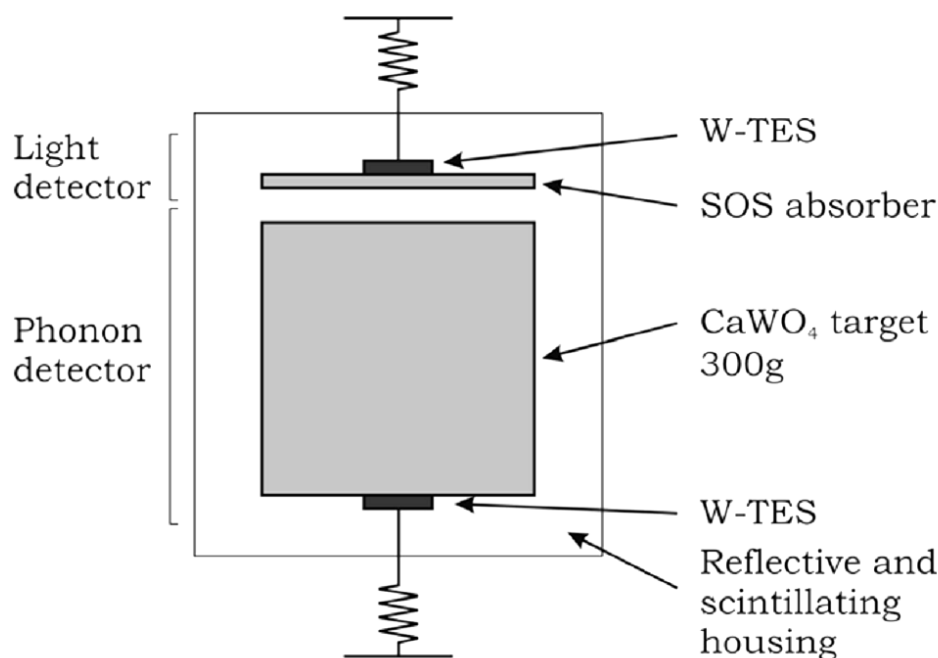
Figure 1.11: Sketch of a CRESST detector module. Both, light and phonon detector are equipped with Tungsten transition edge sensors (TES). The typical critical temperature of these sensors is $\sim 15\,mK$. The common housing is made of highly reflective, scintillating foil to enhance the light collection and discriminate surface events via the additional scintillation light produced in the foil. [49]

The light signal is used to provide event-by-event particle identification, as most, if not all, of the remaining signals will still be due to standard model particles, since the crystals themselves and the holder structure, cabling and so on will also contain radioactive isotopes although all the materials are pre-selected after extensive checks for radiopurity. A major improvement has recently been achieved by our colleagues at TU Munich, who managed to grow $CaWO_4$ crystals in a dedicated Czochralski setup, using only high-purity materials, thus lowering the intrinsic radioactivity of the crystals substantially, compared to commercially available crystals [50]. To identify the remaining background, one determines the light-to-phonon ratio, e. g. the measured energy of light and phonon detector, which is shown in fig. 1.12.

The γ and β events show a high light signal which is set to 1 per definition (upper line, black). α-events are found at roughly 1/5 (green). Nuclear recoil events - as expected from WIMPs - on oxygen (brown) and tungsten (lower line, red) are found at lower light yields. Note that the recoil events in the plot are
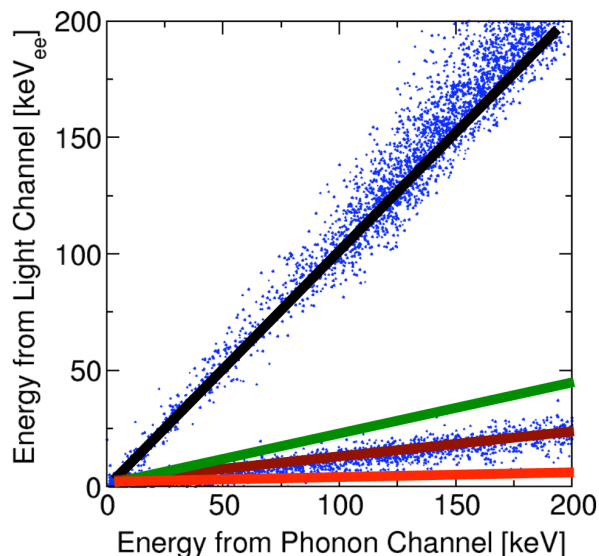
Figure 1.12: Light versus phonon signal discrimination plot: γ and β events show a high light signal which is set to 1 per definition (upper line, black). α-events are found at roughly 1/5 (green). Nuclear recoil events - as expected from WIMPs - on oxygen (brown) and tungsten (lower line, red) are found at lower light yields. Note that the recoil events in the plot are due to neutrons originating from an AmBe-source used to calibrate the recoil bands. [51]

due to neutrons originating from an AmBe-source used to calibrate the recoil bands. The Calcium recoils lie in between the Oxygen and Tungsten events and have been omitted for clarity. The fact that particles of different types produce different amounts of light for a given energy is called quenching. The quenching of nuclear recoils can be determined by the slope of the lines in fig. 1.12, provided there are enough events in the bands. A dedicated accelerator experiment to determine the exact values has been set up at the Maier-Leibnitz-Laboratorium. Results have been published in [50, 52–54]. Also in this experiment a moderate energy dependence of the quenching factors has been found, which can be seen in fig. 1.13. In addition, quenching factors can vary on the order of 10 % depending on the crystal. This can be taken into account by performing a neutron calibration. Details can be found in [50, 54]. The quenching has to be considered when comparing experiments measuring electron recoils as compared to nuclear recoil experiments. To emphasize the different energy scale, electron equivalent energies are often indicated as eV_{ee}. This will be important in sec. 3.1.

The light versus phonon discrimination plots are usually given with the light signal being normalized to the phonon signal, yielding flat bands. The so called light yield (LY) is thus defined as

$$ LY \propto \frac{E_{LD}}{E_{PD}} \tag{1.19} $$

where E_{LD} and E_{PD} are the respective energies in the light and phonon detector. The absolute value is fixed by setting the LY to one for the signal of a 122 keV gamma recoil in the module. Fig. 1.14 shows such a LY plot, again for a neutron calibration run with an AmBe source [55]. The calculated 90 % C.L. lines for the Oxygen recoil band are shown in red. The WIMP analysis window is indicated by the dashed lines. The width of the bands, and thus the discrimination power, is mainly determined by the resolution of the light detector. As the bands widen toward lower energies, even the electron-recoil band and the nuclear-recoil bands overlap, thus setting the discrimination threshold, which is the lower bound for the WIMP analysis window. It is fixed at the energy, where one γ is expected to leak into the WIMP search window. Assuming a "perfect" light detector, the width of the bands should be mainly limited by the photon statistics. When
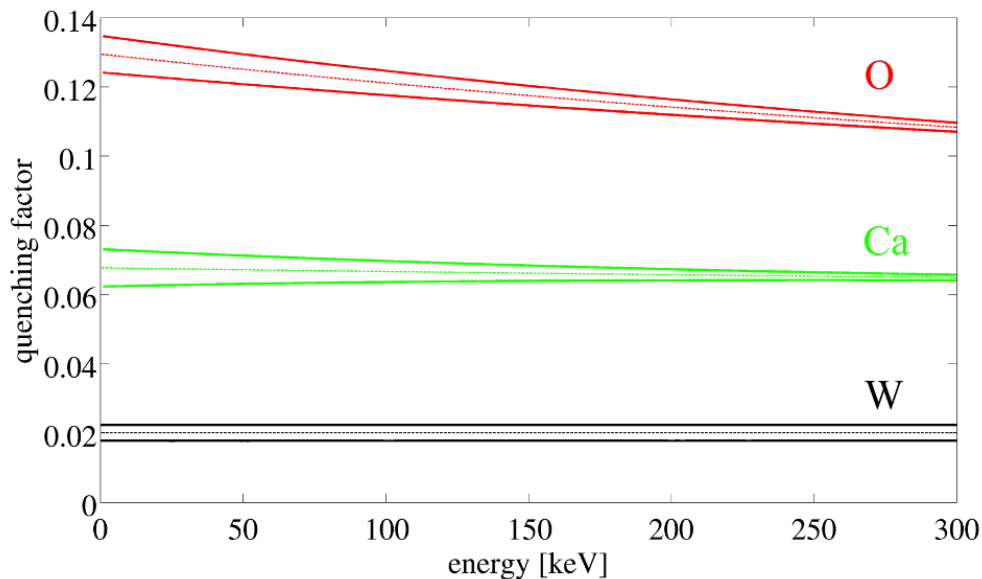
Figure 1.13: Energy dependent quenching factors of Ca, W and O, measured at mK temperatures as found in the CRESST accelerator experiment. [50]

looking for new target materials for CRESST detector modules, a high light output at low temperatures is thus desired.

CRESST II has published results of a 730 kg d run in 2012. Sixty-seven events were found in the acceptance region, where WIMP recoils are expected. However there were significant contributions from background sources that were carefully taken into account in [55].

As the clamps holding the crystals were not scintillating, a small fraction of surface α-events due to ^{210}Po contaminations could not be vetoed. ^{210}Po is a decay product of ^{222}Rn. ^{222}Rn gas accumulates underground as it diffuses out of the rock, where it is created in the ^{238}U decay chain. Thus ^{210}Po can be present on or implanted in the surfaces of the crystals or the surrounding material, e. g. the clamps [55]. The Polonium nuclei will decay as follows:

$$^{210}\text{Po} \rightarrow\ ^{206}\text{Pb} + \alpha \ (5.3\,\text{MeV})$$

(1.20)

where the Lead nucleus will get the recoil energy of 103 keV, assuming the ^{210}Po to be at rest. If the decaying Polonium nucleus was implanted in the target crystal, the deposited energy will therefore be ≥ 103 keV, depending on the fraction of the energy that is deposited by the emitted α-particle. Fig. 1.15 gives an illustration of this process. If the Polonium was located on the surrounding surface, the Lead nucleus might be emitted toward the crystal and deposit an energy of ≤ 103 keV there. In principle all of these events should be vetoed, as the 5.3 MeV α-particle will create sufficient additional light in a scintillating surface (either the foil or the crystal). Yet, it might go undetected if it hits the non-scintillating clamp areas. Then only a recoil event will be registered, mimicking a WIMP signal, if the deposited energy is degraded down to the acceptance region as also the Lead nucleus can be slightly implanted in the surrounding surface. Vice versa, also α-particle implanted in the surface and ejected toward the crystal can be degraded down in energy, while the recoiling Lead nucleus goes unnoticed as it hits the non-scintillating clamp area. The effect of this can be seen in fig. 1.16, where the data of one detector module is shown in the light versus phonon plane.

The events around light yield of 1 are due to electron recoil background (e/γ). The *black line* denotes the
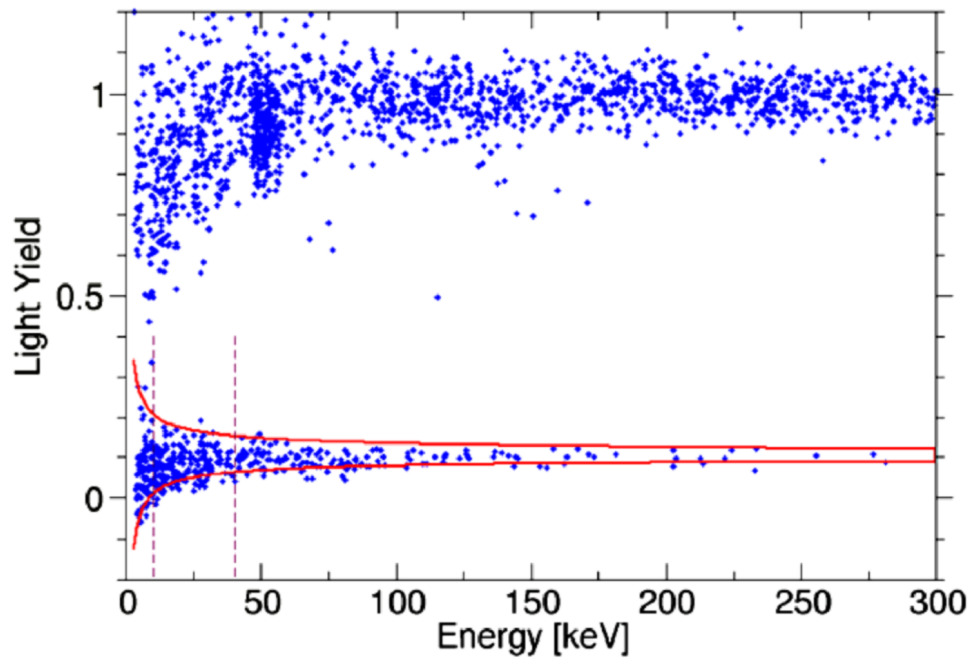
Figure 1.14: CRESST II light versus phonon discrimination plot of a neutron calibration run, where the light signal is normalized to the phonon signal, yielding flat bands. The calculated 90 % C.L. lines for the Oxygen recoil band are shown in red. The WIMP analysis window is indicated by the dashed lines. [55]
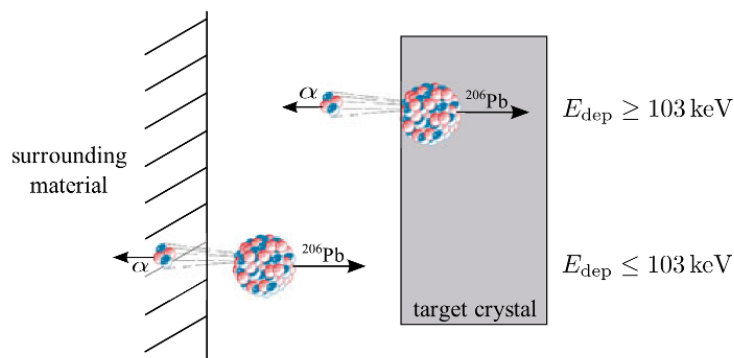
Figure 1.15: Illustration of ^{210}Po decays on and slightly implanted in the surface of the surrounding material. In a fully scintillating environment all these events will be vetoed due to the additional light by either the α-particle or the recoiling nucleus. However, if there are non-scintillating areas, this might mimic WIMP signals. See text for details. [55]
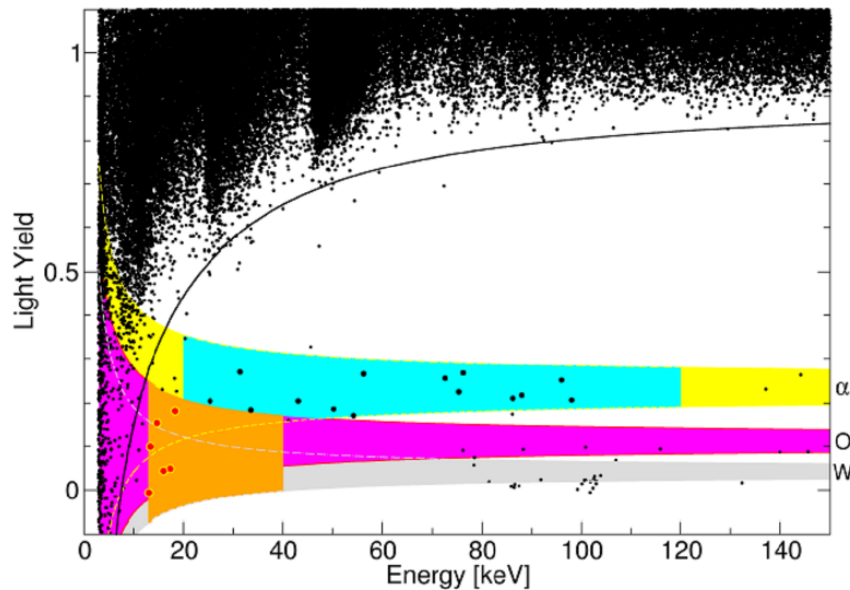
Figure 1.16: CRESST II data of detector module Ch20. The events around light yield of 1 are due to electromagnetic background (e/γ). The *black line* denotes the boundary below which only 0.1 % of e/γ-events are expected. The α (*yellow*), Oxygen (*violet*) and Tungsten (*gray*) recoil bands are indicated. The acceptance region is displayed in *orange*. The *blue* area is the overlap-free α-region, that can be used to estimate the α-leakage into the acceptance region. Note the low energy α-events due to energy-degradation by implantation. [55]

boundary below which only 0.1 % of e/γ-events are expected. The α (*yellow*), Oxygen (*violet*) and Tungsten (*gray*) recoil bands are indicated. The acceptance region is displayed in *orange*. The *blue* area is the overlap-free α-region. Assuming a flat energy spectrum in the region of interest the events in this area can be used to estimate the α-leakage into the acceptance region. Note the low energy α-events due to energy-degradation by implantation. The Lead recoils can be seen at 103 keV, also trailing down to lower energies, as explained above. Again, one can measure the spectrum of these recoils in the overlap-free region and extrapolate down to the acceptance region, in order to estimate the leakage events.

Taking these processes into account and estimating the e/γ leakage and the neutron background was done in a full maximum likelihood analysis. Yet, the resulting background contributions could not explain all of the observed counts. Including a WIMP signal in the likelihood analysis resulted in two likelihood maxima, labeled M1 and M2, with a statistical significance of 4.7 σ for M1 over the no-WIMP hypothesis and of 4.2 σ for M2.

However one has to be cautious, as the background modeling has a large influence on these results. The CRESST II collaboration thus concluded that minimizing the discussed background sources is of utmost importance. These results will be discussed together with other current results in sec. 1.4.

In the next section an alternative approach to the event-by-event discrimination will be presented.

1.3 The DAMA signal

In 1986 Drukier, Freese and Spergel discussed the possibility that dark matter to normal matter interaction might lead to a small modulating signal rate in a large scale detector due to the varying relative motion of Earth with respect to a possible dark matter halo [56]. Freese, Frieman and Gould refined the idea and discussed some possible scenarios for different target materials and dark matter candidates in [44]. The

astrophysical parameters quoted in the following section are taken from these sources.

Earth moves around sun with velocity $v_{\oplus} = 30\,\text{km/s}$. The plane defined by it's motion, the ecliptic, is inclined by $\gamma = 60°$ to the galactic plane. So Earth's projected motion has to be considered in addition to the solar velocity $v_{\odot} = 232\,\text{km/s}$ with respect to a possible dark matter halo. The WIMP velocity can thus be written as

$$v_\chi = v_\odot + v_\oplus cos(\gamma)cos\omega(t - t_0) \tag{1.21}$$

with $\omega = 2\pi/T$ where $T = 1\,\text{yr}$. The phase t_0 should be around 2nd of June $\pm 1.3\,\text{days}$, when Earth's velocity with respect to the halo is at a maximum[11]. It is important to realize that this does not coincide with the perihelion transit, where Earth's trajectory velocity is maxed, or another special state like a solstice. The phase is thus a very distinct signature. Now, assuming a non-rotating, isothermal dark matter halo with a Maxwellian velocity distribution, defined by the velocity $\bar{v}$, the circular velocity of objects within this system is directly connected to $\bar{v}$ via

$$v_{circ} = \sqrt{2/3}\bar{v} \tag{1.22}$$

Expressing eq. 1.21 in units of v_{circ} yields the dimensionless WIMP velocity signature

$$\eta(t) = \eta_0 + \Delta\eta cos\omega(t - t_0) \tag{1.23}$$

with $\eta_0 = 1.05$ and $\Delta\eta = 0.07$. As $\Delta\eta \ll \eta_0$, a first order Taylor approximation is justified for the signal rate in the k-th energy bin

$$S_k\left[\eta(t)\right] = S_k\left[\eta_0\right] + \left[\frac{\partial S_k}{\partial \eta}\right]_{\eta_0} \Delta\eta cos\omega(t - t_0) = S_{0,k} + S_{m,k}cos\omega(t - t_0) \tag{1.24}$$

with $S_{0,k}$ as the annual average and $S_{m,k}$ as the *absolute* modulation rate per bin. As Drukier and Freese et al. have shown, the *relative* modulation S_m/S_0 grows with increasing threshold of the experiment [44]. Considering coherent scattering cross sections for the WIMP-nucleon interaction, the resulting recoil energy spectra will drop sharply with rising energy. So the biggest modulation effect is expected in the lowest energy bins, while it should be absent at higher energy range [57].

Measuring the time averaged WIMP signal $S_{0,k}$ will not be possible in a pure counting experiment, as eq. 1.24 has to be supplemented with a background rate $B(t)$ yielding

$$\bar{S}(t) = B(t) + S(t) = B(t) + S_0(t) + S_m cos\omega(t - t_0) \tag{1.25}$$

So a counting experiment has to focus on S_m. Multiple conditions have to be met, to verify that a modulation signal is not just connected to ordinary matter interactions:

The signal should exhibit a period of one year, with peaking phase around 2nd of June. This is an effective filter for modulating background signals varying with e.g. the season. Yet recently Lee et al. [58] showed, that due to gravitational focusing (GF) another modulation effect has to be considered that can shift the phase by a maximum of 21 days for light WIMP masses and low thresholds. This is due to the fact that the DM density is also time dependent due to Earth's position relative to the DM wind. As the Earth is behind the sun relative to the on-streaming particles, which occurs around 1st of March, additional DM particles get focused on the Earth-bound detector, changing both the density and the velocity distribution of the incident WIMPs. However this shift can be calculated for a specific detector material and a known energy threshold. So the phase is still left to be a crucial observable.

As discussed above, the highest sensitivity of a rate-only experiment is reached at low recoil energies. The modulation should thus be present at the lower end of the spectrum and absent for higher energies.

Since a counting experiment will consist of multiple single detectors to reach a high target mass, the coincidence between signals in different detectors can also be used to discriminate against standard model

---

[11]The error is due to the uncertainty of the motion of the sun with respect to the local standard of rest (LSR), see [44].

background: Due to their small interaction cross section WIMPs are highly unlikely to scatter on multiple detectors. The signal should then only be present in the single-hit events.

Concerning the amplitude of a modulated signal Lewin and Smith have shown, that the $6-7\%$ change in velocity translates to a change in rate of roughly 3%, assuming a Maxwellian velocity distribution of the WIMPs [45]. Yet the differential rate, e. g. the rate per energy bin, can be significantly larger, if the threshold of the counting experiment is low enough, as the modulation of dR/dE_R changes sign with energy – see fig. 2 in [45] for details. Thus a bin-wise analysis of the data can further enhance the effect.
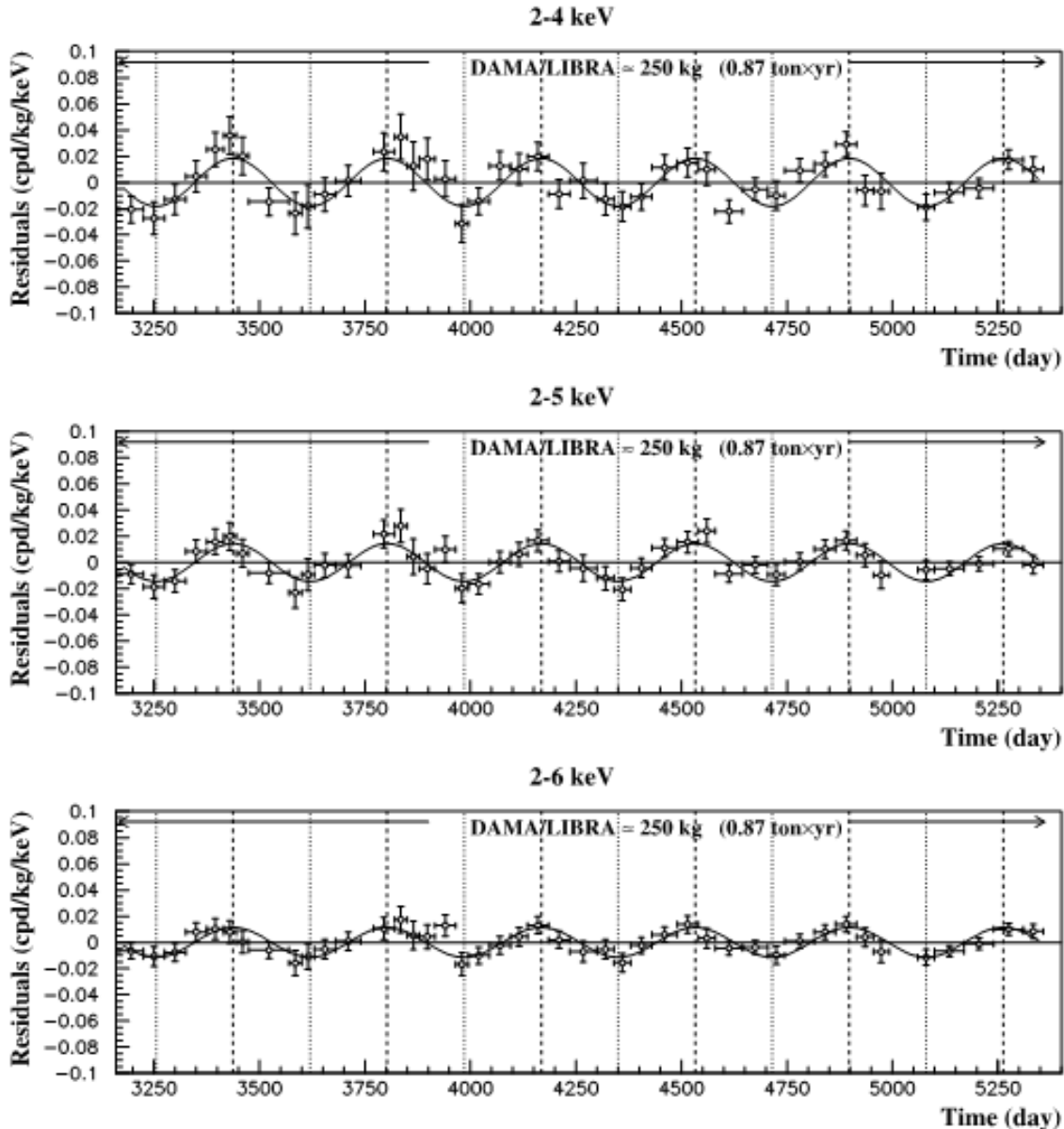

Figure 1.17: The DAMA/Libra oscillation data in the 2-4 keV, 2-5 keV and 2-6 keV range over a period of ~ 6 years. Only the residual rate of the efficiency-corrected data is given. [59]

The DAMA collaboration has built an experiment in order to measure such a signal. A single detector consists

of a high purity NaI(Tl) crystal, coupled to two low-radioactivity photomultiplier tubes (PMTs) with high quantum efficiency. Up to 25 of these detectors where simultaneously used in a low background environment in the Gran Sasso National Laboratory in Italy. In different configurations described in detail in [59, 60] they measured a total of 13 annual cycles with a total net exposure of $1.17 \, \mathrm{ton \, yr}$ and found a modulation of single-hit events in their low energy bins ($2 \, \text{-} \, 6 \, \mathrm{keV}$ range) corresponding to $(0.0116 \pm 0.0013) \, \mathrm{cpd/kg/keV}$. The modulation period was found to be $(0.999 \pm 0.002) \, \mathrm{yr}$ and a phase of (146 ± 7) days, which is compatible with 2$^{\mathrm{nd}}$ of June. Also Lee et al. [58] state that the DAMA phase should not be affected by the GF modulation, at least if one assumes the DM scatters off Sodium. For Iodine scatters the maximum should appear around 21$^{\mathrm{st}}$ of May, which is also compatible with the value reported in [59].

The residual rate of the efficiency-corrected data for the last six reported cycles can be found in fig. 1.17. No modulation was found in the higher energy range, e. g. $6 \, \text{-} \, 14 \, \mathrm{keV}$. The significance of the signal with respect to the *no signal present* scenario was derived with a maximum likelihood test and found to be $8.9 \, \sigma$ [59]. Also no modulation could be found in the multiple-hit rate, rendering the explanation of e. g. a muon-induced, showering, background signal mimicking the signature very unlikely.

Yet for some years now, the result is in contradiction with other direct dark matter search experiments. An overview of the current status will be discussed now.

1.4 Overview on the current experimental status

As mass and cross section of the WIMPs are both unknown, experimental results of the allowed parameter space are given in the mass versus cross section plane. For spin-dependent WIMP-nucleon interaction, the current exclusion limits can be found in fig. 1.18. The *red* and *blue* curves are the 90 % C.L. exclusion contours of direct search experiments, namely COUPP, KIMS, PICASSO and SIMPLE-II (all references to these projects can be found in [61]), while the black curves are limits obtained by indirect searches in the SuperK and IceCube data. The area indicated in *grey* is preferred by theory[12]. COUPP, KIMS and PICASSO use superheated liquids to detect WIMP recoils, as a nuclear recoil will cause bubble nucleation, while e/γ-background will deposit energy alongside a long trace, not inducing bubble formation (or, in case of muons, generating long tracks, that can be easily rejected). KIMS is using CsI(Tl) crystals coupled to photomultipliers. The setup is similar to the DAMA project discussed in sec. 1.3, though KIMS is using pulse-shape analysis (PSA) to disentangle nuclear recoils and electromagnetic background. The separation can only be achieved on a statistical level, not event-by-event. Yet the experiment can be performed at room temperature, making scaling-up the target mass much more convenient.

The current situation for spin-independent WIMP-nucleon interactions is presented in fig. 1.19. Again, the lines denote the 90 % C.L. exclusion curves, e. g. the parameter combination above this line is excluded with 90 % probability. The closed contours are the favored regions in case of a signal, that can not be attributed to background. The lower shaded region (*orange*) denotes the area, where the data will be dominated by coherent neutrino scattering from solar (*left*) and atmospheric/diffuse supernova background neutrinos (DSNB, *right*). This is considered to be a limit for direct detection experiments [63].

As covered in sec. 1.3, the DAMA collaboration [59] claims a dark matter related signal due to the annual modulation of single scatters in their detector. The corresponding energy spectrum of the modulated rate has been published and can be interpreted as a WIMP recoil spectrum. The resulting DAMA-favored region (*light gray*, 3-σ) is shown in fig. 1.19 as interpreted in [64]. There are two solutions due to the composite nature of the target crystal material. The lower mass solution corresponds to Sodium recoils, the higher mass region to Iodine.

The previously discussed CRESST-favored regions [55] due to the events left after background estimation are shown in *dark gray*, corresponding to the 2-σ contours. Also here, two solutions are due to the composite

---

[12]This particular prediction is based on a constrained Minimal Supersymmetric Model (cMSSM). [62]
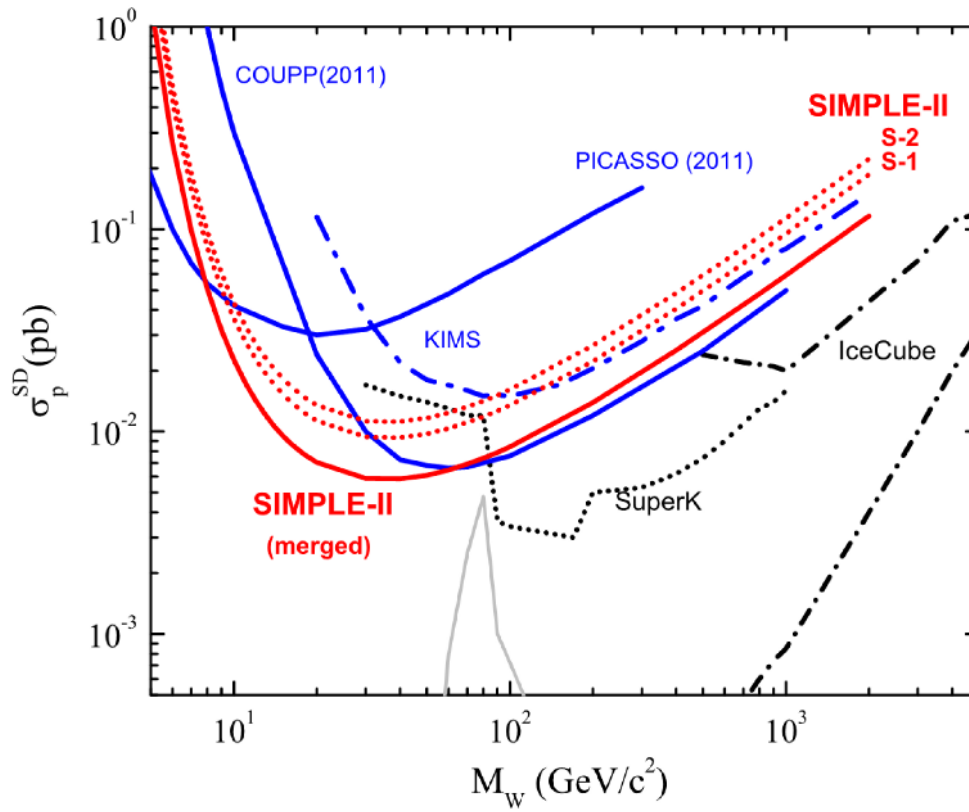
Figure 1.18: Current status of the WIMP direct dark matter searches. Limits for spin-dependent WIMP-nucleon interaction. [61]
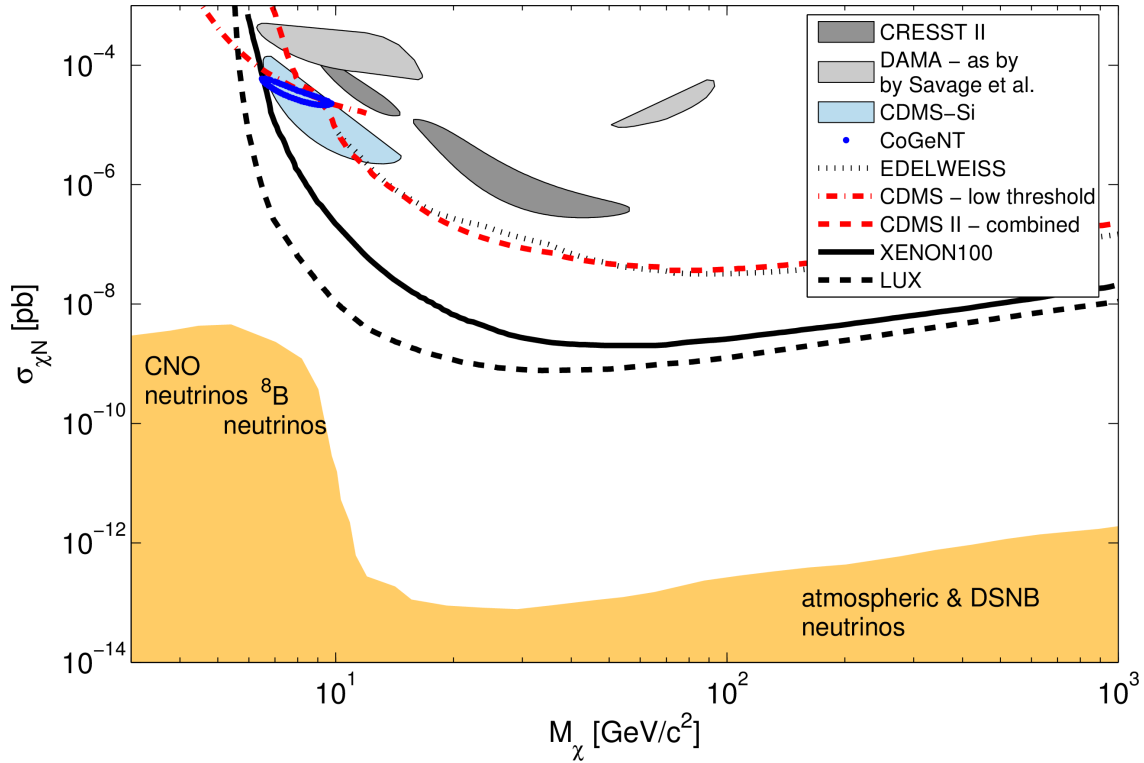
Figure 1.19: Current status of the WIMP direct dark matter searches: Limits and favored regions for spin-independent WIMP-nucleon interaction. Citations of the displayed data sets can be found in the text. Note that there is a strong tension between the results.

nature of the target crystal. For the low mass solution M2 the WIMP mass is too low in order to produce Tungsten recoils above threshold, while the high mass solution M1 is dominated by those.

CoGeNT [65] is another direct DMS experiment, using a 440 g, high-purity point-contact Germanium detector in a low-background environment. Surface events can be rejected using a cut on the rise-time of the events, as the highly inhomogeneous field in the detector influences this quantity. The collaboration reported an excess of events above background expectation [65] as well as a modest hint for an annually modulating signal [66]. The resulting favored region is given as the *blue points* contour. Recently the collaboration published the analysis of their extended dataset, covering a period 3.4 years [67]. They confirmed the presence of a modulation yet report a lower significance of $2.2\,\sigma$ than in [66], where they claimed a value of $2.8\,\sigma$. They attribute this to the newly introduced surface event cut, leading to lower statistics overall, compared to the former data release.

The super-CDMS experiment [68] also uses Germanium as a target, yet in form of low temperature detectors. They read out both, phonon and the ionization signal in the crystals, which enables them to identify recoil events and filter out e/γ-background. The current iZIP (interleaved Z-sensitive Ionization Phonon) detectors can also reject surface events due to a special field configuration, revealing surface events, e. g. due to α-decays, as single-face charge signals. They have published two limits, one with ionization discrimination (*red dashed line*) [69] and a limit where discrimination was given up in order to lower the threshold (*red dash-dotted line*).

A small fraction of CMDS detectors is using Silicon instead of Germanium. With these detectors, the collaboration also observed a number of counts exceeding background expectation [70]. The corresponding 68 % C.L. area is shaded in *light blue*.

The EDELWEISS collaboration [71] is also utilizing charge-phonon discrimination in Germanium calorimeters. The discrimination is similar to the CDMS technique, although the surface rejection is realized in a different design, named Ge-ID (Germanium Interdigit Detectors). They observed no signal above background expectation in their $384\,\mathrm{kg\,d}$ data published in 2011. The resulting limit is given as the *black dotted* curve.

The lowest limits up to date are achieved by two-phase Xenon experiments. Here one takes advantage of the charge and scintillation signal produced by recoils in liquid Xenon. The light is detected using photomultiplier tubes (PMTs), while the charge signal is extracted into the Xenon gas phase via a drift field, where the signal is amplified in a collision cascade. Using the light pattern and the drift time information, e.g. the delay between light signal S1 and charge signal S2, the position of the events can be reconstructed and surface events can be rejected by a fiducial volume cut. The difference in the scintillation light output is used to discriminate nuclear recoils from electron recoil background. As Xenon is a high Z material, it provides excellent self-shielding against e/γ background.

This technique was successfully implemented by the XENON 100 collaboration, also finding no WIMP signal in their 225 live days run published in 2012 [72]. The corresponding exclusion limit is shown in *solid black*. There were some discussions on the sensitivity of the experiment at low WIMP masses [73], but recently LUX, another Xenon two-phase experiment, published an even lower limit, confirming the result of the XENON 100 collaboration.

The LUX collaboration [74] has published their first 85.3 live days data set, after they finished the installation of their experiment in 2013. Their fiducial volume of $118\,\mathrm{kg}$ is roughly double that of XENON 100, also they achieve lower threshold, which leads to a lower limit than the XENON 100 result, even within less live days. It can be found as the *black dashed* line.

Evidently the different results strongly disagree. First of all, the low mass WIMP regions do not agree reasonably well. Second, the regions are ruled out by both Xenon results. Also, the DAMA region has been excluded, in addition to the Xenon results, by CMDS II, EDELWEISS and CRESST II. Yet one has to keep in mind, that these exclusion limits are quite model-dependent. The DAMA collaboration has stressed this for quite a while (see e.g. [59]). They claim their detection to be model-independent, which is not true, strictly speaking, as also some astrophysical input is necessary for the interpretation of their results as well as detector physics input in order to perform the efficiency correction of the data. Yet there are no assumptions made on the cross section (e.g. coherent scattering) and form factors.

Several issue have been discussed in order to reconcile the different results. Chang et al. have proposed inelastic dark matter (iDM), assuming an excited WIMP state with mass splitting in the order of $100\,\mathrm{keV}$, comparable to the kinetic energy of the WIMPs in the halo. In order to induce a recoil, a WIMP must then have the minimum velocity

$$v_{min} = \sqrt{\frac{1}{2m_T E_R}\left(\frac{m_T E_R}{\mu} + \delta\right)} \qquad \boxed{1.26}$$

where E_R is the recoil of the target nucleus with mass m_T and μ denotes again the reduced mass of the WIMP-nucleon system, as in sec. 1.1.4. This basically creates an additional threshold for recoiling particles, favoring heavier targets over lighter ones, suppressing recoils at low energies and enhancing a possible modulation [75]. Yet this model, under standard halo assumptions, was ruled out by CRESST [76, 77] and CDMS data.

The DAMA collaboration stated [78], that ion channeling in the crystal might also influence the allowed region in fig. 1.19, which was discussed in detail by Savage et al. [64]. DAMA only measures the energy deposited in form of scintillation light, which is just a fraction of the total deposited energy, determined by the quenching. Deposition in phonons and other channels, that basically all end up in heat, goes unnoticed. Thus nuclear recoils along the characteristic axes of the crystal might produce different signals with respect

to those, that hit the crystal in random fashion since those "channeled" recoils transfer their energy mostly to the electrons, which is showing up in the scintillation channel. The unchanneled recoils will deposit most of their energy in the "invisible" heat system. The channeling effect can lead to recoils that are basically unquenched. The fraction of recoils with quenching $\simeq 1$ at a given energy was estimated in [78] and the implications on the DAMA-allowed regions was evaluated in [64]. The respective exclusion plot can be found in fig. 1.20. Although the low mass solution is shifted toward lower cross section values, the contradiction with the Xenon results can not be removed.
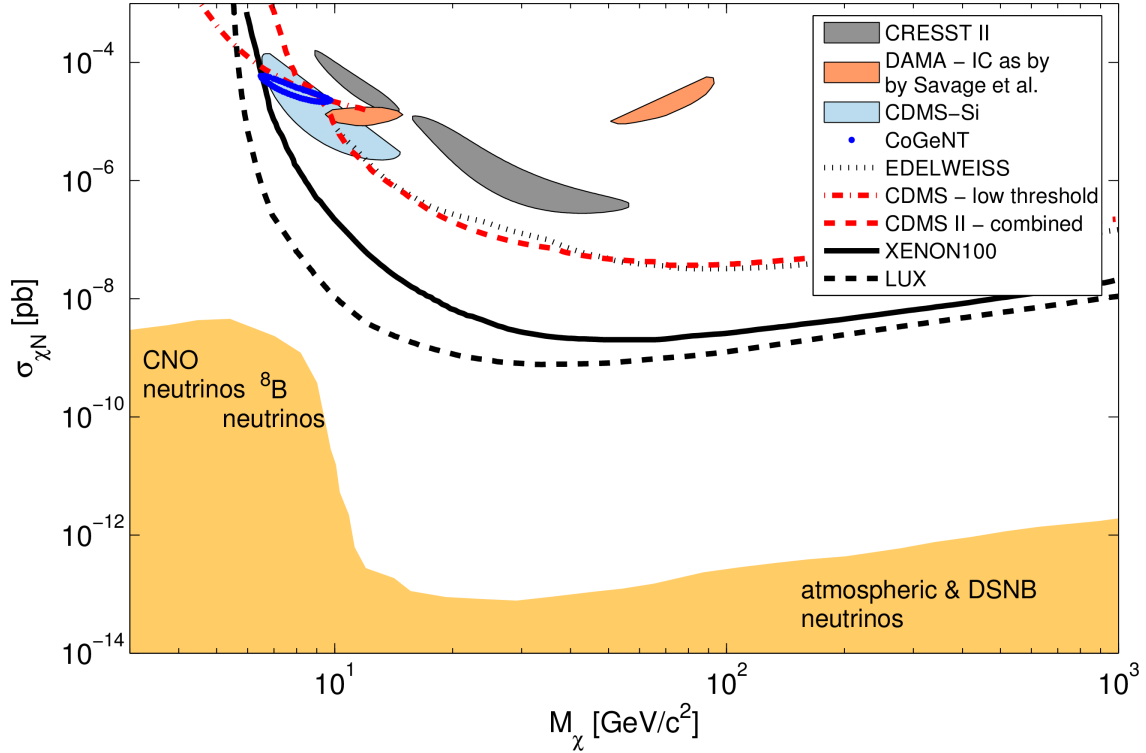
Figure 1.20: As fig. 1.19, but with DAMA data corrected for channeling. The contradiction between the Xenon and DAMA results can not be removed.

As mentioned in sec. 1.2, the CRESST-allowed regions are strongly influenced by the background modeling. Triggered by suggestions of the CRESST collaboration, Kuźniak et al. have suggested in [79] that the additional events might be related to sputtered ions of the clamp material, due to ^{206}Pb recoils. According to the authors, considering a certain surface roughness, the measured recoil spectrum of the excess events and the light yield distribution could be simulated. As this process is also related to the non-scintillating contact areas of the clamps, this can be verified in the new CRESST run with fully scintillating detector module housings, which was started in September 2013.

Like for CRESST II, the signals of CoGeNT and CDMS-Silicon might also be related to uncertainties in the background modeling, yet the situation stays unclear: No convincing explanation has been given so far that could explain the DAMA modulation signal, besides the WIMP interpretation, which is now observed over full 13 years cycles. Therefore several groups try to reproduce the DAMA result by replicating the experiment, like KIMS [80] and DM-ice [81, 82]. It is however quite challenging to reach mass, threshold and radiopurity achieved by the DAMA collaboration. Also, no additional information on the origin of the signal would be gained, which is why in this thesis another approach is investigated. The basic idea will be discussed in the next section.

1.5 A possible way to cross-check scattering and annual modulation data?

As shown in the last section, the DAMA claim of a WIMP modulation signal seems to be hardest to refute. In order to clarify the situation, several questions should be addressed in future:

- Is the DAMA interpretation, namely that the modulation is caused by DM interactions, justified? Up till now no convincing "standard model" mechanism has been proposed that might mimic the signal. The attempts to duplicate the experiment might not lead to a conclusive answer, as the modulation signal would just be confirmed, while no new insights on it's origin could be gained, assuming the effect is not related to the specific DAMA installation. Therefore particle identification should be achieved.

- Is the contradiction between DAMA and the experiments using event-by-event discrimination caused by the additional model-dependent assumptions that enter in the analysis-procedure? One way to check this would be to look for modulations in Xenon or bolometer detector data. As the active volume of such experiments is expected to increase significantly during the next decade, this might become feasible in near future. The XENON 1T collaboration has already started construction of their detector with an expected fiducial mass of several hundred kilograms of Xenon and the European solid state experiments CRESST, EDELWEISS and a few additional groups will join their efforts in EURECA, which will have a comparable sensitive mass.

- If the DAMA signal is really caused by DM, could the dark matter interaction with standard matter depend on the target's properties? Several theories have tried to reconcile the contradicting results by postulating, e.g. material-dependent DM interactions, inelastic effects, as discussed in sec. 1.2, and even "xenophobic", e.g. isospin-violating DM [83]. The best ansatz to test material-dependent interactions is to use a multitude of different targets. The charge-phonon technique is basically limited to Germanium and Silicon. Up till now liquid-gas two-phase detectors with the needed discrimination power have only been realized with Xenon. Attempts to use Argon or Neon are ongoing. Superheated liquids are also quite limited in the choice of the detection material. The most promising technique for interchangeable targets is the scintillation-phonon discrimination implemented by the CRESST experiment. There are a vast number of scintillating crystals available that might be used in a direct DMS experiment. One of the goals of this thesis was therefore to investigate alternative target materials for CRESST-type DM detectors.

- It would be desirable to achieve a "cross-calibration" of event-by-event discrimination experiments and rate-only DM searches like DAMA. Therefore a *hybrid detector* is suggested in this thesis: Using the DAMA target material (NaI) with CRESST-type nuclear recoil discrimination. If this could be realized, the nature of the DAMA signal could be directly tested: If material-dependent scenarios applied, the hybrid detector would be unaffected and the signal could be observed. If *no signal* could be measured in the device, the DAMA signal has to be related to the electron-recoil channel.

In order to further address the raised issue, this thesis will be structured as follows:

Chapter 2 will describe the working principle of cryogenic bolometers and the necessary infrastructure needed to operate CRESST-type detectors. The latter was established and tested as a part of this thesis. Chapter 3 will then explore the question, if a NaI-hybrid detector can be built at all, considering technical issues, light-yield and phonon properties as well as giving theoretical estimates on the performance of such a device. Chapter 4 will then discuss the properties of LiF, another alternative target material that has been investigated in this work.

2

Cryogenic detector development

One of the objectives of this thesis was to establish a new shallow underground facility for the operation and characterization of CRESST/EURECA detectors and for the development of new cryogenic detectors implementing the light-phonon technique. Therefore the basic principles of such devices will be presented in this chapter and – where possible – illustrated by data obtained during test runs of the new setup. In sec. 2.1 the crystal properties and the signal formation will be discussed. Also the event-by-event discrimination technique will be presented in more depth. Sec. 2.3 will then focus on the superconducting thermometers, also called *Transition Edge Sensors* (TES). These thermometers are needed to detect the small temperature change occurring in a cryogenic detector upon particle interaction. Selecting a TES with proper characteristics is crucial for optimal detector performance. Therefore sec. 2.4 will then discuss the necessary measurements and criteria for the selection process. The following sections 2.5 and 2.6 will describe the SQUID and the data acquisition (DAQ) systems. Finally the operating conditions and techniques for cryogenic detector operation will be considered in sec. 2.8 and data of a conventional cryogenic bolometer will be presented to demonstrate the good performance of such devices and to demonstrate that the Tübingen Shallow Underground Laboratory (see [84] for details) is now fully operational.

2.1 Working principle of cryogenic detectors

2.1.1 A simple calorimeter model

In a simplified picture a cryogenic detector can be regarded as a calorimeter consisting of an absorber crystal as target for incident particles, equipped with a thermometer that is weakly coupled to a heat sink, see fig. 2.1.
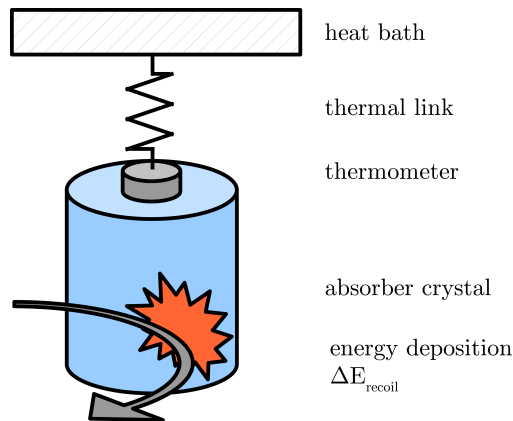

heat bath

thermal link

thermometer

absorber crystal

energy deposition
ΔE_{recoil}

Figure 2.1: Simple calorimeter model of a cryogenic detector.

Impinging particles will deposit the energy ΔE_{recoil} in the absorber, resulting in a temperature rise given by

$$\Delta T = \frac{\Delta E_{recoil}}{C} \tag{2.1}$$

where C is the heat capacity of the crystal. As cryogenic detectors are operated in the mK temperature range, the approximations of the Debye model are valid, as the deposited energies are smaller than the thermal energies related to the Debye temperature Θ_D as $\hbar\omega \ll k_B\Theta_D$. The Debye model predicts that the heat capacity of a dielectric crystal at a certain temperature T is governed by the phonon properties and thus can be described as

$$c_v = \frac{12\pi^4}{5}nk_B\left(\frac{T}{\Theta_D}\right)^3 \tag{2.2}$$

where n is the number density, k_B the Boltzmann constant and Θ_D the Debye temperature of the crystal (see e.g. [85]). The Debye temperature can be regarded as a kind of Fermi energy for the phonons in the respective crystal, separating the temperature regions where one has to consider quantum effects from the classical regime where the law of Dulong-Petit applies, namely

$$c_v = 3nk_B \tag{2.3}$$

which is independent of T. As the typical values for Θ_D are in the order of a few hundred degrees Kelvin, for cryogenic experiments only eq. 2.2 has to be considered. In the mK temperature regime the heat capacity of the absorber crystal thus drops with T^3, yielding a high temperature rise ΔT. Typical values for recoil energies in the keV range are a few µK. Since the absorber is weakly coupled to a heat sink, the excess energy will be removed within a few milliseconds, depending on the relaxation time

$$\tau = C/G \tag{2.4}$$

where G is the thermal coupling to the heat bath. Usually Gold bond wires are used, which allows to calculate G using the Wiedemann-Franz law

$$G = \mathcal{L}\frac{T}{R} \tag{2.5}$$

with the Lorenz number $\mathcal{L} = 2.44 \cdot 10^{-8}$ $\mathrm{W\,\Omega\,K^{-2}}$ and the electrical resistance R.

As the thermometer consists of a superconducting metal operated in the transition, eq. 2.2 cannot be applied here, as one has to account for the heat capacity of the electrons as well. In normal-conducting state one obtains in the Debye limit

$$c_v = c_{ph} + c_e = \frac{12\pi^4}{5}nk_B\left(\frac{T}{\Theta_D}\right)^3 + \gamma T \tag{2.6}$$

with the material dependent constant γ. As the linear term will dominate at low temperatures, the phonon heat capacity can be neglected [85, 86]. At the critical temperature T_c the heat capacity abruptly increases to 2.43 times the normal-conducting value [86], so

$$c_v = c_e + 1.43\,c_e(1 - R_{op}/R_{nc}) \tag{2.7}$$

where R_{op} is the resistance value at the operating point and R_{nc} the resistance in normal-conducting state.

In order to explain the pulse formation in a realistic cryogenic detector, one needs to refine this simple calorimetric model. This has been done in detail by Pröbst et al. in [87]. Cozzini [88] gives a good summary of [87] and the next sections will give an overview using both sources.

2.1.2 Pulse formation model for cryogenic detectors

A more realistic model than the simple calorimeter picture should take the different heat capacities of the phonons in the absorber and the electrons in the thermometer into account. Fig. 2.2 gives a schematic

overview of the subsystems and related variables as in [87]. As the absorber is a dielectric crystal, the phonon system is the relevant quantity for the heat capacity C_a, and therefore described by eq. 2.2 at low temperatures. The phonons will be in thermodynamical equilibrium (TDE) with the other subsystems, until a recoil deposits energy in the absorber, disturbing the TDE and leading to different temperatures in the respective subsystems. The electrons in the thermometer will then be at temperature T_e, depending on the heat capacity of the electrons in the thermometer C_e described by eq. 2.7, while the phonon distribution in the absorber will be at temperature T_a.
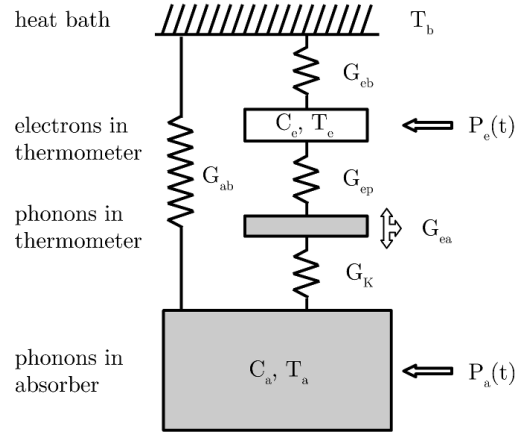

Figure 2.2: Thermal model of a detector as in [87]. The electrons in the thermometer can be at a different temperature T_e than the phonons in the absorber at T_a. P_e and P_a are the time dependent power inputs by non-thermal phonons, C_e and C_a the heat capacities of the subsystems and G_{ab}, G_{eb}, G_K and G_{ea} the respective thermal conductances.

The thermal conductance between absorber and heat bath is described by $G_{ab} \propto T^3$. It can not be avoided as the absorber needs to be fixed in a holding structure. Usually it is minimized by the use of insulating materials and a small contact area. G_K is the thermal conductance related to the Kapitza boundary coupling between the phonon system of the crystal and the phonons in the thermometer and is thus proportional to T^3. The electrons and phonons in the thermometer at very low temperatures are coupled via $G_{ep} \propto T^5$ which is discussed in detail in Appendix A in [87]. Also at low temperatures the heat capacity of the phonons in the TES can be neglected and thus the effective coupling between absorber and the electrons in the thermometer can be defined as

$$G_{ea} = \left(\frac{1}{G_{ep}} + \frac{1}{G_K} \right)^{-1}$$

(2.8)

Finally the conductance to the heat bath is G_{eb}, allowing the TES temperature to relax back to the TDE value.

Now, considering a particle interaction in the absorber, one needs to distinguish between two processes:

Energy deposition due to an *ionizing particle* will first generate mostly highly excited electrons which in turn excite electron/hole pairs or transfer their energy to other electrons via scattering processes. The electron/hole production will stop when the particle energy drops below twice the gap energy of the absorber and the electron/hole pairs will recombine emitting optical phonons and also, depending on the crystal, by a small fraction optical photons. The optical phonons will decay within a few *ps* timescale into acoustic phonons of about half the Debye frequency

$$\nu_D = \frac{k_B}{h} \Theta_D$$

(2.9)

yielding an almost monoenergetic phonon distribution [88].

A *nuclear recoil* will mainly excite a population of non-thermal *acoustic* phonons by direct scattering or interacting with structural defects leading to a wide spectral distribution of phonons.

The different interaction processes for these two particle classes are used to discriminate nuclear recoils from electron, alpha and gamma interactions by detecting the amount of light produced in a single interaction.

Both phonon distributions are still out of TDE and will decay due to anharmonic processes with a rate $\Gamma \propto \omega^5$. The differences between the two distributions will thus be washed out. After a few surface reflexions the high frequency phonons are distributed uniformly in the absorber. Typical timescales can be estimated using the crystal size, e.g. diameter D, and the averaged[1] sound velocity v as L/v. For a few cm sized crystal this will be in the μs scale.

The high frequency phonons can now enter the thermometer where they are efficiently absorbed on the free electrons in the metal. As the electron-electron interaction in the metal is strong, the absorbed energy is quickly distributed along the whole thermometer, yielding a rise in the electron temperature T_e. This drives the time dependent power input $P_e(t)$ and leads to a fast signal. As the electron system is coupled to the heat bath via G_{eb}, part of the energy can escape. The rest of the energy will be emitted back to the absorber as *thermal* phonons, slowly heating the absorber T_a. As the coupling G_{ep} is proportional to T^5, this heat flow can be suppressed at very low temperatures.

The additional time dependent power input in fig. 2.2 into the absorber, labeled $P_a(t)$, represents the direct power input into the thermal phonon distribution due to thermalization of high frequency phonons on the crystal surface.

The energy density $\Delta E/V_a$, where ΔE is the deposited energy and V_a the volume of the absorber, is assumed to be uniform and the thermalization rate of the high frequency phonons is considered independent of their frequency. A fraction ϵ of those phonons is thermalized in the thermometer, the remaining $(1 - \epsilon)$ in the absorber. Assuming that the initial phonon distribution is present right after particle interaction, e.g. neglecting the randomization time, one can express the power inputs as follows

$$P_e(t) = \Theta(t)P_0 e^{-t/\tau_n}, \qquad \qquad (2.10)$$

$$P_a(t) = \frac{1 - \epsilon}{\epsilon} P_e(t) \qquad \qquad (2.11)$$

where P_0 is given by

$$P_0 = \frac{\epsilon}{\tau_n} \Delta E \qquad \qquad (2.12)$$

and the time constant for thermalization of the non-thermal phonons is

$$\tau_n = \left(\frac{1}{\tau_{film}} + \frac{1}{\tau_{crystal}} \right)^{-1} \qquad \qquad (2.13)$$

as the time constants for thermalization in the film τ_{film} and in the absorber $\tau_{crystal}$ will differ. The former is proportional to V_a/A where A is the contact area of the thermometer, the latter is expected to scale like V_a/O_a where O_a is the surface of the absorber [87, 88].

Neglecting the finite thermal conductivity along the thermometer one can describe the model shown in fig. 2.2 using the two coupled differential equations

$$C_e \frac{dT_e}{dt} + (T_e - T_a) G_{ab} + (T_e - T_b) G_{eb} = P_e(t) \qquad \qquad (2.14)$$

$$C_a \frac{dT_a}{dt} + (T_a - T_e) G_{ea} + (T_a - T_b) G_{ab} = P_a(t) \qquad \qquad (2.15)$$

---

[1]The average has to be performed over all directions and modes in the lattice.

and the initial conditions, defining thermodynamical equilibrium before particle excitation,

$$T_a(t=0) = T_e(t=0) = T_b \tag{2.16}$$

yielding the following solution for the time-dependent temperature rise of the electrons relative to the bath temperature $\Delta T_e(t) = T_e(t) - T_b$

$$\Delta T_e(t) = \Theta(t) \left[A_n \left(e^{-t/\tau_n} - e^{-t/\tau_{in}} \right) + A_t \left(e^{-t/\tau_t} - e^{-t/\tau_n} \right) \right] \tag{2.17}$$

where the time constants are given as

$$\tau_{in} = \frac{2}{g_1 + \sqrt{g_1^2 - 4g_2}} \qquad\qquad \tau_t = \frac{2}{g_1 - \sqrt{g_1^2 - 4g_2}} \tag{2.18}$$

using g_1 and g_2 as abbreviations for the terms

$$g_1 = \frac{G_{ea} + G_{eb}}{C_e} + \frac{G_{ea} + G_{ab}}{C_a} \qquad\qquad g_2 = \frac{G_{ea}G_{eb} + G_{ea}G_{ab} + G_{eb}G_{ab}}{C_e C_a} \tag{2.19}$$

The amplitudes are given by

$$A_n = \frac{P_0(\tau_{in}^{-1} - (G_{ab}/C_a))}{\epsilon(\tau_{in}^{-1} - \tau_t^{-1})(\tau_{in}^{-1} - \tau_n^{-1})} \left(\frac{\tau_t^{-1} - (G_{ab}/C_a)}{G_{eb} - (C_e/C_a)G_{ab}} - \frac{\epsilon}{C_e} \right) \tag{2.20}$$

$$A_t = \frac{P_0(\tau_t^{-1} - (G_{ab}/C_a))}{\epsilon(\tau_t^{-1} - \tau_{in}^{-1})(\tau_t^{-1} - \tau_n^{-1})} \left(\frac{\tau_{in}^{-1} - (G_{ab}/C_a)}{G_{eb} - (C_e/C_a)G_{ab}} - \frac{\epsilon}{C_e} \right) \tag{2.21}$$

While τ_{in} and τ_t are the time constants of the homogeneous equations, τ_n is the life time of the non-thermal phonon population introduced by $P_e(t)$ and $P_a(t)$. As eq. 2.17 shows, the solution consists of an non-thermal component with the amplitude A_n and a thermal contribution, given by A_t. As for a macroscopic absorber with a small thermometer $C_e \ll C_a$ will usually hold, eqs. 2.18 and 2.20 can be approximated as follows:

$$\tau_{in} \approx 1/g_1 \approx \frac{C_e}{G_{ea} + G_{eb}} \tag{2.22}$$

$$\tau_t \approx g_1/g_2 \approx \frac{C_a}{G_{eb}G_{ea}/(G_{eb} + G_{ea}) + G_{ab}} \tag{2.23}$$

$$A_n \approx \frac{P_0}{(G_{ea} + G_{eb})(1 - (\tau_{in}/\tau_n))(1 - (\tau_{in}/\tau_t))} = \frac{-\epsilon\Delta E}{C_e(1 - (\tau_n/\tau_{in}))(1 - (\tau_{in}/\tau_t))} \tag{2.24}$$

The denominator in eq. 2.22 represents the total thermal coupling of the thermometer. Thus τ_{in} can be interpreted as the intrinsic time constant of the thermometer. Likewise the denominator in eq. 2.23 is the total thermal coupling of the absorber and hence τ_t is its thermal relaxation time.

As eq. 2.24 shows, the ratios of τ_n/τ_{in} and τ_{in}/τ_t control the sign of A_n and thus the contribution of the non-thermal component to the signal. For a strong coupling of the electrons to the bath G_{eb} and weak coupling G_{ab} the intrinsic time constant τ_{in} will be small compared to τ_t and τ_n. Thus eq. 2.24 yields a positive value for A_n and simplifies to roughly $A_n \approx P_0/(G_{ea} + G_{eb})$. The rise time is given by τ_{in}, the fast decay by τ_n. So the non-thermal signal is directly proportional to the power input $P_e(t)$. As a detector operated in this mode is measuring the *flux* of non-thermal phonons, this mode is referred to as *bolometric mode*.

Obviously this is not the case for $\tau_{in} \gg \tau_n$, as eq. 2.24 will yield $A_n \approx -\epsilon\Delta E/C_e$. Since A_n integrates $P_e(t)$ and thus measures the *total energy* of the high-frequency phonons absorbed in the thermometer, this is usually called *calorimetric mode*. This mode can be realized by a weak coupling G_{eb} of the thermometer to the bath at very low temperatures where $G_{eb} \gg G_{ea}$ can still hold, despite of small values of G_{eb} itself.

In [87] Pröbst et al. also consider the finite thermal conductance along the thermometer. As this only effects the quantitative aspects of the intrinsic parameters and does not change the qualitative behavior of the solution described in this section, the modified model will not be discussed here.

The detectors presented in this thesis were operated in calorimetric mode. Thus the signals consist of a positive non-thermal contribution, proportional to the power input $P_e(t)$, with a fast decay time and a slower thermal part, e.g. several ms long. Therefore the acceptable interaction rate with the detector is quite limited. As Irwin and Lee et al. have shown in [89, 90], this situation can be improved substantially by implementing *electrothermal feedback* (ETF). This will be discussed in detail in sec. 2.8. Fig. 2.3 shows a fit adapting the presented model to real data. The undershoot after the pulse is an effect of the electronics and is not accounted for in the fit model. Yet the data can be reproduced quite well. The individual components, the non-thermal and thermal signal respectively, are also shown.
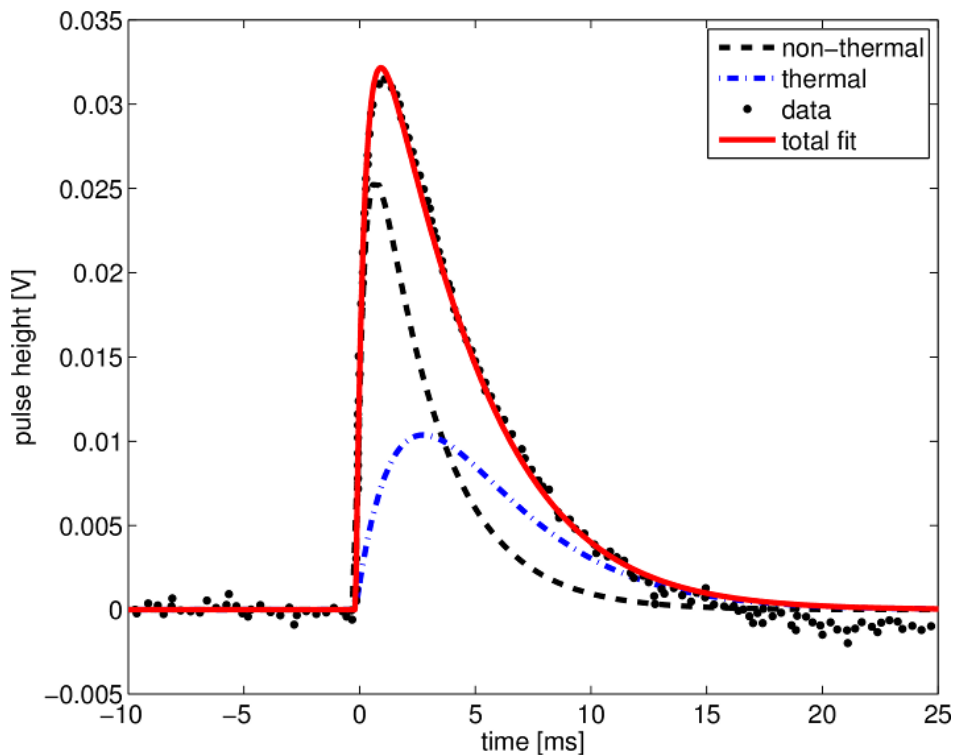

Figure 2.3: Real detector pulse recorded in this work and fitted model after Pröbst [87]: The undershoot after the pulse is an effect of the electronics and not accounted for in the fit model. The individual components, the non-thermal and thermal signal respectively, are also shown.

As mentioned above, recoils in dielectric crystals also produce a small amount of photons. These photons can be measured by a second cryogenic detector that is optimized for optical photon absorption. Usually black silicon or silicon on Sapphire (SOS) is used as target crystal. Such a pair of detectors is called detector module and allows the simultaneous measurement of the recoil energy and the amount of light produced by the particle hit. As recoils produced by particles that interact electromagnetically, like $e^{+/-}$, α and γ produce more light than nuclear recoils, this can be used for event-by-event discrimination. This has already been discussed in sec. 1.2.

Label (outer connector)	from	to	material
Customer 1	300K	Mixing chamber	Constantan
Customer 2	300K	Mixing chamber	Constantan
Experimentle 1	300K	1K stage	Copper
Experimentle 2	300K	1K stage	Copper
ext. Exp1	1K stage	Mixing chamber	superconducting wire
ext. Exp2	1K stage	Mixing chamber	superconducting wire

Table 2.1: Fixed wiring of the dilution refrigerator. Outer connectors are vacuum-tight 24-pin Fischer type, cold connectors are micro D-Sub 25-pin.

2.2 Measuring at the mK scale

Cryogenic detectors are operated at mK temperature scale. To provide such low temperatures a Kelvinox 400 HA dilution refrigerator is used in the Tübingen Shallow Underground Laboratory. It was set up, tested and described in a previous work [84]. The nominal cooling power of the cryostat is $\geq 460\,\mu W$. The system is equipped with several shielded and thermally well coupled cables, each accessible by micro D-Sub 25-pin connectors on the cold stages. These connectors are known to be suitable for mK measurements, see e. g. [91]. Table 2.1 gives an overview on the respective wiring. The room temperature sockets are vacuum-tight 24-pin Fischer connectors of type 105 A093 (DBEE).

Constantan wires should be used for heaters and temperature sensors. The latter should be connected using the 4-wire method in order to prevent resistance contributions from the wiring.

The superconducting wires are used for the SQUID system that will be described in detail in 2.5 and is basically used as a highly sensitive amperemeter. As usual resistor values for this kind of measurements are in the $m\Omega$ range, there should be no residual resistance introduced by the wires.

The wiring starting at the mixing chamber and connecting the experiment is changing, depending on the connected setup. In general only shielded twisted-pair superconducting NbTi wires are used. To minimize high frequency noise in the SQUID circuit, symmetrical cold low-pass filters are used as shown in figs. 2.4 and 2.5. The heater lines can also be equipped with such filters, yet it proved to be sufficient to have the low-pass on the room temperature stage. Therefore a simple filter box with BNC connectors was produced. It can be connected or removed, as needed.

In order to compactly place the necessary shunt resistors (see sec. 2.4) for up to eight SQUIDs in the cryostat, a Copper box with eight metal film resistors of $20\,m\Omega$ each, was made and can be connected via micro D-Sub 25-pin connectors. The resistors are glued to a Copper plate using thermally conductive Stycast$^{\textregistered}$ 2850 FT allowing to easily remove the dissipated energy. The shunt box is mounted on the mixing chamber temperature stage to minimize the thermal noise in the SQUID's load circuit.

2.3 Transition edge sensors

To measure the small temperature change in an absorber crystal induced by an impinging particle, special thermometers are required. Besides NTD sensors[2], which require a high impedance readout that is prone to high frequency pick-up[3], the mainly used devices are superconducting films operated in the transition between superconducting and normal conducting phase. These so called transition edge sensors need to meet certain criteria: As CRESST-like detectors usually are operated in the 7 to 30 mK range to maximize

---

[2] *Neutron transmutation doped* thermistors, for these type of experiments mainly made of Germanium.

[3] For high frequency signals the capacitance of the insulating material can become relevant, especially for large signals. Charge storage in the material can lead to signal distortions. This effect can be reduce by choosing low absorption insulators like e. g. Teflon.
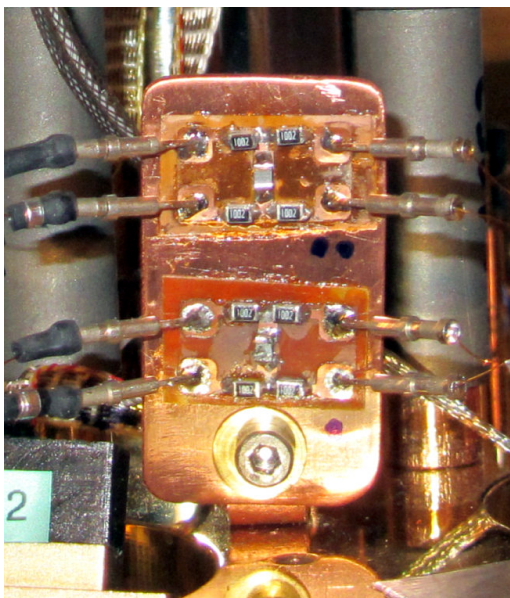
Figure 2.4: Photo of the cold stage low-pass filters. The two filters are heat-sinked on a Copper plate.
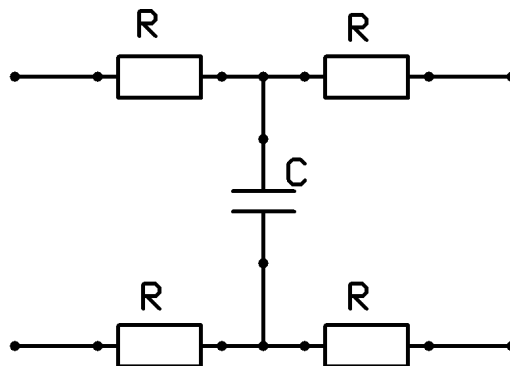
Figure 2.5: Symmetrical low-pass filters used in the SQUID circuits. R is chosen to be $5\,\mathrm{k\Omega}$, C is $820\,\mathrm{pF}$.

the detector response (see sec. 2.1) the transition temperature T_c of the superconducting film should also lie within this range. This can be achieved by using α-Tungsten films, see [48] for details. The width of the transition is usually smaller than $0.5\,\mathrm{mK}$, resulting in a steep rise of the resistance with rising temperature and as such yielding a high amplification. To ensure that the signal response is linear, the R(T) curve should exhibit no features like shoulders or even local minima.

TES selection according to these criteria is therefore crucial and was one of the tasks within this work. In the following section the basic principle of measuring R(T) curves will be explained.

2.4 Measuring R(T) curves

The setup for measuring the resistance of a TES as a function of temperature, shown in fig. 2.6, consists of a known reference resistor, also called shunt resistor R_s, in parallel with the TES. The current in the TES branch produces a magnetic flux in the input coil of a SQUID as the coil is in series with the TES. The change in I_{TES} and thus in flux in the input coil is sensed and amplified by the DC-SQUID which will be discussed in detail in section 2.5. When applying a bias current I_0 to the parallel circuit, it will be split according to the ratio of R_s/R_{TES} where R_{TES} varies with T. As the shunt resistor provides a constant voltage in the TES branch, this is also called *voltage bias mode*.

Recording the R(T) curves can in principle be achieved using two different methods: Keeping the holder temperature constant and adjusting the bias current or selecting a constant bias current I_0 for the TES sample and sweeping the temperature of the holder. As a higher current I_0 also introduces a higher self-heating power $P = R_{TES}(T) \cdot I_0^2$ and thus shifts the superconducting transition to higher temperatures T_c it is desirable to use a low, constant bias current I_0 and sweep the holder's temperature. This has been described in detail by Schnagl[92]. Thus the latter method has been used in this work. In order to avoid problems with SQUID resets and offset voltages, one usually likes to alternate the current steps between $\pm I_0$. Then, the measured current can easily be converted to resistance values using the following equation:
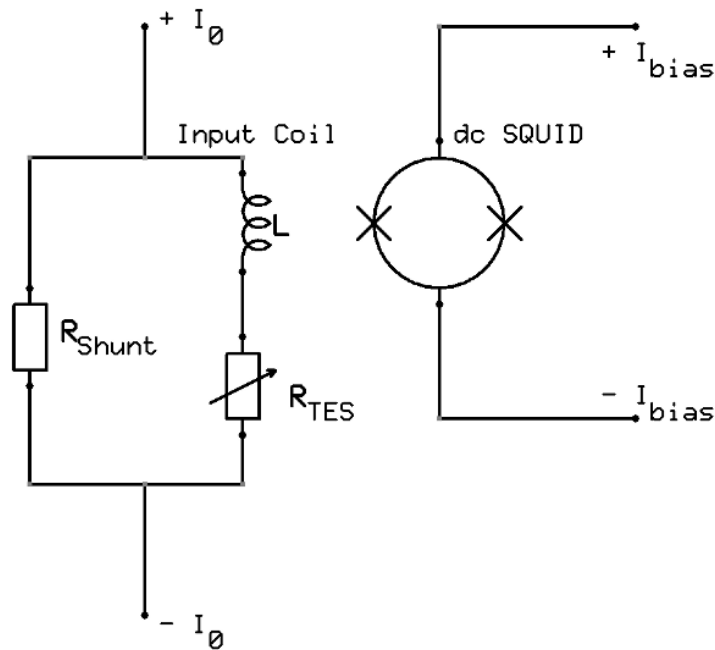
Figure 2.6: Setup for $R_{TES}(T)$ measurements. The shunt resistor value is know, the current I_0 is split according to the ratio R_s/R_{TES}.

$$R_{TES} = R_s \left(\frac{2I_0}{\Delta I_{TES}} - 1 \right)$$

(2.25)

The factor two is needed as the total ΔI is two times I_0 in a bipolar measurement.

When selecting the current source to generate the current I_0, it has to be considered that the measurement should be performed in floating mode, which means that the ground potential is defined by the connected sensor, in order to monitor the absolute baseline level of the SQUID signal. The baseline data can be used to check and correct for events with flux quantum losses, as those will appear as baseline jumps of distinct values, depending on the SQUID's transfer coefficient (see sec. 2.5). Also, as will be discussed shortly in sec. 2.8, there might be a ground connection in the TES circuit due to the Gold bond providing thermal coupling of the metal film. This can in principle be omitted during R(T) measurements yet it is advantageous to have a single current source for all applications. So the current source for the TES or detector bias current needs to operate in floating mode.

As the CRESST experiment is also using such devices, a circuit diagram was provided by our colleagues at the Max-Planck Institute Munich. The design had to be adapted slightly. The operational amplifiers had to be replaced by different versions since the old ones were no longer available. Also the power supply had to be changed because the original plans were tailored to use the power racks already available at the CRESST experiment. The final design can be found in the Appendix in fig. A.1. The reference current is amplified, then split symmetrically around ground and amplified again. Basically the source is built such, that it demands exactly the current value on the negative branch that is sent on the positive side. Thus no current is allowed to escape over possible ground connections in the load circuit. The ground level of the source itself is defined by the connected cable's shielding, thus floating with the cryostat as required.

The current source is also equipped with an external reference voltage connector. It can be used to modulate the current signal, which is necessary for measuring transition curves as described above. Since the cold filters

described in sec. 2.2 are an additional load to the bias circuit, the source was calibrated using an Alcron 2020 multimeter and a $20\,\mathrm{k\Omega}$ load resistance to simulate the cold filters. Up to $5\,\mathrm{V}$ excitation voltage the output current is linear for all range settings. The respective coefficients for voltage to current conversion can be found in Appendix A.1. The internal reference can be used by selecting the desired range (labeled *Stufe*) and using the potentiometer *Ref. intern* for fine-tuning. The output current is found to scale linearly with the reference voltage up to $30\,\mathrm{mA}$ output current. The respective coefficients for voltage to current conversion can be found in Appendix A.1 as well. Fig. 2.7 shows a photograph of the current source. The output is using a Triax connector to provide optimal shielding for the low bias currents.

Figure 2.7: Front panel of the floating current source. Connecting a function generator to *Ref. Extern*, current pulses can be generated.

Using the floating current source in combination with a Tektronix AFG 3021 arbitrary function generator connected to the external reference port, multiple TESs have been measured using the pulsed method presented earlier. To access the TES circuit wiring a break-out box has been produced. This box diverts the pins labeled *I1* and *IGND1* in the SQUID electronics manual to a Triax connector. There is also a switchable break-out box for up to three channels, allowing to use either the SQUID electronics's current source (see sec. 2.5) or the floating current source described above. A picture of this adapter can be found in fig. 2.8.

Two different types of contacting transition edge sensors have been investigated during this thesis: The standard method is using bond wires which is shown in fig. 2.11. A typical transition for such setups can be found in fig. 2.9. The TES is a sputtered Tungsten film that has been produced by S. Roth at TU Munich. The production process is described in [93]. The hysteresis between sweeping the temperature up (stars) and down (open circles) is less than $0.4\,\mathrm{mK}$ as the sweeps were performed slowly with low bias current of $0.6\,\mathrm{\mu A}$, keeping self heating effects at a minimum. Fig. 2.10 shows the effect of a higher I_0 on the transition curve on another sputtered W-TES: Due to the higher power input to the TES, the transition curve is significantly broadened. In this measurement the mixing chamber thermometer was used to record the temperature. The thermal offset between T_{MC} and T_{TES} changes with the power injected via I_0, thus the value for T_c for the $7\,\mathrm{\mu A}$ data will actually be higher than in fig. 2.10.

Since the small bond wires used to connect the TESs might be prone to vibrations as they have to span quite a distance (usually in the order of 5–$10\,\mathrm{mm}$), this might lead to changing magnetic flux inside of the TES branch which will increase noise. Therefore Aluminum clamps have been tested as a second connection method, as proposed and first checked by Isaila [94]. This contacting method could also be an option when working with hygroscopic material, see ch. 3. A photograph of the setup can be found in fig. 2.12. As in [94] the results obtained are quite satisfying. The respective transition curve can be found in fig. 2.13. But since the clamps take up more space than the bond wires, this type of connection is not always an option. Also

Figure 2.8: Switchable break-out box for three FLL electronics channels, enabling access to an external current source.
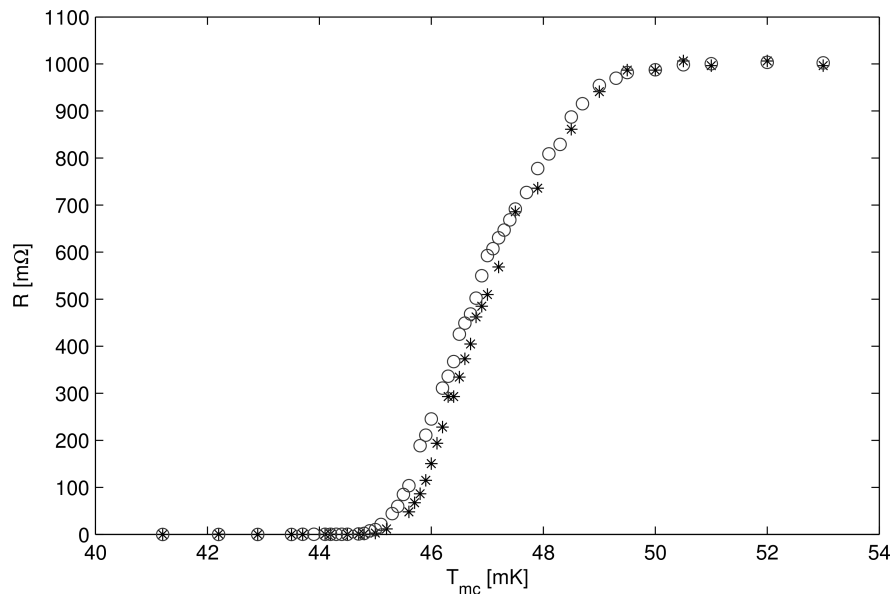

Figure 2.9: Transition curve of a sputtered Tungsten TES. Bias current was $0.6\,\mu A$. The hysteresis between sweeping the temperature up (stars) and down (open circles) is less than $0.4\,mK$ as the sweeps were performed slowly with low bias power, keeping self heating effects at a minimum.
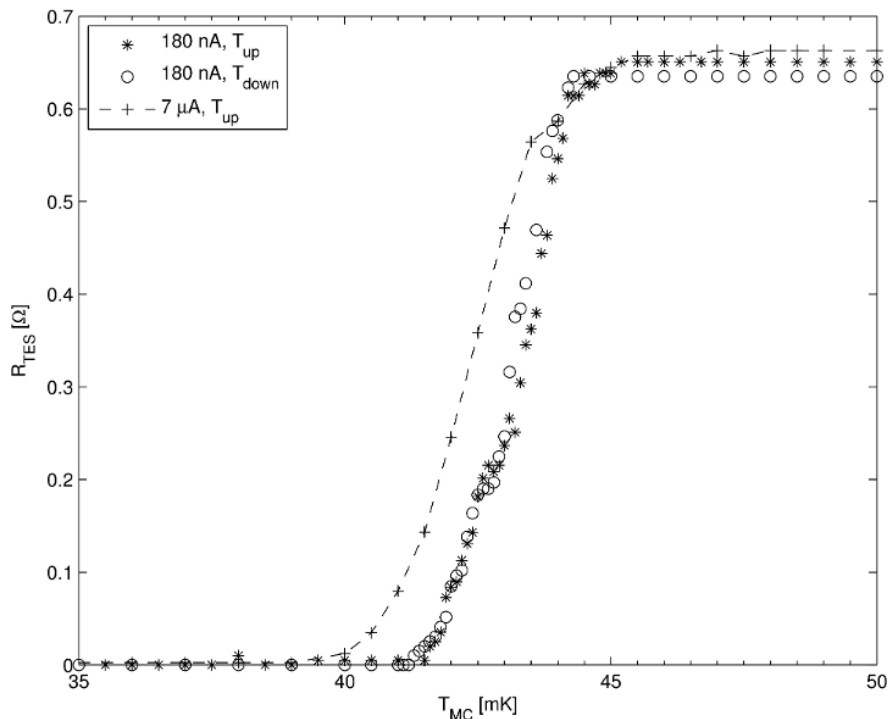
Figure 2.10: The effect of I_0 on the transition curve: a higher current leads to a higher power input to the TES, broadening the transition. The recorded temperature of the mixing chamber T_{MC} differs from the actual TES temperature, so T_{MC} for the $7\,\mu A$ data is actually higher than suggested by this plot.

the TES might be damaged by the clamps, if the clamps are moved sideways by accident.

In order to check the noise level and general performance of two C4-type SQUID-array sensors produced at PTB Berlin by the group of J. Beyer, a single sputtered Tungsten film of $8\,mm\,x\,8\,mm$ on a Sapphire carrier was connected to those SQUIDs. Also this thermometer was produced at TU Munich. A picture of the setup can be found in fig 2.14. On channel 1 the TES was connected directly to the input coil, without a shunt resistor. On channel 2 the TES connection was standard TES fashion (see fig. 2.6), making use of the $1.1\,\Omega$ resistor on the SQUID chip. Fig. 2.15 shows the connection schemes. The bond wires to the carrier of the TES were placed to improve the cooling of the substrate for temperatures above the critical temperature of Aluminum. While channel 2 can be measured as described above, channel 1 has to be treated differently since there obviously is no current division as in the shunted case.

The SQUID feedback voltage for channel 1 can be recorded to take noise samples at different temperatures. A fast scan down in temperature showed a sudden rise in the noise level at around $37\,mK$. Assuming that the signal in the TES circuit is dominated by thermal noise, the mean current power density can be expressed [96] as

$$\bar{i^2} = \int 4k_B T / R_{TES} df \qquad \text{(2.26)}$$

with i denoting the instantaneous current fluctuation around the mean value and k_B the Boltzmann constant. The integral has to be performed over all frequencies f within the system's bandwidth. As the SQUID voltage V_s is proportional to the current in the TES branch, the variance δ^2 of the voltage in a noise sample at a certain temperature T is a measure for $\bar{i^2}$. Since thermal noise is independent of the frequency, the integration for a given system will be just a scaling factor. Therefore one can derive the resistance of the TES as

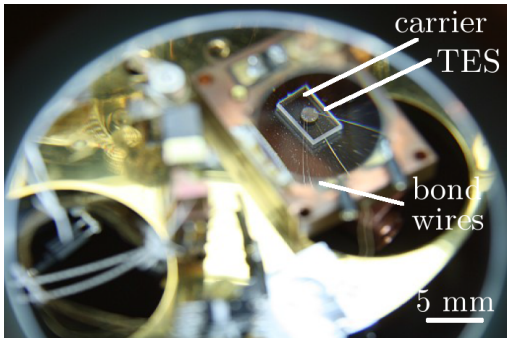$$R_{TES} = \kappa 4k_B T / \delta^2 (V_s) \qquad \text{(2.27)}$$

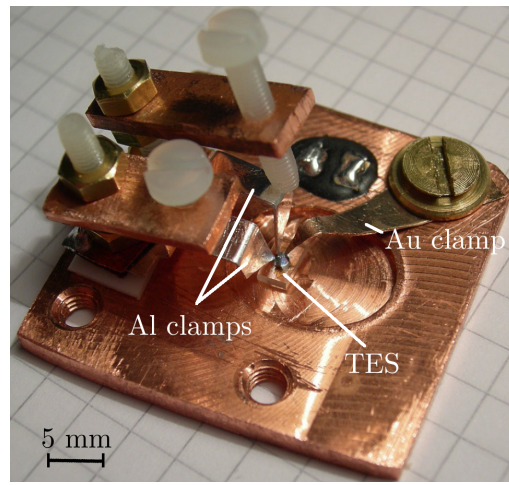Figure 2.11: A Tungsten TES with standard bond connections to the SQUID.

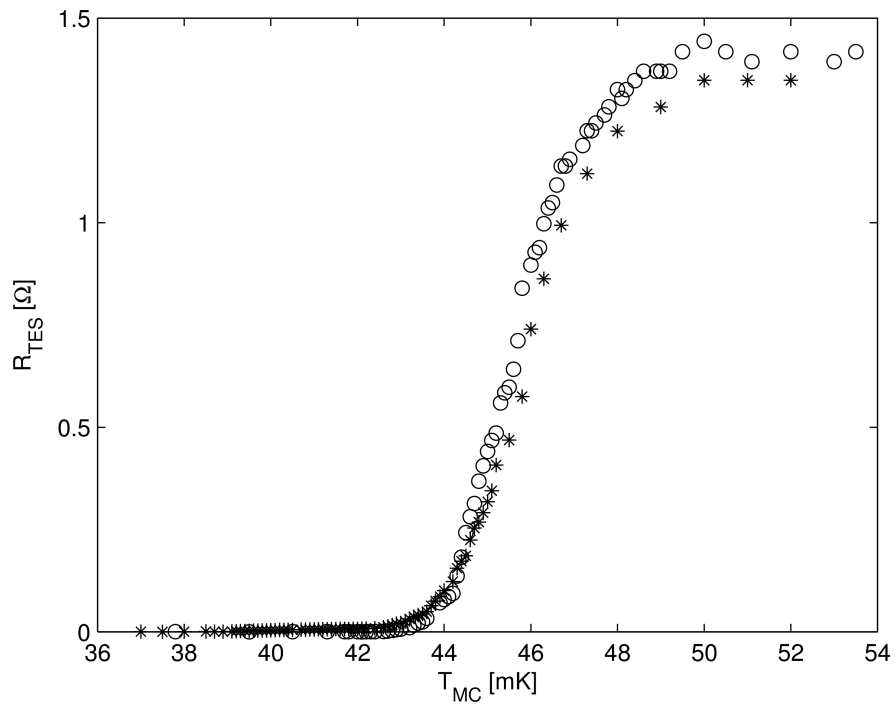Figure 2.12: A Tungsten TES connected using Aluminum clamps.

Figure 2.13: Transition curve of a Tungsten TES held by Aluminum clamps. I_0 was $2\,\mu A$.
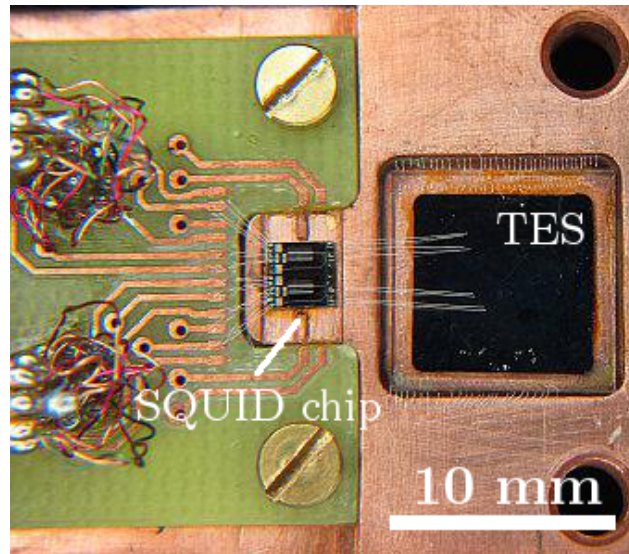
Figure 2.14: Sputtered Tungsten TES (right) directly bonded to two separate SQUIDs (middle).
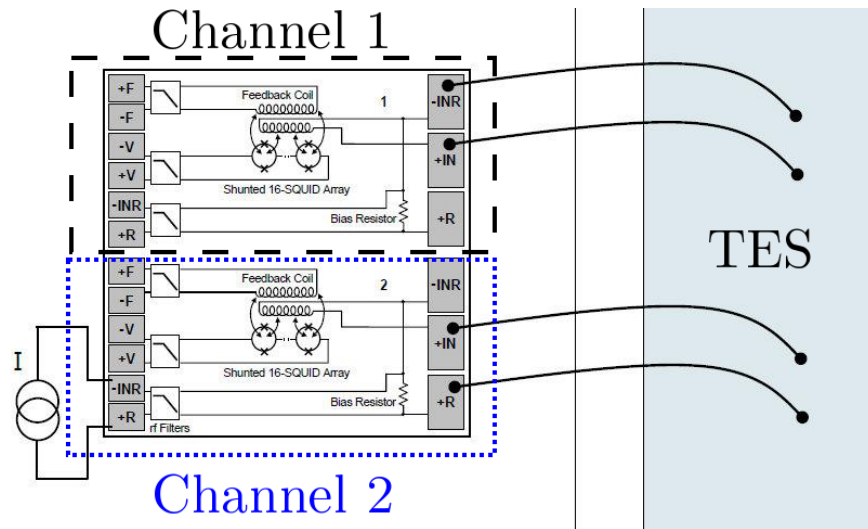

Figure 2.15: Two different connection schemes on a common sputtered Tungsten TES. Channel 1 (top) is connected directly to the input coil, without a shunt resistor. Channel 2 (bottom, *blue*) is connected in standard TES fashion, making use of the $1.1\,\Omega$ resistor on the SQUID chip. Image based on: [95]

with the constant κ resulting from the integration over the system bandwidth and the conversion of SQUID voltage to the current I_{in} in the TES circuit. In feedback mode the latter can be calculated as

$$I_{in} = \frac{V_s}{R_f} \frac{M_f}{M_{in}}$$

(2.28)

where R_f is the value of the feedback resistor. M_f and M_{in} are the respective mutual inductances of the feedback and the input coil [97].

The resistance of the TES was calculated from noise samples of channel 1 in temperature bins of 2 mK each using eq. 2.27. The resulting transition curve can be found in fig. 2.16.
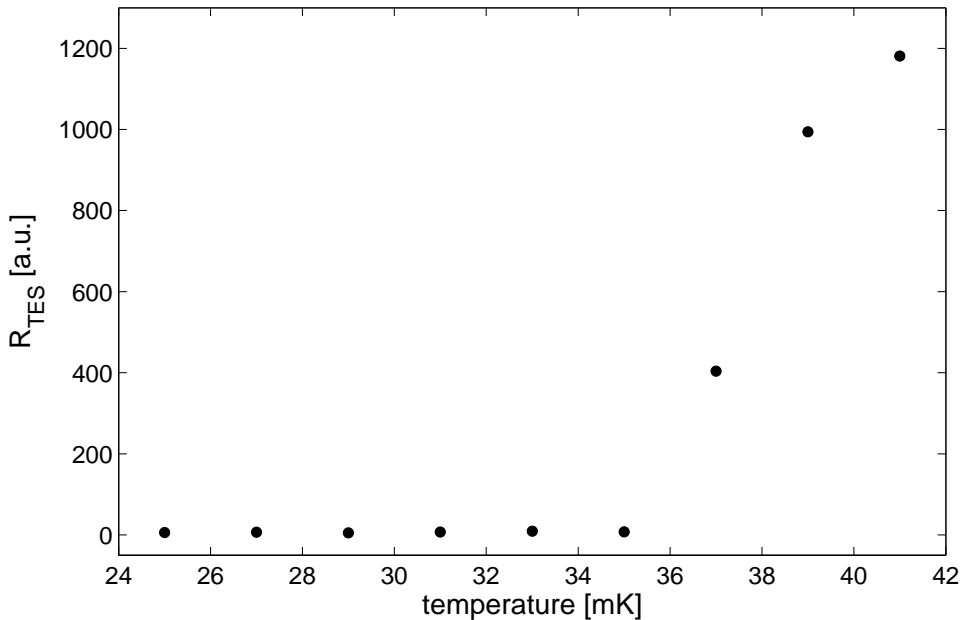

Figure 2.16: Tungsten transition curve derived from a noise power amplitude measurement. Temperature bin size was 2 mK.

For the standard TES measurement on channel 2 a T_c of 43 mK was measured with a bias current I_0 of 180 nA. This is rather high as compared to the transition temperature measured on channel 1, which is around 38 mK. It seems unlikely, that such a low bias current can lead to a difference of 6 mK in T_c due to heating. Rather the local critical temperatures of the Tungsten film seem to differ quite a lot. This is supported by comparable measurements carried out at PTB Berlin [95].

Yet it has been shown that superconducting transitions can be measured by un-shunted connection of the SQUID without applying a bias current. This removes the effect of self-heating and simplifies the readout circuit. It is therefore suggested to repeat the measurement with a finer temperature binning to check if the transition curve features can be resolved as well. Also estimating the system's bandwidth for such a measurement would even allow to scale to absolute values. This could then be used to cross check with the room temperature value R_{TES}.

In conclusion all sputtered Tungsten films showed a smooth transition. Yet T_c is still quite high compared to films produced by dedicated UHV evaporation systems. Also the width of the transitions should be reduced further.

Additionally to the presented standard procedure for transition measurements with the CRESST-type current source there are two other options available: Using the analog output of the DAQ to generate the I_0 pulses which will be described in sec. 2.6 or using the SQUID electronics's internal current source. As at present both alternative methods are not as fast and flexible in configuration as the one using the floating current source, this chapter has focused on the latter. The SQUID system will be discussed in the next section.

2.5 SQUID System

As mentioned in the previous section 2.4, a DC-SQUID sensor is used to measure and amplify the change of current occurring in the TES branch when the temperature of the Tungsten film changes. The SQUIDs used in this work have been provided by Magnicon GmbH, Hamburg. The eight sensors are of the C5 Single Stage design which exhibit large values for the transfer coefficient V_ϕ e. g. $\sim 900\,\mu V/\Phi_0$ and a maximum voltage swing of around $40\,\mu V$. Due to the large area intermediate coil on the SQUID wafer these sensors should be operated in Niobium magnetic shields to minimize noise pick-up. Care has to be taken when connecting the sensors, as electrostatic discharge (ESD) can destroy the input coil of the sensors, rendering them unusable. The SQUID sensors are enhanced by the use of additional positive feedback (APF) increasing the transfer coefficient on the positive slope of the V-Φ pattern. Thus the signal in figure 2.17 is not symmetric. APF is achieved by adding a parallel branch to the SQUID, consisting of a resistance R_{APF} in series with an inductance M_{APF} that is magnetically coupled to the SQUID. Fig. 2.18 shows the basic diagram. Locking the SQUID on the increasing V-Φ pattern a flux change in the SQUID is generating a voltage in M_{APF}, resulting in a higher SQUID output voltage. Conversely, locking on the decreasing side a flux change in the SQUID results in a negative voltage in M_{APF}, lowering the output voltage, thus leading to the asymmetry in the V-Φ pattern. Although the maximum voltage swing is reduced slightly by this method, the slope of the V-Φ pattern and thus the transfer coefficient can be greatly enhanced. More details on the C5 SQUID design have been published in [98, 99].
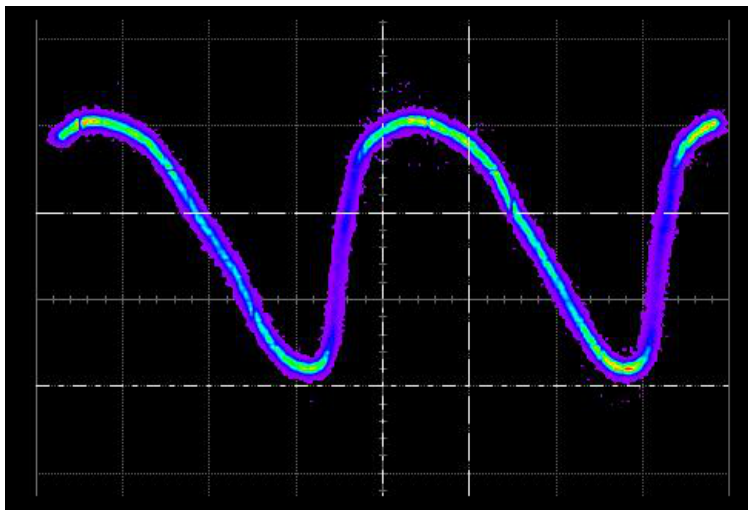

Figure 2.17: SQUID voltage (y-axis) as a function of coupled flux (x-axis). The asymmetry is a result of Additional Positive Feedback (APF). The maximum voltage swing after pre-amplification for this sensor is $\sim 60\,mV$. In FLL mode this highly non-linear function is linearized by the electronics.

Usually one operates these SQUIDs in flux-locked loop (FLL) mode which means that the change of flux in the SQUID induced by the pick-up coil is compensated by the reversed flux in a feedback coil. The current necessary to cancel out the flux is feed through an adjustable feedback resistor R_f yielding a linear output signal of the FLL electronics, as long as the system's bandwidth is not exceeded. Thus the repetitive SQUID
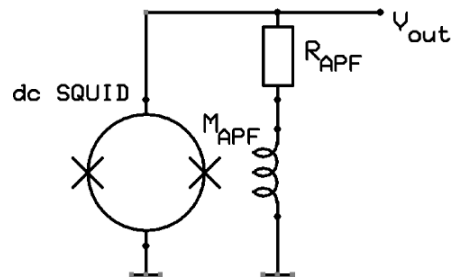
Figure 2.18: Basic circuit for additional positive feedback (APF). Locking on the increasing V-Φ pattern a flux change in the SQUID is generating a voltage in M_{APF}, resulting in a higher SQUID output voltage. Conversely, locking on the decreasing side a flux change in the SQUID results in a negative voltage in M_{APF}, lowering the output voltage. The steepness of the rising pattern and thus the amplification factor for a working point on the positive slope is enhanced significantly.

V-Φ pattern is linearized and the dynamic range of the system is largely extended.

Figure 2.19: The FLL electronics's Bias palette: Bias current *Ib*, voltage *Vb* and flux compensation *Phib* can be adjusted for the selected channel.

A fast FLL electronics system with high bandwidth of up to 20 MHz manufactured by Magnicon is used in the Tübingen Underground Lab to read out up to eight channels at once. Details on the XXF-1 electronics are published in [100]. The SQUIDs can be configured using the SQUID *Viewer*™ software and parameter sets for single channels or for the whole system can be saved and restored as needed. In order to optimize the FLL operating point several steps have to be performed in the SQUID *Viewer*™ *Bias palette*, that is displayed in fig. 2.19 :

1. In *Amp* mode the V-Φ pattern is displayed on an oscilloscope using the FLL electronics's internal function generator to modulate the flux *Phib* in the feedback coil on the y-axis and the SQUID system's

monitor port (black) on the x-axis. The monitor port just generates a triangular voltage signal that allows to display the patter in sync e. g. no triggering is required to keep the pattern from moving on the x-axis.

2. Using the SQUID bias voltage *Vb* the pattern can be moved up and down as a voltage offset is generated. The pattern should be centered around zero bias voltage. Therefore all oscilloscope couplings should be set to DC and all offsets have to be zero. As the FLL electronics will lock to zero output voltage, no FLL operation is possible if the pattern has no intersection with y = 0. This can happen if there is an uncompensated offset due to the wiring and/or *Vb* is not adjusted correctly.

3. Using the feedback current *Phib* any residual flux should be canceled out so that the point with the largest gradient of the V-Φ pattern is set to zero on y and x scale. Thus one achieves the highest amplification and maximum dynamical range. Note that the constant current to generate the needed offset is superimposed with the modulating signal of the function generator needed to display the signal. In case that a large flux got trapped in the SQUID during the cooling procedure, the Josephson junctions can be heated using the *Heater palette*. Thus the SQUID is shortly heated to normal-conducting state, allowing the trapped flux to escape.

4. The bias current *Ib* should be adjusted such, that the voltage swing of the pattern is maxed. The SQUID bias current should not be confused with the bias current I_0 in the load circuit of the SQUID. *Ib* is the current applied directly to the superconducting ring of the SQUID, leading to the characteristic interference of the currents across the two Josephson junctions, while I_0 inductively couples to the SQUID via the input coil.

5. As a last step the function generator needs to be deactivated and the mode needs to be changed from *Amp* to *FLL*.

Even with optimized FLL parameters the SQUID electronics can be kicked out of FLL mode which means that the signal can no longer be followed by the feedback electronics, either by high frequency noise exceeding the system's bandwidth or by large signals, e. g. muon induced signals, when measuring with high amplification. To reset the system automatically, the electronics has a built-in overload detection that can be used to auto-reset it.

Another useful feature is the already mentioned on-board function generator: It can either be used to modulate the feedback coil current or the bias current I_0 in the input coil circuit. As there is also a pulsed mode available, one can measure the transition of a TES sensor as described in sec. 2.4 even without using an external current source. There are some restrictions though: Alternating between +I_0 and -I_0 is not possible as the pulsed output is unipolar and the pulse duration is limited to 2 ms at maximum. The maximum current provided is 500 µA.

The SQUID output signals are accessible via standard BNC connectors. There is also a switchable warm-stage 10 kHz anti-alias filter available at the SQUID systems connector box which reduces high frequency noise considerably and should thus be used when measuring. However, it has to be considered that this significantly limits the bandwidth of the system and that subsequent digital sampling should be performed with at least twice the cutoff frequency as demanded by the Nyquist-Shannon sampling theorem [101]. The connector box is needed to optically isolate the connection to the PC. In order to record the SQUID signal, a data acquisition system is needed. This will be presented in the next section.

2.6 Data acquisition system

To record the SQUID output signals a PXI based data acquisition system was purchased from National Instruments™. PXI stands for *PCI eXtensions for Instrumentation* and is basically an improved version of the PCI bus, allowing for integrated timing and synchronization which makes it easy to use common

timing and allows for internal triggering. Fig. 2.20 shows the PXI-1033 chassis with and Optical Link PXI-8336 Connector and two PXI-6115 Simultaneous Sampling Cards. The optical link decouples the cryostat electrically from the PC which is desirable as the system can thus be kept floating and the high frequency of the PC's processor does not disturb the FLL electronics. The BNC-2110 trigger board is used to connect the SQUID's BNC output signals and to provide basic filtering and timing. The analog input impedance of the card is $1\,\mathrm{M\Omega}$ for signals in the range $\pm 10\,\mathrm{V}$ which should be taken into account when measuring pulse heights.
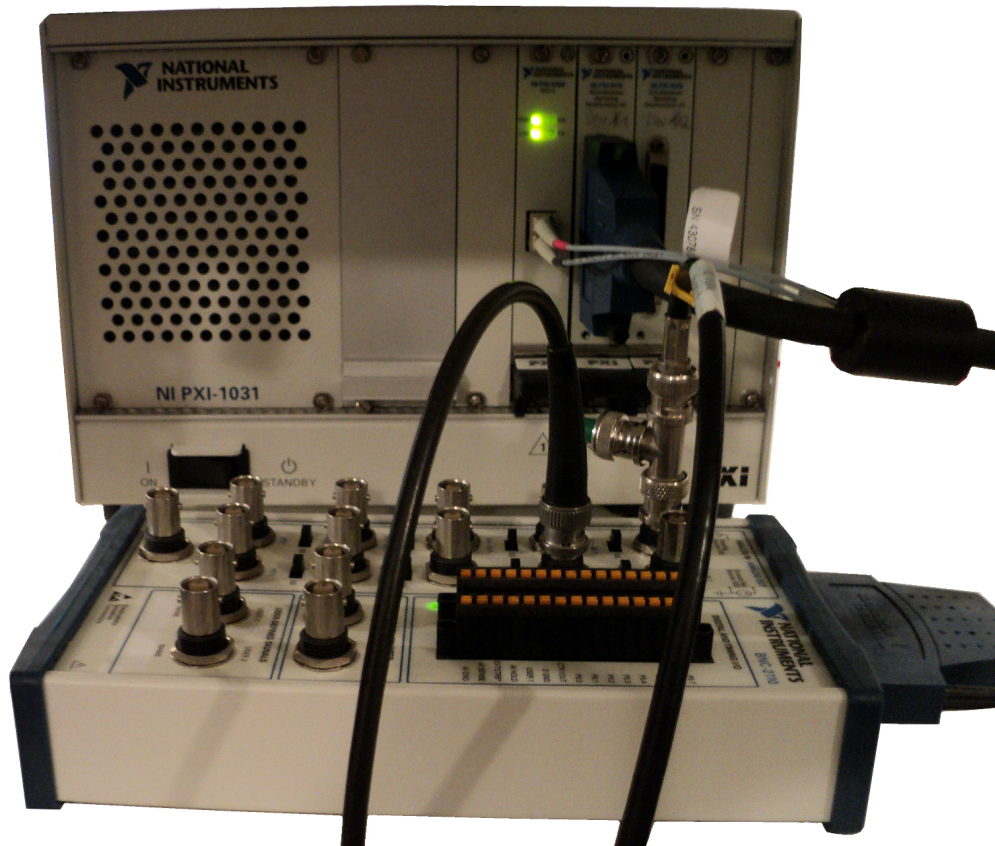

Figure 2.20: The PXI DAQ system: PXI-1033 chassis (back) with Optical Link PXI-8336 and two PXI-6115 Simultaneous Sampling Cards (left to right in crate). The BNC-2110 trigger board (front) is used to connect the SQUID's BNC output signals and to provide basic filtering and timing.

The LabVIEW-based software used to read out the signals was developed by Wolfgang Westphal at TU Munich [102] and consists of several subprograms, so called VIs (Virtual Instruments). A screenshot of the main application can be found in fig. 2.21. The software relies on LabVIEW traditional drivers which are now replaced by the DAQmx system. This should be considered during the installation process. Details can be found in the Appendix A.2.

Besides selecting and enabling up to four DAQ channels and defining their respective settings, like range and coupling, the trigger can be configured in this VI. Available options are *analog*, *digital A*, *digital A and B* and *scan clock gate*. A detailed description of those settings can be found in the PXI-6115 documentation. The pulses are displayed in realtime allowing for easy adjustment of record length and trigger parameters. The software can also perform a simple left-right baseline cut to suppress noisy events and a rough range check to detect FLL resets. The *MCA* button calls the Multi Channel Analyzer VI which allows to get a rough pulse height spectrum. This can be used to optimize the detector's operating point which will be discussed
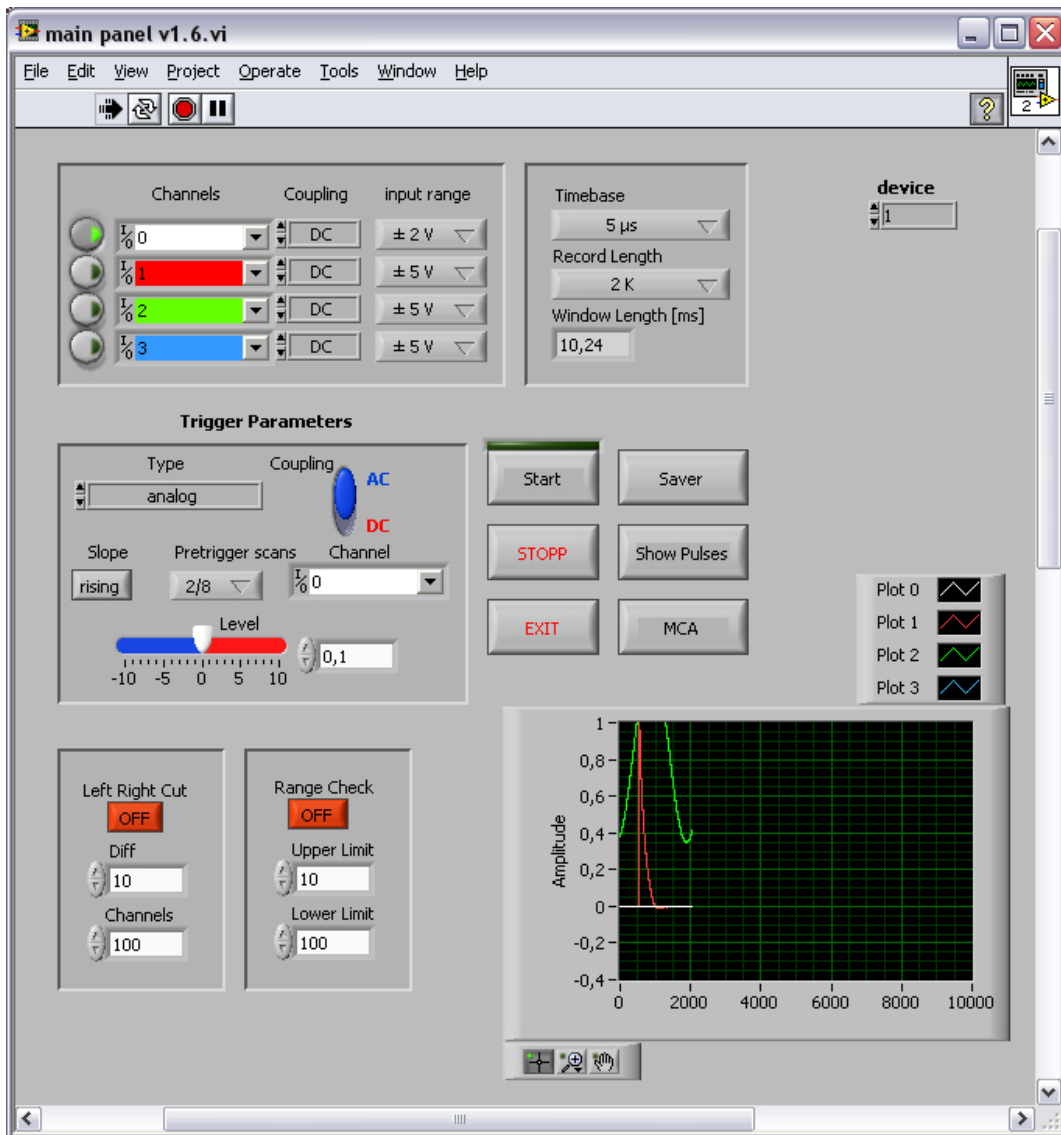
47

Figure 2.21: Screenshot of the main panel of the DAQ software. Up to four channels can be used simultaneously. Internal and external triggering can be used. Triggered signals are displayed in realtime to allow for easy adjustments of record length and trigger parameters.

in section 2.8.1. As this VI is quite CPU heavy it should be turned off while recording data [102]. The button *Show Pulses* opens a more versatile display for the live events than the small graph that is integrated in the main application. This VI should also be kept closed during recording but is quite useful for optimizing the settings. Finally the *Saver* button calls a VI that allows to record a predefined number of triggered events in the CRESST data format *.rop, allowing the use of standard software for data analysis. The current version has a file size limit of 2 GB.

All other VIs were written and tested during this thesis. Recording of resistance versus temperature data uses the AVS_writeTFile_v2 VI, see fig. 2.22. This program was written using the LabVIEW drivers for GPIB communication provided by PICOWATT [103]. GPIB, also called IEEE-488.2, stands for *General Purpose Interface Bus* and is a parallel bus allowing up to 31 devices on a single shared line. Each device has a unique device number consisting of five bits allowing for separate addressing. To ensure data integrity a three stage handshake consisting of the status messages *ready*, *valid* and *accepted* is used. The IEEE-488.2 plugs can be stacked, thus allowing daisy-chaining the devices. Both used AVS47-IB resistance bridges are equipped with optical fibers, connecting to a PICOWATT computer interface that is connected to the computer's GPIB controller provided by National Instruments. This is done to decouple the PC from the cryostat, preventing high frequency noise, e. g. from the micro controller, to spoil the resistance reading by introducing additional heating power. The VI can remotely change the AVS settings like range, excitation voltage etc. and stores the resistance reading and respective timestamps in a file. The block diagram can be found in the Appendix A.4 in fig. A.3.
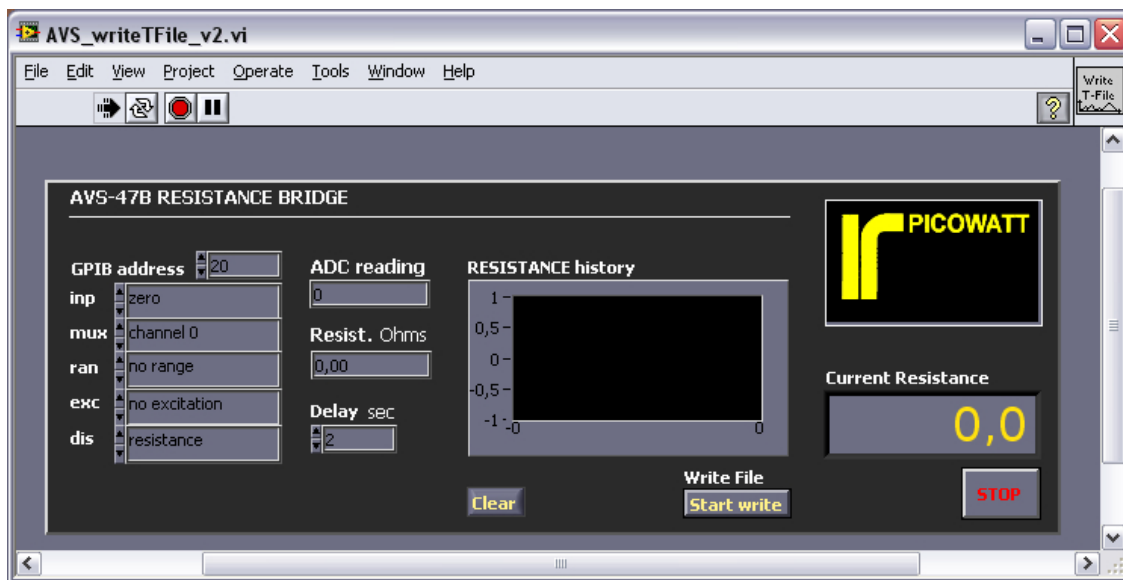

Figure 2.22: Screenshot of the AVS-47B VI.

Recording transition curves with the PXI-6115 cards is done using the TES_withDAQ_3 VI. A screenshot of the interface can be found in fig. 2.23. The current version 3.0 allows not only to record the raw voltage signal of the SQUID response, which can then be converted to resistance values using eq. 2.25 but also has multiple filtering options implemented. This can be very useful when working with small bias currents which should be the general case, as the heating power of the introduced measuring current changes the TES's temperature and thus broadens the transition curve. This has been discussed in sec. 2.4. Small currents correspond to a small voltage signal and thus the signal to noise ratio decreases since the noise is not dominated by the bias current contribution. As explained in sec. 2.4 the pulse frequency is in the order of a few Hertz or even lower. Thus the high frequency noise can be suppressed by either averaging (used when excitation is a current step) or a low pass or band pass filter (for all other signals). All three options are implemented in the program

and can be selected in the *Select Data Operation* menu. The frequency cut-off fields are only used, when applicable. The menu *Record this* allows to select which parameter should be written to a given file. Options are *Filtered Amplitude* and *High State* or *Low State*. The latter two cases are used for positive and negative unipolar signals respectively. In addition, the raw signal voltage (peak to peak) is always recorded.

As the PXI-6115 also provides two analog output channels with 12-bit resolution and $\pm 10\,\text{V}$ range it is in principle possible to generate and record the I_0 current pulses necessary for the TES measurements described in sec. 2.4 only using the DAQ system connected to the external reference of the floating current source. Some tests on this have already been performed but a respective VI has yet to be written and tested in detail.

2.7 Resistance bridge and temperature controller

In order to record R(T) curves or to stabilize a detector at a certain temperature, reliable thermometers are needed. Standard thermometers at mK scale to monitor a sample temperature are RuO_2 resistors with calibrated R(T) behavior. To avoid residual resistance contributions from the sensor wiring, the RuO_2 thermometers are connected using the 4-wire method. Measuring the resistance at mK temperatures is quite challenging, as a measuring current I_m will introduce the heat $P_m = R \cdot I_m^2$, thus changing the actual temperature reading. Using a resistance bridge and minimizing the excitation current I_m is therefore crucial to get reliable values.

In this work two AVS 47B resistance bridges by PICOWATT were used. These devices use only passive components, hence they do not generate high frequency noise that might couple into the sensor and heat it up. The drawback is a rather slow analog to digital conversion, but as thermal systems are quite inert, this can be accepted. Eight 4-wire channels can be read out with one device, as it has a built-in multiplexer.

The connecting cables should be as short as possible, twisted pairs and well shielded. The AVS bridges are equipped with optical fiber connections to isolate the bridges from the PC. The latter is connected using a GPIB interface. As explained in sec. 2.6, GPIB uses a common line for multiple devices, thus the PC can manage both bridges using the same GPIB controller. The respective VI for remote control and sampling of the data has been discussed in sec. 2.6.

If stabilizing to a certain set temperature is required, two TS-530A temperature controllers, also manufactured by PICOWATT, can be used. These are low noise PID (*P*roportional, *I*ntegral, *D*ifferential) controllers, allowing to control the temperature by adjusting the output to a connected heater on the sample. Procedures for setting the PID parameters can be found in [104]. A photo of the AVS 47B resistance bridge and TS-530A temperature controller can be found in fig. 2.24.

After covering the hardware and the TES selection process, the next section will concentrate on the operation of cryogenic detectors.

2.8 Operating conventional cryogenic detectors

As a large part of this work was focused on setting up a complete experimental site for cryogenic detector operation, the present setup and its verification will be described in detail in this section. The setup was tested by operating a known standard cryogenic detector. Also the data analysis procedure for determining the detector resolution will be presented here. After having gained an understanding of the basic detector operation, the next chapters will then move on toward new applications for such detectors in Astroparticle physics.
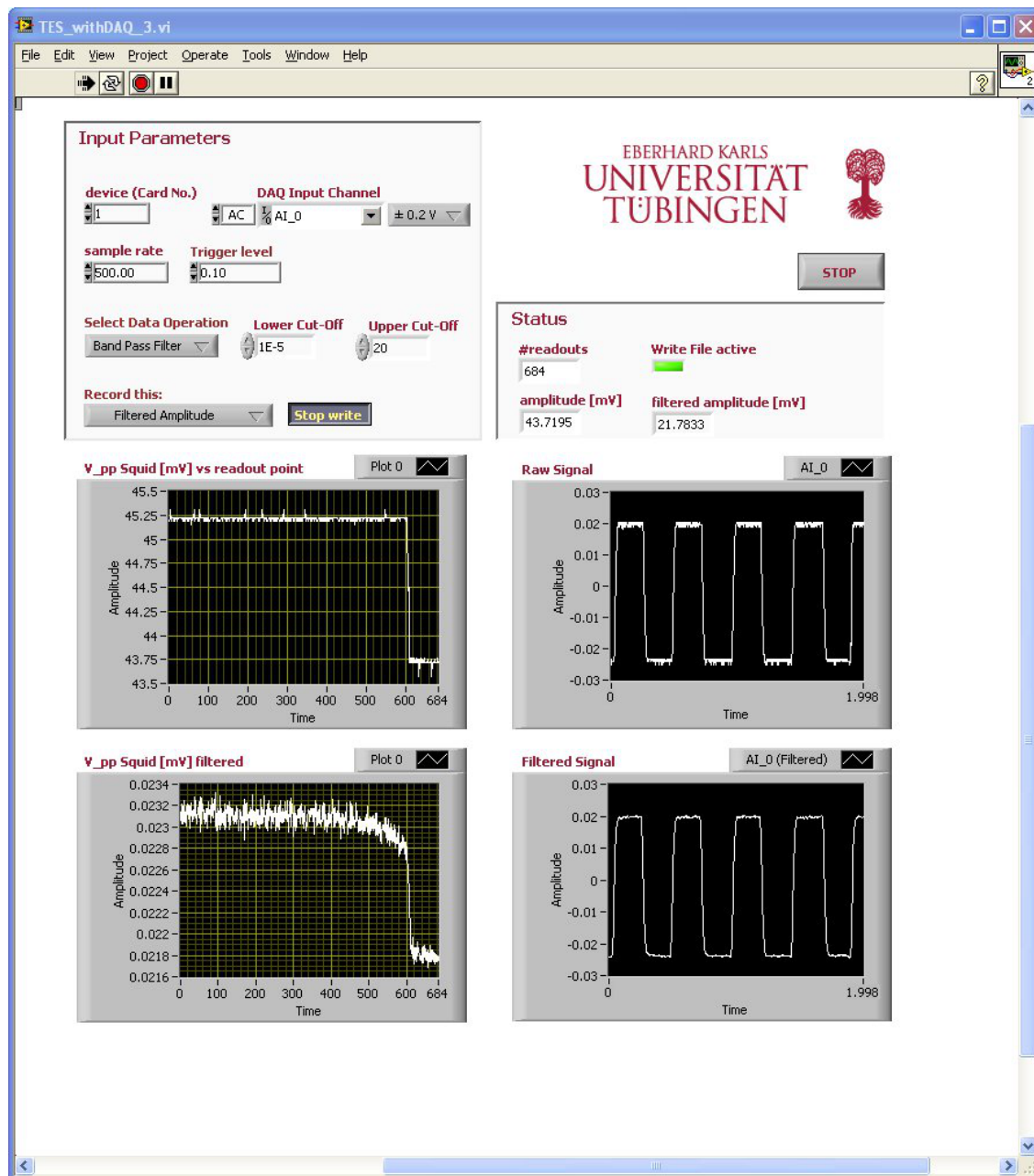
Figure 2.23: Recording transition curves using the PXI-6115 sampling card. The VI provides three different types of data processing: Averaging a constant signal or filtering arbitrary signals using either a low or a band-pass.

Figure 2.24: AVS 47B resistance bridge (top) and TS-530A temperature controller (bottom).

2.8.1 Setting the operating conditions

To test the setup in the Tübingen Underground Lab, a cryogenic phonon detector with a Sapphire absorber was used. It was manufactured at TU Munich by Roth [93] and consists of a $10 \times 20 \times 1 \, mm^3$ Sapphire absorber and a sputtered Tungsten thermometer on a Sapphire carrier, which is glued to the absorber using EPO-Tek 301-2 epoxy resin. A picture of the detector can be found in fig. 2.25. The detector was thermally coupled to the mixing chamber plate using brass screws. The coupling of the TES to the Copper holder consisted of a standard $25 \, \mu m$ Gold bond wire. The detector was irradiated from below, opposite of the TES, with a collimated ^{55}Fe source to prevent direct thermometer hits. The transition curve of the TES used on this detector was already presented in sec. 2.4 and can be found in fig. 2.9. In order to get a linear detector response and fixed pulse heights for a given recoil energy, the detector has to be set to a fixed point in the transition. This point, also called the *Operating Temperature T_{op}*, should be chosen such that the maximum linear rise in R_{TES} is used. A T_{op} of $43 \, mK$ was selected for the described detector and could be stabilized either directly via the Mixing Chamber PID controller available in the Oxford gas handling system or using an AVS-47B resistance bridge (see sec. 2.7), reading the RuO_2 thermometer on the Copper holder of the detector in combination with a TS-530A temperature controller adapting the power input to the holder's heater resistance. Note that the bias current in *detector mode* is usually much higher than during R(T) measurements as one wants to work in electrothermal feedback mode:

As Irwin has shown in [89], the Joule heating P_J can be used as negative feedback in a TES. Since $P_J = R_{TES}(T) \cdot I_{TES}(T)^2$ depends on the actual resistance and the respective current of the TES, the film can regulate itself within the transition, if the substrate temperature is well below the critical temperature T_c of the film. Considering a film with heat capacity C and a small temperature increase due to particle excitation, the decrease to the TDE state can be described as:

$$C\frac{d\Delta T}{dt} = -\frac{P_0 \alpha}{T}\Delta T - g\Delta T \qquad \boxed{2.29}$$

where P_0 is the TDE Joule power, $\alpha = (T/R)(dR/dT)$ the unitless measure of the steepness of the transition and $g = dP/dT = nKT^{n-1}$ the thermal conductance. K and n are defined by the heat loss to the substrate, going as $K(T^n - T_s^n)$, were K is a material dependent constant and $n = 4$ if Kapitza coupling dominates between film and substrate, or $n = 5$–6 if electron-phonon decoupling is relevant. The value depends on the model for the respective temperature range. Thus the first term on the right hand side of eq. 2.29 describes the reduction in Joule heating and the second term the increased heat flow to the substrate. For $T_s \ll T$ the TDE power can be considered $P_0 \approx KT^n = gT/n$ which leads to a recovery time

$$\tau_{eff} = \frac{\tau_0}{1 + \alpha/n} \qquad \boxed{2.30}$$

with the intrinsic time constant of the film $\tau_0 = C/g$. As values for α can well reach 1000, τ_0 can be reduced

by more than two orders of magnitude. Since the Joule power depends on the TES current squared, the effect is larger for higher currents. Therefore a high bias current is favorable.

Thus the operating temperature of $43\,\mathrm{mK}$, measured at the mixing chamber, does not represent the temperature of the TES as following fig. 2.9 this would not even be in the transition region. Due to the injected bias power, the TES temperature will be higher and in the linear region, which was checked by varying T_{op}.
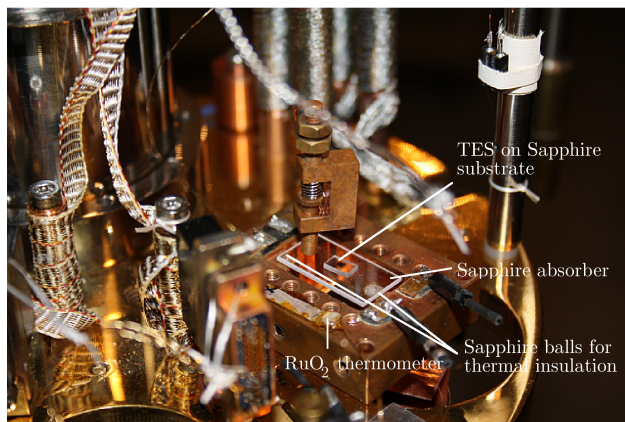
Figure 2.25: Photography of the Sapphire detector used.

As T_{op} is fixed, the detector bias current needs to be optimized to achieve maximum amplification and linearity. This can be done in several ways: The particle pulses of a calibration source in the desired recoil energy range can be maximized by varying the bias current in the Magnicon SQUID *Viewer*™ or the CRESST floating current source (see sec. 2.4) with external bias connected, e.g. using the break-out box. Another way is to use the MCA VI provided by the DAQ software to optimize the spectral resolution. This is usually done using a ^{55}Fe source.

As a last step the record length and voltage range of the DAQ have to be adapted to the respective pulse parameters. These parameters depend on the detector's coupling and the total amplification factor.

2.8.2 Measurement and analysis procedure for cryogenic detector data

After selecting the operating temperature and stabilizing the detector, a set of 40,000 pulses was recorded using the LabView DAQ described in sec. 2.6. The detector was irradiated by a collimated ^{55}Fe source with an activity of $490\,\mathrm{kBq}$. The collimator is necessary to prevent pile-up and direct γ hits in the TES. A Copper encapsulation was made to cool the source efficiently. A picture of the setup can be found in fig. 2.26. The bias current was set to $100\,\mu\mathrm{A}$. Two exemplary pulses for the $5.90\,\mathrm{keV}$ and the $6.49\,\mathrm{keV}$ gamma energies can be found in fig. 2.27.

The data was analyzed using OxRop 4.8 [105]. This software package was developed at the University of Oxford by the group of H. Kraus and is currently used for data analysis in the CRESST, EDELWEISS, cryoEDM and EURECA experiments.

The general idea of the analysis is to create a "standard event" from a set of raw pulses that are not affected by e.g. pile-up or strong noise. Using this "reference pulse shape" all events can be fitted and a cut can be applied to select the recoil-like events. This is an effective filter and also applied in the CRESST analysis. In more detail, the following cut procedure was applied to the data presented here:
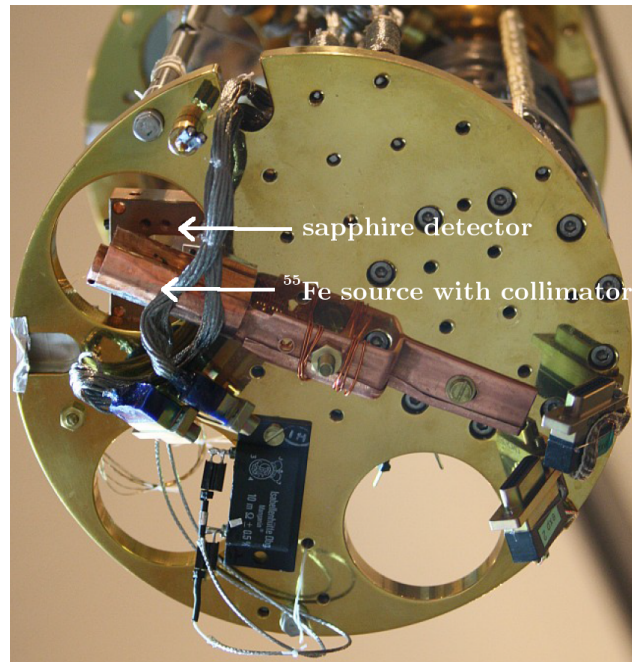
53

Figure 2.26: Setup for the Sapphire detector measurement. The source is collimated to prevent pile-up and direct TES hits.
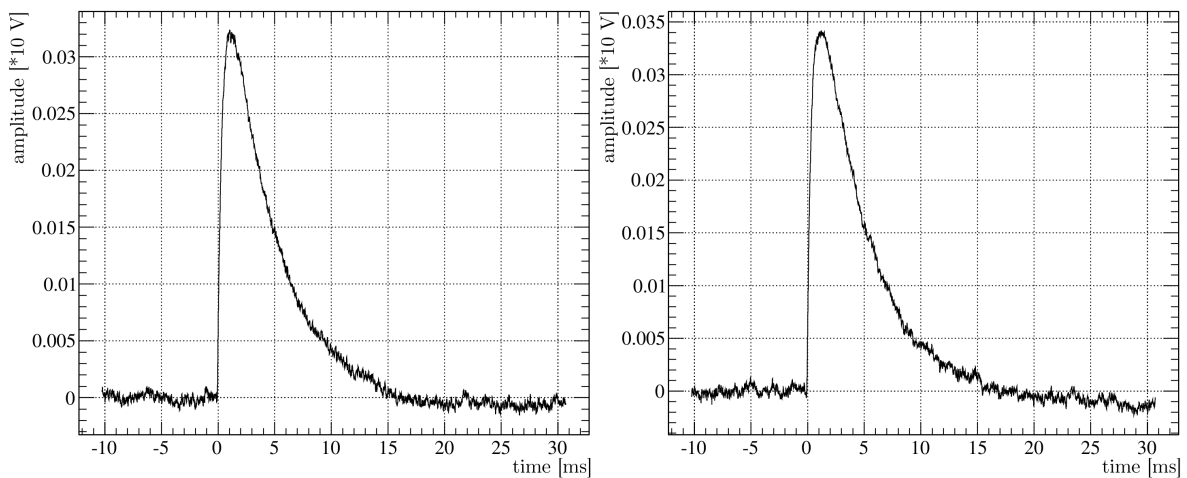

Figure 2.27: Two ^{55}Fe pulses in a Sapphire phonon detector. Respective pulse height at 5.90 keV (left) and at 6.49 keV (right). Note that pulse heights have to be scaled times 10, as this was not accounted for in the `*.rop` file header.

As a first step, the raw pulse height of all events was plotted against the parameter *integral/raw pulse height* which can be considered to be an effective decay time. The result is shown in fig. 2.28. One can easily identify several classes of events, labeled 1-5.

Class number one pulses originate from pile-up signals with time differences Δt smaller than the rise time or from events that suffered from flux quantum losses in the SQUID system. To demonstrate, that these traces are similar to close follow pile-up, consider a SQUID locked to the negative (*positive*) slope of the V-Φ-pattern (see fig. 2.17). A flux quantum loss will then lead to a step-like increase (*decrease*) in the output voltage, which could be observed in DC-coupled mode. As the data analyzed here was recorded with AC-coupling, the baseline after the jump will be restored. Fig. 2.29 illustrates the effect: The left panel shows a standard pulse with no flux quantum loss. A DC-coupled event where a flux quantum loss occurred, will show up as in the middle panel. The right panel shows the additional effect of AC-coupling. These events could in principle be easily corrected for if one monitors the absolute baseline level, but as those events are few in numbers and the recoil energy region of interest is on the low end (few keV) of the spectrum, these events can be removed by a cut.
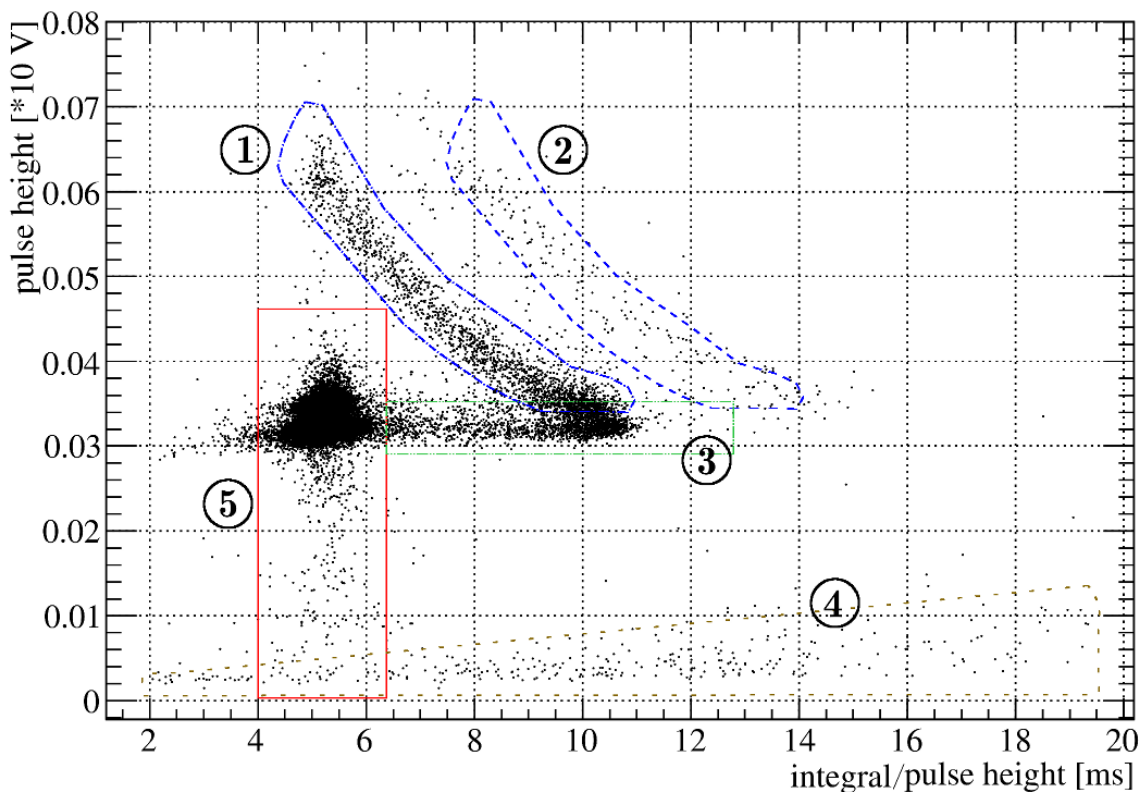

Figure 2.28: Pulse height displayed over the effective decay time parameter *integral/pulse height*. The following event classes can be identified: (1) Pile-up events that occur at Δt shorter than the rise time or pulses that suffered from flux quantum losses in the SQUID system (2) Events containing class one pulses and an additional pulse (pile-up). (3) Regular pulses with a partial second event within the record length. (4) Noise triggered events. (5) Mostly valid events, subjected to an additional standard event cut, see text.

Event class two is similar to class one, there is just one additional event in the same record, yielding a higher integral at similar pulse height. As these are pile-up events, they are removed as well.

Class three can be seen extending down on the x-axis to the central region where the majority of events cluster. These are regular pulses with a partial secondary event within the record length. Depending on the recorded fraction of the second pulse, this gives varying contributions to the integral, while the pulse height remains unchanged. These events can also be removed by a cut, but as they extend down to the central region, it is harder to set the cut threshold. Since OxRop allows for visual inspection of the events in a certain cut windows, the overlap region was investigated in small bins until no more pile-up events remained. Of course this removes also some valid events, but as this procedure is only used to build a standard pulse, this is not critical.

Class four are noise triggered events, mostly without valid pulses within the record. This can happen due to microphonics, most likely originating from bubbling Helium in the cryostat's main bath, which occurs from time to time in a burst-like fashion. Keeping the main bath Helium level below 70 %, these events can be minimized. The cut to remove these events has to be chosen such that it does not remove events in the central region.

Class five are considered valid events. Visual inspection confirms this. Exemplary pulses for the discussed event classes can be found in fig. 2.30. All these cuts remove about 15 % of the total events.
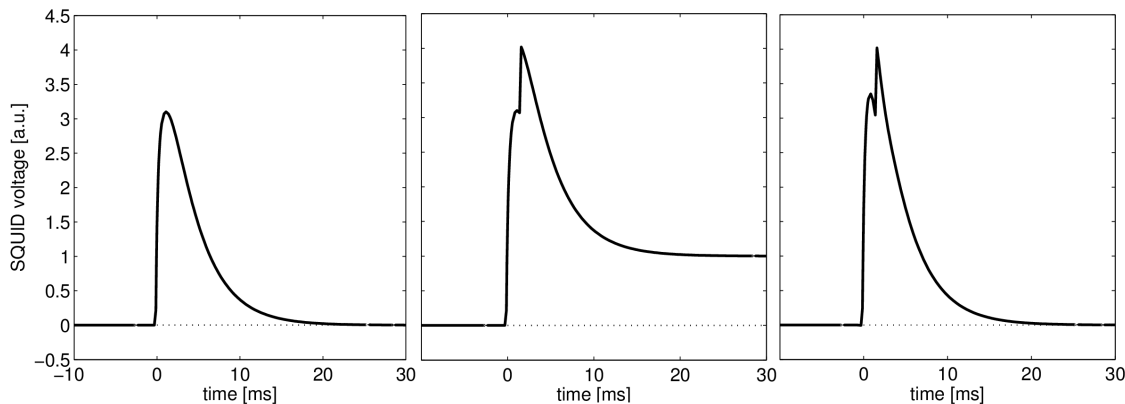

Figure 2.29: Illustration of the effect of flux quantum losses for a SQUID coupled to the falling slope of the V-Φ-pattern: The left panel shows an event with no flux quantum loss. Events where a flux quantum loss occurred are shown in the middle (DC-coupled) and on the right (AC-coupling).

In a second step, a standard pulse is built by selecting roughly 200 events from the central region, containing the valid events by simply summing up and normalizing. OxRop can then perform a fit, comparing each event to this template. It has been found in the CRESST experiment that this is a most sensitive filter. The RMS of this fit can be found in fig. 2.31. The valid pulses center round the mean noise level value of about 4 mV. Inspecting the distribution for all events, another cut can be performed, removing the high RMS tail of the spectrum. Again the cut was checked by visually inspecting the discarded and the adjacent remaining events. This final cut removes roughly 20 % of the total events.

Using the remaining 32,000 events one obtains fig. 2.32 for the pulse height versus runtime data. Although the detector was stabilized using the TS-530A, there is still a low-level drift visible. This obviously effects the source spectrum and thus the detector resolution. To correct the drift, the data was exported to MATLAB and the pulse height versus runtime data was histogrammed in small time bins Δt_i where Δt_i is much bigger than the event rate. The 5.9 keV line was fitted with a Gaussian and the position was tracked bin-wise. Fitting the drifting 5.9 keV position with a high order polynomial, weighted with the 95% C.L. errors, a drift correction could be obtained and applied to the pulse height data. This approach is of course only justified, if the detector is operated in linear mode. As mentioned before, this was checked during the optimization procedure of the working point. However it is possible to verify this in the recorded data as well: When
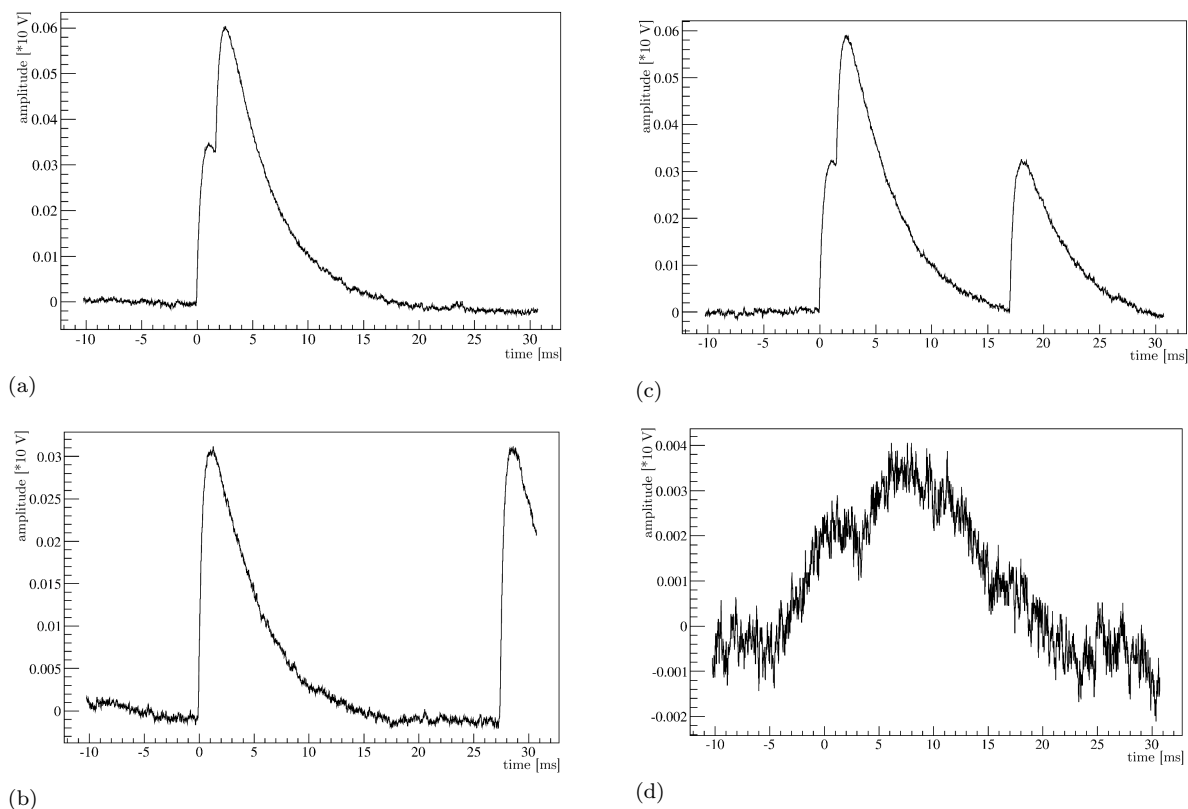
(a)

(b)

(c)

(d)

Figure 2.30: Four classes of background removed by the cut procedure. (a) Close follow pile-up and signals suffering from flux quantum losses due to the finite bandwidth of the FLL electronics. (b) Multiple events within one record length. The contribution to the trace integral can vary depending on the fraction of the additional recorded signals. (c) A combination of case (a) and (b). (d) Noise triggered traces due to microphonics.
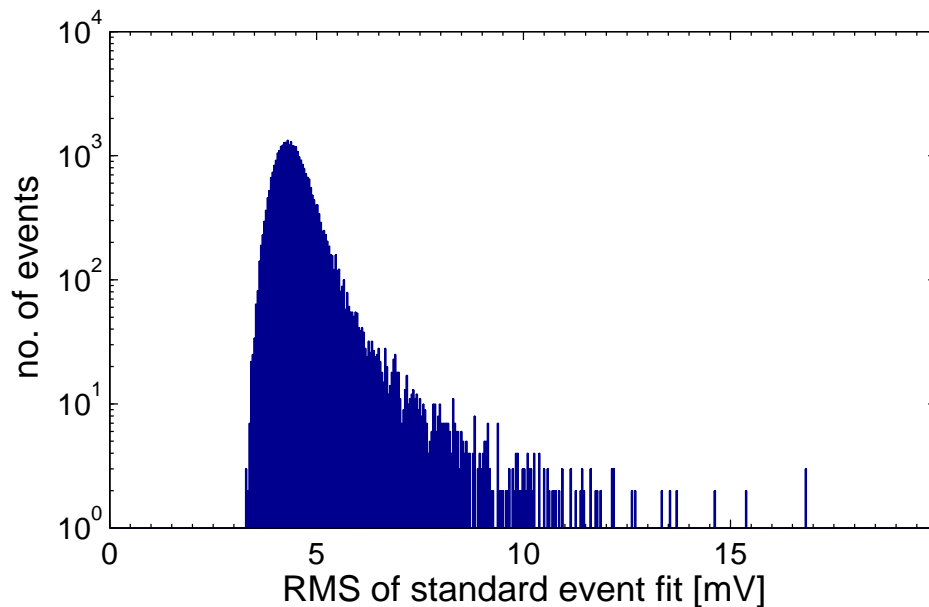
Figure 2.31: Distribution of the standard event fit RMS. This is a measure of the deviation of each event from the standard pulse defined after the earlier cuts. The valid pulses center round the mean noise level value of about 4 mV. A cut is applied to remove the high RMS tail, to select the relevant events.

plotting the recorded pulse height of an event versus the amplitude reconstructed by a no-truncated standard event fit, linear behavior should result in a straight line, while non-linear behavior will result in a distortion of the band. As can be seen in fig. 2.33, the detector's response is perfectly linear.

Using the presented correction procedure a resolution of 5.6 % (FWHM) at 5.9 keV could be obtained, as compared to 6.0 % for the uncorrected data. Since the resolution can in principle be infinitely improved by selecting smaller and smaller time bins, the resolution of the 6.49 keV line should be taken as a measure, as the correction was performed only using the 5.9 keV line fit. At 6.49 keV a resolution of 6.9 % (FWHM) is achieved after correction. The uncorrected data gives a value of 7.2 %. This is roughly double the value quoted by Roth, yet over time also the critical temperature T_c of the TES has almost doubled, which is an aging effect of Tungsten films that is sometimes observed. Taking this into consideration, the values agree quite well.

The corrected data is displayed in fig. 2.34. Short time variations remain even after the correction, as the time bin size can not be chosen arbitrarily small: Each bin needs to contain enough entries to allow for a reasonable fit and the bin size should not be smaller that the inverse event rate. The latter restriction has already been discussed above. Applying the drift correction also improves the reduced χ^2 of the double-Gaussian fit of the spectrum to 0.994 as compared to 0.936 for the uncorrected spectrum. The corrected spectrum is shown in fig. 2.35.
In this chapter it has been shown that all the necessary infrastructure for low temperature detector (LTD) operation is now available in the Tübingen Shallow Underground Laboratory: A cooling system providing mK-range temperatures, a SQUID system to measure TES transition curves and to amplify the small temperature change in a low temperature bolometer, a suitable floating current source, resistance bridges and PID controllers to stabilize cryogenic detectors and a DAQ system, suitable for the different tasks. All components have been tested, calibrated and showed reasonable performance during the respective measurements.

The possibility to measure transition curves of multiple Tungsten films in a short time will also be of importance in the near future, as at present there is a dedicated ultra-high vacuum (UHV) system established in Tübingen, dedicated to mass-produce TES sensors for the EURECA project [106]. Fig. 2.36 shows the
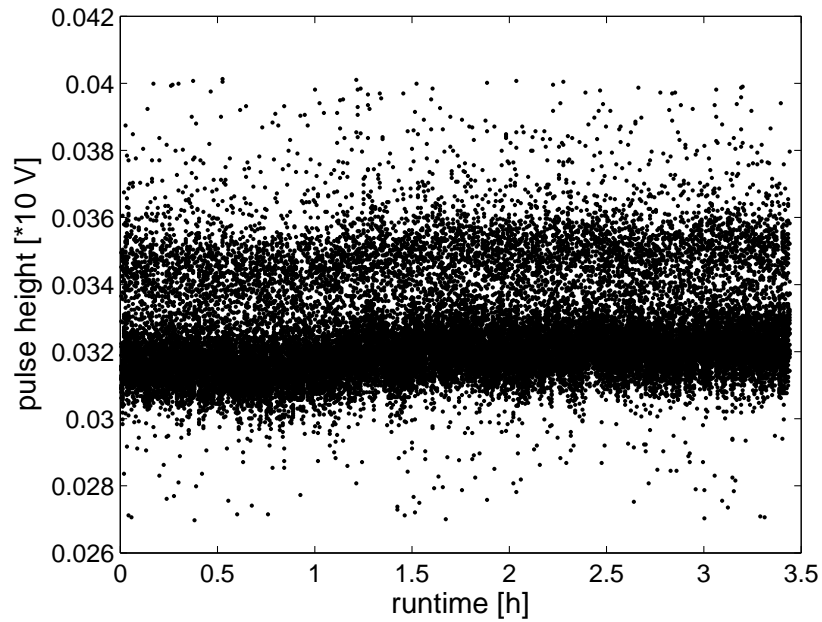
Figure 2.32: Pulse height of the Sapphire detector over runtime. The two ^{55}Fe lines are clearly visible. As the operating temperature of the detector is not perfectly stable, the bands are not flat. To some extent this can be corrected in the analysis (see text for details).
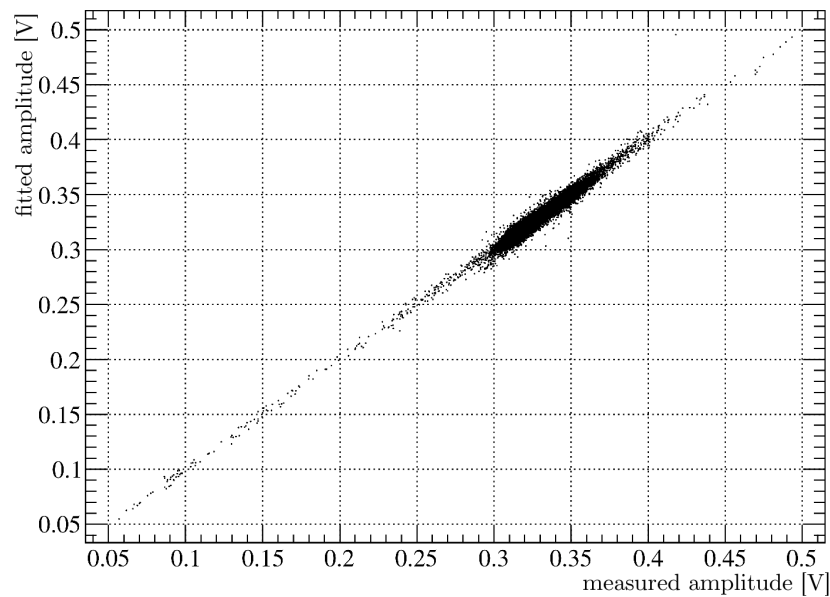

Figure 2.33: Linearity check. The amplitude derived by a non-truncated standard event fit scales with the recorded amplitude. In the case of non-linear behavior the band would bend as soon as the pulse height probes the upper end of the TES transition curve.
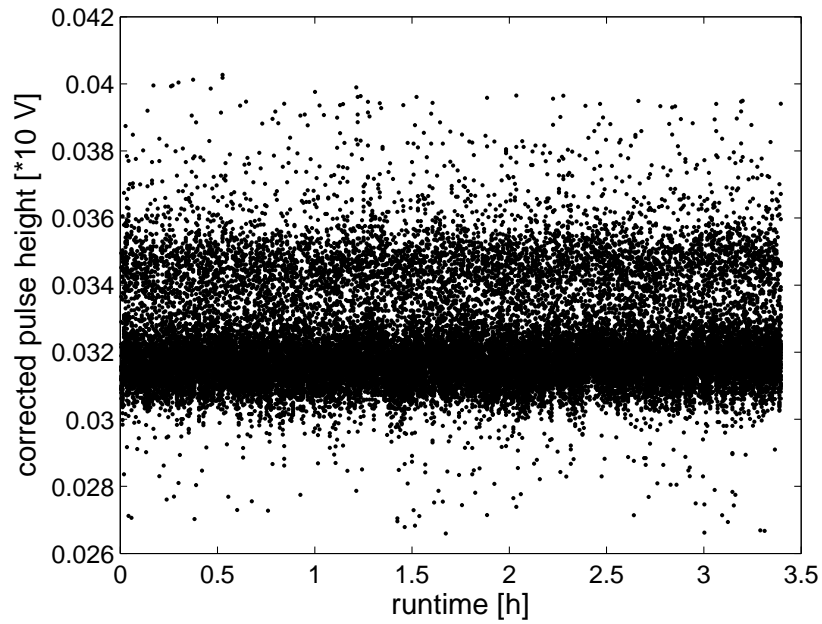
Figure 2.34: Pulse height over runtime after the stability correction.
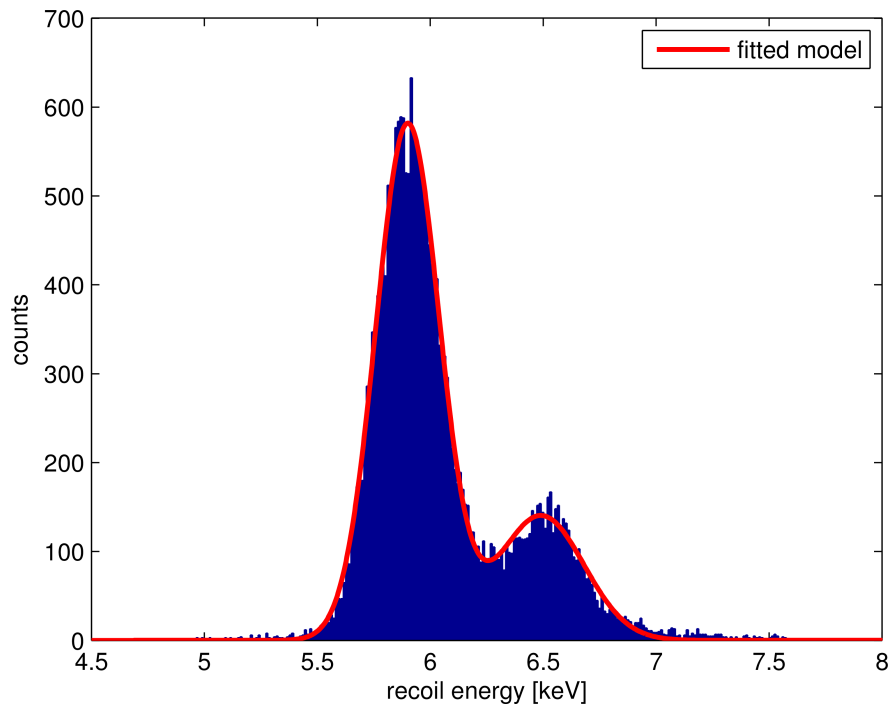
Figure 2.35: ^{55}Fe spectrum and two Gaussian fit result after the stability correction. The obtained resolution is 5.6% (FWHM) at 5.9 keV.

first transitions of Tungsten films produced in Tübingen, also measured during this thesis as described in sec. 2.4. The critical temperature is still too high for the use as low temperature detector thermometers, but optimizing the evaporation process parameters should improve the situation.

In order to characterize the large amount of sensors on a reasonable timescale, another thesis currently explores the possible use of cold-stage multiplexing [107]. The next chapters will investigate the possible use of new scintillating materials, namely NaI (ch. 3) and LiF (ch. 4), for direct Dark Matter Search experiments.
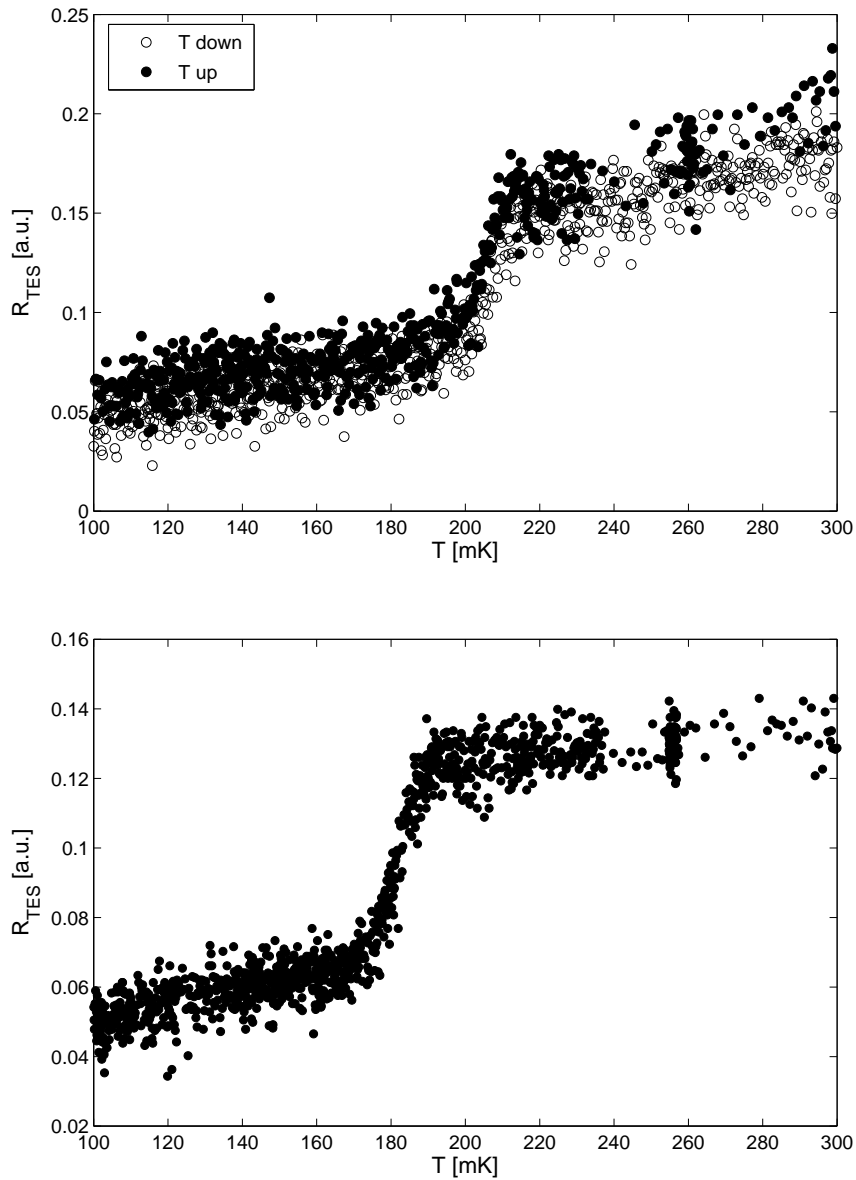
Figure 2.36: Two transition curves of Tungsten films produced at Tübingen. Upper TES labeled "16.07.13 - middle", the lower TES "01.07.13 - middle". The measuring current was 180 nA. The critical temperature is still too high for the use as low temperature detector thermometers, but optimizing the evaporation process parameters should improve the situation.

3

A Sodium Iodide cryogenic detector

As shown in section 1.3 the DAMA collaborations claims a WIMP signal well within the excluded 90 % C.L. regions of several other experiments. As the observed signal exhibits quite distinct features that presently can not be associated to any kind of known background, there remains a contradiction between the results of the event-by-event discriminating dark matter experiments and DAMA. As discussed in sec. 1.4, several theories have been suggested, to reconcile the experimental results. As most of those theories suggest that NaI seems to be more favorable for WIMP interaction than other materials, it would be desirable to build a hybrid detector, employing the DAMA material - namely NaI - but using the recoil-discrimination approach. As NaI is a well known scintillator, this might be feasible in a CRESST-like setup, measuring phonon and light signal simultaneously. One of the tasks of this thesis was to investigate, if such a hybrid detector could be operated. This chapter will therefore explore this possibility by first looking at the theoretical properties of NaI in Sect. 3.1, then presenting the data concerning the scintillation properties of NaI at low temperatures obtained during this thesis in sect. 3.2. The technical challenges in building a NaI cryogenic detector and the current status will then be presented in sect. 3.3 and the results will be summarized and discussed in sect. 3.4.

3.1 Theoretical considerations

To check if a NaI cryogenic detector can be used to investigate the nature of the DAMA signal, several aspects need to be considered: First of all the phonon properties of the crystal should be such, that recoils of a WIMP in a mass range from $10\,\mathrm{GeV/c^2}$ up to $100\,\mathrm{GeV/c^2}$ can be measured. This will be discussed in section 3.1.1. Second, in order to discriminate between WIMP and background events one needs to measure the scintillation light of the respective recoils. The scintillation properties of NaI will thus be briefly discussed in section 3.1.2. Third, one needs to calculate the respective recoil spectra for NaI in the relevant scenarios and needs to estimate the expected count rates and expected backgrounds for such a detector to verify, if such an experiment can be performed within reasonable timescales and at affordable costs. This will be done in section 3.1.3.

3.1.1 Phonon properties of NaI

As covered in sec. 2.1.1, the temperature rise ΔT, and thus the phonon signal of a low temperature detector is proportional to Θ_D^3 at fixed temperature T. The Debye temperature of NaI is $163 \pm 1\,\mathrm{K}$, according to [85, 108]. This is about a factor of 1.5 less than for $CaWO_4$ with $\Theta_D = 246.5\,\mathrm{K}$ [109]. Using eq. 2.2 as a rough estimate, in NaI one would expect about 29% of the signal of $CaWO_4$ at a certain recoil energy E which should still be sufficient to detect a reasonable signal. In the CRESST II experiment, phonon signals in $CaWO_4$ of well below $1\,\mathrm{keV}$ can still be triggered at 100% efficiency. Therefore one would naively expect, that a trigger threshold of $3.5\,\mathrm{keV}$ in NaI is feasible. As will be shown in sect. 3.1.3, this is well below the threshold needed to probe the DAMA signal. However this is just an estimate and does not consider the transmission properties of phonons from the absorber to the thermometer.

To demonstrate that this simple estimate is yet well justified, one can compare the prediction for the phonon signal in CsI with published data by our colleagues at MPI Munich: As Schäffner et al. [110] report, the

pulse height of 122 keV γ-recoils in pure CsI is approximately 0.1 of that in $CaWO_4$ at the same operating point. Performing the estimate with the value $\Theta_D = 125\,K$ cited there, one obtains 0.13 which is in very good agreement.

CRESST-type detectors measure in calorimetric mode, thus integrate pulses and do not rely on fast timing. However one can also check how the lower Debye temperature affects the pulse formation. The timing can be estimated using Θ_D: As the heat capacity is related to the speed of sound in a crystal (see e.g. [85]), the phonon velocity can be calculated using the linear dispersion relation for the Debye model

$$\omega(k) = v_{gr} \cdot k \qquad \qquad (3.1)$$

where k is the value of the corresponding wave vector in the reciprocal lattice and $v_{gr} = \partial\omega/\partial k$ the group velocity of the phonons in the crystal. This is obviously just an approximation, as it does not account for the different velocities of different directions due to the crystal structure. As $\hbar\omega = k_B\Theta_D$, the speed of sound is directly proportional to Θ_D. Thus one expects phonons in a sodium iodide cryogenic detector to be 1.5 times slower than in $CaWO_4$. This should not affect the signal formation much, as for comparison the reduction in velocity of sound between CRESST I, using Sapphire crystals, and CRESST II, employing $CaWO_4$ was a factor of 4.2. The results of CRESST II are at present mostly limited by the discrimination threshold (see 1.2) and not by the intrinsic threshold of the phonon channel [49, 55, 88], so neither the phonon signal amplitude, nor the pulse timing parameters are expected to be problematic *a priori*.

Yet, as briefly discussed in sec. 2.1.2, many factors contribute to the signal formation, e. g. the transmission probability from the crystal into the TES-carrier substrate and the metal film itself, which is covered in detail in [87] and [93]. This should be checked in an experimental setup.
The phonon propagation in a crystal is degraded by impurities in the lattice. Therefore it is desirable to use undoped material to build a NaI cryogenic detector. However it is not excluded that due to the low level of Thallium in NaI(Tl), Bernabei et al. [111] give a value of 0.1 % weight, doped material could also be utilized, which should also be verified experimentally. Yet the main focus in this work will be on pure NaI.

Since the discrimination threshold defines the actual threshold of the detector module, the scintillation light output of NaI at low temperatures appears to be even more crucial than it's phonon properties. They will be discussed in the following sec. 3.1.2, while experimental data will be given in sec. 3.2.

3.1.2 Scintillation properties of NaI

The scintillation mechanisms in insulating, ionic crystals, where the valence band and the conduction band are separated by the gap energy E_g, are in general complex processes involving electron/hole (e/h) pairs, phonons, color centers and other lattice defects. Color centers are lattice defects like missing anions, usually compensated by localization of one ore more electrons (called F-centers, derived from the German word *Farbzentrum*) or hole states trapped by two neighboring anions, basically forming a molecule in the crystal – or more complicated combinations of those configurations. A trapped hole state is called a V_k center and is illustrated in fig. 3.1 for NaI. This is the most common color center in alkali halides [85] and has been extensively studied [112]. Color centers act as traps for electrons and holes, releasing and absorbing light. Hence they are responsible for the crystal's color, which explains the origin of the name.

The initial electronic excitation, e. g. by an incident γ- or α-particle, usually generates hole states in the core energy band, well below the valence band and a population of hot electrons [113]. The latter will lose energy due to inelastic electron-electron scattering, generating e/h pairs until they reach the threshold of $\sim 2\,E_g$. The initial hole population can likewise generate e/h pairs, until the Auger threshold is reached. These processes occur on attosecond time-scales. Fig. 3.2 illustrates this in the leftmost time-segment. Next, the generated electrons and holes will thermalize due to interaction with the lattice phonon (ph) population, which is depicted in segment two. At about picosecond time-scale, holes can get localized on the lattice, forming V_k centers due to the electromagnetic deformation by the "excess" charge. Electrons can get captured on cations, releasing their energy mostly to the phononic system or can be bound to the V_k centers, forming
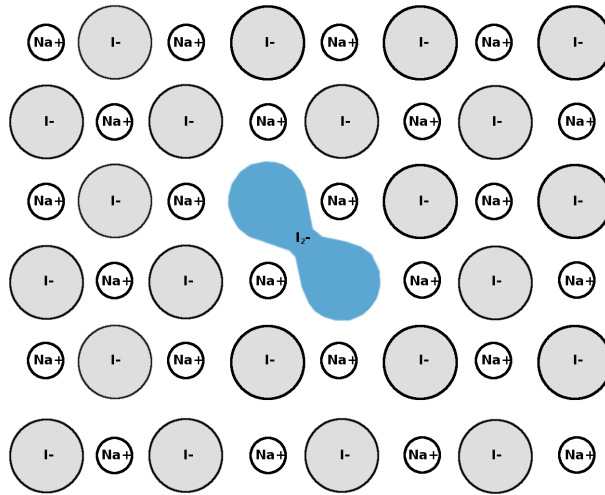
Figure 3.1: Illustration of a V_k center in NaI: A hole is captured by two Iodine anions, effectively forming an I_2^- molecule. This is the most common color center in alkali halides.

self-trapped excitons (STEs). As the binding energy of the STEs reduces the gap energy, the exciton band can be found below E_g. This is illustrated in time-segment four in fig. 3.2. Excitons are instable to radiative recombination [112], thus they will eventually emit photons of energy $h\nu$ on the time-scale of a few nanoseconds.

The band gap for NaI is given as $5.9\,\mathrm{eV}$ by [114], yet the dominant wavelength in the spectrum of pure NaI is $310\,\mathrm{nm}$ at room temperature [115], which is equivalent to $4\,\mathrm{eV}$. Fig. 3.3 shows the emission spectra of three NaI samples excited by $60\,\mathrm{keV}$ γ-rays from a ^{241}Am source: All three samples show the emission at $310\,\mathrm{nm}$, which is characteristic for pure NaI, yet the samples (B) and (C) have additional peaks due to impurities. The $410\,\mathrm{nm}$ band for sample (C) is typical for Thallium-doped crystals.

The difference between E_g and the emitted recombination luminescence for pure NaI shows immediately, that the model discussed above, which does not lead to generation of photon energies corresponding to E_g is likely to apply here. Indeed van Sciver attributed the scintillation mechanism in pure NaI to exciton emission in [116]. Decay times are thus expected to be on the nanosecond scale, if the model presented above holds to some extent. Van Sciver also estimated the classical exciton binding energy in Sodium Iodide to be $0.8\,\mathrm{eV}$ and concluded, that [...] *thus we must assume a degeneration or relaxation of the exciton* [...] *This can occur if we are willing to think of the exciton as captured in the perfect lattice by adjustment of the position of the neighboring ions, thereby "creating" a luminescent center*, which basically means that the excitons are self-trapped[1]. This leads to a smaller "effective" band gap at the color centers, resulting in the recombination emission peaking at $310\,\mathrm{nm}$.

A common problem in pure crystals is the higher self-absorption compared to doped scintillators. The dopant, in case of NaI usually Thallium, shifts the emission spectrum to longer wavelengths, as the dopant energy levels lie within the band gap of the pure material. The luminescent centers in doped NaI are Tl^+ sites [117], the associated dominant emission, as already quoted above, $410\,\mathrm{nm}$. Since the main scintillation process in pure NaI involves STE recombination, the problem of self-absorption is alleviated to a certain extent. However this should be kept in mind, when building a cryogenic detector of large sized crystals.

Another issue to be considered when performing light yield (LY) measurements at low temperatures is the possible emission of thermoluminescence: A crystal that has been exposed to energy irradiation might emit

---

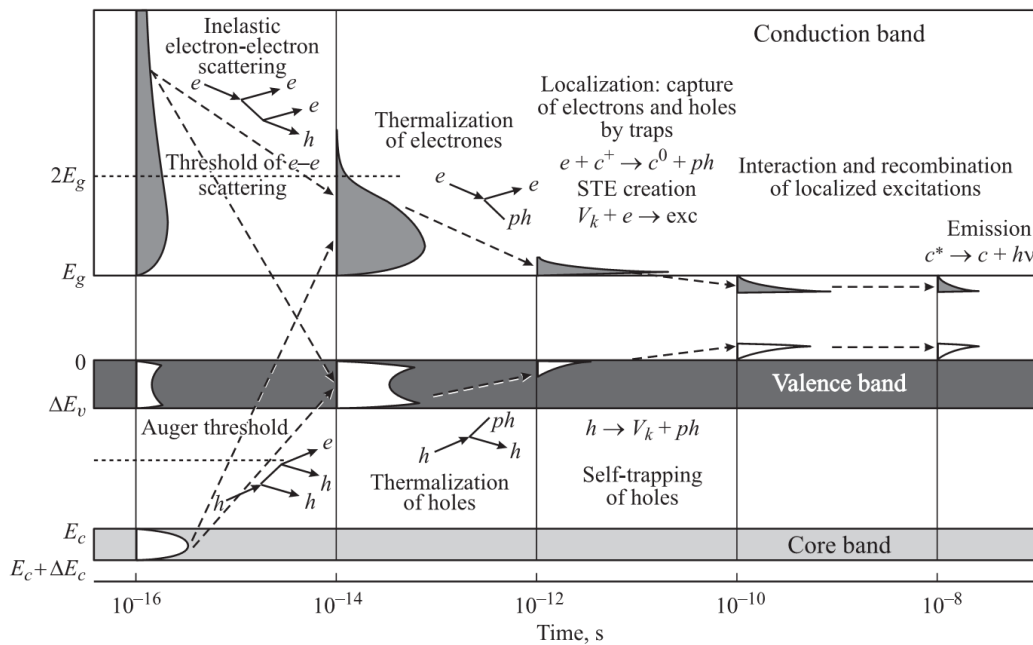[1]This is sometimes denoted as "SX".

Figure 3.2: General scintillation mechanisms in insulating crystals as a time sequence. Energy is denoted on the y-axis. The respective bands are only schematic. E_g is the gap energy of the material, (e) denotes electrons, (h) holes e.g. electron vacancy sites, (c) cations, (exc) excitons, (ph) phonons and (V_k) the respective color center, where a hole state is localized between two lattice anions. See text for details. Figure as in [113]
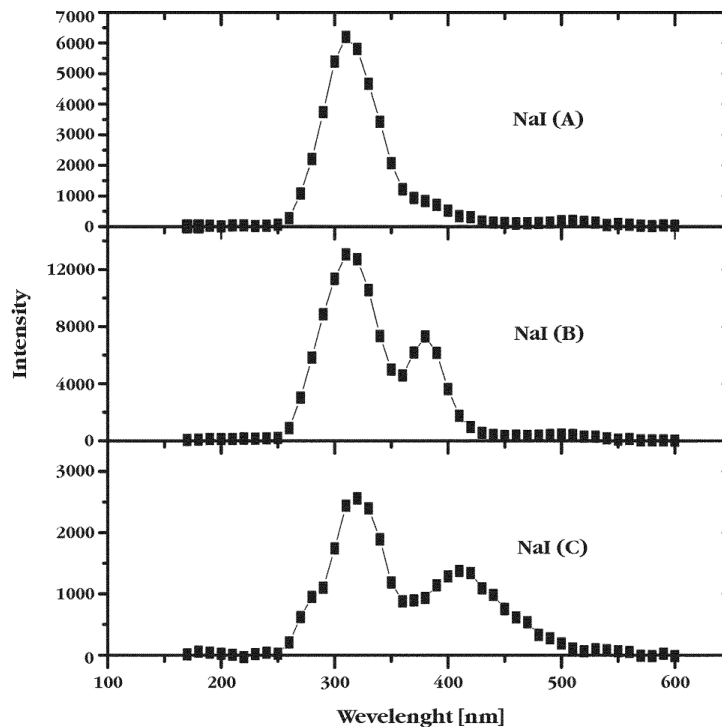
Figure 3.3: The spectra of pure (A) and trace-Thallium NaI (C) excited by $60\,\mathrm{keV}$ γ-rays. Sample (B) is affected by other impurities. Figure from [115]

light upon heating. As van Sciver [116] points out, thermoluminescence dominantly occurs upon γ excitation, while it is absent when using e.g. an α source. This is related to the fact, that γ-rays dominantly produce electrons and holes that can place the Tl-centers in metastable states by successive captures, while α-particles primarily produce excitons. Even though γ-sources are used to calibrate dark matter experiments, thermoluminescence will however not affect a cryogenic NaI detector, as such devices are operated at a fixed temperature for extended periods of time.

As the emission of pure NaI lies in the ultraviolet (UV) regime, the light detector for a NaI DM detector should be optimized for absorption in this band. So far the temperature dependence of the scintillation parameters has not been discussed. This will be done in sec. 3.2 on the basis of experimental data obtained during this thesis. Before that, the next section will examine if a NaI cryogenic detector can perform well enough to test the DAMA result at all within a reasonable time-scale and with affordable experimental effort.

3.1.3 Expected count rates in a NaI cryogenic detector

It has been discussed in sec. 1.3 that the DAMA collaboration observes an annually modulated rate of $(0.0116 \pm 0.0013)\,\mathrm{cpd/kg/keV}$ in the energy range of $2\text{-}6\,\mathrm{keV}_{ee}$. The collaboration attributes the signal to DM induced recoils varying according to the relative motion of earth to the DM halo. This modulated rate is of course connected to an unmodulated "bulk" rate, that can not be disentangled from background contributions in a rate-only experiment. Assuming a non-rotating, isothermal DM halo a modulated rate of at least $3\,\%$ amplitude is expected [45], but other scenarios can even lead to $100\,\%$ modulation.

Considering a CRESST-like NaI detector (CND), not only the modulated but also the bulk rate could be detected due to the event-by-event discrimination. Therefore one does not have to operate $250\,\mathrm{kg}$ cryogenic target mass in order to check the DAMA claim. In this section it will be shown that $1\,\mathrm{kg\,yr}$ of cryogenic NaI

is enough to test the DAMA region, if a comparable threshold can be achieved. The latter condition will be discussed below in more detail.

In order to compare the DAMA experimental data to a cryogenic setup, the quenching has to be considered, since DAMA is measuring scintillation light which is inducing electron-hull signals. The quenching factor relates the measured scintillation energy to a phonon signal in the respective material. Quenching factors for Na and I are reported to be $q_{Na} = 0.3\pm0.01$ and $q_I = 0.09\pm0.01$ respectively [60]. The resulting nuclear recoil energies and corresponding uncertainties are given in tab. 3.1.

E	[keV$_{ee}$]	2	–	4	2	–	5	2	–	6
E$_{Na}$	[keV]	$6.7^{+0.2}_{-0.2}$	–	$13.3^{+0.5}_{-0.4}$	$6.7^{+0.2}_{-0.2}$	–	$16.7^{+0.5}_{-0.6}$	$6.7^{+0.2}_{-0.2}$	–	$20.0^{+0.7}_{-0.6}$
E$_I$	[keV]	$22.2^{+2.8}_{-2.2}$	–	$44.4^{+5.6}_{-4.4}$	$22.2^{+2.8}_{-2.2}$	–	$55.6^{+6.9}_{-5.6}$	$22.2^{+2.8}_{-2.2}$	–	$66.7^{+8.3}_{-6.7}$

Table 3.1: Nuclear recoil energies of DAMA binned data for quenching factors cited in [60] and corresponding uncertainties. The lowest discrimination threshold achieved in the CRESST-II run 32 was 10.2 keV with phonon thresholds below 1 keV. A phonon threshold of 3.5 keV can be expected in NaI. The discrimination threshold in a NaI module will depend on the NaI light output, the light detector resolution and the level of intrinsic contamination.

As already discussed in sec. 3.1.1 the phonon signal in NaI is expected to be degraded with respect to that of CaWO$_4$. The degraded phonon channel resolution could limit the discrimination capabilities of a CND severely. However it will be shown in the following (see sec. 3.2.3), that the output of scintillation light of NaI is significantly higher than that of CaWO$_4$. This could very well compensate for the loss in the phonon signal. Yet the light collection efficiency, the transmission probability of the phonon signal to the TES and other practical limitations are uncertainties that can only be checked by operating a prototype detector module. These uncertainties or possible limitations should be kept in mind during the following discussion.

For recoils on Iodine the DAMA threshold translates to a phonon channel threshold of 22.2 keV in a CND. The phonon channel threshold in CRESST is well below 1 keV [118] and most likely not limited by the intrinsic phonon properties but by the readout circuit's noise. As covered in sec. 3.1.1 the phonon signal in NaI is expected to be only about 29 % of that of CaWO$_4$. So even in the case of a phonon limited CRESST threshold, a CND could achieve a value of below 3.5 keV in the phonon channel. Yet the relevant value to compare is the *separation threshold* between light and phonon signals (see sec. 1.2), which strongly depends on the resolution of the light detector (and, as long as one is not limited by photon statistics, also on the crystal's intrinsic purity). A typical value for the separation threshold in CRESST II is 12–13 keV [55]. Thus Iodine recoils are expected to be well detectable. The threshold for Na recoils is more challenging to achieve: About 6.7 keV threshold energy is needed to be competitive. The lowest threshold reported in [55] was 10.2 keV. However, the used crystals in the reported run exhibited quite a lot of intrinsic background, which can be seen by the vast number of events in the electron-recoil bands. As mentioned in sec. 1.2 there are purer crystals available for the new run. Thus it can be expected, that the threshold can be further reduced. Also there are currently attempts by the CRESST collaboration to improve the light detector sensitivity by the use of black silicon and altered TES-designs. Therefore it is not unrealistic to assume, that a threshold of 6.7 keV for Na recoils can be realized.

Assuming comparable sensitivity to the DAMA recoil range of 2 - 6 keV$_{ee}$, the expected count rate in 1 kg yr of cryogenic NaI data can be simply derived by scaling the E$_{ee}$ energy range to E$_{nr}$ and taking into account the modulated fraction and the exposure. The expected count rates for 1 kg year exposure of a NaI cryogenic detector as function of the modulated fraction with respect to the total WIMP rate are given in fig. 3.4. At least a 3% variation is expected [45], but some scenarios can even lead to 100 % modulation, like e. g. iDM models (see sec. 1.4. The different values for 2 - 4 keV$_{ee}$ (a), 2 - 5 keV$_{ee}$ (b) and 2 - 6 keV$_{ee}$ (c) range published

in [59] are used. The orange bands are derived from the uncertainties quoted there. The red lines and gray shaded areas give a background estimate, derived from the CRESST II run 32 data [55]. The details of this estimate will be discussed in the next section.

Background estimation

In order to estimate the background in a NaI-cryogenic experiment with 1 kg yr exposure, data from the CRESST II run 32 [55] is used. Obviously the detector materials differ, but CRESST provides a model for a low-background environment with scintillating background rejection. The possible difference in intrinsic contamination of the different materials should be low, as will be discussed further below. It has to be pointed out that this is just an estimation, assuming that the intrinsic and external backgrounds of CRESST and the CND setup are on comparable levels and the CND's phonon resolution is not degraded such, that the discrimination threshold mentioned above can not be reached.

To derive a first, simple background estimate, the detector with lowest threshold of the reported CRESST dataset has been chosen, in which 9 counts/88.5 kg d where observed in the acceptance region, starting at separation threshold 10.2 keV up to 40 keV. Here, a flat energy distribution of background is assumed. The number of expected background events under the premise that all of this is irreducible background can be found as the dash-dotted red line in fig. 3.4. This line corresponds to a signal-to-noise ratio of one. It has to be stressed, that this is a very conservative expectation, as part of these counts are considered a possible signal and there was additional α-induced background in the cited CRESST II run, originating from impurities in the clamps holding the crystals (see sec. 1.2). As discussed, the background introduced by the clamps has been addressed in a likelihood analysis and estimates for the different background contributions where given for all detectors combined. Assuming that these background events are more or less evenly distributed in the detector modules, one can use the likelihood numbers to derive a more realistic background estimate[2]. Four scenarios have to be considered:

- The signal is due to an unidentified background source and the clamp-induced background can not be reduced: The total cited rate in the acceptance region should be considered as background. This is the simple background estimate mentioned above and represented as dash-dotted line in figs. 3.4 and 3.5.

- The signal is due to DM recoils and the clamp-induced background can not be reduced: Then, the signal events have to be removed from the cited accepted events number. The resulting curve is given as dashed line in fig. 3.4.

- The signal is due to DM recoils and the clamp-induced background can be reduced, e. g. by a fully scintillating housing: Then, the signal events and the α-/Pb recoils have to be removed from the cited accepted events number. The resulting curve is given as dashed line in fig. 3.5.

- The signal is related to the clamp-induced background (see sec. 1.4) which can be reduced: Considering a background estimate, this leads to the same result as the previous case. Only the e/γ- and the neutron events remain as background counts.

The gray bands in figs. 3.4 and 3.5 have been derived from the likelihood errors stated in [55]. As these errors are asymmetric, they were added using the method suggested by Barlow [119]. Note that the leakage γ-events are present by definition of the WIMP analysis window, as explained in sec. 1.2. They can not be reduced further. Yet, considering the full run 32 neutron background is a conservative estimate as the newly installed inner PE shield (see 1.2) might reduce this contribution even further. Since the given background estimates only indicate the signal-to-noise ratio of one and statistical considerations like the event distribution over run time could also be taken into account, one can conclude that in a CRESST II NaI experiment with present background levels modulated DM scenarios could be check with 1 kg yr exposure, if the modulated fraction

---

[2]The cited publication gives two solutions for the maximum likelihood, called M1 and M2, with slightly varying numbers for the α and related Pb-recoil background. In the following, the numbers of the M1 solution were used, as this is the slightly more favored solution with 4.7 σ.
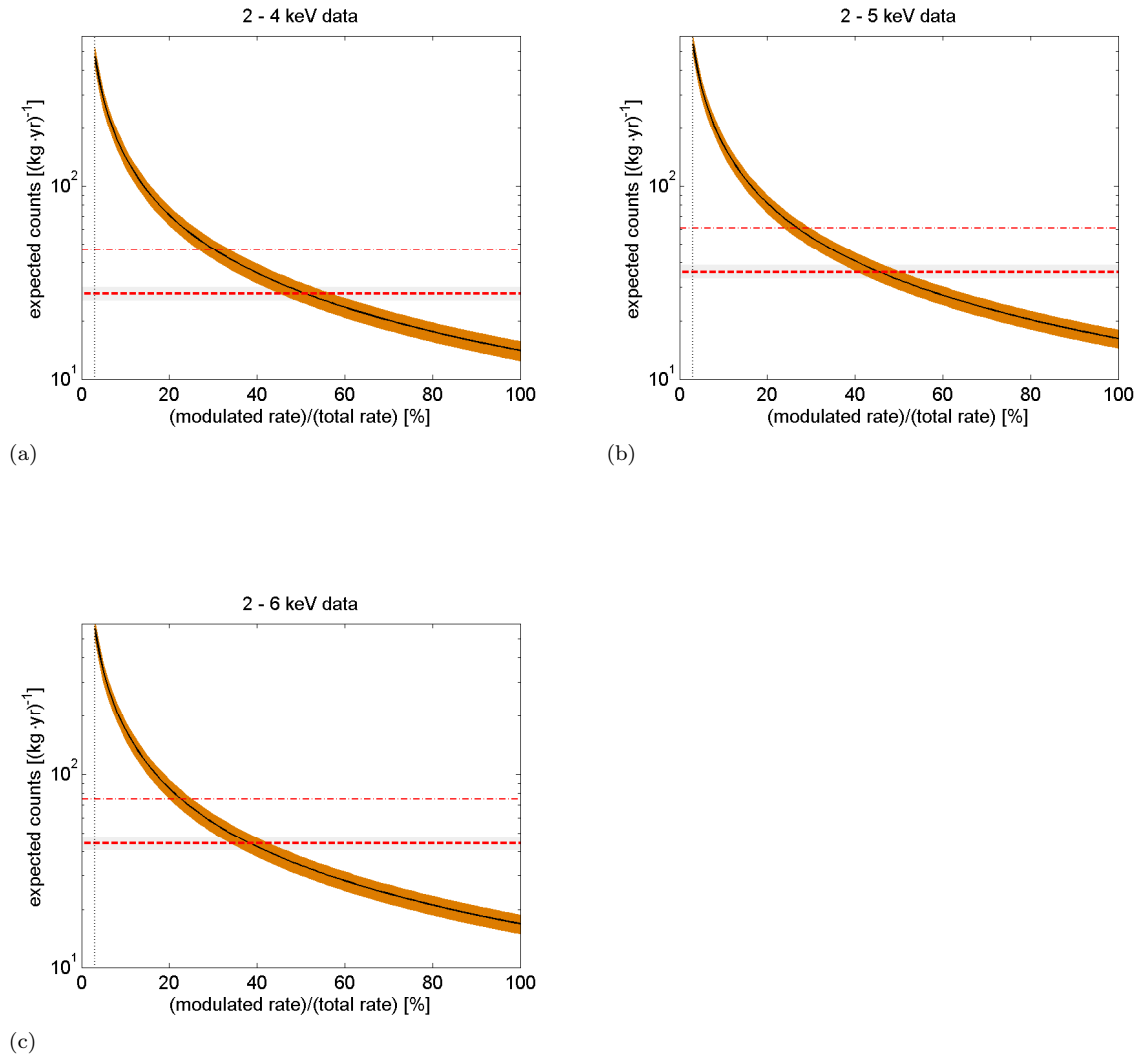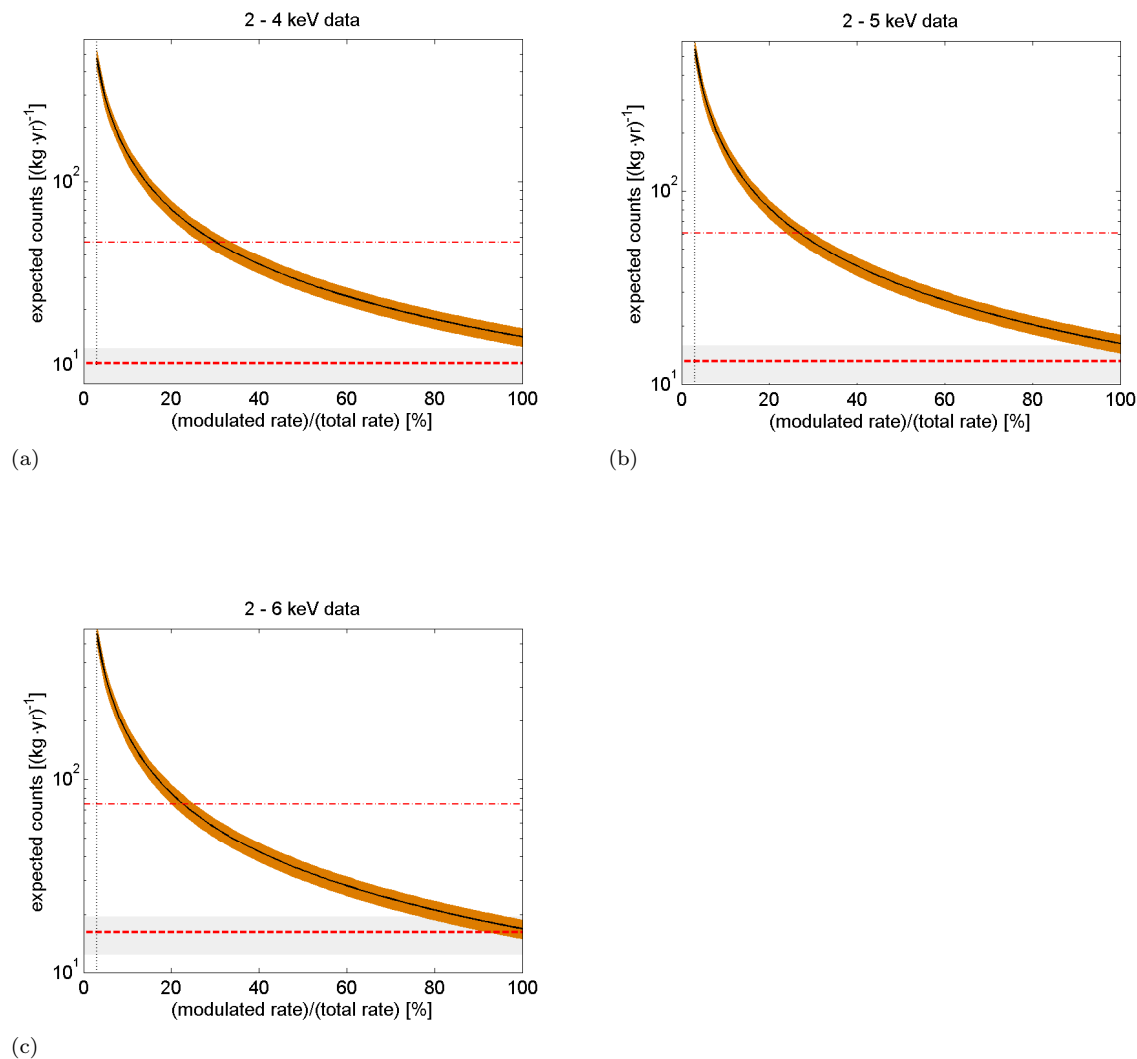
Figure 3.4: Expected count rates for 1 kg year exposure of a NaI cryogenic detector as function of the modulated fraction with respect to the total WIMP rate. At least 3 % amplitude is expected (*dotted* vertical line), but some scenarios can even lead to 100 % modulation. The different values for 2 - 4 keV (a), 2 - 5 keV (b) and 2 - 6 keV (c) range published in [59] are used. The *orange* bands are derived from the uncertainties quoted there. The *upper dashed line* line gives a rough (conservative) background estimate, derived from CRESST II run 32 data [55], see text for details. The *lower red dashed* line and the corresponding error band (*gray*) give a more realistic estimate, assuming the clamp-induced background can not be reduced.

is approximately smaller than 50 %. In an improved CRESST II setup with fully scintillating modules even fully modulated model are accessible.

(a)

(b)

(c)

Figure 3.5: Again, expected count rates for 1 kg year exposure of a NaI cryogenic detector as function of the modulated fraction with respect to the total WIMP rate. Here, the red dashed line and the corresponding error band (*gray*) give an estimate on the background, if the clamp induced background can be reduced, e. g. by a fully scintillating detector module housing. As one can see, even fully modulated scenarios could be investigated.

Finally, the question of intrinsic contaminations of $CaWO_4$ and NaI should be addressed: As high rates in the e/γ-band lead to higher separation thresholds, which has been discussed above, the intrinsic radioactive impurities of the used crystals should be as low as possible. Impurities in the best CRESST crystals are in the range of 3 mBq/kg [120]. The DAMA collaboration unfortunately states no total activity per crystal, but the activities for the main contributions of Uranium and Thorium decay chains are given in [111]. Summing up the contributions yields a value about 10 times lower than for the best CRESST crystals. It thus seems safe to state, that impurities in NaI are at least on a comparable level to $CaWO_4$ or even lower, if DAMA-grade NaI crystals are employed.
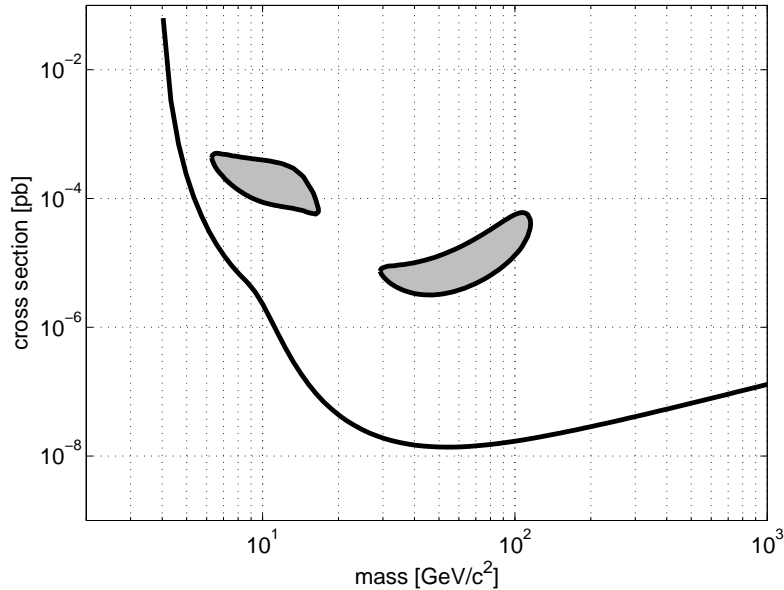
Figure 3.6: Expected exclusion limit for 1 kg yr CND data with threshold comparable to DAMA assuming standard halo parameters with no events observed in the DM analysis window. The DAMA allowed regions are shown in gray and lie well within the excluded regime. Thus the DAMA signal can be fully tested with the given exposure.

The discussion so far can be considered model-independent in the sense that the same assumptions have been made as by the DAMA collaboration. One can of course also use the model dependent approach presented in sec. 1.1.5 using the astrophysical parameters $\rho_\chi = 0.3 \, \text{GeV/cm}^3$, $v_0 = 220 \, \text{km/s}$, $v_{esc} = 600 \, \text{km/s}$ and $v_\odot = 232 \, \text{km/s}$, assume coherent scattering, account for the coherence loss using the Helm form factor and calculate the recoil spectra and rates to derive an exclusion limit for 1 kg yr exposure of a CND for the case that no signal is observed. This is shown in fig. 3.6. For comparison, the DAMA allowed regions are added. This demonstrates again, that the DAMA signal is testable by a CND with moderate efforts.

So far it has been shown that there are no a priori reasons why it should not be possible to cross-check the DAMA signal using a CND experiment. The remaining part of this thesis will thus present the practical steps undertaken to experimentally check the feasibility of the project. As a first step, light yield measurements at low temperature have been performed. The data obtained will be presented now.

3.2 NaI light yield measurements at low temperatures

As shown in sec. 1.2 the absorber material in a CRESST-like setup should yield a light signal upon particle excitation to allow for event-by-event particle discrimination. Therefore it is crucial to study the light yield of candidate crystals in a low temperature setup. The cooling properties of NaI were unknown and the light yield behavior from room temperature down to 4 K was only studied by van Sciver et al. [121] so far. They measured the light yield at eight temperature values, showing an increase with falling T peaking at roughly 80 K. Since these findings have so far not be confirmed by other studies a setup providing temperatures down to 1.5 K was chosen to experimentally verify and improve the available data. The setup for the measurements will be described in detail in sect. 3.2.1 and sect. 3.2.2 and results for the light yield of NaI and NaI(Tl) will be presented in sect. 3.2.3. The decay time properties will then be discussed in sect. 3.2.4. Some parts of the data on NaI and NaI(Tl) given in the following sections have already been published in [122] and those sections and figures will not be marked separately. They can be regarded as an extensive quote of the published

paper, while some parts have been supplemented with more detailed content not published in [122].

3.2.1 Cryogenic dark room setup

In order to cool down crystals, a Helium bath cryostat by Janis Research, model SVT-400, has been set up in a dark room by C. Oßwald as described in detail in [123]. To allow direct optical measurements with warm-stage photomultipliers, the cryostat is equipped with four Indium-sealed Suprasil II windows transmitting more than 90 % of the light for wavelengths greater than 190 nm. The opening angle with respect to the sample tube center is 38 °. As the sample tube of the cryostat is surrounded by several heat shield stages, one "window" actually consists of three successive windows, which has to be considered when deriving absolute light yield information. As fig. 3.7 shows, the size of the windows is chosen such, that the opening angle of 38 ° is conserved while the transparent area is minimized.[3] The crystal sample is cooled by direct contact with vaporized liquid Helium providing temperatures as low as 1.7 K. Theoretically 1.2 K can be achieved, but it is not possible to get stable temperature conditions at such low values. In order to measure and stabilize the temperature, the cryostat is equipped with two DT-670 B-SD diodes by Lakeshore, one measuring the bath temperature at the vaporizer, the other one mounted on the sample holder. A 25 Ω heater on the sample holder is connected to a Lakeshore 331 S temperature controller, allowing to stabilize temperatures to a precision of up to 0.01 K or better, depending on the temperature range. To prevent moisture from condensing on the cold optical windows a fan and an air dehumidifier are installed.

3.2.2 Experimental setup

Two Sodium Iodide samples have been used in this work. Both were produced by Saint-Gobain Crystals [125]. The samples are cubic shaped with an edge length of 1 cm where one crystal is doped with Thallium and the other one is made of pure NaI. To ensure that the pure NaI sample was not accidentally doped with Thallium remnants, it was grown in a dedicated mold.

As NaI is highly hygroscopic the crystals were placed in a Copper housing with quartz glass windows manufactured by Aachener Quarz-Glas Technologie Heinrich [126]. The Copper holder was assembled in a Nitrogen purged glove box and sealed with Indium wire. To prevent the remaining Nitrogen inside of the capsule from condensing on the optical windows, a custom made cryogenic pump utilizing charcoal was added. Fig. 3.8 shows a drawing of the holder. Gluing the quartz glass windows proved to be challenging, as the linear thermal expansion coefficients of Copper and glass differ approximately by a factor of two. Some of the windows cracked due to thermal stress that could not be compensated by the layer of Stycast® 2850 FT epoxy glue. It is therefore proposed that future designs will either have the windows glued on top of the Copper and not as done here inside a groove or will be sealed by Indium wire. Nevertheless a functioning holder could be obtained after some iterations.

Alpha particles from an ^{241}Am source with an activity of 840 kBq was used to irradiate the crystal inside the housing. An α source was chosen as the samples are too small to allow for decent photo absorption rates when working with standard gamma sources such as ^{137}Cs or ^{60}Co. To achieve a reasonable photo absorption signal one could, in principle, use a low energy gamma source. This was not done as there was no such source available that could be operated safely at cryogenic temperatures. Also the α particles with $E_\alpha = 5.486$ MeV yield a high scintillation signal, which is desirable to get a high signal to noise ratio.

As the maximum of the spectral emission of pure NaI shifts to ~ 300 nm at lower temperatures [127], type 9235 QB quartz glass photomultiplier tubes produced by ET Enterprises were used to prevent light losses due to UV absorption in standard borosilicate PMT glass. These PMTs provide a high quantum efficiency ≥ 25 % for λ between 180 nm and 440 nm, see fig. 3.9.

---

[3]Due to Boltzmann radiation, optically transparent windows always act as heat leaks in low T setups.
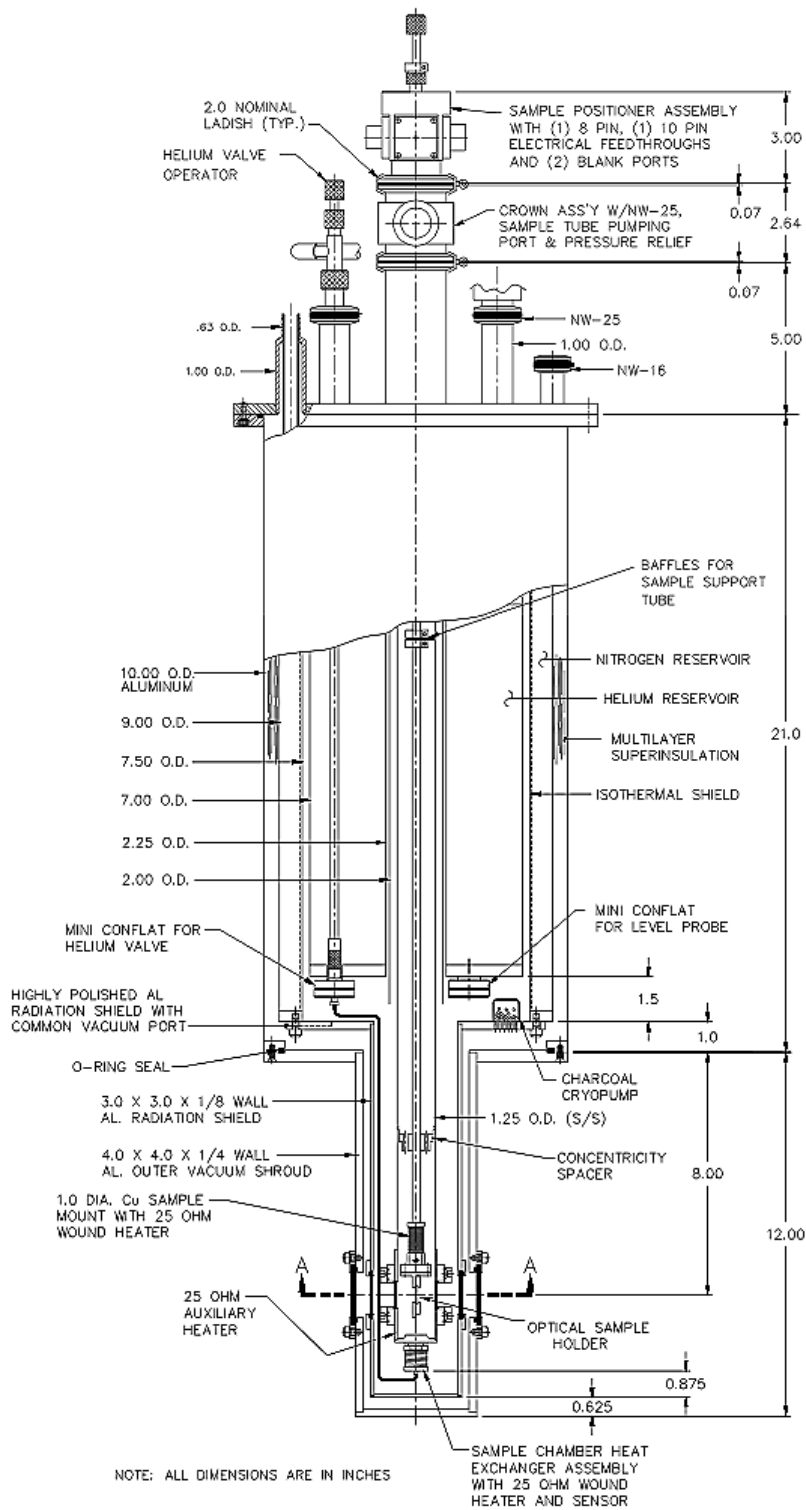
Figure 3.7: Technical drawing of the Janis Helium bath cryostat. [124]
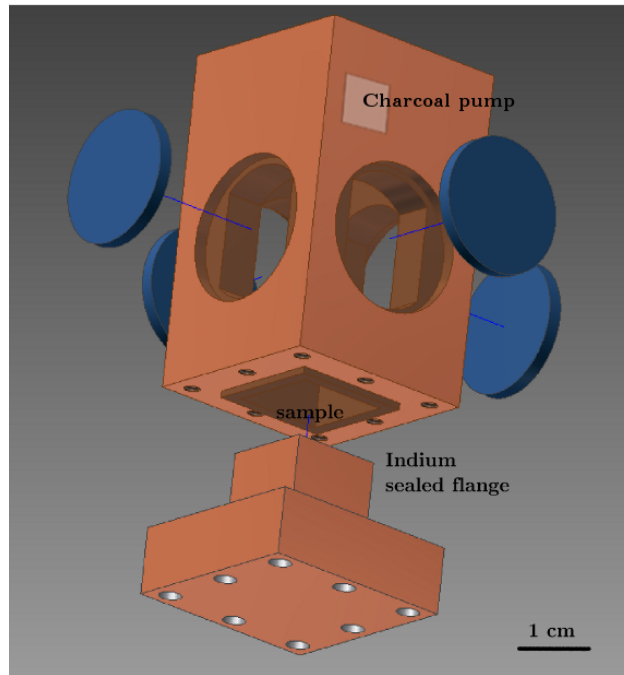
Figure 3.8: Indium sealed Copper housing for optical measurements in the Helium bath cryostat.
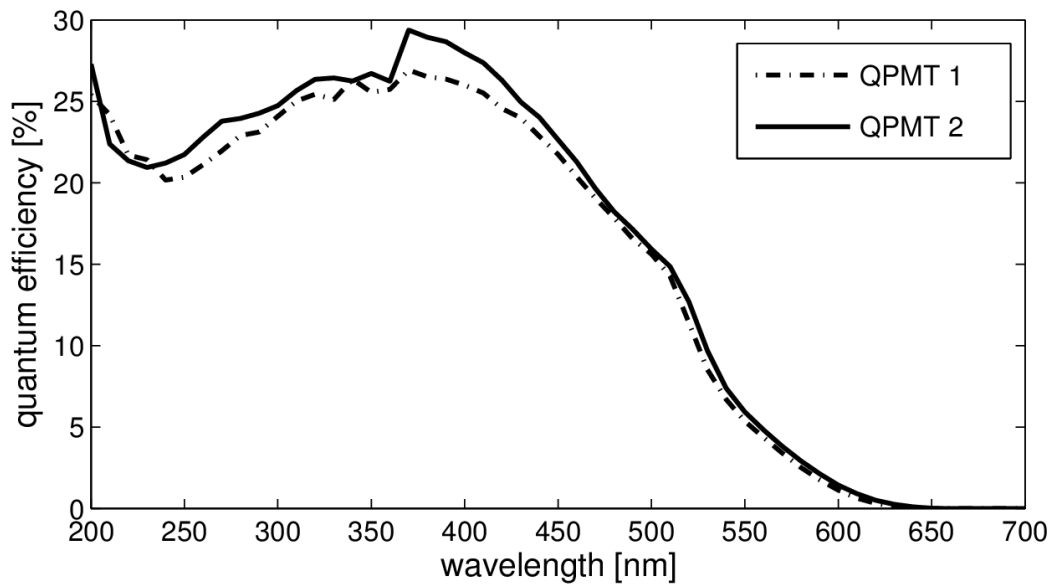
Figure 3.9: Quantum efficiency of the used 9235 QB PMTs. Data provided by ET Enterprises.

The PMT signals were fed into Ortec TF 474 amplifiers where they were amplified and integrated for 20 ns. The signal was duplicated in a LeCroy 428F Fan In - Fan Out module (FiFo) and connected to a CAEN N840 leading edge discriminator with low threshold of a few photoelectrons that was used to get a trigger signal. The respective NIM logical pulses were then fed into a LeCroy 622 Quad Coincidence module to realize a logical AND trigger for coincident signals in the two PMTs. The coincident readout is not necessary in terms of background reduction since the signals are sufficiently high. Yet it allows to reduce the systematical errors. The amplified signal from the FiFo and the trigger pulse were connected to a SIS 3301 FADC that recorded the traces of the scintillation events with a sampling rate of 100 MS/s. For every triggered event the software also recorded both temperature readings. Figure 3.10 shows a sketch of the setup.
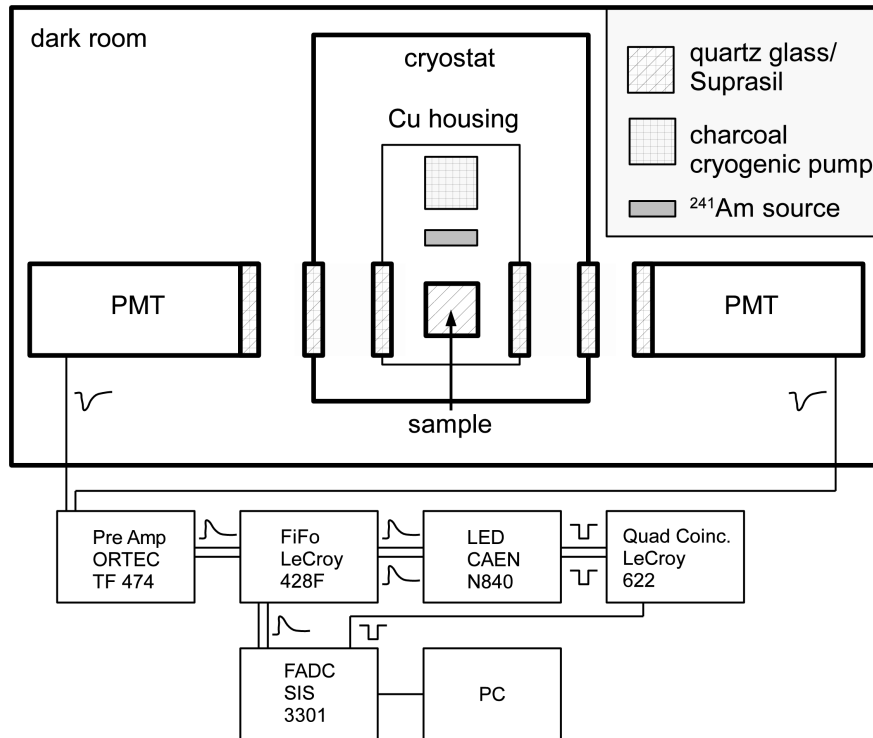
Figure 3.10: Sketch of the experimental setup for the light yield measurements.

For both samples the temperature was varied from room temperature down to $\sim$2 K. At each temperature 512,000 scintillation events were recorded from the NaI(Tl) and 1,024,000 from the pure NaI. A cut was applied to remove traces with nonzero pretrigger mean values. This removes roughly 7 % of the total events. The light output is proportional to the integrated PMT signals. Figure 3.11 shows an exemplary spectrum in pure NaI observed by PMT 1 and PMT 2 at a temperature of 178 K. At higher values the peak exhibits a shoulder which can be attributed to double α hits during one record length. These events were not removed by a cut. Rather a fit with three Gaussians was applied to account for baseline noise and both α distributions. The positions of the maximum of the single α distribution were determined for both channels separately and the resulting values were added. Statistical errors are omitted, as they are negligible. Systematical errors have been derived from variation of the fit, using the 95 % confidence interval for the peak position of the single α peak. The two PMTs were not operated at equal gain due to limitations in the electronics of PMT 2. The gain of PMT 1 was set to a higher value as compared to PMT 2 in order to increase the trigger rate. As all given values are relative quantities, this does not affect the results.

The decay time constants of the signals from the two samples differs, which could already be noticed on the oscilloscope. The pure NaI was recorded with 2.56 μs record length, the NaI(Tl) data with 5.12 μs. To illustrate the temperature dependence, a mean decay time constant was derived in three representative
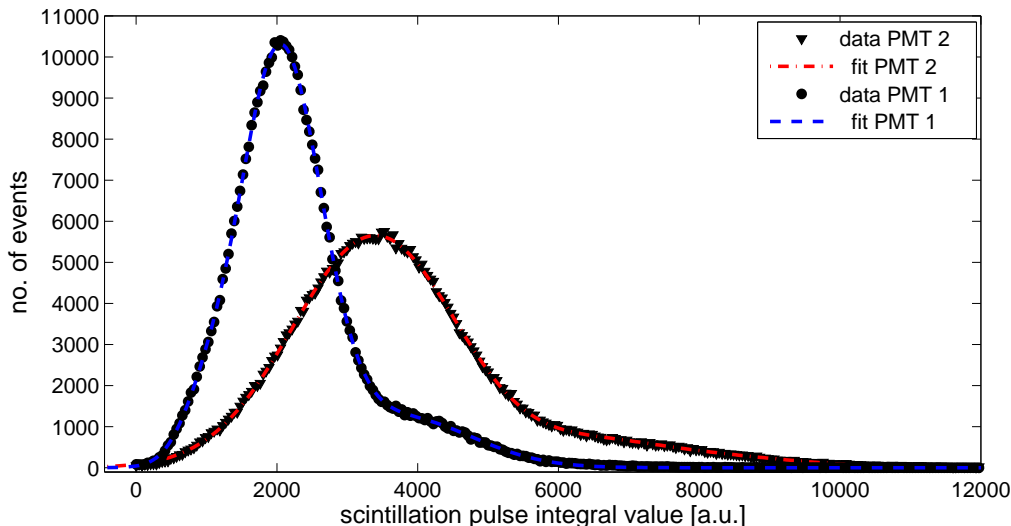
Figure 3.11: Exemplary histogram of integral values for scintillation events seen by PMT 1 and PMT 2 at 178 K. The fit accounts for baseline noise and the two α distributions (see text for details). The PMTs were operated at different gain, therefore the peak positions vary.

temperature regimes for each crystal. This was done by selecting a sample of scintillation events with a cut on the ratio between pulse height and integral to prevents double events from faking long decay time constants. For each sample a summed pulse was then fitted with two exponential decay times. The decay time behavior of NaI and NaI(Tl) has been studied in more details in the next paragraph 3.2.3. Note that due to the time resolution of the FADC used, fast components in the order of several nanoseconds can not be resolved. Also the 20 ns shaping time in the preamplifier will slightly affect short values of τ.

3.2.3 Light yield of NaI and NaI(Tl) as function of the temperature

Figure 3.12 shows the results for the light yield of pure NaI, Figure 3.13 the data for NaI(Tl) respectively. The light yield axes are scaled such that the room temperature value of NaI(Tl) is set to one.

As fig. 3.12 shows, the light yield of pure NaI at room temperature is low, amounting to $\sim 6\,\%$ of the value of NaI(Tl) at such temperatures. Cooling below 220 K it starts to rise, reaching a nearly constant value of $\sim 91\,\%$ below liquid Nitrogen temperature. Between 50 K and 40 K the maximum value of 95 % is found. Cooling further the LY decreases again, reaching a value of 65 % at 1.7 K.

For the Thallium-doped crystal the light yield increases slightly (up to 110 % of the room temperature value) when cooling to temperatures around 250 K. Further decreasing the temperature lowers the LY to 93 % at 200 K. Down to 160 K another increase to 112 % can be observed. Then, the LY falls rapidly, reaching a minimum at a value of 20 % around 60 K. Cooling further, a substantial increase in light output can be observed, reaching another maximum (73 %) at 25 K and the slightly decreasing to $\sim 65\,\%$ at 2 K.

Discussion of the LY results

For pure NaI the general light yield curve published by van Sciver and Bogart [121] is confirmed by the measurement. The presented results extend the available data below 4 K which allows to further study the decrease in light output after the maximum at about 50 K. The temperature resolution has also been increased, as van Sciver only measured at 8 different temperatures. It is striking that the maximum value
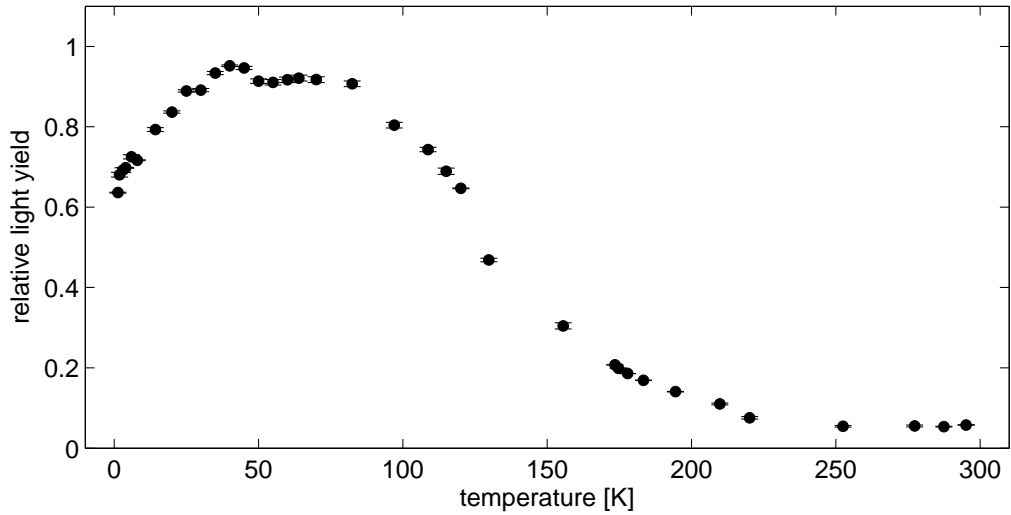
Figure 3.12: Light yield of pure NaI as function of temperature relative to the value of NaI(Tl) at room temperature. Errors are dominated by systematics, see text.
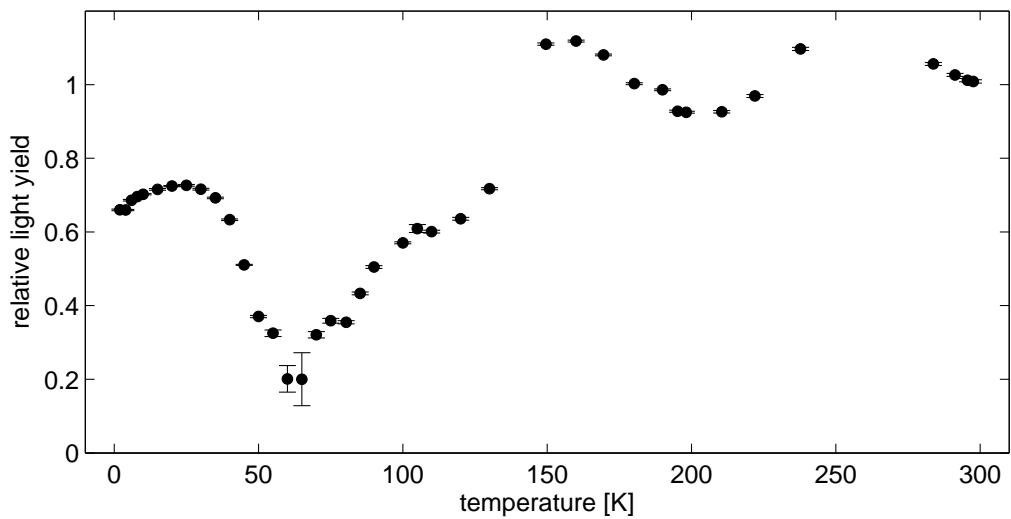

Figure 3.13: Light yield of NaI(Tl) as function of temperature relative to the value at room temperature. Errors are dominated by systematics, see text for details.

of pure NaI at around 50 K is almost comparable (95 %) to the light yield of Thallium doped NaI at room temperature. Yet van Sciver and Bogart reported approximately double the room temperature conversion efficiency of NaI(Tl), peaking at Nitrogen temperature. In order to compare the results, a few things need to be considered: Van Sciver et al. used the unintegrated pulse height to deduce the light yield verus temperature curve [121]. In this work the integral was used to take into account the varying decay time. Fig. 3.14 illustrates why this choice was made: The averaged scintillation signal for NaI at 80 K, near the maximum LY reported by van Sciver et al., is compared to the averaged signal of NaI(Tl) at room temperature. The pulse height of pure NaI is almost double that of NaI(Tl), yet it's integral is only at 90 % of the value of NaI(Tl). Since the pulse form is not affected by the electronics, which will be shown when discussing the decay times in sec. 3.2.4, the integral corresponds to the summed single photo-electron pulses. Deriving the LY just by the pulse height can be misleading, when the decay times change over temperature.
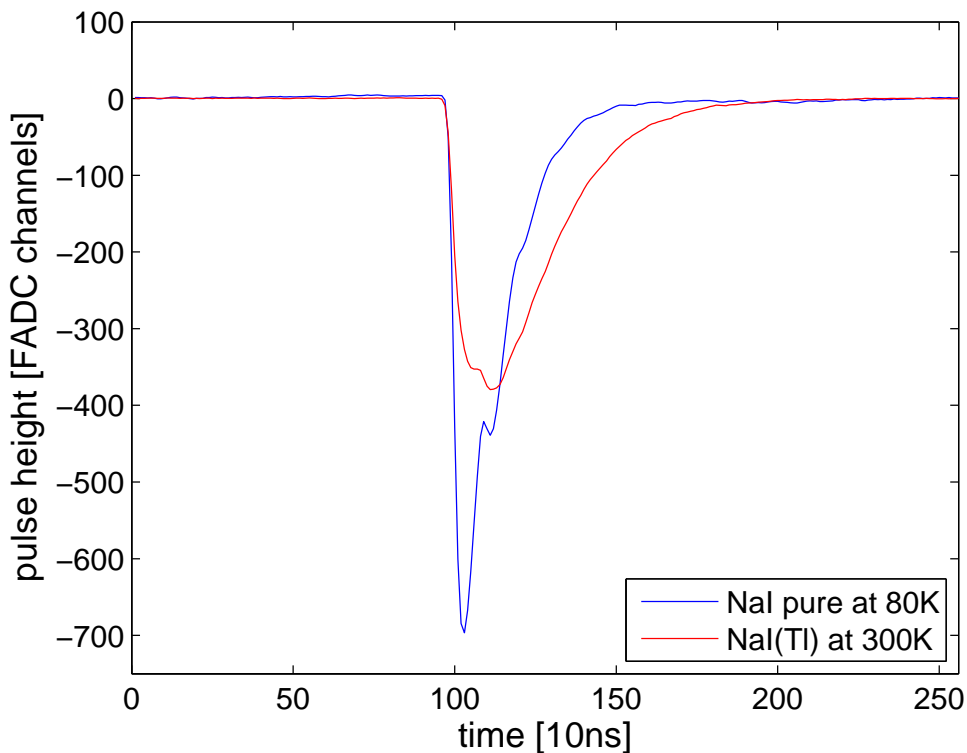
Figure 3.14: Comparing pulse height and integral as LY measure: The signal for NaI at 80 K is compared to the signal of NaI(Tl) at room temperature. The pulse height of pure NaI is almost double that of NaI(Tl) while the integral is comparable (90 % of NaI(Tl)). The structure on the pulse was due to the PMT base design and does not effect the measured values. Both signals were averaged to reduce noise and statistical effects.

Due to the different measurement quantities, the maximum of the light emission for van Sciver et al. (see fig. 4 in [121]) is found at higher temperatures as compared to fig. 3.12. The authors also report the total conversion efficiency η as a function of temperature, which is the ratio of detected light energy to the total deposited energy. In the maximum of this curve at 77 K they give a value $\eta = 25\,\%$ for the photo absorption peak of γ-particles of ^{137}Cs. As van Sciver has shown in [116], the emission spectrum of pure NaI at low temperatures peaks narrowly around 303 nm. Therefore it is well justified to use this value as the mean photon frequency $\bar{\nu}$ for the scintillation light of the crystal. The mean photon number $\bar{N}$ for 661.7 keV

gamma energy deposition can thus be calculated as

$$\bar{N} = \frac{E_\gamma \eta}{h \bar{\nu}}$$

<div align="right">(3.2)</div>

where h is the Planck constant. Therefore a value of 61,100 (ph/MeV) can be derived from the data in [121]. For NaI(Tl) at room temperature they state $\eta = 13\%$. The emission spectrum of Thallium-doped NaI peaks at 415 nm (see [128] for details), which gives the absolute light yield value of 28,800 (ph/MeV). Since NaI(Tl) is a widely used scintillator, the production process has been optimized to achieve a higher light output. Today a common accepted value for the light yield of NaI(Tl) at room temperature is 44,000 (ph/MeV), see e. g. [129, 130]. Therefore it is crucial to know how the LY values were obtained when comparing results.

Moszyński et al. [115] have also measured the light yield of three samples of pure NaI from room temperature down to 78 K. For two samples they get maximum LY values of $69,000 \pm 7000$ (ph/MeV) and $84,000 \pm 9000$ (ph/MeV) respectively. The third sample contained Thallium impurities and is thus not considered here. Their results were obtained by comparing the position of the 661.7 keV photo absorption peak position of ^{137}Cs to the position obtained for a known reference crystal. They used a charge sensitive preamplifier and varied the shaping time of the consecutive spectroscopy amplifier, which should yield comparable results to the method used in this work. Thus it is unclear, why they get more than double the LY at liquid Nitrogen temperature. Assuming a similar performance of the crystals used in this work compared to the samples used by Moszyński et al. [115] one can estimate the absolute light yield using the mean value for the two pure samples reported there, namely 3,900 ph/MeV at 295 K and 76,500 ph/MeV at 78 K to scale fig. 3.12. This gives a value of 54,500 ph/MeV at 1.7 K. Since cryogenic detectors are operated at temperatures of several mK, it is of interest to estimate the LY near T $= 0$ K. Extrapolating conservatively to mK temperature range, an absolute light yield of 44,400 ph/MeV can be estimated using the data of Moszyński et al..

As presented earlier, in this work the maximum light output of pure NaI was found to be 95 % of NaI(Tl) at room temperature. Since the NaI(Tl) reference crystal was purchased from Saint-Gobain [125], one of the main manufacturers of scintillation material, the absolute LY of the NaI(Tl) will be around the already quoted value of 44,000 (ph/MeV), which gives a light yield of roughly 41,800 (ph/MeV) in the maximum of pure NaI. At 1.7 K the light yield of pure NaI amounts to approximately 65 % of the room temperature value of NaI(Tl), which corresponds to 28,600 (ph/MeV). Again, a linear extrapolation of the steepest decline in fig. 3.12 gives a conservative estimate for the light yield at mK range. Using the values obtained in this thesis one obtains 24,200 (ph/MeV).

To summarize the situation, the values at room, liquid Nitrogen temperature and 4 K are compiled in tab. 3.2.

	T $= 295$ K	T ~ 78 K	T $= 4$ K
Moszyński et al. [115]	3,900[a]	76,500[a]	–
van Sciver and Bogart [121]	3,300[b]	61,100[b]	30,700[b]
this work	**2,650[c]**	**41,800[c]**	**30,800[c]**

Table 3.2: Comparison of pure NaI light yield values in (ph/MeV) at room, liquid Nitrogen temperature and at 4 K.
[a] Averaged value of two samples.
[b] Calculated from conversion efficiency.
[c] Using the pulse integral, assuming 44,000 (ph/MeV) for NaI(Tl) at 295 K.

Despite the discrepancies that might be due to the used methods, the measured crystal samples can also differ in light output quite significantly e. g. due to trace impurities. Following tab. 3.2 it can however be safely concluded that pure NaI has a high light yield at low temperatures. At 78 K the LY is at least comparable to the light output of NaI(Tl) at room temperature. Estimates for the light yield at the mK temperature

range vary from 24,200–44,000 (ph/MeV), as has been discussed above.

Comparing the LY of NaI to CaWO$_4$

Since the CRESST experiment is using CaWO$_4$ crystals, it is interesting to compare the obtained values for pure NaI to those of CaWO$_4$. The room temperature value has been measured by Moszyński et al. [131], with the mean of the two investigated samples of 15,000 (ph/MeV). Since Kraus and Mikhailik [132] report a light enhancement factor of 1.8 from room temperature to 6 K, the LY at 6 K is 27,000 (ph/MeV). The respective value for pure NaI derived in this thesis is 31,900 (ph/MeV). Using the light yield curve scaled to Moszyński et al. [115] one would get 58,000 (ph/MeV). Thus in conclusion pure NaI has a light yield of 1.2–2.15 times that of CaWO$_4$.

Further discussion of the increase in the LY curve of NaI(Tl) below 60 K

As pointed out earlier, for NaI(Tl) a strong suppression in light output is observed down to 60 K. This has been known for quite some time [128]. However, in this work a substantial increase in light yield is observed when lowering the temperature further. At 2.0 K a value of roughly 65 % relative to the room temperature value of NaI(Tl) can be derived which is comparable to the results obtained for pure NaI.

This raises the question if the increase of light output below 60 K for NaI(Tl) could be related to the intrinsic properties of pure NaI or it is due to another scintillation mechanism. To check this, the decay times at three temperatures have been measured as described in subsection 3.2.2. Results can be found in Table 3.3.

NaI pure			
T	290 K	150 K	6 K
τ_1	20 ns	101 ns	-
τ_2	115 ns	503 ns	163 ns
NaI(Tl)			
T	300 K	150 K	6 K
τ_1	-	-	23 ns
τ_2	216 ns	646 ns	122 ns

Table 3.3: Decay times derived from double exponential fit.

The values for pure NaI in tab. 3.3 differ slightly (mostly $\mathcal{O}(10 \, \text{ns})$ from the ones published in [122], as the analysis was performed with more stringent cut parameters for this work, which allowed to disentangle the fast and slow component also at room temperature. Considering the 10 ns time resolution of the FADC the decay times in tab. 3.3 and the published ones still agree quite well.

As the values in tab. 3.3 indicated some interesting features like the slow emission at intermediate temperatures and very fast decay times at low T, the decay time data was investigated further and the results will be discussed in the next section.

3.2.4 Decay time behavior of NaI and NaI(Tl) as function of the temperature

As shown in fig. 3.15 for pure NaI the decay time slightly increases toward lower temperatures with a strong increase starting at 175 K and dropping sharply at 120 K. Van Sciver and Bogart reported the same overall

tendency – except for the intermediate peak – but give much smaller values, especially at room temperature [121]. Yet Pooley and Runciman [133] state that those decay time values might not be reliable due to trace impurity concentrations. More recently Moszyński et al. [115] have performed measurements using the single photon method and found four contributions to the decay time spectrum at room temperature: Two fast ones of 1.24 ns and 5.10 ns, an intermediate one of 23 ns which corresponds most likely to the component observed by van Sciver and is in good agreement with the 20 ns observed here and finally a long component of 93 ns, which is more or less comparable to the 112 ns at 295 K derived in this work. Due to the limited time resolution of the FADC the very fast decay times could not be observed in the measurement performed in this thesis.
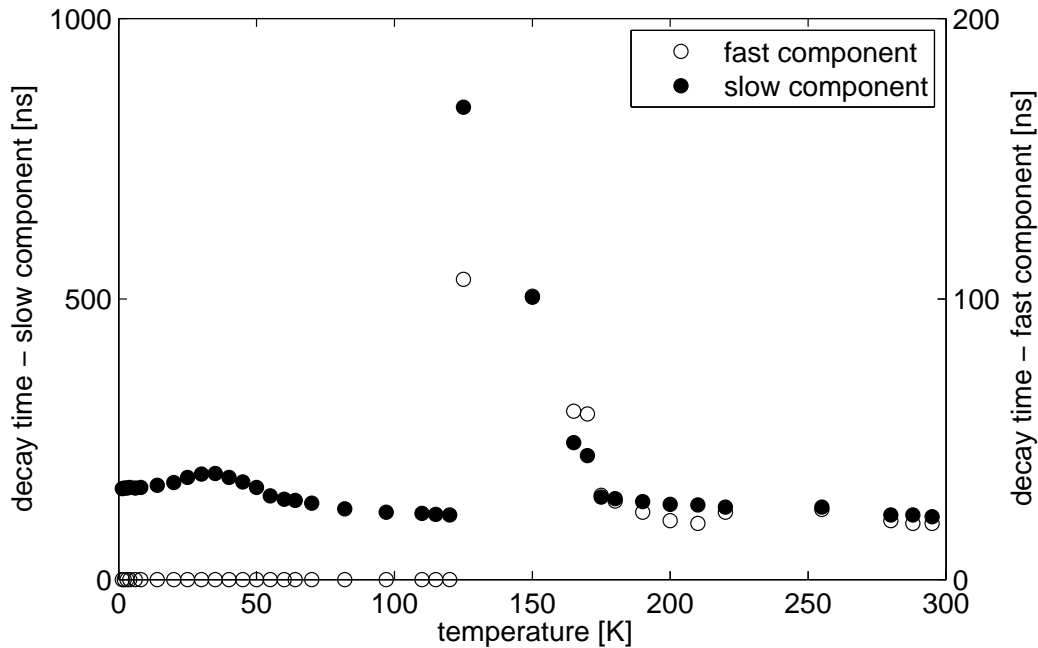
Figure 3.15: Decay time behavior for pure NaI. Note the different axes for the slow (solid circles) and fast components (open circles). The feature at around 120 K differs from the NaI(Tl) decay time data, see fig. 3.16.

For the decay time of NaI(Tl) at 300 K one finds 216 ns which is in very good agreement with the literature value [134] of 230 ns at 293 K considering the FADC's time resolution of 10 ns per point which is why the values in this work are considered reliable. As fig. 3.16 shows, decreasing the temperature of the NaI(Tl) sample leads to longer decay times peaking around 150 K. Quite unexpectedly at 6 K the pulses are fast again, even faster than at room temperature. The measured 122 ns are close to the value of 110 ns for intrinsic luminescence in pure NaI reported in Fontana et al. [135] for band to band excitation. So it seems possible, that at low temperatures the light yield of NaI(Tl) is dominated by the intrinsic properties of the NaI lattice. This seems to support the conclusion of Fontana et al. that *at high temperatures the scintillation time constant seems then to be mainly determined by the energy transfer mechanism, and not by the intrinsic behavior of the luminescence center* [135]. To investigate this further, the decay time behavior was studied over the whole temperature range. The result can be found in Figure 3.16. The decay times for the fast component are presented using another y-axis scaling as the values are rather small. Two steep drops can be observed at around 230 K and 65 K, corresponding to the suppression dips in Figure 3.13. The value at liquid Nitrogen temperature has recently been confirmed by Sibczyński et al. [136]. Below 65 K the decay times are stable, which is an indication that no further light yield suppression occurs at lower temperatures. This remains to be verified in a setup at mK temperatures.
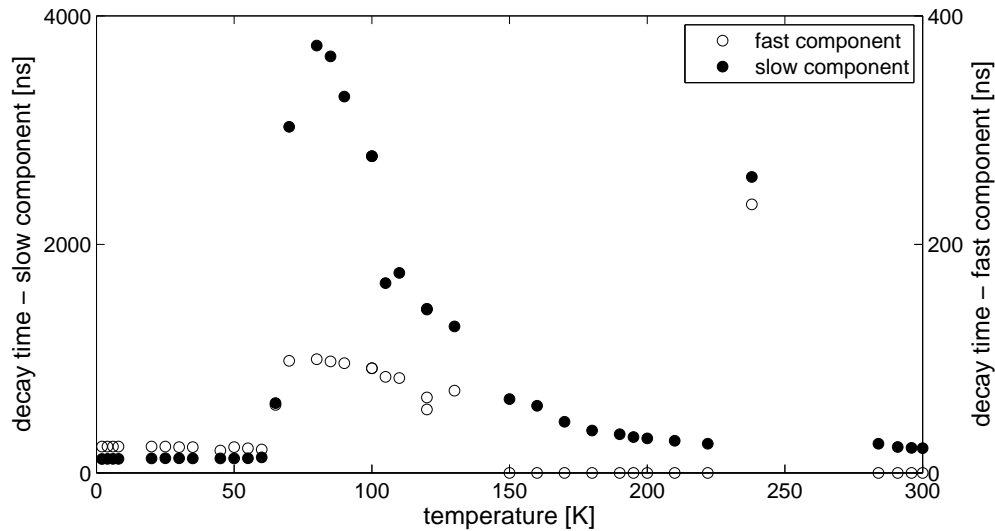
Figure 3.16: Decay time behavior for NaI(Tl). Note the different axes for the slow (solid circles) and fast components (open circles). The sharp drops at around 230 K and 65 K correspond to the suppression dips in the light yield curve.

Of course it cannot be excluded that the change in decay time is solely due to the deformation of the unit cell when lowering the temperature. The associated shift in energy, suppressing and delaying the light emission at certain temperatures would also explain the data. The similar light output and decay times at lowest temperature values would then be just considered an uncorrelated coincidence which however seems unlikely. The hypothesis that the scintillation mechanism might change at around 60 K mentioned above and already published in [122] is also supported by studies of V_k centers in NaI by Murray and Keller: They find that the V_k centers become mobile at temperatures above 58 K. Above these temperatures, the holes of the self-trapped states get captured at Thallium sites, leading to an increase in the bands typical for Tl^+ emission. A similar behavior was observed in Potassium Iodide (KI) at a temperature of 105 K by the same authors [137]. The light yield curve of NaI(Tl) can thus be interpreted as follows: Below 58 K the light emission is governed by STE annihilation. Above 58 K the holes of the self-trapped states become mobile, leading to a strong suppression of the STE emission. With increasing temperature the now mobile hole states produced by the incident α particles get captured on Thallium sites where they annihilate with the well known temperature dependent behavior, increasing the light yield again. The sharp drop at 60 K in the decay time plot fig. 3.16 is then related to the "freeze-in" of V_k centers in the lattice, allowing efficient STE emission below this temperature. This interpretation is also supported by the fact, that the decay time is nearly constant below 60 K, which is expected in case of SX emission.

The results of the measurements presented in this section can thus be summarized as follows:

The light yield of both, NaI and NaI(Tl) at around 2 K is higher with respect to $CaWO_4$, amounting to 65 % of the light output of NaI(Tl) at room temperature for the investigated crystal and the presented method. However there are reports of higher values, as discussed above. This might be related to the different methodical approaches. As the light in CRESST-type detectors is measured calorimetrically, the integral as a measure of LY is considered reliable, since decay time measurements have shown that the scintillation pulse form measured here is due to the scintillation process and not affected significantly by the readout electronics. A comparison of the LY of pure NaI to that of $CaWO_4$ showed that NaI exceeds the present CRESST target material by a factor of 1.2–2.15, where the lower value is more conservative. Extrapolations for $T \to 0$ K indicate that the same is true for the mK regime. The extrapolation seems to be justified, based on the fact that the emission process is identified and thus no sudden changes in the scintillating system are expected.

Also, the decay times at low temperatures are fast compared to typical thermal signals. This means that all the light produced by a recoiling particle can be collected within the relevant time-scales in a CND.

As NaI(Tl) at low temperatures exhibits a similar LY behavior compared to NaI, it is in principle possible to use it as target material in a CND. This would allow to utilize exactly the same absorber crystal as the material used in DAMA. Yet it has been discussed in sec. 3.1.1, that the phonon signal in NaI is expected to be significantly smaller than in $CaWO_4$ which should be an even stronger effect in NaI(Tl) due to the lattice defects introduced by the Tl ions. Also the Tl centers might introduce a position dependency of the light yield, if the dopant is not distributed homogeneously. Nevertheless it is proposed to investigate this in a mK setup. The main focus should however be on pure NaI.

As another result of the analysis of the presented data it has been shown that the light emission of NaI(Tl) crystals below 58 K is very likely dominated by self-trapped exciton emission.

The next section will now discuss the practical challenges in building a CND and report on the present status.

3.3 Preparations for building a cryogenic prototype NaI detector

Several issue have to be considered in order to build a prototype CND: The crystal handling, the cooling properties, the technical and thermal holder design as well as the gluing and contacting of the thermometer. This section will discuss these issues and possible solutions.

Since NaI is highly hygroscopic, the handling of the crystal is challenging. Even a two minutes exposure to standard humidity levels of ambient air will lead to a degradation of the crystal's surface, turning them white and thus hindering the light emission: As van Sciver and Bogart [121] reports, the white surface leads to substantial light reflexion. This can be avoided by careful handling using desiccators for transport and storage and a glove box for the assembly of the detector module. Relative humidity levels below 10 % have been found to be unproblematic, even for extended periods of exposure. Fast transfers from the glove box to the cryostat have also been carried out in a loosely covered Argon flooded container, which also proved viable.

For the prototype detector four new samples of pure NaI without encapsulation were ordered from Hilger Crystals [138]. All four are cylindrical shaped with 1.5 cm diameter and 1.5 cm height. As all of the ordered samples arrived with degraded surfaces despite proper packaging and silica gel bags added, the crystals had to be polished and cleaned. Fig. 3.17 shows two of the samples, the left one as it arrived from the supplier and the right one roughly polished. Removing the abrasive proofed to be difficult, as NaI is highly soluble in all types of alcohols and common cleaning agents like acetone. As the binding of NaI is of ionic nature, an unpolar cleaning agent, namely toluol (C_7H_8), was tested and proved to yield very good results.

Assembling and connecting a NaI detector module without exposing the crystal to humidity can in principle be done under Nitrogen atmosphere, using oxygen masks or similar systems. As this is quite costly, another approach was favored for the prototype module: A vacuum tight, low temperature proof encapsulation was designed to allow installation in the cryostat under normal ambient conditions. The technical sketch can be found in fig. 3.18. Normal O-ring seals are not suitable for mK temperatures. Therefore Indium sealed flanges with tongue and groove faces have been chosen to connect the lid (top), the phonon detector holder (middle) and the light detector housing (bottom). The electrical feed throughs were sealed with Stycast®. They are not visible in fig. 3.18. The phonon detector can either be placed on a quartz glass plate or can be fixed on the middle ring using clamps. The latter is preferable, as the quartz glass reduces the light collection efficiency. To provide electrical contact to the TES, insulated clamp contacts can be mounted on the upper holder ring. Thermal coupling to the Copper housing can be achieved by a thin Copper clamp that has been coated with Gold. It has been shown in sec. 2.4 that this method of contacting works in principle.

As the light detector in general needs to be operated at a different operating temperature than the PD,
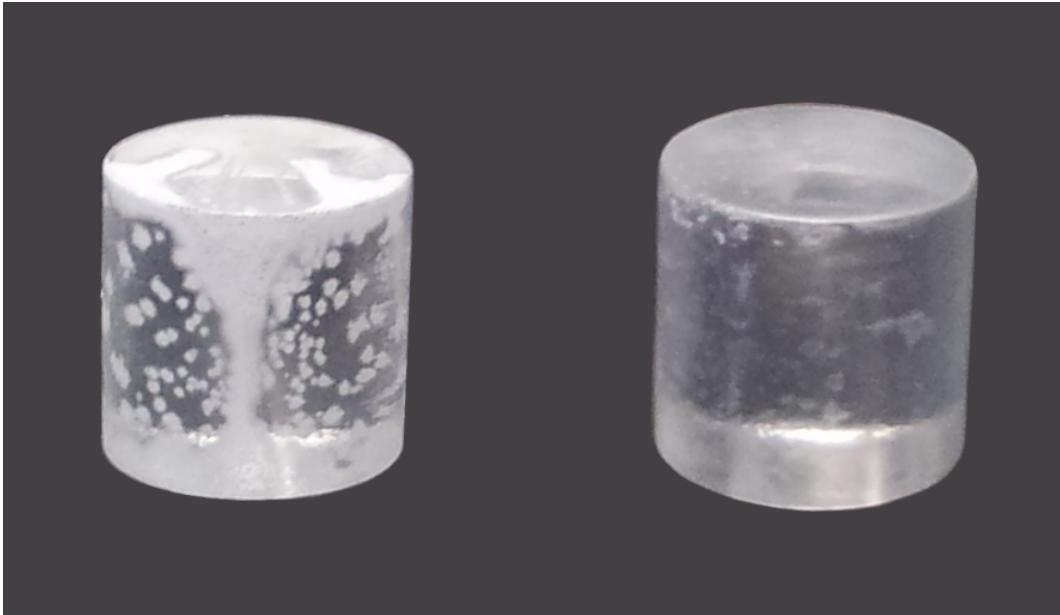
Figure 3.17: The surface of NaI is strongly affected by humidity even for short exposure times (left). By careful polishing and cleaning the remnants with toluol (C_7H_8) the optical properties can be restored. The crystal on the right side is already roughly polished.

thermal decoupling of the LD is realized with Sapphire balls and insulating screws. It is connected via insulated bond pads on the LD holder ring and thermally coupled to it using Gold bond wire. Since the heat capacity of the LD holder ring is small compared to the PD heat sink, the transition temperature of the LD TES should be chosen to be higher than that of the PD thermometer. To cool the LD holder a Copper wire connected to the housing is used. That way, by changing the diameter, the coupling to the heat bath can be regulated according to the heat load generated by the LD heater. Currently there is only a 2 cm x 2 cm Silicon light detector with an IrAu TES available. It should be replaced in future runs, because of it's high T_c of 54 mK. Also a top-down installation should be attempted so that direct TES hits are no longer possible, thus maximizing the sensitive area. This can be achieved with minor modifications to the design. A picture of the currently mounted detector is shown in fig. 3.19. In order to calibrate the LD, a calibration source, e. g. a low activity ^{55}Fe source, can be placed on the bottom inside the encapsulation.

The holder can be assembled in a glove box that is purged with dried Nitrogen gas. However the Nitrogen inside the encapsulation would freeze to the cold surfaces when cooling the detector to mK temperatures. Therefore the detector module volume can be evacuated inside the glove box by a small copper capillary which is then sealed by crimping, cut and finally closed by soldering it. This way no valve is needed[4]. The remaining few centimeters of the capillary can be rolled up and fixed by tape. Since Copper can be soldered without problems, the capillary can be easily replaced once it gets too short.

The holder in fig. 3.18 has been manufactured from oxygen-free high conductivity (OFHC) Copper by the Tübingen University workshop. The parts before assembly are shown in fig. 3.20. The encapsulation has been assembled, evacuated and tested for tightness using a Helium leak detector.

As a next step, the gluing of the TES to the NaI crystal was tested. A Tungsten TES with 2 mm diameter on a a 5 x 3 x 1 mm^3 Sapphire substrate with $T_c = 41$ mK was glued to one of the cylindrical NaI samples[5] using

---

[4]Valves usually are O-ring sealed and thus not suitable for such low temperatures. Also space inside the cryostat is limited.

[5]A lower value of T_c would be desirable to maximize the phonon signal (see eq.2.1), however there was no suitable sensor available at the time.
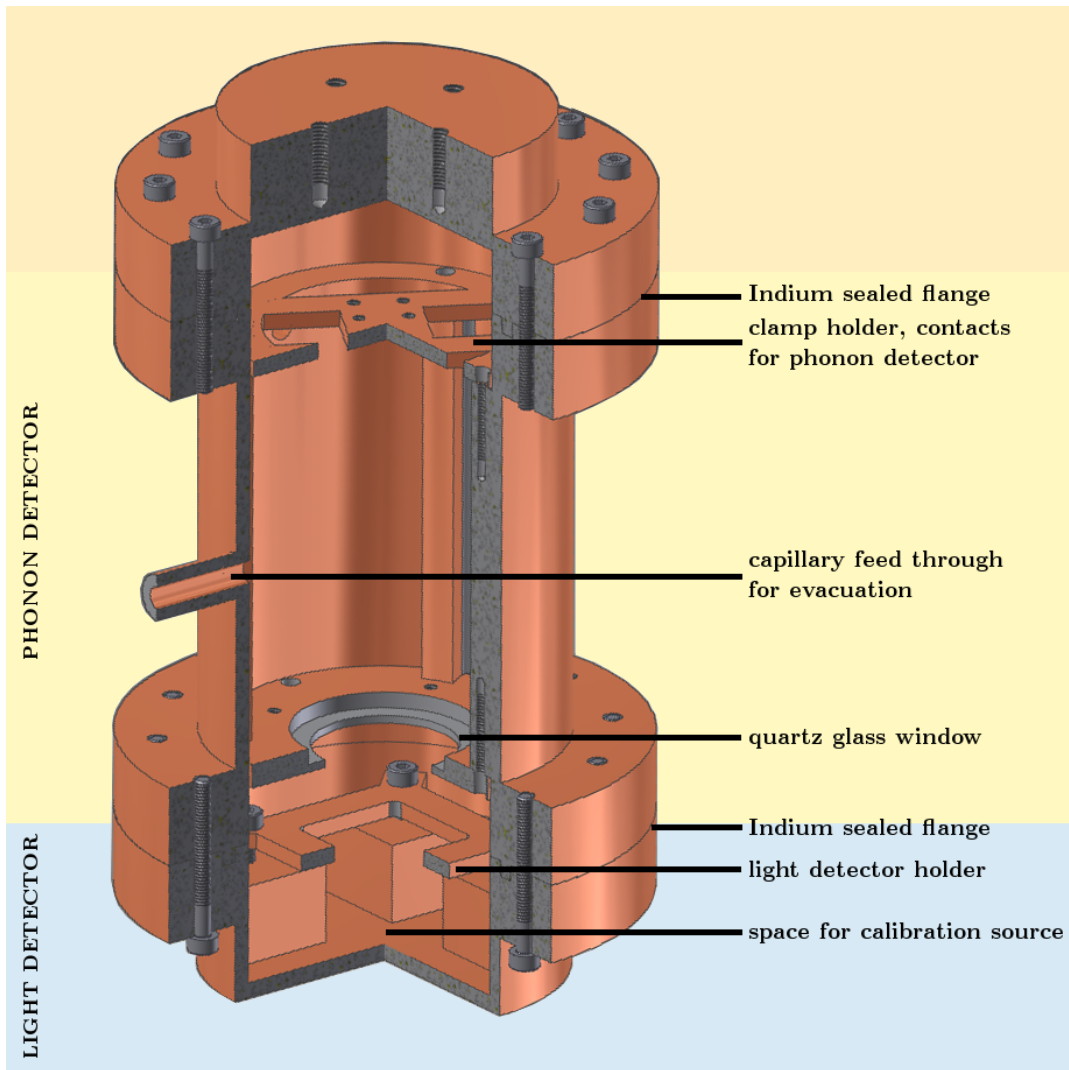
Figure 3.18: Drawing of the vacuum tight encapsulation for a NaI prototype module. The Stycast®-sealed cable feed troughs are not visible in this view. The lid (upper part) and the phonon (middle) and light detector (lower part) sections are connected with Indium sealed flanges. Thermal decoupling of the light detector is realized with Sapphire balls and insulating screws. The phonon detector can either be placed on a quartz glass plate or can be fixed on the middle ring using clamps.
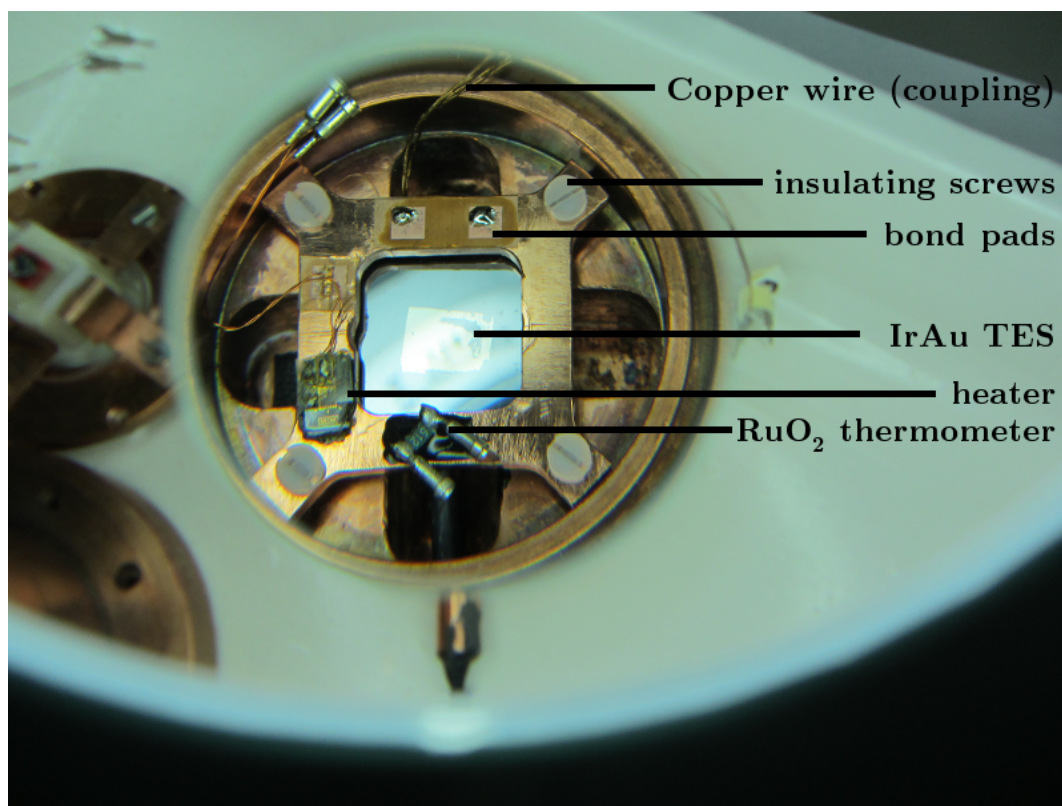
Figure 3.19: Mounted light detector inside the NaI module for first checks: The IrAu TES has a T_c of 54 mK.

Figure 3.20: OFHC Copper parts of the NaI encapsulation before assembly.

EPO-Tek 301-2 epoxy resin. The crystal was placed inside the encapsulation, connected using the clamp ring, sealed off and mounted in the dilution refrigerator, as shown in fig. 3.21. All electrical connections were checked at room temperature. A slow cooldown was performed, as the crystal can crack due to the skin effect if the thermal gradient inside the crystal gets to high. Yet at mk temperatures the electrical connection to the PD TES was lost. As the clamps are rather long ($\mathcal{O}(2\,\mathrm{cm})$) it is likely that their position changed due to the thermal contraction. Therefore it is suggested that a guide for the clamps is added in future. Also Indium press contacts could be considered. Bonding the TES was not possible, as there is no facility available at Tübingen University, where contacts can be bonded under a protective atmosphere. This should however be aimed for as it is the most reliable method of contacting, also providing better control on the thermal coupling, as the Gold bond wire diameter is well known which is not the case for the Au-clamp tip contact area.
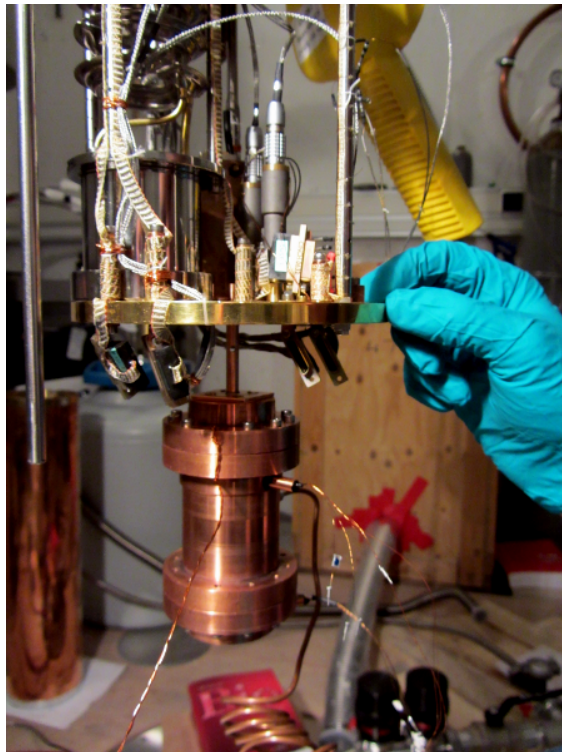
Figure 3.21: Picture of the mounted encapsulation with NaI and light detector in the dilution refrigerator.

Visual inspection of the crystal after the cooldown showed no damage due to the cooling, neither in the bulk crystal nor on the TES contact area which is very promising. Also no optical degradation of the crystal's surface could be observed, as fig. 3.22 shows[6]. The holder and handling concept thus work as intended. Therefore, despite all challenges it has been demonstrated that implementing NaI as an absorber in a cryogenic detector is possible.

The last section will now summarize the current status and provide an outlook for further investigations.

---

[6]The uneven spot on the lower right of the surface was already present before the cooldown. It is a remaining defect by the shipping damage that could not be removed entirely, as it would have been necessary to grind down almost 0.5 mm of the material.

Figure 3.22: The NaI crystal with a glued TES after being cooled down to mK temperatures in the Copper encapsulation: No damage by the cooling or degradation of the surface can be observed. The holder and handling concept thus work as intended. Therefore, despite all challenges it has been demonstrated that implementing NaI as an absorber in a cryogenic detector is possible.

3.4   Summary and outlook

In this chapter it has been discussed either by theoretical arguments or by measurements and practical tests, that it is possible to build a CRESST-like detector using NaI as a target material despite its hygroscopic nature. The phonon signal was estimated to be on the order of 29 % of $CaWO_4$ (sec. 3.1.1). The scintillation properties have been discussed (sec. 3.1.2) and the light yield has been measured down to 1.7 K. A comparison to $CaWO_4$ showed a factor of 1.2 higher LY under the assumption of a typical light yield of 44,000 (ph/MeV) for the NaI(Tl) reference crystal (see sec. 3.2.3). Scaling the results to other available LY data can even lead up to a factor of 2.15, yet it has been shown that the large difference might be related to the different measurement methods. Another possible reason might be a strongly varying difference in light output of the different investigated crystal. Yet it can be safely concluded that pure NaI exhibits the LY of $CaWO_4$ at low temperatures.

As discussed, this could help to decrease the separation threshold between light and phonon signal which is necessary to achieve a value E_{min} of $6.7\,keV_{nr}$, corresponding to the $2\,keV_{ee}$ in DAMA. Assuming that the phonon-channel resolution is small enough and light and phonon collection efficiencies sufficient, it was pointed out in sec. 3.1.3 that with 1 kg yr exposure of CND data the DAMA signal is well testable, even for fully modulated scenarios. The scintillation light decay time constants at low temperatures were also measured (sec. 3.2.4) and found to be short enough for the CND application. Finally the gluing of the thermometer and the handling of the hygroscopic material were successfully tested and a cooldown was performed in a mK cryostat. Only the reliable electrical contacting could not yet be achieved. This is however considered to be solved in the near future. Preparations to operate a prototype CND detector have been made and further test will be carried out in future work by Martin Uffinger and Igor Usherov-Marshák.

The following issues remain to be addressed by experiments with such a prototype detector, before attempting to build a larger scale setup:

- The actual size of the phonon signal should be measured and compared to the theoretical expectation. Therefore it is suggested to use Tungsten films with lower T_c than the ones utilized in this work to maximize the thermal signal. Also the phonon-signal resolution in the keV recoil-energy range should be determined.

- The TES carrier material should be selected such that phonon transmission from the absorber to the thermometer carrier is maxed. Up till now only the gluing of Sapphire carriers has been tested.

- The holder design could be optimized: To enhance the light collection efficiency, the inner volume should be covered with scintillating foil. Also the distance to the light detector could be reduced. The lower part of the capsule could be thermally decoupled from the upper part, which would allow more flexibility in the choice of T_c for the two TES sensors.

- For larger sized NaI absorbers ($\mathcal{O}(250\,\text{g})$) self absorption of the emitted light might lead to a position dependence in the light output. This should be tested, preferably at the Gran Sasso test facility as the muon rates in shallow labs might be to high for large crystals. This could be done by varying the position of a collimated source inside the detector housing. Larger crystals are preferable to minimize the readout channels in a DM-detector array.

Running four large CNDs in CRESST or EURECA, the planned next generation DDMS experiment of all European solid state DM collaborations, would already be enough to obtain exposures large enough to directly check the DAMA claim *using the same target material*. The impact of the model dependent assumptions entering the exclusion limits presented in figs. 1.18 and 1.20 could thus be verified experimentally. If such an experiment will not detect WIMP recoils compatible with the DAMA signal it would be very likely that the DAMA events are related to electromagnetic interaction, which would be very intriguing.

4

Lithium Fluoride as multipurpose bolometer?

Lithium Fluoride is a common material for slow neutron detection due to the large neutron cross section for the isotope ^{6}Li, which is present in natural Lithium at 7.59 % abundance [139]. The thermal cross section[1] is reported to be 940 ± 4 b by [141, 142]. Since neutrons are a dangerous background for direct DMS experiments, this chapter will examine if LiF can be used as an absorber in a CRESST-like experiment to monitor neutrons. Sec. 4.1 will explore the question, if such a detector can provide extra knowledge of the actual neutron background in a specific setup, while sec. 4.2 will discuss if LiF can be used to look for DM interactions as well. This is especially of interest, as Fluorine is a sensitive target for spin-dependent interactions. In order to examine this, the light yield and decay time measurements performed in this work will be presented. All results will be summarized and discussed in sec. 4.3.

4.1 A LiF bolometer as a neutron detector

A precise knowledge of the neutron background in a DM experiment will be crucial, once a signal is encountered and it's origin needs to be clarified. Since LiF is a material well known for it's excellent neutron detection properties due to the large neutron cross section of ^{6}Li, the idea to use such crystals as low temperature bolometers inside a cryogenic DM experiment is obvious.
There have been reports by Smith et al. [143] on a thermal neutron capture peak in a LiF bolometer which triggered de Marcillac et al. [144] to study this in detail with a 2 g LiF single crystal. Their findings will be summarized in this section.

The main channel contributing to the large neutron cross section of ^{6}Li is the capture of neutrons as

$$n + {}^6\text{Li} \rightarrow \alpha + {}^3\text{H} \tag{4.1}$$

with a Q-value of 4,782.1 keV. Fig. 4.1 gives the cross section for the reaction (blue solid line) and the total neutron cross section (black dotted line). The thermal cross section is marked with the red dashed line. Neutrons with incident energies within the gray shaded region can produce Oxygen and Tungsten recoils in the range of 10–40 keV. Since this is the WIMP search region for CRESST (see sec. 1.2), those are the most dangerous background neutrons. The integrated ^{6}Li(n,α)^{3}H cross section for those events is 1.79 barn. The value for the total cross section in this energy window is 5.10 barn where the biggest additional contribution is the elastic channel.

With a 2 g LiF bolometer, operated below 100 mK, de Marcillac et al. [144] have demonstrated an energy resolution of 16 keV at the Q-value energy of the neutron capture reaction. This is a signal that can be easily identified using the phonon signal only, as it lies well above the highest natural γ lines. In order to compare the LiF phonon signal to CaWO$_4$ data one can again make use of the estimate introduced in sec. 3.1.1 using the Debye temperature of LiF reported as 722 ± 6 K by [146]. This is about a factor of 2.9 more than for CaWO$_4$. Following eq. 2.2, one expects about 25-times the signal of CaWO$_4$ which is perfectly measurable.

---

[1]The thermal neutron energy is the energy at which neutrons are in TDE with their surrounding. The value is given as $(1/40)$ eV, see e. g. [140]
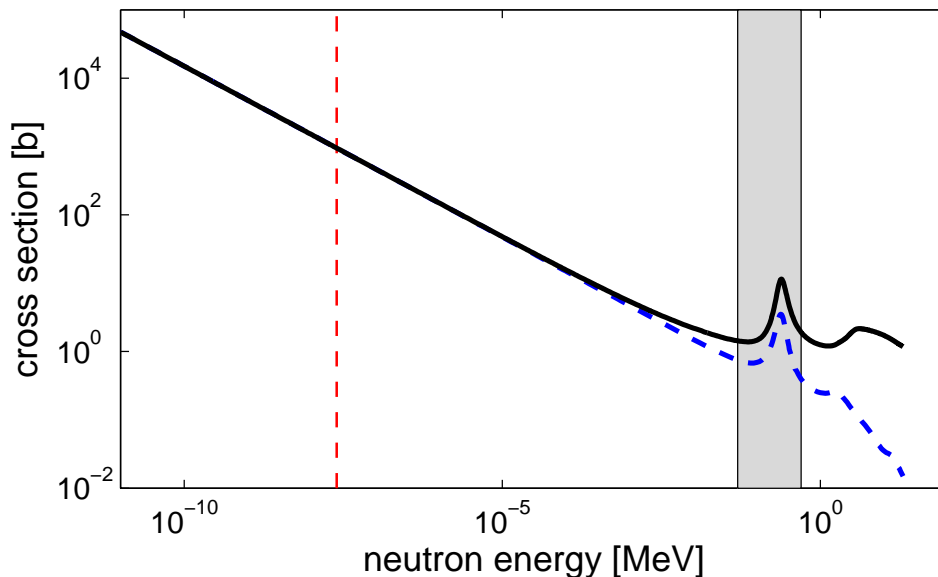
Figure 4.1: Total neutron cross section (black solid) for ^{6}Li and cross section for ^{6}Li(n,α)^{3}H (blue dashed line). The value for thermal neutrons is marked with the red dashed vertical line. The gray shaded area indicates incident neutron energies that produce Tungsten recoils in the range of 10–40 keV which are especially dangerous for CRESST. Data provided by ENDF [145]

For thermal neutrons the α and the ^{3}H are emitted back-to-back. Their total range does not exceed 50 μm, thus they are fully contained within the crystal [144]. This still holds for the gray-shaded energy region in fig. 4.1.

There are basically two ways in which such a LiF cryogenic bolometer could contribute to an improved understanding of the neutron background in a direct DMS experiment:

(a) The measured total rate of neutrons in the setup or the thermal neutron rate exclusively could be used to calibrate Monte Carlo simulations or to monitor the tightness of the PE shielding

(b) The detector could be used as a veto since neutrons can scatter multiple times within the setup. They will be degraded in energy by depositing energy on a CaWO$_4$ module (or other material) and can consecutively be captured by a LiF absorber. Of course the veto information will strongly depend on the geometrical factor and the mean residence time of the neutrons within the setup due to reflections in the PE shield.

Considering case (a) first, it has been shown by Smith et al. [143] and de Marcillac et al. [144] that the thermal neutron rate can indeed be measured. Using the measured and simulated neutron "bath" spectra for the ambient and cosmogenic neutrons at an experimental site, the moderated spectrum inside the shielding of the respective experiment could be simulated and the thermal flux could be compared to actual measured values. However care has to be taken when analyzing the thermal neutron peak as there can be multiple α lines of the Radium series present nearby due to radioactive contaminations. This is shown in figs. 4.2 and 4.3: The lines in fig. 4.2 were observed in early 2004 with a 300 g CRESST-II prototype detector module [48] and can be attributed to internal contaminations of the crystal itself - the only exception is the ^{210}Po peak labeled "extern" which is a result of Radon decaying on the crystal's surface (see sec. 1.2). Fig. 4.3 shows the relevant decays for the energy region discussed here:
The α decay of ^{226}Ra $\rightarrow ^{222}$Rn$+\alpha$ gives a line at 4,784 keV, which overlaps strongly with the thermal Lithium

peak, assuming the energy resolution of 16 keV by de Marcillac et al. However they report a shift in the thermal peak position of - 30 keV compared to the expected value when calibrating with external α energies which they can only partially explain by energy loss due to light emission. This might remedy the situation. There is also the possibility to estimate the contribution of the ^{226}Ra alpha counts to the thermal peak: As fig. 4.3 shows, the half life of ^{230}Th is roughly 47 times larger than that of the daughter nucleus ^{226}Ra. Therefore one can assume that the two decays are in secular equilibrium as there is no other contribution to the population of ^{226}Ra. Thus one can derive the Radium event's contribution to the thermal peak using the number of counts observed in the ^{230}Th line at 4,687 keV.
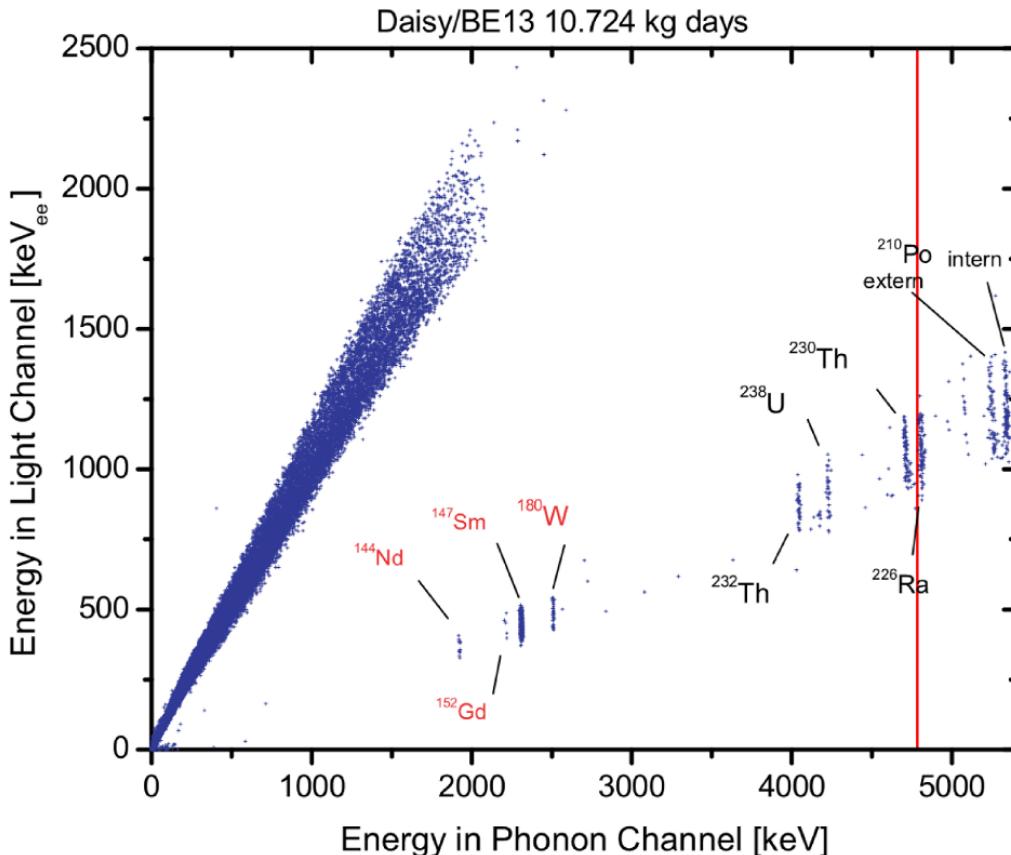
Figure 4.2: The α background measured in CRESST-II as reported in [48]. The red line indicates the Q-value of the ^{6}Li(n,α)^{3}H reaction.

Although measuring the thermal neutron rate can be valuable information it would be more useful to measure the rate of neutrons in the energy interval from 50–500 keV, as those can produce recoils in the WIMP region of interest (ROI) of CRESST that are indistinguishable from recoiling light WIMPs. As explained in sec. 1.2 those neutron induced recoils can be estimated by carefully analyzing the Oxygen scatters at higher energies. A LiF neutron detector should thus be able to detect higher neutron rates in the ROI than a standard $CaWO_4$ bolometer, since it would occupy one "slot" in the experiment that could also be used for a DM module. Therefore fig. 4.4 shows a comparison of the neutron cross sections for ^{6}Li and ^{16}O. In principle also ^{7}Li, ^{19}F and the heavier target nuclei of $CaWO_4$ should be considered, yet those cross sections are dominated by elastic scattering. Unlike the ^{6}Li(n,α)^{3}H channel elastic scattering does not produce a distinct feature that can be attributed to neutrons alone. Even if the induced recoils on those nuclei could be detected and discriminated form electromagnetic background there would be little gain: The recoils could still not be distinguished from light mass WIMP events. Thus it is enough to compare the inelastic ^{6}Li reaction and
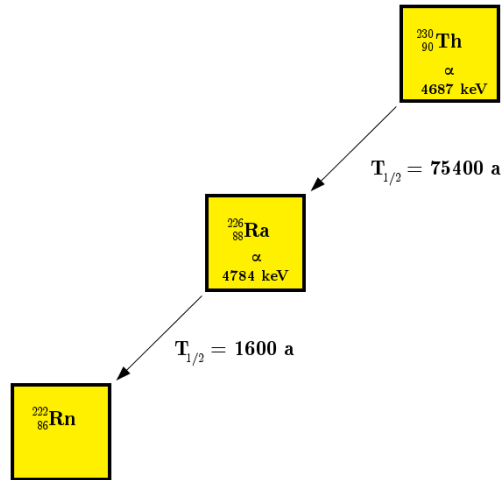
Figure 4.3: Radium series α-emitters with α energies near the ^{6}Li(n,α)^{3}H Q-value and their respective half lives. The Q-value is marked by the red line.

the total cross section of ^{16}O. The cross section for ^{6}Li(n,α)^{3}H integrated over the relevant energy range is 1.79 b, the respective value for ^{16}O is 5.91 b. A standard module of ~ 300 g CaWO$_4$ contains roughly 4 mol Oxygen, while a LiF crystal of similar weight contains only ~ 1 mol of ^{6}Li. The total rate R can be calculated following

$$R = \sigma \Phi_n N_t \tag{4.2}$$

with the incident integrated neutron flux Φ_n and the number of target nuclei N_t. The ratio between the number of tagged neutrons of the relevant energy in LiF and the total rate of Oxygen scatters observed in the CaWO$_4$ is independent of the flux and can thus be estimated with the above numbers to a value of 0.076. Therefore it is much more favorable to add another CaWO$_4$ module to the setup.

Scenario (b) concerns the question if a LiF bolometer can be used as a veto detector. Since the relevant neutron cross sections are high enough to allow multiple scatters in the experiment, this needs to be examined further. Also Angloher et al. [55] have shown, that neutrons produced by muons exhibit a higher multiplicity spectrum than ambient neutrons, as they are showering events, hitting multiple detector modules within a short timescale. This is shown in fig. 4.5. If the cosmogenic neutrons are produced after the muon has passed the muon veto, these events will be easily identified. If they are however produced in the vicinity of the experiment, they can penetrate the shielding and cause recoils in the Oxygen band. This is possible as the incident energies can be too high to be moderated below threshold by the PE shield. A spectrum of cosmogenic neutrons measured at LNGS by the LVD (Large Volume Detector) collaboration can be found in fig. 4.6.

Using the tagged neutrons from the ^{6}Li(n,α)^{3}H reaction all coincident events in the Oxygen band of CaWO$_4$ could be clearly identified as neutrons. However this is true for all coincident events as well, as the chances of a double scattering of WIMPs are extremely small. So the question remains, if a LiF detector can out-perform a CaWO$_4$ module. As already shown, this is not the case if one compares the capture reaction on Lithium and the total cross section of Oxygen. Yet on does not have to restrict oneself to the capture events. Every recoil above threshold can be considered, which is why also the ^{7}Li and ^{19}F neutron cross sections will contribute. The cross sections for all relevant isotopes of LiF and CaWO$_4$ integrated over the energy range of 50–500 keV can be found in tab. 4.1. The Calcium isotopes with less than 3 % natural abundance have been neglected. The respective values for N_t in units of the Avogadro constant for a 300 g crystal are also given. Adding up the rates using eq. 4.2 for CaWO$_4$ and LiF one can again take the ratio between the two which yields 0.30. Thus the LiF detector will measure roughly 3.3 times the neutron rate of a CaWO$_4$ module at
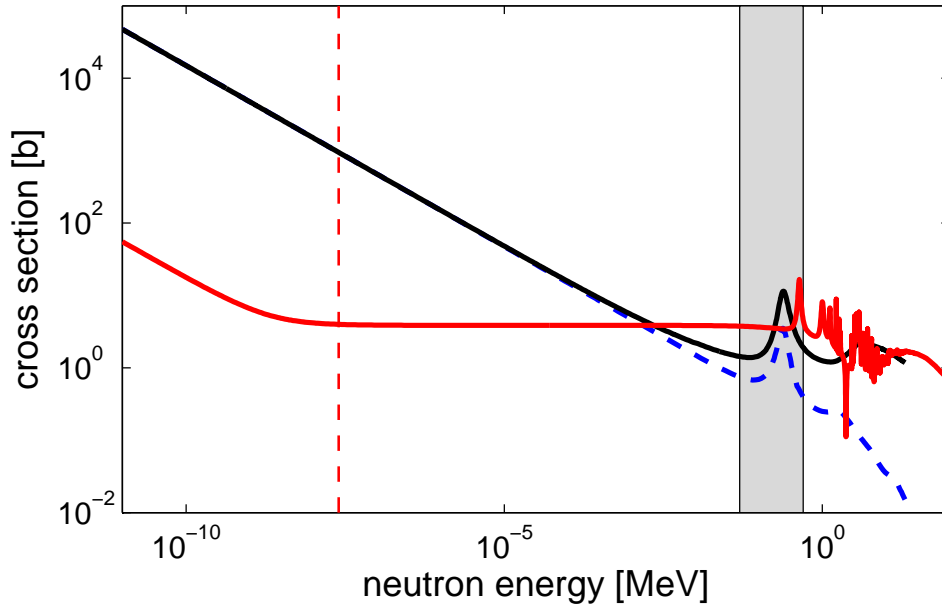
Figure 4.4: Comparison of ^{6}Li and ^{16}O neutron cross sections: As in fig. 4.1 the total neutron cross section for ^{6}Li (black solid) and cross section for ^{6}Li(n,α)^{3}H (blue dashed line). The total cross sections for Oxygen (red solid) has been added. Data provided by ENDF [145, 147]
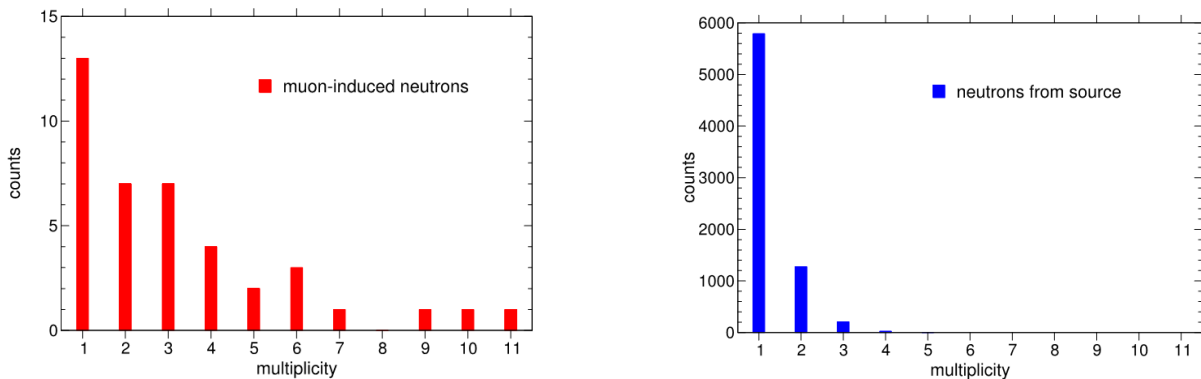
Figure 4.5: Multiplicities of cosmogenic (left) and ambient/"source"-like (right) neutrons in CRESST. Note that for the ambient spectrum a calibration source was used, thus the high statistics. [55]
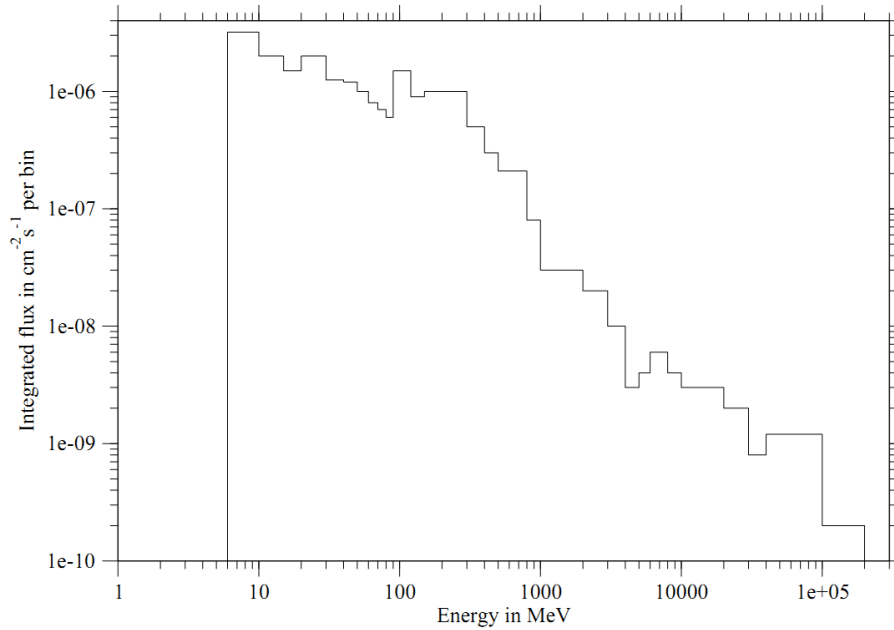
Figure 4.6: Cosmogenic neutron spectrum at LNGS. Data by Dementyev et al. [148], interpreted by Scholl [149]

comparable incident neutron flux. In addition the probability for a neutron to get captured on ^{6}Li will be enhanced further for second scatters in LiF, as the neutrons get degraded in energy upon their first recoil and the cross section for the ^{6}Li(n,α)^{3}H channel increases strongly toward lower energies (see fig. 4.1).

isotope	^{6}Li	^{7}Li	^{19}F	^{40}Ca	^{182}W	^{183}W	^{184}W	^{186}W	^{16}O
σ_{int} [b]	5.10	2.47	8.21	4.21	9.65	7.99	8.36	8.34	5.91
N_t [N$_A$] in a 300 g crystal	1.01	10.55	11.57	1.04	0.28	0.15	0.32	0.30	4.17

Table 4.1: Cross sections of all relevant isotopes of LiF and CaWO$_4$, integrated over the energy range of 50–500 keV. The Calcium isotopes with less than 3 % natural abundance have been neglected. The respective values for N_t in units of the Avogadro constant for a 300 g crystal are also given.
Data by ENDF [145, 147, 150–156]

A LiF bolometer will thus increase the fraction of multiple scattered events. Yet one loses one DM-sensitive module in return – unless LiF produces sufficient light to allow for particle discrimination at low recoil energies. This will be studied in the next section.

Since the LiF detector would be located near the CaWO$_4$ modules, radiopurity of the crystal itself and the build-up of the beta emitter Tritium is also of concern. For a LiF doped with 1 % of Tungsten Belli et al. [158] report a 90 % C.L. upper limit on the total activity of less than 13 mBq/kg which is comparable to the average CRESST crystals.

The build-up of Tritium can be estimated as follows: Using the LNGS neutron flux for cosmogenic (see fig. 4.6) and ambient production (see fig. 4.7) reported by Wulandari [157] and Scholl [149] and the cross section values for the ^{6}Li(n,α)^{3}H reaction one can calculate the expected rate for a 300 g detector. A low value of $\sim$ 73 counts/yr is obtained. However this is only a lower limit, as the unmoderated spectra were
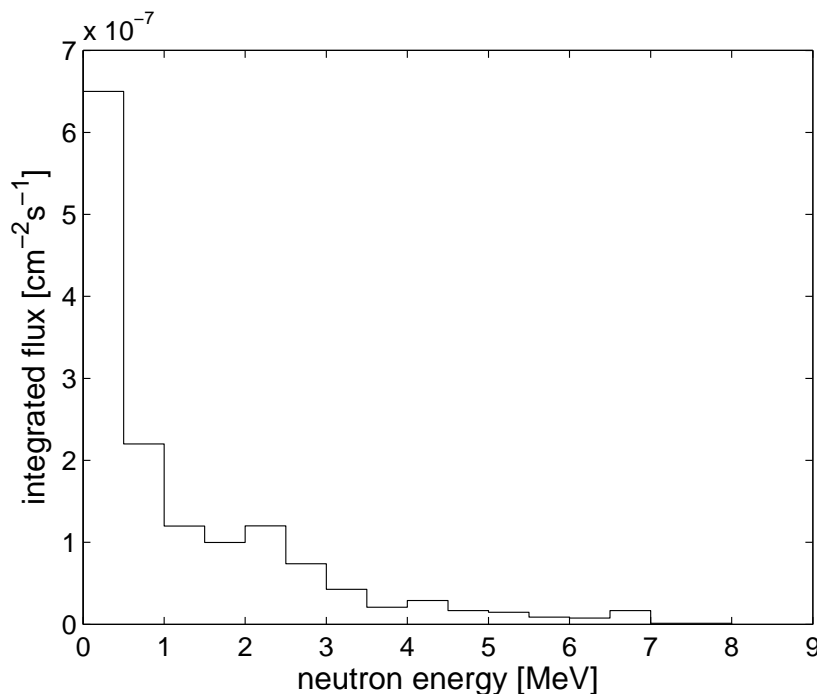
Figure 4.7: Simulated ambient neutron spectrum at the CRESST experiment after Wulandari [157]. Extrapolation to lower energies by Scholl [149].

used. The polyethylene shielding will shift the neutron energies to lower values, where the cross section is enhanced. Also the neutron flux will be significantly higher during the necessary neutron calibration campaigns. In fig. 4.5 the total events for such a calibration run are given in the multiplicity spectrum: Roughly 1,000 events per module can be observed in the 10–40 keV region. As the LiF detector will also capture neutrons with low incident energies that can not produce recoils in the $CaWO_4$ ROI, a several thousand ^3H nuclei might be produced.

Yet the half life of Tritium is 12.32 years and the β mean energy is 5.69 keV with an end-point energy of only 18.59 keV [159]. Since the CRESST modules are surrounded by a highly reflective foil, it is quite unlikely for the β particles to reach the $CaWO_4$ absorbers. Only diffusion and consecutive deposition on the crystal surfaces might be a concern. But as most β particles are below threshold and can be discriminated if above, there is no danger to spoil the data. Only when considering a low threshold analysis where particle discrimination is given up, this might become an issue.

4.2 LiF bolometers as dark matter detectors?

As previously discussed a LiF bolometer in a CERSST-like setup will replace a conventional module and thus limit the deployable mass for DM detection. Therefore naturally the question arises if LiF can also be used for DM detection. Then the neutron detector mass would also contribute to the WIMP-sensitive mass. As DM signal are expected in the low energy regime of the recoil spectrum, event-by-event discrimination is needed (see sec. 1.2). Therefore the light yield of LiF at low temperatures needs to be studied. Analogous to NaI the crystal structure of LiF is similar to that of Sodium Chloride (face-centered cubic, fcc). As discussed in sec. 3.1.2 these crystals tend to form V_k centers which is why their luminescent behavior is usually governed by STE emission. This is also true for LiF, however it's LY is strongly reduced by strong resonant absorption and reemission of the STE luminescence, as has been shown in [160].

Only a limited amount of data is available on the light output of LiF at low temperatures, published by Golovin et al. [161], de Marcillac et al. [144] and Lisitsyna et al. [160]. Golovin et al. have measured the temperature dependent luminescence of pure LiF crystals that were populated with color centers by irradiating the crystal with a strong ^{60}Co source down to 4 K temperature. They report two rather slow decay times with 14 ms and 1 ms where the broad spectrum of the first component peaks in the optical at 380 nm and the more pronounced spectrum of the latter one in the UV region at 220 nm. The "fast" component is reported to rise below liquid Nitrogen temperature and to saturate at around 40 K. Following Golovin et al. [161] it dominates at low temperatures.

The reported decay times are somehow in tension with results given by Lisitsyna et al. [160] who studied short-lived primary radiation defects in LiF in the temperature range of 11–150 K in a pulsed electron-beam setup. For the dominant emission at 220 nm at 11 K they derive 30 μs and 700 μs. They also found a more or less temperature independent long decay time with 8 ms at 354 nm. For the total light intensity the findings of Golovin et al. are confirmed: A rising light output setting in between 60–80 K and saturating at around 40 K.

De Marcillac et al. [144] also studied the LY of pure LiF at eight temperatures between 2 K and 50 K and find a similar behavior as Golovin et al., yet they observe the rise in light output only below 30 K. The authors suspect this to be caused by a temperature offset due to the indirect thermal coupling of the sample and the cryostat. However they could derive absolute light efficiencies for γ and α-excitation by comparing the values to a calibrated CaF_2(Eu) crystal. For a mean α energy $E_\alpha = 5.4$ MeV they state a light efficiency of 0.30 ± 0.06 % of the deposited energy. Using the 220 nm reported above and the stated uncertainties of de Marcillac et al. one can thus calculate an estimated α-LY of 530 ± 80 (ph/MeV) at a temperature of ~ 2 K.

As the LY of different crystal samples can vary significantly, e.g. due to trace impurities, and since there was no additional data available to check these findings, it was decided to use the optical setup presented in ch. 3 to measure the temperature dependence of the LY of LiF. If the light output of LiF is sufficiently high, a LiF detector could be used as a multipurpose bolometer: Measuring the neutron rate directly inside a DMS experiment while the recorded events at low energies can simultaneously be included in the WIMP search analysis.

4.2.1   Light yield measurements of LiF at low temperatures

Two samples of $(0.9 \times 1.4 \times 0.1)$ cm^3 size, kindly provided by B. Lubsandorzhiev, were available for measurements. One was synthetically grown, the other one cut out from a natural sample. Both samples were placed such inside the cryostat that the (0.9×1.4) cm^2 surfaces were facing the PMTs, as fig. 4.8 illustrates. To stimulate the luminescence of the crystals α-particles of a collimated ^{241}Am source were used. Note that due to the positioning of the ^{241}Am source the solid angle for PMT 1 was slightly reduced. Since Golovin et al. reported decay times in the ms regime, the collimated α rate was checked by using plastic scintillator and PMT 2 in direct contact with the source by setting a threshold above the 60 keV γpulses. A rate of 850 ± 50 s^{-1} was measured which does not cause significant pile up for decay times shorter than 250 μs, yet would be problematic for decay times in the range reported by Golovin et al.. The available SIS-3301 FADC module is not suited for measuring traces on the order of milliseconds, as the maximum usable record length allows to record signals with 655 μs. Assuming the 1 ms decay time of Golovin et al. to be the only scintillation component, this would record about 40 % of the total signal. Some test cooldowns were performed, varying the record length from 20 μs to the maximum value. No significant variation in the obtained LY results at different record lengths was observed. It therefore seems unlikely, that a long decay time on the order of a few milliseconds contributes significantly to the LY of LiF which is why 20 μs was selected as record length for the presented data. Yet it is important to check the effect of even longer sampling times on the result. Therefore another FADC suitable for measurement of longer decay times than 655 μs has already been installed and measurements with longer record lengths are currently performed by M. Uffinger and B. Cebeci, to check if

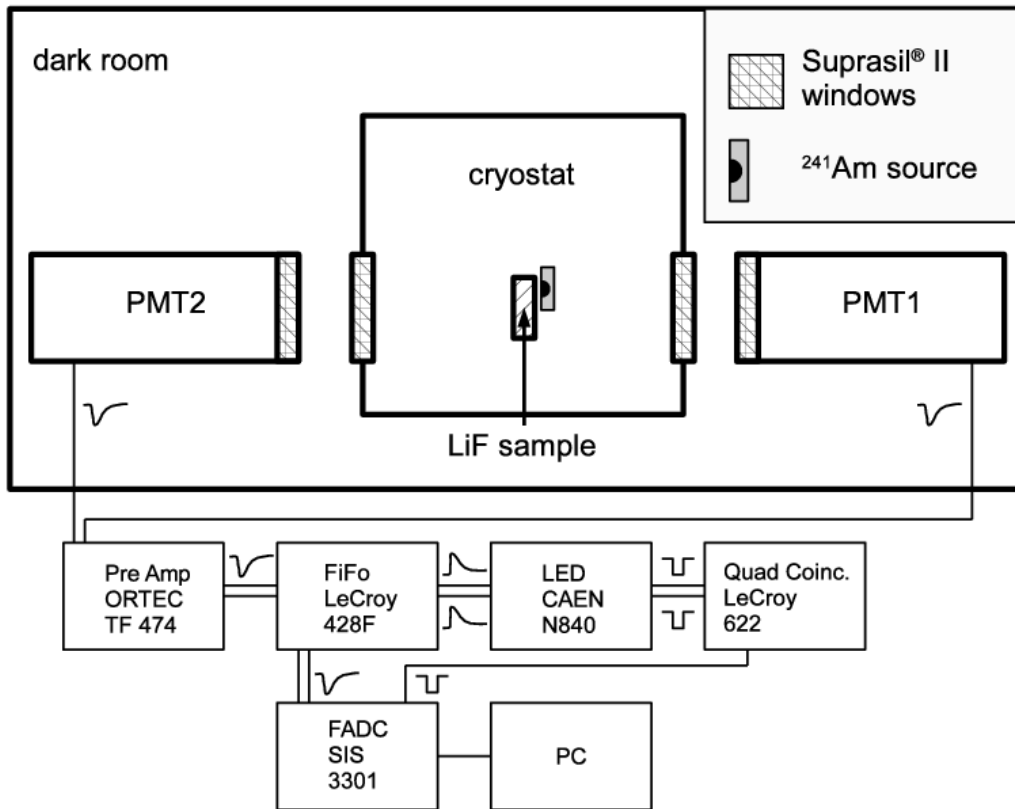there is indeed a very slow component contributing to the LY.

Figure 4.8: Setup for the LiF light yield measurement. Note that due to the positioning of the ^{241}Am source the solid angle for PMT 1 is slightly reduced. Therefore lower values for the mean number of detected p.e. are expected for PMT 1. The TF pre-amplifier module was used to build a low pass filter by integrating to reduce radio pickup noise.

As LiF is not hygroscopic, handling is much easier compared to NaI. Yet measuring the light yield is more challenging. Even for excitation with 5.486 MeV α-particles only single photo electron (p.e.) traces can be observed, as shown in fig. 4.9. Those events were registered at 3.9 K near the maximum of the light yield curve, as will be discussed below. Therefore a slightly different approach as described for NaI (see sec. 3.2) was chosen: Two PMTs at comparable gain were operated in coincidence, using a threshold below 1 p.e. and the respective traces were recorded by the FADC for offline analysis. The TF pre-amplifier module (see fig. 4.8) was just used to build a low pass filter by integrating to reduce radio pickup noise. The coincidence logic is the same as discussed in sec. 3.2.2. Here the coincidence was used as an effective filter to discard single p.e. events that are caused by the PMT's dark current. The random coincidence rate due to two dark current electrons within the coincidence window of $\Delta t = 100$ ns can be easily be calculated with $R_{DC1} = 1,200$ Hz and $R_{DC2} = 300$ Hz as

$$R_{rand} = R_{DC1} \cdot R_{DC2} \cdot \Delta t = 0.036 \, \text{s}^{-1} \tag{4.3}$$

This leads to errors less than 0.5 % below 150 K and a maximum of 3.5 % at room temperature as the LiF light emission at high temperatures is strongly suppressed which increases the measuring time significantly.

For both samples 1,280 events were stored at each temperature and the elapsed measuring time was also
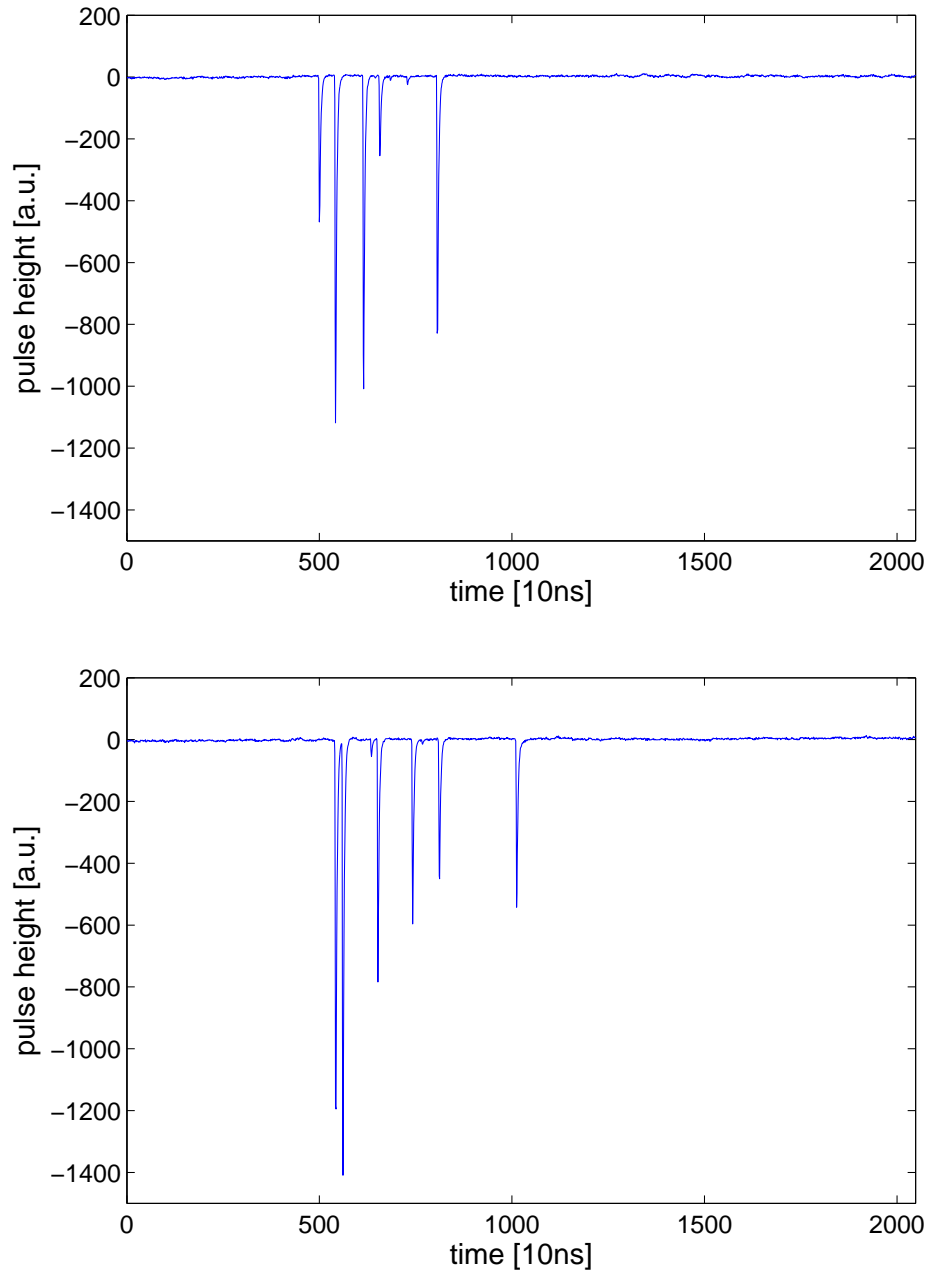
Figure 4.9: Two exemplary α-induced scintillation events in LiF at 3.9 K. Only a succession of single p.e. events can be observed.

recorded to allow to estimate the random coincidence contribution to the data. To determine the LY in the offline analysis the threshold for accepted p.e. peaks was chosen as follows: A peak detection algorithm was used to check for signals below baseline noise level. All peak values were registered and stored in a histogram such as shown in fig. 4.10. The histogram shows the pedestal at low pulse height values and the 1 p.e distribution for PMT 2, recorded at high temperatures, where only about 1 p.e. per trace is detected. As the pedestal and 1 p.e. positions are fixed at all temperatures the threshold can be set to the minimum between both distributions. This is indicated by the red dashed line. All pulses above this value are accepted as valid photo electron counts, unless a FADC overflow event is detected by a dedicated cut. The respective p.e. number detected per FADC trace is then used to derive a mean value Y for each measured temperature. The statistical error can easily be derived as $\Delta LY_{stat} = \sigma_Y/\sqrt{N}$, where N is the number of accepted pulses. The result for the synthetic sample can be found in fig.4.11, the temperature dependent LY curve for the natural crystal is shown in fig. 4.12.
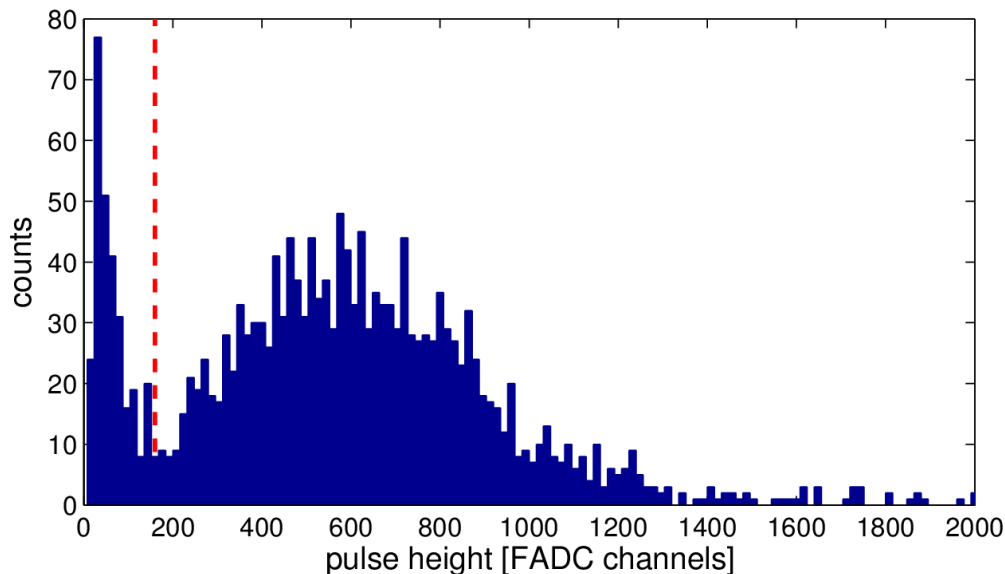
Figure 4.10: Exemplary plot for the selection of the offline threshold for the LiF light yield measurement (here PMT 2 at 8 K). The histogram shows all the pulse heights above baseline noise level registered by the peak detection algorithm. The pedestal an the p.e. distribution can be easily identified and the chosen threshold is indicated by the red dashed line.

For synthetic LiF the light yield starts to increase gradually below 60 K, reaching a plateau at around 40 K. This agrees perfectly with the behavior reported by Golovin et al. [161]. Yet at around 6 K a sharp maximum peaking at 4 K and the dropping fast again is encountered in this work. Preliminary measurements with the new setup that allows for longer record lengths seem to confirm the enhancement at 4 K yet yield a stronger relative rise around 60 K, resulting in a less pronounced feature 4 K [162]. It is therefore concluded that the decay time of the component responsible for the rise at around 60 K is slowly decreasing with temperature, thus leading to higher fractions of detected p.e. of the total emitted number during the relatively short recording times. It would thus be desirable to also measure the temperature dependence of the LiF decay times. First results on this will be presented in the next section. As fig. 4.11 also shows, the data of PMT 1 and PMT 2 agrees well, keeping in mind the slightly reduced solid angle for PMT 1. Errors given are statistical and systematical ones combined. The larger errors at higher temperatures are mainly due to the increased random coincidence contribution as the measuring time for the 1,280 events increases strongly due to the low light output. The maximum of the relative increase in LY for the synthetic sample yields a factor of 2.2 between 200 K and 4 K. Varying the threshold for p.e. detection did not affect this value.
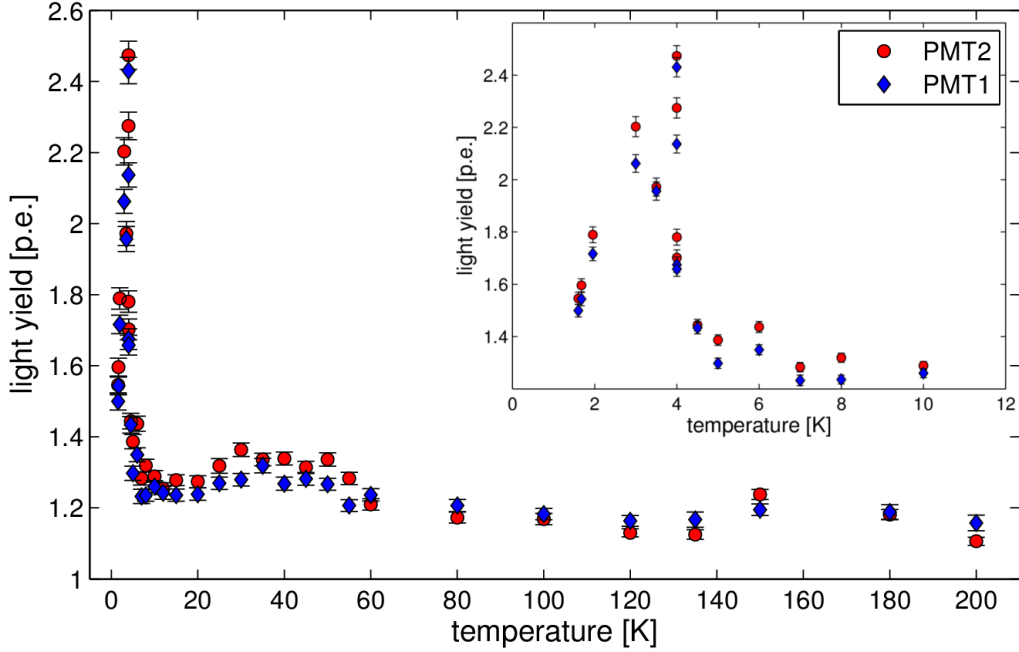
Figure 4.11: Light yield of ^{241}Am α-particles in synthetically grown LiF over temperature. Data as observed by PMT 1 (blue diamonds) and PMT 2 (red circles). Total errors are given. The inset shows the sharp maximum found at around 4 K.

For the natural LiF sample the same overall behavior of LY(T) than for the synthetic crystal can be observed. Yet the initial increase in LY seems to occur already at higher temperatures around 120 K. Also it was possible to determine the light output at room temperature within reasonable timescales which was not the case for the synthetic sample. Again the data for PMT 1 and PMT 2 agrees well, however the suppression of p.e. numbers of PMT 1 compared to PMT 2 is on a higher level as in the synthetic LiF data. Since the source was mounted by hand it can not be excluded that the source holder covered a larger area of the natural sample on the side facing PMT 1 than it did in the measurement with the synthetic crystal. This does however not affect the data of PMT 2. The light yield curve of natural LiF also shows the pronounced peak at around 4 K which leads to the conclusion that this is due to the lattice properties of LiF and not caused by trace impurities.

To compare the light yield of the two samples, fig. 4.13 shows both curves using a logarithmic scaling of the temperature axis to enhance the LY maxima at low temperatures. To exclude effects of the source blocking different fractions of the crystals only the PMT 2 data is used. Both samples yield very similar results. For intermediate temperatures above 80 K the natural crystal performs slightly better. Yet it seems safe to state that there is no significant difference in the overall performance.

As the number of detected p.e. is proportional to the absolute light yield, the data was scaled by carefully considering the uncertainties involved. The PMTs used in this work were calibrated individually by ETL, so the quantum efficiencies (q.e.) are known and can be averaged over the relevant part of the spectrum – the latter being chosen following the curve reported by Golovin et al. [161]. For PMT 2 one obtains $\eta_{q2} = (25.1 \pm 0.2)\,\%$. The solid angle is defined by the 38° opening of the cryostat windows to

$$\Omega = 2\pi(1 - cos(\omega/2)) = 0.34\,\mathrm{sr} \qquad (4.4)$$

thus $(2.7 \pm 0.3)\,\%$ of the total emitted light can be detected per window. The error is derived from the uncertainty connected with geometrically reconstructing the solid angle using the to-scale technical drawings.
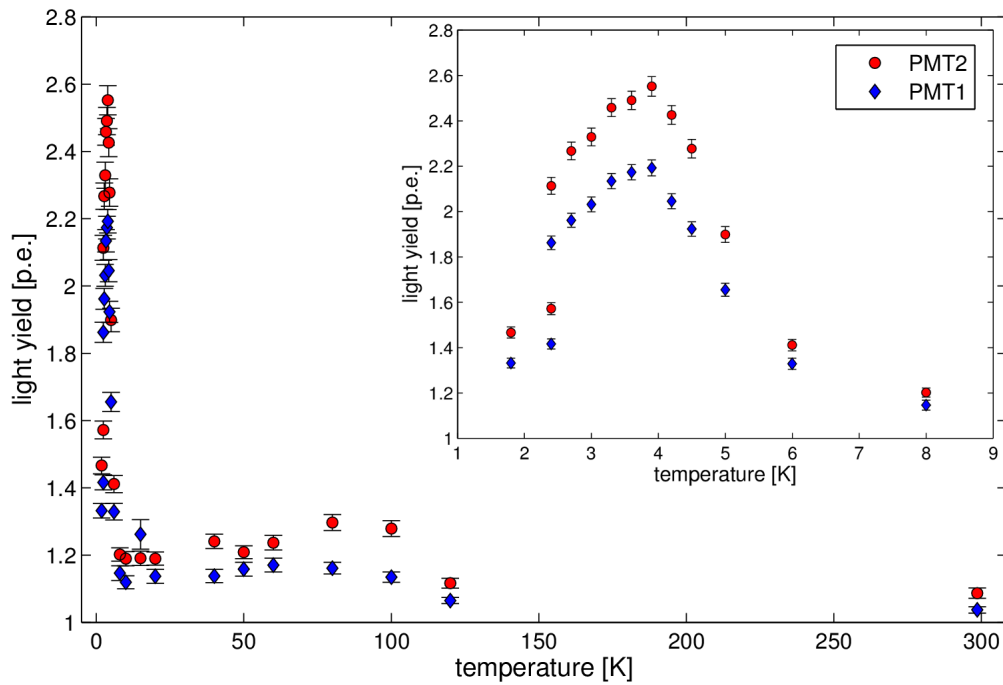
Figure 4.12: Light yield of ^{241}Am α-particles in natural LiF over temperature. As in fig. 4.11 the data for PMT 1 (blue diamonds) and PMT 2 (red circles) are depicted. Also here total errors are given. Like the synthetic crystal the natural sample exhibits a sharp maximum at around 4 K, which is shown in the inset.
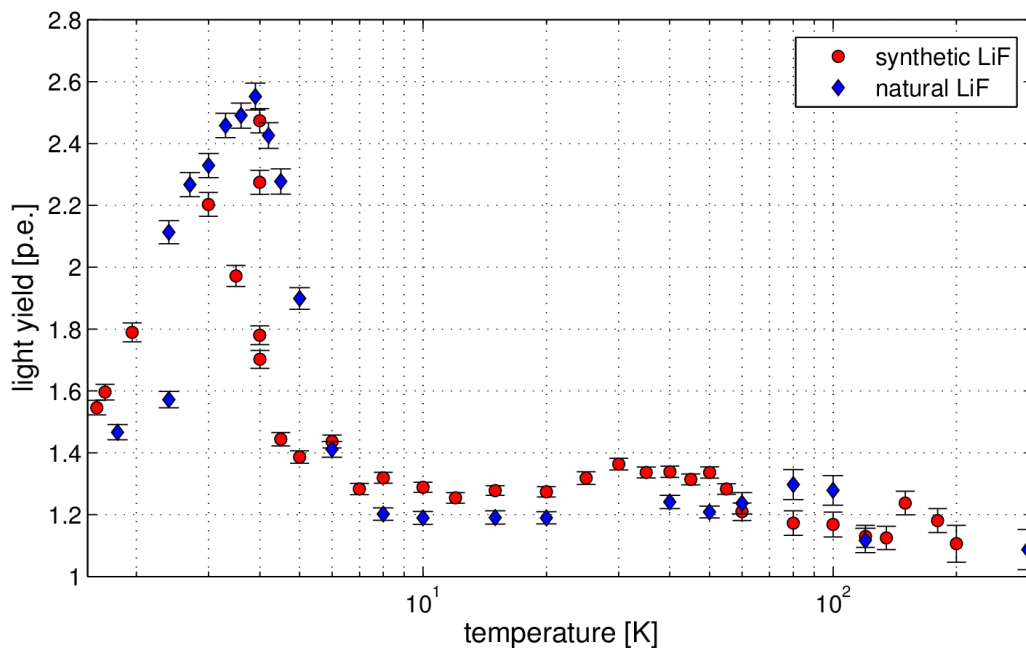
Figure 4.13: Comparison of the light yield of natural (blue diamonds) and synthetic LiF (red circles) upon α-excitation of ^{241}Am. As before, errors are only statistical and as such only lower limits. The temperature axis is displayed in logarithmic mode to enhance the LY maxima at low T. The general temperature dependence agrees well for both crystals.

As a last step the transmittance of the three Suprasil® II windows and the PMT quartz glass window need to be considered. For the relevant part of the spectrum the manufacturer states $92 \pm 1\%$. Using the values and uncertainties given in fig. 4.13 one can thus obtain the total α-LY numbers of $450 \pm 50\,(\mathrm{ph/MeV})$ for the synthetic sample at $1.6\,\mathrm{K}$ and $420 \pm 50\,(\mathrm{ph/MeV})$ for the natural LiF at $1.8\,\mathrm{K}$. This agrees very well with the $530 \pm 80\,(\mathrm{ph/MeV})$ at $\sim 2\,\mathrm{K}$ derived earlier from the data of de Marcillac et al. [144]. The absolute light yield in the maximum at $4\,\mathrm{K}$ for the natural LiF crystal corresponds to $730 \pm 80\,(\mathrm{ph/MeV})$. As de Marcillac et al. also give the ratio of γ/α-light emission as 2.4, the light yield of LiF at $4\,\mathrm{K}$ for γ-excitation is thus calculated to be $1,750 \pm 190\,(\mathrm{ph/MeV})$ and $1,010 \pm 120\,(\mathrm{ph/MeV})$ at $1.8\,\mathrm{K}$.

Since the comparison of all available LY(T) data suggests a significant reduction of the decay time constants involved, TDC measurements were performed at different temperatures. Results will be presented in the next section.

4.2.2   Decay time measurements in LiF

A fast TDC with $75\,\mathrm{ps/ch}$ time resolution and a range of a few μs was used to study the decay times in the already presented natural LiF sample upon α irradiation. Although the values $\tau_1 = 1\,\mathrm{ms}$ and $\tau_2 = 14\,\mathrm{ms}$ reported by Golovin et al. [161] suggest that such a fast TDC should not be suited the LY results with $20\,\mu$s record time were suggesting that there is also a fast decay involved in the scintillation process – at least at temperatures below $80\,\mathrm{K}$. The arrangement of crystal and PMTs was similar to the LY setup (see fig.4.8), yet PMT 2 was moved back from the cryostat until 0.25–0.30 p.e. were detected on average. Setting a ~ 3 p.e. threshold on PMT 1 as a *start* signal for the TDC and using the signal of PMT 2 as *stop* signal data was recorded in the range of $2\,\mathrm{K}$ to $60\,\mathrm{K}$. For each temperature the spectrum, as shown in fig. 4.14, was fitted using one and two exponential decays, as well as varying the onset of the decay in the spectrum for each model to estimate the decay time uncertainty. Over the whole range the fit always favored the one exponential-only values. Where the two exponential fit converged and gave reasonable results there was always a slow component with maximum values between 1–18 ms involved. The value for the fast decay time derived with the one exponential fit is $5 \pm 0.8\,\mathrm{ns}$. As far as known to the author, this fast decay has not yet been reported anywhere. Measuring the TDC spectrum at $60\,\mathrm{K}$ was already challenging due to low event rates. Above this temperature no measurement was possible anymore. It is thus concluded that the fast decay is associated with the increase of the LY observed in LiF when cooling below $60\,\mathrm{K}$. Interestingly also Lisitsyna et al. [160] report their measured decay times to be nearly temperature independent below $150\,\mathrm{K}$. The fact that they did not observe the fast decay measured in this work might be attributed to the pulse electron-beam technique used in their work: The authors claim to have covered the time interval of 10^{-8}–$10\,\mathrm{s}$ after pulse excitation, which barely misses the component reported here.

4.3   Discussion and conclusions

In conclusion the data for the LY of LiF at low temperatures obtained in this work agrees well with the already published findings. It is confirmed that the initial increase in light output occurs when cooling below $60\,\mathrm{K}$, as reported by Golovin et al. [161] and Lisitsyna et al. [160]. The general LY(T) behavior is also consistent with de Marcillac et al. [144], considering the large temperature uncertainty assumed by the authors. The luminescence maximum at $4\,\mathrm{K}$ has not yet been reported anywhere: Yet it should be kept in mind that the relative increase in LY might actually be smoothed out when increasing the sampling time. This is suggested by recent data by Uffinger [162]. It can be safely concluded that the LY enhancement at low temperatures is at least partially connected to the fast decay with $\tau = 5 \pm 0.8\,\mathrm{ns}$, that has also been measured for the first time in this work. The fact that it is nearly temperature independent below $60\,\mathrm{K}$ is in line with the findings of Lisitsyna et al. [160] for the longer decay times in this temperature regime.

The absolute LY for α-irradiation has been determined to $450 \pm 50\,(\mathrm{ph/MeV})$ for the synthetic sample at $1.6\,\mathrm{K}$ and $420 \pm 50\,(\mathrm{ph/MeV})$ for the natural LiF at $1.8\,\mathrm{K}$ which agrees very well with the $530 \pm 80\,(\mathrm{ph/MeV})$ at $\sim 2\,\mathrm{K}$ derived from the data of de Marcillac et al. [144]. Besides a slightly better light yield at temperatures
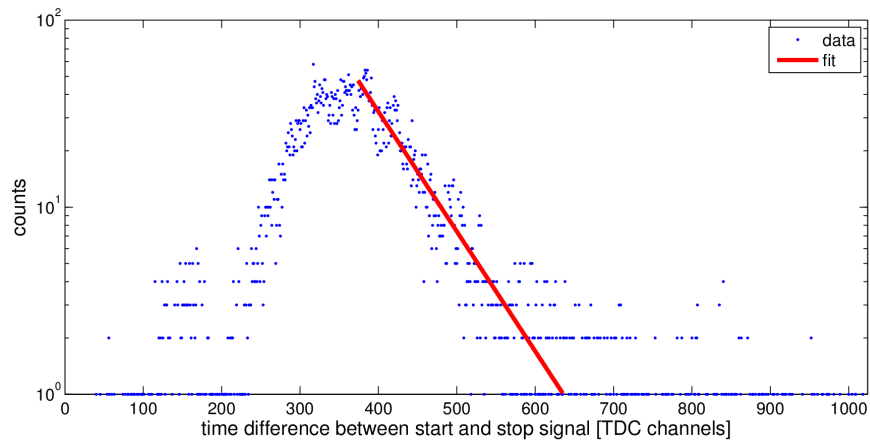
Figure 4.14: Decay time spectrum of LiF at $12\,\mathrm{K}$ for fast scintillation light. The time histogram shows the time difference in TDC channels of the first p.e. signal detected by the *start* PMT to the second p.e. pulse registered in the *stop* PMT. TDC data is given in blue, the one exponential fit in red. The derived decay time of $5 \pm 0.8\,\mathrm{ns}$ was measured for the whole temperature range from 2–60 K.

around 80–100 K for the natural sample, no significant difference in the light output could be observed. The values obtained for LiF amount to less than $6.5\,\%$ of the LY of $CaWO_4$ which suggests that the use of such crystal as CRESST-type DM detectors is not promising since the particle discrimination at low recoil energies will not be possible.

However the application of LiF as an in-experiment detector for thermal neutrons is possible, as de Marcillac et al. and Smith et al. have shown.
Tagging the dangerous neutron events that produce recoils in the CRESST ROI, using the neutron capture peak events as a veto, does however not seem a viable option. As discussed in sec. 4.2 a standard $CaWO_4$ will yield higher rates when considering multiple scatters. Yet it has been pointed out that one does not need to restrict a veto detector on the capture events: When treating the LiF detector recoil data like the standard CRESST modules, e.g. accepting all pulses as veto event to a coincident scatter in another module, the rate observed in LiF will exceed the $CaWO_4$ by a factor of 3.3.

Operating such a module would however be penalized by losing one DM channel (e.g. $\sim 300\,\mathrm{g}$ target mass) and might introduce additional background into the low threshold analysis region. Since interest in the low mass WIMP sector is still fueled by recent indications for a possible signal, the latter could severely decrease CRESST's abilities to probe that region.
As the information gain does not seem to outweigh the risks and the disadvantages (especially the loss of sensitive mass), the operation of a LiF bolometer in CRESST and EURECA is presently not recommended.

Appendix A

A.1 Floating current source - technical details

Calibration data of the CRESST-type floating current source for an external reference voltage was carried out with an Alcron 2020 Multimeter. Load resistance was $20\,\mathrm{k\Omega}$, consisting of four resistors with $5\,\mathrm{k\Omega}$ at 1% tolerance each. This is comparable to the resistors used in the cold filters described in sec. 2.2. Parameters for conversion can be found in tab. A.1.

Stufe setting	slope [μA/V]	offset [μA]
1	0.20	+0.00
2	1.95	+0.01
3	16.74	-0.40
4	66.83	-2.07
5	95.80	-3.27
6	100.05	-3.25

Table A.1: Calibration parameters for external reference voltages of the CRESST-type floating current source. $I(x) = slope * x + offset$ yields I in μA for x in V. Valid up to $5\,\mathrm{V}$.

Testing the internal reference without a load of $20\,\mathrm{k\Omega}$ shows a linear behavior up to $30\,\mathrm{mA}$ output current. Parameters for conversion can be found in tab. A.2.

Stufe setting	slope [μA/V]	offset [μA]
1	0.1	+0.0
2	1.0	+0.0
3	10.0	+0.2
4	100.0	+0.1
5	1000.50	-2.5
6	$\approx$10000	$\approx$30

Table A.2: Calibration parameters for the CRESST-type floating current source with internal reference voltage selected. $I(x) = slope * x + offset$ yields I in μA for x in V. Only valid up to $30\,\mathrm{mA}$.
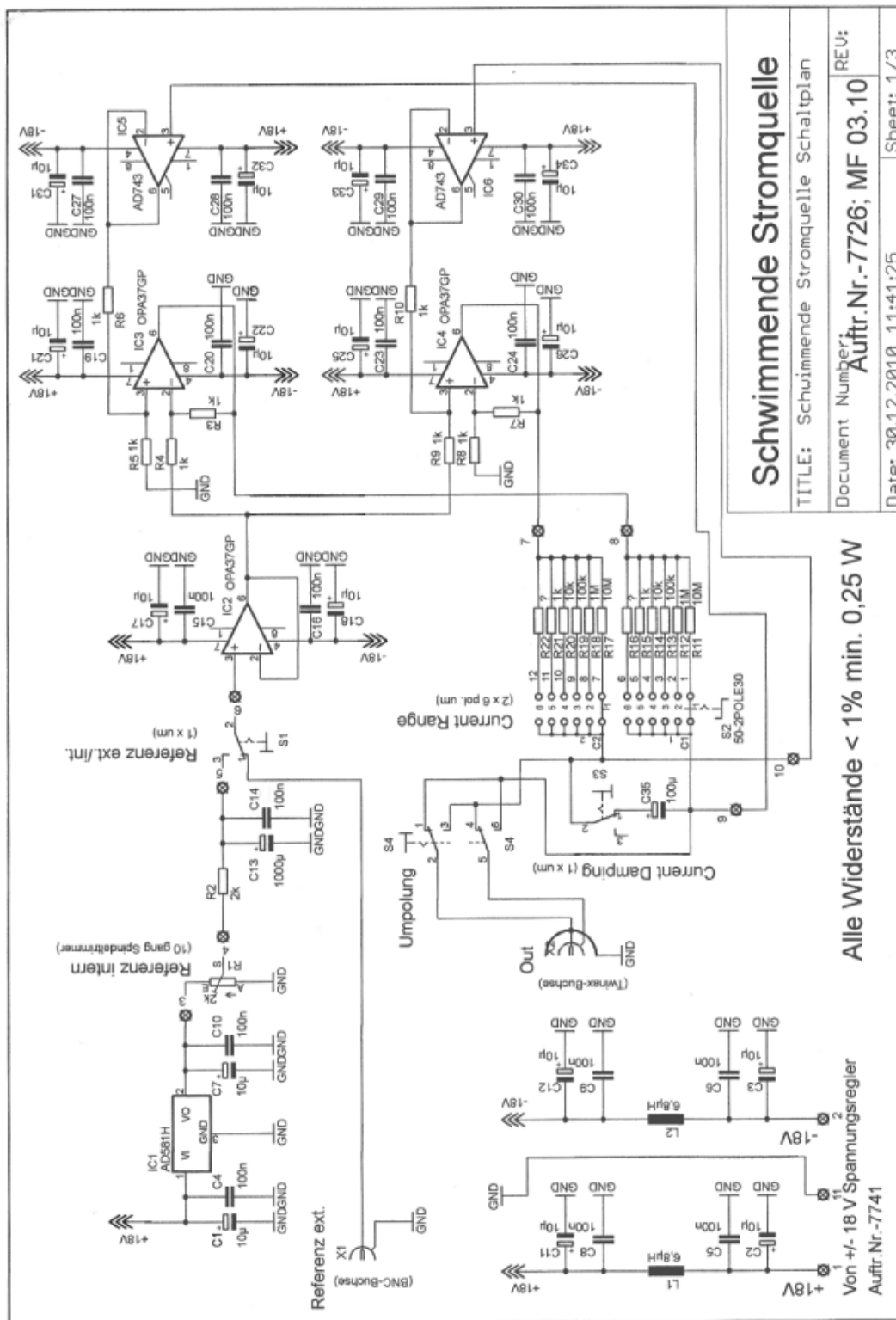
Figure A.1: Circuit diagram of the floating current source. The reference current is amplified, then split symmetrically around ground and amplified again. Drawing by [163], based on a diagram kindly provided Dr. F. Pröbst.

A.2 System requirements for the DAQ software

The system requirements for the TUM DAQ software are:

- LabVIEW 8.2

- Traditional drivers (Legacy) Version 7.4.2

- VISA version 4.0

- Windows XP Professional

Since Windows XP setup is not running on newer machines with SATA drives, a customized setup needs to be created, including the correct drivers. The necessary `*.iso` images can currently be found at:

`home/astro/sailer/UGL/LabVIEW`

In the Measurement and Automation Explorer (MAX) the default device numbering should be changed as the controller will be device 1 per default. As a last step, virtual channels should be created in MAX, matching the numbering of the BNC-2110 trigger board to ensure easy identification.

Instrument libraries, such as the AVS libraries provided by PICOWATT (see sec. 2.6), should be copied to the `instr.lib` folder which is found in the respective LabVIEW program folder.

A.3 SQUID bond layout for TES application

Fig. A.2 shows the bond connection scheme for TES application as can be found in [164]. Note that all the SQUIDs are already properly connected on the CAR-1.1 carrier. The feedback circuit can be accessed via the brass screws. Under normal circumstances no bonding is necessary.

Figure A.2: SQUID bond layout for TES application. [164]

A.4 AVS VI for writing temperature data

This program was written using the LabVIEW drivers for GPIB communication provided by PICOW-ATT [103]. The used custom made subVIs are:

- `startwritefile.vi` - creating the file, writing a header storing the used settings and defining the data structure.

- `create_timestamp.vi` - this VI generates three timestamp/date outputs:
  human readable e.g. `YYYY:MM:DD` and `HH:MM:SS`, *UTC format* as integer and string and a *filename conform* version that can be used to generate filenames automatically.

The block diagram of the main VI can be found in fig. A.3.
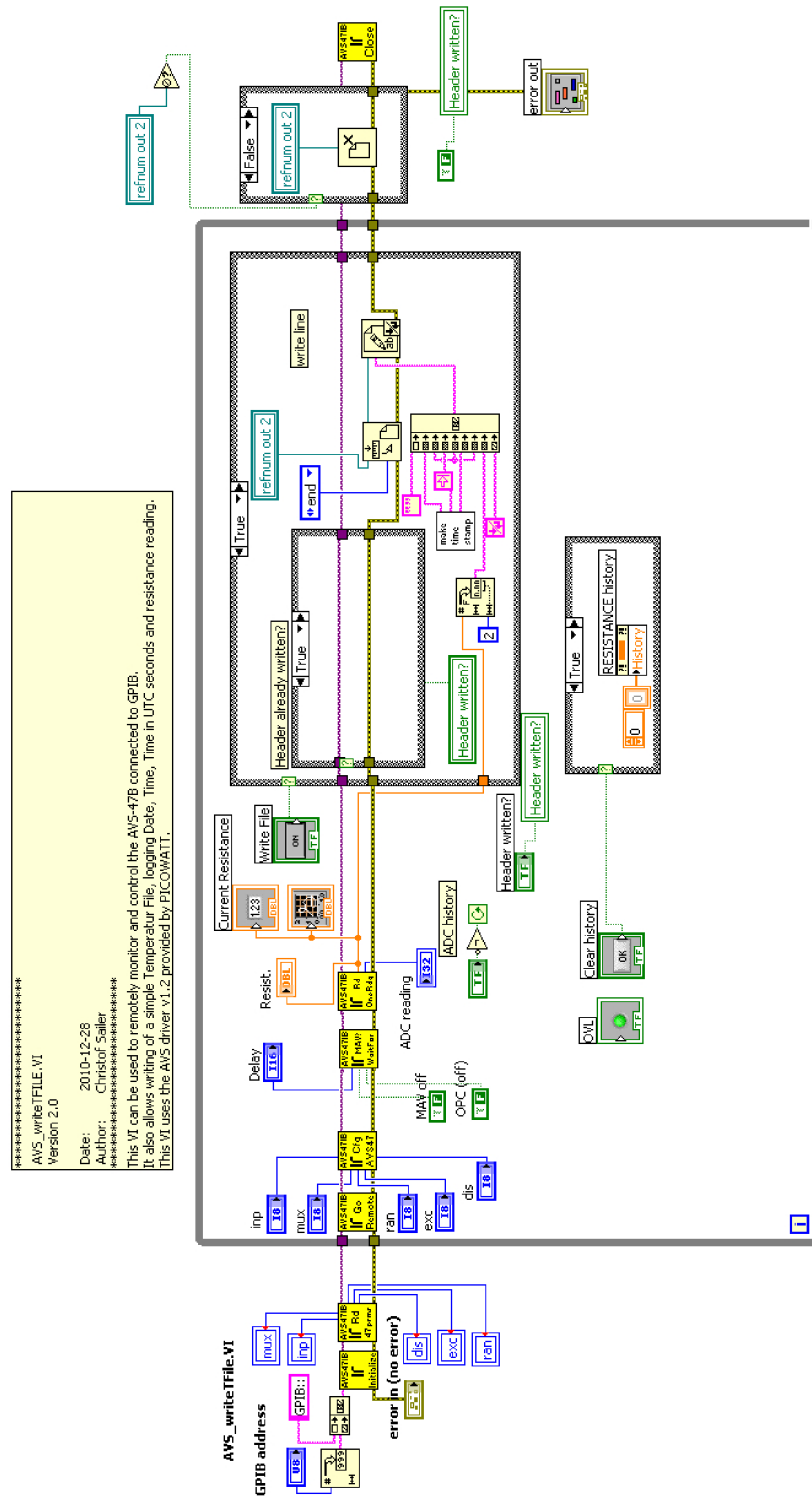
Figure A.3: Block diagram of the AVS-47B VI.

A.5 Installation and details of the low activity Lead shield

To shield the cryostat against radiation from the surrounding concrete and soil, a Lead shielding was designed during this work. It was manufactured by JL Goslar company using 8 t leftover Lead from the OPERA experiment. The OPERA collaboration measured the intrinsic contamination to be around 80 Bq/kg [165].

A standard ring has a height of 20 cm and weighs about 250 kg. In order to move the rings, there are three threads per ring available, as shown in fig. A.4. *Only use the swivel eye bolts* for transport. Due to the phase in the middle of the rings they are self-centering and the gaps between the layers show no direct line of sight.
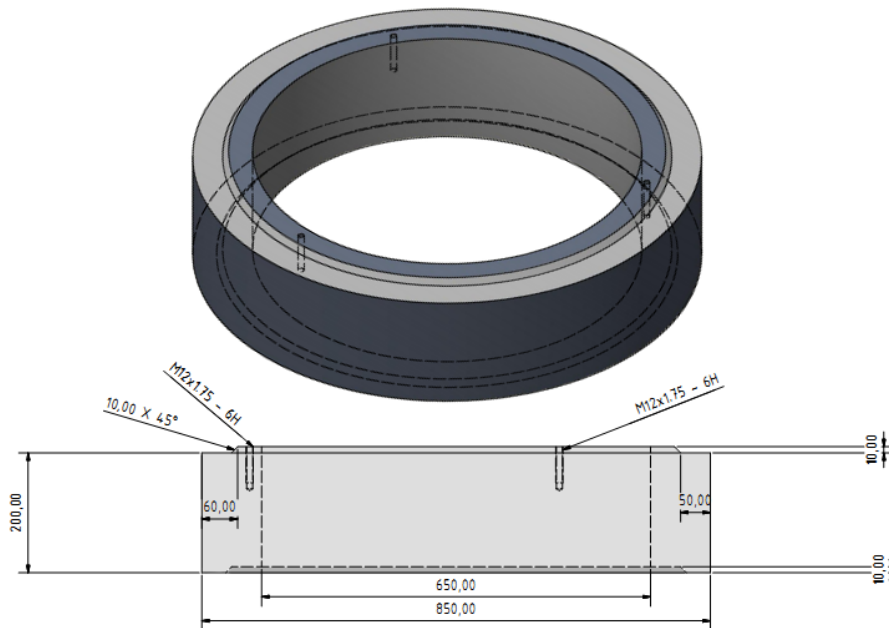
Figure A.4: Drawing of a standard Lead ring. The three threads can be used to move the ring using the installed crane. *Only use the swivel eye bolts* for transport! The rings are self-centering and leave no direct line of sight. All measures are given in mm.

A drawing of the complete shielding can be found in fig. A.5. The PE rings (white) are currently manufactured, the Lead shielding is already in place.
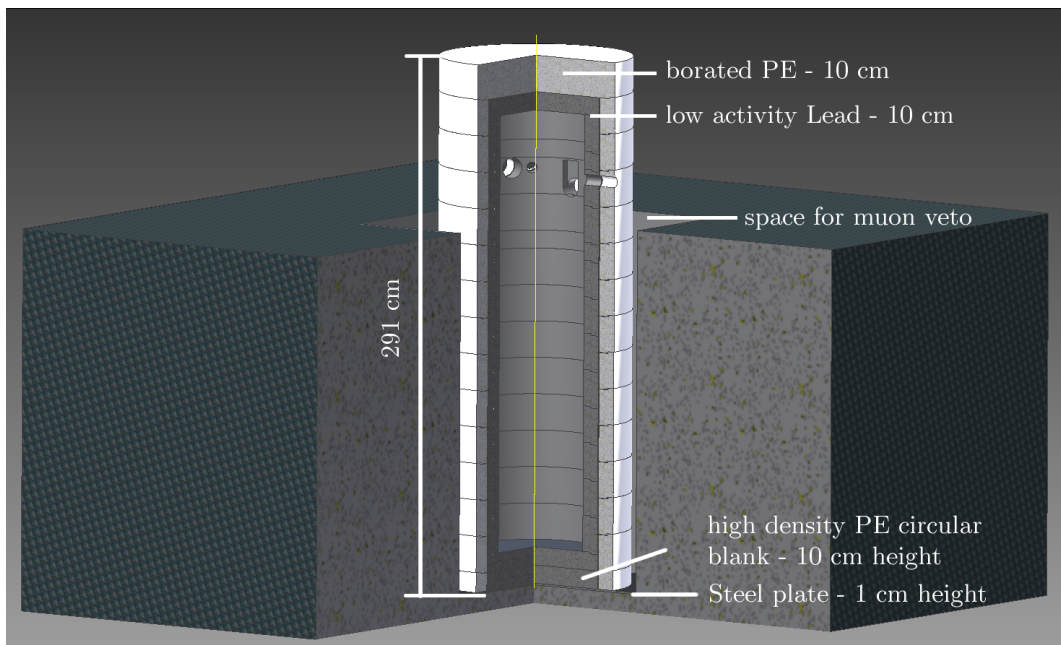
Figure A.5: Drawing of the cryostat's shielding. The PE rings are currently manufactured, the Lead shielding is already in place. The used Lead is taken from leftovers of the OPERA experiment. It's intrinsic contamination is around 80 Bq/kg.

Acknowledgments

Man überschätzt wohl leicht das eigene Wirken und Tun in seiner Wichtigkeit gegenüber dem, was man nur durch andere geworden ist.

Dietrich Bonhoeffer
(DBW 8, 157 f.)

Zuallererst möchte ich mich bei meinem Betreuer Prof. Dr. Josef Jochum für die Ermöglichung dieser interessanten, breit gefächerten Arbeit bedanken. Seine Begeisterung für die Astroteilchenphysik hat mich bereits im Studium inspiriert. Besonders bedanken möchte ich mich auch für seine Geduld und Unterstützung während meines längeren, krankheitsbedingten Ausfalls. Sein breites physikalisches Wissen, seine Fähigkeit schnell die richtigen Fragenstellungen zu erkennen und auch seine Mitarbeiterführung, die trotz aller fachlicher Herausforderung nicht den Menschen aus dem Blick verliert, sind mir ein Vorbild.

Weiterhin gilt mein Dank Prof. Dr. Peter Grabmayr für alle Beratung, besonders im Hinblick auf die Anschaffung der Plastikszintillatoren, SiPMs und Photomultiplier und die Unterstützung bei den Zollformalitäten.

Vielen Dank an Prof. Dr. Lachenmaier, besonders für die gesamte Organisation der Beschaffungen für das Untergrundlabor während der PostDoc Zeit in Tübingen, aber auch für alle Diskussionen rund um das SQUID System, Übergangsmessungen, Kryodetektoren und vieles mehr.

Danke an Prof. Dr. Heinz Clement und seine gesamte Arbeitsgruppe für die gute Zusammenarbeit im D4.

Many thanks to Dr. Bayarto Lubsandhorziev! His profound knowledge in the whole field of photon detection is invaluable and he was always ready to support and encourage us in our work. Many thanks also for organizing a lot of different crystal samples, including the LiF samples used in this work.

Danke an Dr. Thorsten Hehl für alle Hilfestellung bei Fragen zum Strahlenschutz, PMT-Base-Design und vielem mehr. Vielen Dank an Dr. Günter Lang, Frau Walz, Frau Eiskant und natürlich unseren Sekretärinnen Gaby Behring und Sonja Hierlemann, die uns viel Arbeit abgenommen haben. Danke auch an Herrn Brendle, der uns selbst im Ruhestand stets mit Rat und Tat zur Seite stand. Vielen Dank an unseren Systemadministrator Roland Speith für alle Unterstützung, vor allem bei der Beschaffung der neuen CAD-Lizenzen.

Besonderer Dank gilt Dr. Jörn Beyer an der PTB Berlin für seine Bereitschaft, uns immer wieder bei Fragen zur SQUID-Elektronik weiterzuhelfen und uns bei der Entwicklung in Richtung Multiplexer zu unterstützen.

Meinen Kollegen der Tübinger Arbeitsgruppe danke ich für alle Unterstützung, die gute Arbeits- (und darüber hinaus) Atmosphäre und alle Klinikbesuche, Telefonate etc. Danke an Igor für alle Unterstützung im UGL. Von deiner Erfahrung im Bereich der Tieftemperaturphysik habe ich sehr profitiert. Danke für deine Geduld und Ausdauer während unserer zweieinhalb-monatigen Lecksuche! Unsere gemeinsamen Meetings, Ausflüge und die legendäre "Bergsteiger"-Schicht in Italien werden mir in guter Erinnnerung bleiben. Danke Dennis für all die guten Gespräche und all deine Ermutigung.
Danke an Gerhard ("Wahhhhhhhh!"), Daniel (Mr. WarMUX), Markus K., Florian, Markus (der von der "Küste" :-) ...), Stephan "The Wiki" Scholl, Michael, Marcel, Klemens (danke fürs Korrekturlesen!) und Kai (danke für den BIBTEX Support!). Danke an Christian und Raphael, die mich in ihrer Diplomarbeit "ertragen" durften, und Martin (danke fürs Korrekturlesen!) und Büsra für die produktive Zusammenarbeit.

Acknowledgments

List of own publications

Diploma thesis:

C. Sailer, *Realisierung eines Messplatzes für Tieftemperatur-Detektoren*, Diplomarbeit, Eberhard-Karls Universität Tübingen, 2008.

Refereed contributions:

G. Angloher et al., Commissioning run of the CRESST-II dark matter search. *Astroparticle Physics*, 31:270–276, 2009. doi:10.1016/j.astropartphys.2009.02.007

J.-C. Lanfranchi et al., Neutron Scattering Facility for Characterization of CRESST and EURECA Detectors at mK Temperatures. *Opt. Mat.*, 31:1405–1409, 2009. doi:10.1016/j.optmat.2008.09.015

R. F. Lang et al., Discrimination of Recoil Backgrounds in Scintillating Calorimeters, *Astroparticle Physics*, 33:60–64, 2010. doi:10.1016/j.astropartphys.2009.11.004

R. F. Lang et al., Electron and Gamma Background in CRESST Detectors. *Astroparticle Physics*, 32:318–324, 2010. doi:10.1016/j.astropartphys.2009.09.009

R. V. Vasiliev et al., Measuring the Light Yield in a $CaMoO_4$ Scintillating Crystal. *Instruments and Experimental Techniques*, 53:795–799, 2010. doi:10.1134/S0020441210060059

F. Petricca et al., Latest results from the CRESST-II Dark Matter Search, *J. Phys.: Conf. Ser.*, 375:012003, 2012. doi:10.1088/1742-6596/375/1/012003

R. Falkenstein et al., Extensive studies of MRS APDs for plastic scintillator muon veto detectors of cryogenic experiments. *NIM A*, 695:330–333, 2012. doi:10.1016/j.nima.2011.10.031

G. Angloher et al., Results from 730 kg days of the CRESST-II Dark Matter Search. *Eur. Phys. J. C*, 72:1971, 2012. doi:10.1140/epjc/s10052-012-1971-8

C. Sailer et al., Low temperature light yield measurements in NaI and NaI(Tl). *Eur. Phys. J. C*, 72:2061, 2012. doi:10.1140/epjc/s10052-012-2061-7

R. Strauß et al., Neutron Scattering Facility for the Measurement of Light Quenching Factors of Dark Matter Detectors at Low Temperatures. *Journ. of Low Temp. Phys.* , 167:1063–1068, 2012. doi:10.1007/s10909-012-0536-4

R. Strauß et al., Precision Measurements of Light Quenching in $CaWO_4$ Crystals at mK Temperatures. *ArXiv e-prints*, 2014. arXiv:1401.3332, submitted to *Phys. Rev. Lett.*

Bibliography

[1] F. Zwicky. Die Rotverschiebung von extragalaktischen Nebeln. *Helvetica Physica Acta*, 6:110–127, 1933.

[2] S. van den Bergh. The Early History of Dark Matter. *Publications of the Astronomical Society of the Pacific*, 111:657–660, 1999. doi:10.1086/316369.

[3] M. Colless and A. M. Dunn. Structure and Dynamics of the Coma Cluster. *Astrophysical Journal*, 458:435, 1996. doi:10.1086/176827.

[4] F. Zwicky. On the Masses of Nebulae and of Clusters of Nebulae. *Astrophysical Journal*, 86:217–246, 1937. doi:10.1086/143864.

[5] D. Walsh, R. Carswell and R. Weymann. 0957+561 A, B: twin quasistellar objects or gravitational lens? *Nature*, 279:381–384, 1979.

[6] P. Young et al. The double quasar Q0957 + 561 A, B - A gravitational lens image formed by a galaxy at Z = 0.39. *Astrophysical Journal*, 241:507–520, October 1980. doi:10.1086/158365.

[7] K. M. Ashman. Dark Matter in Galaxies. *Publications of the Astronomical Society of the Pacific*, 104:1109–1138, 1992. doi:10.1086/133099.

[8] H. W. Babcock. The rotation of the Andromeda Nebula. *Lick Observatory Bulletin*, 19:41–51, 1939.

[9] J. P. Ostriker, P. J. E. Peebles and A. Yahil. The size and mass of galaxies, and the mass of the universe. *ApJ Letters*, 193:L1–L4, 1974. doi:10.1086/181617.

[10] C. Carignan and C. Purton. The "Total" Mass of DDO 154. *Astrophysical Journal*, 506:125–134, 1998. doi:10.1086/306227.

[11] M. Milgrom. A modification of the Newtonian dynamics as a possible alternative to the hidden mass hypothesis. *Astrophysical Journal*, 270:365–370, July 1983. doi:10.1086/161130.

[12] D. Clowe et al. A Direct Empirical Proof of the Existence of Dark Matter. *The Astrophysical Journal Letters*, 648(2):L109, 2006. doi:10.1086/508162.

[13] M. Bradač et al. Revealing the Properties of Dark Matter in the Merging Cluster MACS J0025.41222. *The Astrophysical Journal*, 687(2):959, 2008. doi:10.1086/591246.

[14] R. H. Sanders. Clusters of galaxies with modified Newtonian dynamics. *Monthly Notices of the Royal Astronomical Society*, 342(3):901–908, 2003. doi:10.1046/j.1365-8711.2003.06596.x.

[15] G. W. Angus, B. Famaey and H. S. Zhao. Can MOND take a bullet? Analytical comparisons of three versions of MOND beyond spherical symmetry. *Monthly Notices of the Royal Astronomical Society*, 371(1):138–146, 2006. doi:10.1111/j.1365-2966.2006.10668.x.

[16] D. J. Fixsen. The Temperature of the Cosmic Microwave Background. *The Astrophysical Journal*, 707(2):916, 2009. doi:10.1088/0004-637X/707/2/916.

[17] G. F. Smoot et al. Structure in the COBE differential microwave radiometer first-year maps. *Astrophysical Journal*, 396:L1–L5, September 1992. doi:10.1086/186504.

[18] C. L. Bennett et al. Four-Year COBE DMR Cosmic Microwave Background Observations: Maps and Basic Results. *The Astrophysical Journal Letters*, 464(1):L1, 1996. doi:10.1086/310075.

[19] E. Komatsu et al. Seven-year Wilkinson Microwave Anisotropy Probe (WMAP) Observations: Cosmological Interpretation. *Astrophysical Journal Supplement Series*, 192:18, 2011. doi:10.1088/0067-0049/192/2/18.

[20] P. A. R. Ade et al. (Planck Collaboration). Planck 2013 results. XVI. Cosmological parameters. *ArXiv e-prints*, 2013, arXiv:1303.5076.

[21] P. A. R. Ade et al. (Planck Collaboration). Planck 2013 results. XXII. Constraints on inflation. *ArXiv e-prints*, 2013, arXiv:1303.5082.

[22] D. J. Eisenstein et al. Detection of the Baryon Acoustic Peak in the Large-Scale Correlation Function of SDSS Luminous Red Galaxies. *The Astrophysical Journal*, 633(2):560, 2005. doi:10.1086/466512.

[23] F. Beutler et al. The 6dF Galaxy Survey: baryon acoustic oscillations and the local Hubble constant. *Monthly Notices of the Royal Astronomical Society*, 416(4):3017–3032, 2011. doi:10.1111/j.1365-2966.2011.19250.x.

[24] L. Anderson et al. The clustering of galaxies in the SDSS-III Baryon Oscillation Spectroscopic Survey: Baryon Acoustic Oscillations in the Data Release 10 and 11 galaxy samples. *ArXiv e-prints*, 2013, arXiv:1312.4877.

[25] E. D. Skillman et al. Neutral hydrogen observations of four dwarf irregular galaxies in the Virgo Cluster. *Astronomy & Astrophysics*, 185:61–76, 1987.

[26] G. Battaglia et al. The radial velocity dispersion profile of the Galactic halo: constraining the density profile of the dark halo of the Milky Way. *Monthly Notices of the Royal Astronomical Society*, 364: 433–442, 2005. doi:10.1111/j.1365-2966.2005.09367.x.

[27] M. Matthias and O. Gerhard. Dynamics of the boxy elliptical galaxy NGC 1600. *Monthly Notices of the Royal Astronomical Society*, 310(3):879–891, 1999. doi:10.1046/j.1365-8711.1999.03022.x.

[28] C. R. Keeton. Cold Dark Matter and Strong Gravitational Lensing: Concord or Conflict? *Astrophysical Journal*, 561:46, 2001. doi:10.1086/323237.

[29] M. Loewenstein and R. E. W. III. Prevalence and Properties of Dark Matter in Elliptical Galaxies. *Astrophysical Journal*, 518:50, 1999. doi:10.1086/307256.

[30] R. C. Hickox et al. The LABOCA survey of the Extended Chandra Deep Field-South: clustering of submillimetre galaxies. *Monthly Notices of the Royal Astronomical Society*, 421:284–295, 2012. doi:10.1111/j.1365-2966.2011.20303.x.

[31] N. Okabe et al. LoCuSS: The Mass Density Profile of Massive Galaxy Clusters at z = 0.2. *Astrophysical Journal Letters*, 769:L35, 2013. doi:10.1088/2041-8205/769/2/L35.

[32] C. Blake et al. The WiggleZ Dark Energy Survey: the selection function and z= 0.6 galaxy power spectrum. *Monthly Notices of the Royal Astronomical Society*, 406(2):803–821, 2010. doi:10.1111/j.1365-2966.2010.16747.x.

[33] A. Morselli. Indirect detection of dark matter, current status and recent results. *Progress in Particle and Nuclear Physics*, 66(2):208 – 215, 2011. doi:10.1016/j.ppnp.2011.01.008.

[34] P. D. Serpico. Status of indirect dark matter detection. *Journal of Physics: Conference Series*, 375(1): 012029, 2012. doi:10.1088/1742-6596/375/1/012029.

[35] J. Bovy and S. Tremaine. On the Local Dark Matter Density. *The Astrophysical Journal*, 756(1):89, 2012. doi:10.1088/0004-637X/756/1/89.

[36] The Dark Matter Scientific Assessment Group. *Report on the Direct Detection and Study of Dark Matter*. High Energy Physics Advisory Panel Reports, July 2007. URL http://science.energy.gov/hep/hepap/reports.

[37] R. D. Peccei and H. R. Quinn. CP Conservation in the Presence of Pseudoparticles. *Phys. Rev. Lett.*, 38:1440–1443, Jun 1977. doi:10.1103/PhysRevLett.38.1440.

[38] A. Kusenko and M. Shaposhnikov. Supersymmetric Q-balls as dark matter. *Physics Letters B*, 418 (12):46 – 54, 1998. doi:10.1016/S0370-2693(97)01375-0.

[39] G. Jungman, M. Kamionkowski and K. Griest. Supersymmetric dark matter. *Physics Reports*, 267 (56):195 – 373, 1996. doi:10.1016/0370-1573(95)00058-5.

[40] W. Hu, R. Barkana and A. Gruzinov. Fuzzy Cold Dark Matter: The Wave Properties of Ultralight Particles. *Phys. Rev. Lett.*, 85:1158–1161, Aug 2000. doi:10.1103/PhysRevLett.85.1158.

[41] P. Chen and R. J. Adler. Black hole remnants and dark matter. *Nuclear Physics B - Proceedings Supplements*, 124(0):103 – 106, 2003. doi:10.1016/S0920-5632(03)02088-7. Proceedings of the 5th International UCLA Symposium on Sources and Detection of Dark Matter and Dark Energy in the Universe.

[42] E. W. Kolb, D. J. H. Chung and A. Riotto. WIMPZILLAS! *Proc. of "DARK98" , Heidelberg, Germany*, FERMILAB-Conf-98/325-A:1, 1999. URL http://lss.fnal.gov/archive/1998/conf/Conf-98-325-A.pdf.

[43] J. F. Navarro, C. S. Frenk and S. D. M. White. A Universal Density Profile from Hierarchical Clustering. *The Astrophysical Journal*, 490(2):493, 1997. doi:10.1086/304888.

[44] K. Freese, J. Frieman and A. Gould. Signal modulation in cold-dark-matter detection. *Phys. Rev. D*, 37:3388–3405, Jun 1988. doi:10.1103/PhysRevD.37.3388.

[45] J. Lewin and P. Smith. Review of mathematics, numerical factors, and corrections for dark matter experiments based on elastic nuclear recoil. *Astroparticle Physics*, 6(1):87 – 112, 1996. doi:10.1016/S0927-6505(96)00047-3.

[46] R. H. Helm. Inelastic and Elastic Scattering of 187-Mev Electrons from Selected Even-Even Nuclei. *Phys. Rev.*, 104:1466–1475, Dec 1956. doi:10.1103/PhysRev.104.1466.

[47] M. Barnabé-Heider et al. Improved spin-dependent limits from the {PICASSO} dark matter search experiment. *Physics Letters B*, 624(34):186 – 194, 2005. doi:10.1016/j.physletb.2005.08.021.

[48] G. Angloher et al. (CRESST-II collaboration). Limits on WIMP dark matter using scintillating CaWO4 cryogenic detectors with active background suppression. *Astroparticle Physics*, 23(3):325 – 339, 2005. doi:10.1016/j.astropartphys.2005.01.006.

[49] G. Angloher et al. (CRESST-II collaboration). Commissioning run of the CRESST-II dark matter search. *Astroparticle Physics*, 31:270 – 276, 2009. doi:10.1016/j.astropartphys.2009.02.007.

[50] R. J. Strauß. *Energy-Dependent Quenching Factor Measurements of CaWO$_4$ Crystals at mK Temperatures and Detector Prototypes for Direct Dark Matter Search with CRESST*. Dissertation, Technische Universität München, München, 2013.

[51] J. Schmaler. *Status of the CRESST Dark Matter Search*. 13th International Workshop on Low Temperature Detectors, Stanford, July 2009.

[52] J. C. Lanfranchi et al. Neutron scattering facility for characterization of CRESST and EURECA detectors at mK temperatures. *Optical Materials*, 31(10):1405–1409, 2009. doi:10.1016/j.optmat.2008.09.015. 4th Workshop on Cryogenic Scintilation, Inst. Phys. Nucl. Lyon, FRANCE (June 2008).

[53] R. Strauß et al. Neutron Scattering Facility for the Measurement of Light Quenching Factors of Dark Matter Detectors at Low Temperatures. *Journal of Low Temperature Physics*, 167(5-6, 2):1063–1068, JUN 2012. doi:10.1007/s10909-012-0536-4.

[54] R. Strauss et al. Precision Measurements of Light Quenching in CaWO$_4$ Crystals at mK Temperatures. *ArXiv e-prints*, 2014, arXiv:1401.3332.

[55] G. Angloher et al. (CRESST-II collaboration). Results from 730 kg days of the CRESST-II Dark Matter search. *The European Physical Journal C*, 72:1–22, 2012. doi:10.1140/epjc/s10052-012-1971-8.

[56] A. K. Drukier, K. Freese and D. N. Spergel. Detecting cold dark-matter candidates. *Phys. Rev. D*, 33: 3495–3508, Jun 1986. doi:10.1103/PhysRevD.33.3495.

[57] R. Bernabei et al. Searching for WIMPs by the annual modulation signature . *Physics Letters B*, 424 (12):195 – 201, 1998. doi:10.1016/S0370-2693(98)00172-5.

[58] S. K. Lee et al. Effect of Gravitational Focusing on Annual Modulation in Dark-Matter Direct-Detection Experiments. *Phys. Rev. Lett.*, 112:011301, Jan 2014. doi:10.1103/PhysRevLett.112.011301.

[59] R. Bernabei et al. New results from DAMA/LIBRA. *The European Physical Journal C*, 67(1-2):39–49, 2010. doi:10.1140/epjc/s10052-010-1303-9.

[60] R. Bernabei et al. New limits on WIMP search with large-mass low-radioactivity NaI(Tl) set-up at Gran Sasso. *Physics Letters B*, 389(4):757 – 766, 1996. doi:10.1016/S0370-2693(96)80020-7.

[61] M. Felizardo et al. (The SIMPLE Collaboration). Final Analysis and Results of the Phase II SIMPLE Dark Matter Search. *Phys. Rev. Lett.*, 108:201302, May 2012. doi:10.1103/PhysRevLett.108.201302.

[62] L. Roszkowski, R. R. de Austri and R. Trotta. Implications for the Constrained MSSM from a new prediction for b $\rightarrow$ sγ. *Journal of High Energy Physics*, 2007(07):075, 2007. doi:10.1088/1126-6708/2007/07/075.

[63] J. Billard and E. Figueroa-Feliciano. Implication of neutrino backgrounds on the reach of next generation dark matter direct detection experiments. *ArXiv e-prints*, 2013, arXiv:1307.5458.

[64] C. Savage et al. Compatibility of DAMA/LIBRA dark matter detection with other searches. *Journal of Cosmology and Astroparticle Physics*, 2009(04):010, 2009. doi:10.1088/1475-7516/2009/04/010.

[65] C. E. Aalseth et al. (CoGeNT Collaboration). Results from a Search for Light-Mass Dark Matter with a p-Type Point Contact Germanium Detector. *Phys. Rev. Lett.*, 106:131301, Mar 2011. doi:10.1103/PhysRevLett.106.131301.

[66] C. E. Aalseth et al. (CoGeNT Collaboration). Search for an Annual Modulation in a *p*-Type Point Contact Germanium Dark Matter Detector. *Phys. Rev. Lett.*, 107:141301, Sep 2011. doi:10.1103/PhysRevLett.107.141301.

[67] C. Aalseth et al. (CoGeNT Collaboration). Search for An Annual Modulation in Three Years of CoGeNT Dark Matter Detector Data. *ArXiv e-prints*, 2014, arXiv:1401.3295.

[68] Z. Ahmed et al. (CDMS Collaboration). Results from a Low-Energy Analysis of the CDMS II Germanium Data. *Phys. Rev. Lett.*, 106:131302, Mar 2011. doi:10.1103/PhysRevLett.106.131302.

[69] Z. Ahmed et al. (CDMS Collaboration). Dark Matter Search Results from the CDMS II Experiment. *Science*, 327(5973):1619–1621, 2010. doi:10.1126/science.1186112.

[70] R. Agnese et al. (CDMS collaboration). Silicon Detector Dark Matter Results from the Final Exposure of CDMS II. *ArXiv e-prints*, 2013, arXiv:1304.4279.

[71] E. Armengaud et al. Final results of the EDELWEISS-II WIMP search using a 4-kg array of cryogenic germanium detectors with interleaved electrodes. *Physics Letters B*, 702(5):329 – 335, 2011. doi:10.1016/j.physletb.2011.07.034.

[72] E. Aprile et al. (XENON100 Collaboration). Dark Matter Results from 225 Live Days of XENON100 Data. *Phys. Rev. Lett.*, 109:181301, Nov 2012. doi:10.1103/PhysRevLett.109.181301.

[73] C. Savage et al. XENON10/100 dark matter constraints in comparison with CoGeNT and DAMA: Examining the $\mathcal{L}_{\text{eff}}$ dependence. *Phys. Rev. D*, 83:055002, Mar 2011. doi:10.1103/PhysRevD.83.055002.

[74] D. Akerib et al. (LUX collaboration). First results from the LUX dark matter experiment at the Sanford Underground Research Facility. *ArXiv e-prints*, 2013, arXiv:1310.8214.

[75] S. Chang et al. Inelastic dark matter in light of DAMA/LIBRA. *Phys. Rev. D*, 79:043513, Feb 2009. doi:10.1103/PhysRevD.79.043513.

[76] J. Schmaler. *The CRESST Dark Matter Search – New Analysis Methods and Recent Results*. PhD thesis, Technische Universität München, 2010.

[77] J. Schmaler. *Limits on Inelastic Dark Matter from CRESST*. Poster Session at TAUP2011, Munich, 2011. URL https://taup2011.mpp.mpg.de/?pg=Poster%20Session.

[78] R. Bernabei et al. Possible implications of the channeling effect in NaI(Tl) crystals. *The European Physical Journal C*, 53(2):205–213, 2008. doi:10.1140/epjc/s10052-007-0479-0.

[79] M. Kuźniak, M. Boulay and T. Pollmann. Surface roughness interpretation of 730kg x days CRESST-II results . *Astroparticle Physics*, 36(1):77 – 82, 2012. doi:10.1016/j.astropartphys.2012.05.005.

[80] Y. Kim. *KIMS*. Talk given at the Dark Matter Silver Jubilee Symposium, PNNL, June 2012. URL http://events.pnnl.gov/jubilee/agenda.stm.

[81] R. Maruyama. *DM-Ice: A direct detection experiment for dark matter at the South Pole*. Talk given at TAUP 2011, Munich, Germany, September 2011. URL https://taup2011.mpp.mpg.de.

[82] J. Cherwinka et al. (DM-Ice Collaboration). First Data from DM-Ice17. *ArXiv e-prints*, 2014, arXiv:1401.4804.

[83] J. L. Feng, J. Kumar and D. Sanford. Xenophobic dark matter. *Phys. Rev. D*, 88:015021, Jul 2013. doi:10.1103/PhysRevD.88.015021.

[84] C. Sailer. *Realisierung eines Messplatzes für Tieftemperatur-Detektoren*. Diplomarbeit, Eberhard-Karls Universität Tübingen, 2008.

[85] N. W. Ashcroft and N. D. Mermin. *Festkörperphysik*. Oldenburg Verlag München Wien, 3rd edition, 2007.

[86] C. Enss and S. Hunklinger. *Tieftemperaturphysik*. Springer Berlin/Heidelberg, 2000.

[87] F. Pröbst et al. Model for cryogenic particle detectors with superconducting phase transition thermometers. *Journal of Low Temperature Physics*, 100:69–104, 1995. doi:10.1007/BF00753837.

[88] C. Cozzini. *CRESST Dark Matter Search with Cryogenic Calorimeters*. PhD thesis, Ludwig-Maximilians-Universität München, 2003.

[89] K. D. Irwin. An application of electrothermal feedback for high resolution cryogenic particle detection. *Applied Physics Letters*, 66:1998–2000, 1995. doi:10.1063/1.113674.

[90] A. T. Lee et al. A superconducting bolometer with strong electrothermal feedback. *Applied Physics Letters*, 69(12):1801–1803, 1996. doi:10.1063/1.117491.

[91] Oxford Instruments. *Operator's Handbook Kelvinox 400 HA*. Oxford Instruments Nanoscience Limited, Tubney Woods, Abingdon, Oxon, OX13 5QX, England, 2006.

[92] J. Schnagl. *Entwicklung von Lichtdetektoren mit Phononenkollektoren für das CRESST Experiment*. PhD thesis, Institut für Astro-Teilchenphysik der Technischen Universität München, 2001.

[93] S. Roth. *Sputtered Tungsten Thin Films and Composite Detectors for the Application in the Dark Matter Experiments CRESST and EURECA*. Diplomarbeit, Technische Universität München, 2007.

[94] C. Isaila. *Development of Cryogenic Light Detectors with Neganov-Luke Amplification for the Dark Matter Experiments CRESST and EURECA*. PhD thesis, Technische Universität München, 2010.

[95] J. Beyer. *Private communication*, Nov. 2012.

[96] H. Nyquist. Thermal Agitation of Electric Charge in Conductors. *Phys. Rev.*, 32:110–113, Jul 1928. doi:10.1103/PhysRev.32.110.

[97] T. Lachenmaier. *Messungen mit untergrundarmen Tieftemperaturdetektoren zum hocheffizienten Nachweis des ^{71}Ge-Zerfalls*. Dissertation, Technische Universität München, München, 2005.

[98] D. Drung. High- T_c and low- T_c dc SQUID electronics. *Superconductor Science and Technology*, 16 (12):1320, 2003. doi:10.1088/0953-2048/16/12/002.

[99] D. Drung et al. Highly Sensitive and Easy-to-Use SQUID Sensors. *Applied Superconductivity, IEEE Transactions on*, 17:699–704, 2007. doi:10.1109/TASC.2007.897403.

[100] D. Drung, C. Hinnrichs and H.-J. Barthelmess. Low-noise ultra-high-speed dc SQUID readout electronics. *Superconductor Science and Technology*, 19(5):235, 2006. doi:10.1088/0953-2048/19/5/S15.

[101] C. Shannon. Communication in the presence of noise. *Proceedings of the IEEE*, 86(2):447–457, Feb 1998. doi:10.1109/JPROC.1998.659497.

[102] W. Westphal. *Development and Characterization of Cryogenic Detectors for the CRESST Experiment*. PhD thesis published online posthumously, 2008. URL www.e15.ph.tum.de/fileadmin/downloads/thesis/phd/2008_Wolfgang_Westphal.pdf.

[103] PICOWATT. *Application Note LABVIEW VI:s*. PICOWATT, Veromiehentie 14, FI-01510 VANTAA, Finland, 2nd edition, 2006.

[104] PICOWATT. *TS-530A temperature controller instruction manual*. PICOWATT, Veromiehentie 14, FI-01510 VANTAA, Finland, 1999.

[105] H. Kraus. *The OxRop data analysis software package*, 2013. URL http://www.physics.ox.ac.uk/Users/Kraus/research/oxrop.htm.

[106] J. Loebell. *Mass production and characterization of Tungsten TES sensors*. PhD thesis, Eberhard-Karls Universität Tübingen, in progress.

[107] I. Usherov-Marshak. *SQUID multiplexing*. PhD thesis, Eberhard-Karls Universität Tübingen, in progress.

[108] R. N. Claytor and B. J. Marshall. Specific Heat and Elastic Constants of Sodium Iodide at Low Temperatures. *Phys. Rev.*, 120:332–334, Oct 1960. doi:10.1103/PhysRev.120.332.

[109] M. Gluyas, F. D. Hughes and B. W. James. The elastic constants of calcium tungstate, 4.2-300 K. *Journal of Physics D: Applied Physics*, 6:2025, 1973. doi:10.1088/0022-3727/6/17/309.

[110] K. Schäffner et al. Alternative Scintillating Materials for the CRESST Dark Matter Search. *Journal of Low Temperature Physics*, 167(5-6):1075–1080, 2012. doi:10.1007/s10909-012-0488-8.

[111] R. Bernabei et al. The DAMA/LIBRA apparatus. *Nuclear Instruments and Methods A*, 592(3):297 – 315, 2008. doi:10.1016/j.nima.2008.04.082.

[112] C. Kittel. *Einführung in die Festkörperphysik*. Oldenbourg, 14. edition, 2006.

[113] C. Pédrini. Scintillation mechanisms and limiting factors on each step of relaxation of electronic excitations. *Physics of the Solid State*, 47(8):1406–1411, 2005. doi:10.1134/1.2014478.

[114] P. A. Rodnyi, P. Dorenbos and C. W. E. van Eijk. Energy Loss in Inorganic Scintillators. *physica status solidi (b)*, 187(1):15–29, 1995. doi:10.1002/pssb.2221870102.

[115] M. Moszyński et al. Study of pure NaI at room and liquid nitrogen temperatures. *Nuclear Science, IEEE Transactions on*, 50(4):767–773, 2003. doi:10.1109/TNS.2003.815176.

[116] W. van Sciver. Alkali Halide Scintillators. *Nuclear Science, IRE Transactions on*, 3(4):39–50, 1956. doi:10.1109/TNS2.1956.4315545.

[117] H. B. Dietrich et al. Kinetics of Self-Trapped Holes in Alkali-Halide Crystals: Experiments in NaI(Tl) and KI(Tl). *Phys. Rev. B*, 8:5894–5901, Dec 1973. doi:10.1103/PhysRevB.8.5894.

[118] C. Strandhagen. *Private Communication*, Oct. 2013.

[119] R. Barlow. Asymmetric Systematic Errors. *ArXiv e-prints*, June 2003, arXiv:physics/0306138.

[120] R. Strauß. *R&D for Bolometer based DM Experiments*. Talk at the Workshop on future Dark Matter Experiments, Vienna, October 2013, 10 2013.

[121] W. J. van Sciver and L. Bogart. Fundamental Studies of Scintillation Phenomena in NaI. *Nuclear Science, IRE Transactions on*, 5(3):90 –92, dec. 1958. doi:10.1109/TNS2.1958.4315632.

[122] C. Sailer et al. Low temperature light yield measurements in NaI and NaI(Tl). *The European Physical Journal C - Particles and Fields*, 72:1–4, 2012. doi:10.1140/epjc/s10052-012-2061-7.

[123] C. Oßwald. *Die Szintillationseigenschaften von einkristallinem CaWO$_4$ bei unterschiedlichen Temperaturen*. Zulassungsarbeit, Eberhard-Karls Universität Tübingen, 2007.

[124] Janis. *Operating Instructions for the Janis Research Model SVT-400 Research Cryostat*. Janis Research Company, 2 Jewel Drive, Wilmington, MA, U.S., 2005.

[125] *Supplier's contact details*. Saint-Gobain Crystals, 2014. URL http://www.crystals.saint-gobain.com. (accessed on 2014-02-28).

[126] *Supplier's contact details*. Aachener Quarz-Glas Technologie Heinrich, Im Süsterfeld 4, D-52072 Aachen, Germany, 2014. URL http://www.quarzglas-heinrich.de. (accessed on 2014-02-28).

[127] J. B. West and A. J. L. Collinson. The low temperature scintillation response of unactivated sodium iodide to gamma-rays. *Journal of Physics B: Atomic and Molecular Physics*, 3(10):1363, 1970. doi:10.1088/0022-3700/3/10/014.

[128] Bicron. *Sodium Iodide - Alkali Halide Scintillation Material, Datasheet*. Bicron, Newbury, Ohio, U.S., 1996.

[129] E. Sakai. Recent Measurements on Scintillator-Photodetector Systems. *Nuclear Science, IEEE Transactions on*, 34(1):418–422, Feb 1987. doi:10.1109/TNS.1987.4337375.

[130] I. Holl, E. Lorenz and G. Mageras. A measurement of the light yield of common inorganic scintillators. *Nuclear Science, IEEE Transactions on*, 35(1):105–109, Feb 1988. doi:10.1109/23.12684.

[131] M. Moszyński et al. Characterization of CaWO4 scintillator at room and liquid nitrogen temperatures. *Nuclear Instruments and Methods A*, 553(3):578 – 591, 2005. doi:10.1016/j.nima.2005.07.052.

[132] H. Kraus and V. Mikhailik. First test of a cryogenic scintillation module with a CaWO4 scintillator and a low-temperature photomultiplier down to 6K. *Nuclear Instruments and Methods A*, 621(13):395 – 400, 2010. doi:10.1016/j.nima.2010.05.008.

[133] D. Pooley and W. A. Runciman. Recombination luminescence in alkali halides. *Journal of Physics C: Solid State Physics*, 3(8):1815, 1970. doi:10.1088/0022-3719/3/8/022.

[134] G. F. Knoll. *Radiation detection and measurement; 3rd ed.* Wiley, New York, NY, 2000.

[135] M. P. Fontana, H. Blume and W. J. van Sciver. Properties of Exciton States in NaI I. The Intrinsic Photoluminescence. *physica status solidi (b)*, 29(1):159–166, 1968. doi:10.1002/pssb.19680290117.

[136] P. Sibczyński et al. Study of NaI(Tl) scintillator cooled down to liquid nitrogen temperature. *Journal of Instrumentation*, 7(11):P11006, 2012. doi:10.1088/1748-0221/7/11/P11006.

[137] R. B. Murray and F. J. Keller. Recombination Luminescence from V_K Centers in Potassium Iodide. *Physical Review*, 137:942–948, February 1965. doi:10.1103/PhysRev.137.A942.

[138] *Supplier's contact details*. Hilger Crystals Ltd, Unit R1 Westwood Estate, Margate Kent CT9 4JL, UK, 2014. URL http://www.hilger-crystals.co.uk. (accessed on 2014-03-04).

[139] B. N. L. National Nuclear Data Center. *NuDat (Nuclear Structure and Decay Data)*, March 2008.

[140] W. R. Leo. *Techniques for Nuclear and Particle Physics Experiments*. Springer Berlin / Heidelberg, 2nd edition, 1994. (see p. 64).

[141] F. Ajzenberg-Selove. Energy levels of light nuclei A = 5–10. *Nuclear Physics A*, 490(1):1 – 225, 1988. doi:10.1016/0375-9474(88)90124-8.

[142] S. Mughabghab and N. Holden. *Neutron resonance parameters and thermal cross sections*. Number 1, Part 1 in Neutron cross sections series. Academic Press, 1981.

[143] P. Smith et al. Tests on low temperature calorimetric detectors for dark matter experiments. *Physics Letters B*, 245(2):265 – 270, 1990. doi:10.1016/0370-2693(90)90145-V.

[144] P. de Marcillac et al. Characterization of a 2 g LiF bolometer. *Nuclear Instruments and Methods A*, 337:95 – 100, 1993. doi:10.1016/0168-9002(93)91140-I.

[145] D.-L. Zhou. *CNDC-3.1 MAT 325*, June 1994.

[146] W. W. Scales. Specific Heat of LiF and KI at Low Temperatures. *Phys. Rev.*, 112:49–54, 1958. doi:10.1103/PhysRev.112.49.

[147] Hale et al. *ENDF/B-VII.1 MAT 825*, December 2006.

[148] A. Dementyev et al. Production and transport of hadrons generated in nuclear cascades initiated by muons in the rock (exclusive approach). *Nuclear Physics B - Proceedings Supplements*, 70(13):486 – 488, 1999. doi:10.1016/S0920-5632(98)00478-2.

[149] S. Scholl. *Neutron Background Simulation for the CRESST-II Experiment*. PhD thesis, Universität Tübingen, 2011.

[150] L. Leal. *ENDF/B-VII.1 MAT 7431*, January 2008.

[151] M. Chadwick, P. Young and Arthur. *ENDF/B-VII MAT 7434 (REV 1)*, October 1996.

[152] M. Chadwick, P. Young and Arthur. *ENDF/B-VII MAT 7437 (REV 1)*, October 1996.

[153] M. Chadwick, P.G.Young and Arthur. *ENDF/B-VII MAT 7443 (REV 1)*, October 1996.

[154] A. Koning. *ENDF/B-VII.1 MAT 2025 (REV 1)*, October 2004.

[155] Z. Zhao et al. *ENDF/B-VII.1 MAT 925*, October 2003.

[156] P.G.Young. *ENDF/B-VII.1 MAT 328*, August 1988.

[157] H. Wulandari. *Study On Neutron-Induced Background in the Dark Matter Experiment CRESST*. PhD thesis, Technische Universität München, 2003.

[158] P. Belli et al. Search for 7Li solar axions using resonant absorption in LiF crystal: Final results. *Physics Letters B*, 711(1):41 – 45, 2012. doi:10.1016/j.physletb.2012.03.067.

[159] D. Tilley, H. Weller and H. Hasan. Energy levels of light nuclei A = 3. *Nuclear Physics A*, 474(1):1 – 60, 1987. doi:10.1016/0375-9474(87)90193-X.

[160] L. Lisitsyna et al. Short-lived primary radiation defects in LiF crystals. *Physics of the Solid State*, 43 (9):1680–1685, 2001. doi:10.1134/1.1402223.

[161] A. Golovin, N. Zakharov and P. Rodnyi. Eigen luminescence of Lithium and Sodium Fluorides. *Optika i Spektroskopiya*, 67(2):337–341, AUG 1989.

[162] M. Uffinger. *Private Communication*, Jan. 2014.

[163] M. Faiß. *Schwimmende Stromquelle - Technische Daten*. Elektronik-Werkstatt Universität Tübingen, 2010.

[164] Magnicon. *High Performance dc SQUID Electronics XXF-1*. Magnicon GmbH, v 3.1.4 edition, 11 2006.

[165] A. Anokhina et al. Study of the effects induced by lead on the emulsion films of the OPERA experiment. *Journal of Instrumentation*, 3(07):P07002, 2008. doi:10.1088/1748-0221/3/07/P07002.